Mineralogical and chemical properties of thermally treated and ground illitic clays as precursor materials for geopolymer binders

I n a u g u r a l d i s s e r t a t i o n

zur

Erlangung des akademischen Grades eines

Doktors der Naturwissenschaften (Dr. rer. nat.)

der

Mathematisch-Naturwissenschaftlichen Fakultät

der

Ernst-Moritz-Arndt-Universität Greifswald

vorgelegt von

Jan Dietel

geboren am 09.08.1985

in Rodewisch / Vogtland

Greifswald, 23.11.2015

Dekan:	Prof. Dr. Klaus Fesser
1. Gutachter:	Prof. Laurence N. Warr, Ph.D.
2. Gutachter:	Prof. Dr. Helge Stanjek
Tag der Promotion:	07.04.2016

Table of content

Abstract

Geopolymers (GPs) are inorganic binders created by adding alkaline solution (e.g. KOH) to silicates such as furnace slag, fly ash or clay to dissolve Si and Al that polymerises and precipitates to form an inorganic binder material while hardening.

GP properties are similar to ordinary Portland cement regarding their high compressive strength or low shrinkage but they are particularly notable for a high resistance to acid and fire. However, the most significant advantage of GP cements is their low CO_2 footprint. The most common clay used as GP raw material is kaolin. The aim of this study is to investigate the suitability of illitic clays as a cheaper alternative to kaolin and determine the necessary preparation steps required to produce effective GP binder materials. Three clays dominated by dioctahedral 2:1 layer silicates, in particular interstratifications of mica and smectite were investigated: (1) Illitic clay from Friedland, Northern Germany, containing an irregularly stacked illite-smectite interstratification (*R*0 I-S), (2) rectorite from Arkansas, USA, as a regular interstratification of mica and smectite, and (3) clay stated as "sárospatakite" from Füzérradvány clay deposit, Northern Hungary, containing a long range ordered I-S (*R*3). The three types of I-S interstratification-rich clays were extensively characterised and the Friedland clay, as the most probable raw material for GP production, was studied in more detail including several size fraction analyses. These results are used to investigate and determine the parameters necessary to produce suitable precursors for GP binders.

Different approaches of clay activation to yield a highly reactive material by milling and heating were examined. Milling was found to be suitable as a preparation step after heating breaking up sintering aggregates to create pathways for the alkaline solution, but not as a substitute for heating. Important parameters for the precursor design such as temperature, time, and heating rate are determined and discussed.

Geopolymerisation is considered to be a multi-parameter system and is influenced strongly by the degree of dehydroxylation, Si:Al ratio, or amount of 5-fold coordinated Al. However, in contrast to kaolin-based systems, none of these parameters explain why the illitic Friedland clay heated to 875 °C was found to be most suitable for GP binders. Based on leaching experiments and specific surface area (A_S) measurements of the heated Friedland clay, a conceptual model is presented to explain the observed relationship between the heating temperature and the subsequent compressive strength of the GP cement. An optimum between the counteracting reactions of decreasing A_S (fewer particles must be covered with GP phase) and decreasing Si+Al dissolved (less GP phase created) is necessary, which exists at 875 °C for the Friedland clay. In this state enough GP phase is created to bind all remaining sintering aggregates to form a cement with high compressive strength. This relationship can be expressed as (Si+Al) / A_S (sum of dissolved Si and Al divided by the surface area of grains that must be covered with GP phase), and can be used as a predictive tool for determining the optimal heating temperature.

The results presented in this thesis indicate that illitic clays are suitable raw materials as GP binders if the necessary preparation steps of dehydroxylation, sintering and grinding are made. Proxies used to evaluate the optimal conditions for making GP binders are determined including the (Si+Al) / A_S ratio as a key relationship that controls the cementation process and determines its ultimate hardness.

Zusammenfassung

Geopolymere (GP) sind anorganische Bindemittel, welche aus Silikaten wie Hochofenschlacke, Flugasche oder Ton hergestellt werden. Durch Zugabe basischer Lösungen (z.B. KOH) wird Si und Al gelöst, welches anschließend polymerisiert und während der Aushärtung ein Si-Al-Netzwerk bildet, das als Bindemittel fungiert.

Die Eigenschaften von GP sind bezüglich Druckfestigkeit oder Schrumpfung denen von Portlandzement (OPC) ähnlich, besitzen jedoch Vorteile wie Säure- und Feuerresistenz. Der größte Vorteil von GP gegenüber OPC ist jedoch die geringe CO_2-Emmission während der Produktion. Zurzeit dient Kaolin als häufigster Tonrohstoff für die GP-Herstellung. Ziel dieser Arbeit ist die Eignungsuntersuchung illitischer Tone als kostengünstigere Alternative für Kaolin und die Ermittlung notwendiger Aufbereitungsschritte für die GP-Herstellung. Drei durch dioktaedrische 2:1 Schichtsilikate dominierte Tone, insbesondere Glimmer-Smectit-Wechsellagerungen, wurden untersucht: (1) Ton aus Friedland (N-Deutschland), mit hohem Anteil einer unregelmäßigen Illit-Smectit-Wechsellagerung (*R*0 I-S), (2) Rektorit von Arkansas (USA), als eine regelmäßige Glimmer-Smectit-Wechsellagerung und (3) als “Sárospatakit” bezeichneter Ton aus dem Füzérradvány Tonvorkommen (N-Ungarn), mit hohem Anteil einer I-S-Wechsellagerung mit Reichweite *R*3. Diese Tone wurden ausführlich qualitativ und quantitativ untersucht, wobei der Fokus auf Friedlandton als dem wahrscheinlichsten Edukt für die GP-Herstellung lag. Auf Basis der erlangten Ergebnisse wurden notwendige Parameter zur Herstellung geeigneter GP-Präkursoren bestimmt.

Um ein reaktives Präkursor-Material zu erhalten, wurden Mahlung und Aufheizung als mögliche Aktivierung der Ton-Edukte untersucht. Die Mahlung der Proben stellte sich als geeignet heraus, um die durch Sinterung entstandenen Sinteraggregate aufzubrechen und so Reaktionswege für die basische Lösung zu erhöhen. Als Ersatz für ein Aufheizen ist die Mahlung nicht geeignet. Wichtige Parameter für die Präkursor-Herstellung wie Temperatur, Heizdauer oder Heizrate wurden ermittelt und diskutiert.

Die Geopolymerisation wurde als ein Multiparametersystem identifiziert, welches unter anderem durch den Grad der Dehydroxylation, dem Si:Al Verhältnis oder dem Anteil 5-fach koordinierten Aluminiums beeinflusst wird. Im Gegensatz zu Kaolin-basierten Systemen erklärt jedoch keiner dieser Parameter, warum bei 875 °C aufgeheizter Friedlandton sich als besonders geeignet für die GP-Herstellung erwiesen hat. Basierend auf Löslichkeitsexperimenten und der Bestimmung der spezifischen Oberfläche (A_S) kalzinierten Friedlandtons wurde ein Model entwickelt, welches die Eignung des bei 875 °C aufgeheizten Friedlandtons und das Verhältnis der Druckfestigkeit zur Sintertemperatur erklärt. Zwischen den gegenläufigen Reaktionen abnehmender A_S (weniger Aggregate müssen mit verbunden werden) und abnehmendem Gehalt von gelöstem Si+Al (weniger GP-Phase gebildet), muss ein Optimum gefunden werden. Im Fall des Friedlandtons existiert dieses Optimum bei 875 °C, bei dem ausreichend Geopolymerphase gebildet wird, um alle Aggregate zu verbinden und einen Zement mit hoher Druckfestigkeit bilden zu können. Dieses Verhältnis kann als (Si+Al) / A_S (Summe der gelösten Si+Al-Spezies geteilt durch die spezifische Oberfläche der Aggregate) beschrieben werden, mit Hilfe dessen die optimale Sintertemperatur bestimmt werden kann.

Die in dieser Arbeit präsentierten Resultate zeigen, dass illitische Tone zur GP-Herstellung geeignet sind. Die hierfür notwendigen Aufbereitungsschritte wurden für Labor- und industriellem Maßstab bestimmt. Zudem wurden einfach zu bestimmende Parameter beschrieben, um die optimale Kalzinierungstemperatur, die für jeden potentiell geeigneten Ton bestimmt werden sollte, zu ermitteln.

1 Introduction

1.1 Motivation and Objective

Geopolymers (GPs) are inorganic binder materials formed from aluminum-silicates (Al octahedrally coordinated, Liebau, 1985) or aluminosilicates (Al tetrahedrally coordinated, Liebau, 1985), such as furnace slag, fly ash, feldspar or clay. These silicates are “activated” by an alkaline solution to form an inorganic binder material. GPs were first described by Gluchovskij (1959) and later by Davidovits (1988) who introduced the name “geopolymer” consisting of two words combined to one. The noun polymer refers to the structure which can be regarded as a product of a polycondensation reaction, similar to that in organic chemistry. A geopolymer (GP) is therefore an inorganic polymer whereby the syllable “geo” refers to the origin of the precursor, which is typically an Earth-derived “geo-material” such as clay, feldspars, and the waste products of burning coal or metallic ores (Xu & van Deventer, 2003).

GPs are considered to be as versatile as ordinary Portland cement (OPC) and many properties can be adjusted depending on the application (e.g. Duxson *et al.*, 2007c). The properties are similar to OPCs regarding their high compressive strength or low shrinkage but they are particularly notable for acid and fire resistance. However, the most significant advantage of GP cements, which makes them of particular interest in the context of global warming, is their low CO_2 footprint (Duxson *et al.*, 2007c; McLellan *et al.*, 2011). OPC is commonly produced from limestone (≈85 mass% (% w/w)) with minor additives of clay, sand or iron (e.g. Halamickova *et al.*, 1995). These educts are ground and then heated to ≈1450 °C with the help of rotary ovens to produce clinker by reactions schematically shown in equations 1.1 and 1.2. Calcite is chosen as the representative mineral component of limestone, muscovite for clay, and quartz for sand. The main phases in this clinker material are “alite” (50-70% w/w, C_3S, Ca_3SiO_5) and “belite” (15-30% w/w, C_2S, Ca_2SiO_4) (Gougar *et al.*, 1996). Following chemomechanical activation by grinding of the clinker together with gypsum, cement is produced (Gouger *et al.*, 1996). By hydration with water (50 mol-% water + 50 mol-% cement), ettringite ($Ca_6Al_2(SO_4)_3(OH)_{12}\times26H_2O$) is formed which is transformed over hours and days into calcium silicate hydrate phases (CSH) that are commonly X-ray amorphous or crystalline like thaumasite ($Ca_3Si(OH)_6(CO_3)(SO_4)\times12H_2O$) or tobermorite ($Ca_5Si_6O_{16}(OH)_2\times4H_2O$) (Halamickova *et al.*, 1995; Gouger *et al.*, 1996). Due to heating the highly carbonatic educt (limestone), a large amount of CO_2 is released during oxidation in the oven, most of which enters the atmosphere. Because CO_2 is a greenhouse gas that absorbs some of the thermal radiation emitted from the earth´s surface, the increasing concentration of this gas in the Earth´s atmosphere is considered to be the prime source of current global warming (Lashof & Ahuja, 1990). Globally, OPC production is currently held responsible for at least 5-8% of anthropogenic CO_2 emissions (McLellan *et al.*, 2011; VanDeventer *et al.*, 2011).

$$limestone\ (87\%) + clay(6\%) + sand(4\%) + steel(3\%) \xrightarrow{1450\ ^{\circ}C} \quad 1.1$$

$$C_3S\ (12\%) + C_2S\ (6\%) + C_3A\ (5\%) + C_4AF\ (2\%) + K_2O\ (2\%) + CO_2(69\%) + water(5\%)$$

$$60\ CaCO_3 + 4\ KAl_3[AlSi_3O_{10}|(OH)_2] + 3\ SiO_2 + 2\ Fe_2O_3 \xrightarrow{1450\ ^{\circ}C} \quad 1.2$$

$$10\ Ca_3SiO_5 + 5\ \beta - Ca_2SiO_4 + 4\ Ca_3Al_2O_6 + 2\ Ca_4Al_2Fe_2O_{10} + 2\ K_2O + 60\ CO_2 \uparrow + 4\ H_2O \uparrow$$

Replacing OPC with low-CO_2 furnace slag, fly ash, or clay educts for binder production therefore is of interest in terms lowering CO_2 emissions and helping to counteract the anthropogenic greenhouse effect.

Currently, the most common clay used for GP binder materials is kaolin (e.g. Lee & van Deventer, 2002, Duxson *et al.*, 2007a,b, Temuujin *et al.*, 2009, Hounsi *et al.*, 2013), but due its relatively high costs, finding a cheaper alternative clay for this purpose is of interest. In contrast, using 2:1 layer silicates as raw materials for GP binders, such as mica, smectite or even illite-smectite interstratifications (I-S) has been poorly researched. Using high quality industrial bentonite consisting of more than 60% w/w smectite is generally not of interest due to their relative high expensive of the material. However, illitic clays that contain high amounts of I-S interstratifications and often additionally micaceous phases (e.g. muscovite, phlogopite or annite, or interlayer deficient micas like illite) are notably cheaper and abundant worldwide. According to Galán & Ferrell (2013) clays constitute a major global mineral resource used in industry, for example those used for structural ceramics, whereby 90% of production uses brick type illitic clays and only 10% are more specialised clays such as bentonite or kaolin. Therefore using the common illitic clays as a raw material for GP production is of potential economic interest due to lower raw material costs. McLellan *et al.* (2011) compared kaolin based GP costs with that of OPC and concluded they may range from 7% lower to 39% higher. As a result, illitic clays may have the potential to significantly reduce the cost of GP cements and due to their lower CO_2 emissions could offer a more environmentally friendly, economic and affordable product.

The present work is part of a larger programme of research entitled: “Geopolymers from Friedländer Eocene clay: mineralogical and geochemical studies”, which was funded by European development funds (FuE project 2010-2013). The aim of the programme was to investigate clay from Friedland, Northern Germany, dominated by micaceous material. The primary goal was to research whether or not Friedland clay is suitable as a raw material to produce stable GP binder materials and to establish which preparation steps are necessary to produce the optimal cement. The focus of the research reported in this thesis was to investigate the thermal behaviour of I-S rich clays and I-S interstratifications for GPs and to determine the optimal preparation steps required to produce a highly reactive precursor heated

clay ("metaclay") material. An accompanying study of the alkaline activation of the Friedland "metaclay" is reported in the dissertation thesis of Hu (submitted).

The study presented is based on an extensive characterisation of three types of I-S interstratifications with different contents of micaceous layers, degree of ordering, and dehydration and dehydroxylation behaviour. The complex bulk mineralogy of the clays and the crystal-chemistry of I-S phases were characterised both qualitatively and quantitatively. These results are used to determine the optimal parameters necessary to produce a suitable precursor from these bulk samples. Different approaches of clay activation were examined to yield a highly reactive material such as milling and/or heating and the activated clays were evaluated in terms of their suitability as GP precursor materials. Particular emphasis was given to determining the optimal heating parameters in terms of temperature, time, and heating rate as studied in the laboratory in order to determine the ideal "metaclay" precursor material suitable for large scale industrial applications.

Additionally, some first tests of producing a suitable "metaclay" on the industrial scale were undertaken to evaluate necessary parameters that may differ from those determined in the laboratory. These industrially produced precursors were characterised and compared with laboratory produced precursor materials to evaluate the suitability. The work presented is considered to be relevant to the industrial scale production of a suitable "metaclay" that could be used for a low-cost GP binder material based on illitic 2:1 layer silicates. Such illitic-based GP cements have the potential to be suitable for use as bricks, ceramics, fire and heat resistant materials, low CO_2 cements and concretes, radioactive and toxic waste containment, and materials applicable to astronautics, the automobile industry, the sealing boreholes, as well as a range of other applications (Rangan, 2010).

1.2 How to make a clay based geopolymer

GPs are inorganic binder materials formed by connecting Si and Al atoms into a chain-like polymer structure. To produce more reactive Si and Al species, some preparation steps are necessary, which are described as follows.

Raw clay material is commonly hydrated and exhibits strongly oxygen bonded Si and Al. A high water content leads to dilution of the added base which lowers the reactivity of Si and Al. Hence, the initial water content must be reduced and Si and Al transformed into an easily dissolvable form. Si primarily appears in framework silicates like quartz or feldspars and in layer silicates in the tetrahedral sheet. Al occurs tetrahedrally coordinated as a Si substitute and octahedrally coordinated in the octahedral sheet of layer silicates. Both types of coordination are notably stable and strongly bound in the structure and thus only weakly chemically reactive. To make them more reactive, these types of raw material must be heated to high temperatures ("thermally activated"; Figure 1.1) to dehydroxylate the layer silicates whereby removal of the $(OH)^-$-groups occurs. This leads to a (partial) structure breakdown and a higher

amount of 5-fold coordinated Al (see section 1.4). Such thermally-treated material is much more chemically reactive than 6- or 4-fold coordinated Al.

As a second step, an alkaline solution such as K(OH) or Na(OH) is added to the dehydroxylated clay material in a process referred to as "chemical activation" (Figure 1.1 and Figure 1.2a) to dissolve Si and Al species by alkaline hydrolysis (Duxson *et al.*, 2007c). Bauer *et al.* (1998) and Bauer & Velde (1999) showed that Si and Al are dissolved congruently from I-S and other clay minerals at pH values >13 using a solid:liquid weight ratio between 0.004 and 0.01. The process of dissolution, as commonly assumed, occurs at the edges of the solid particles, although the precise particle dissolution process forming a gel has not yet been confirmed (Duxson *et al.*, 2007c).

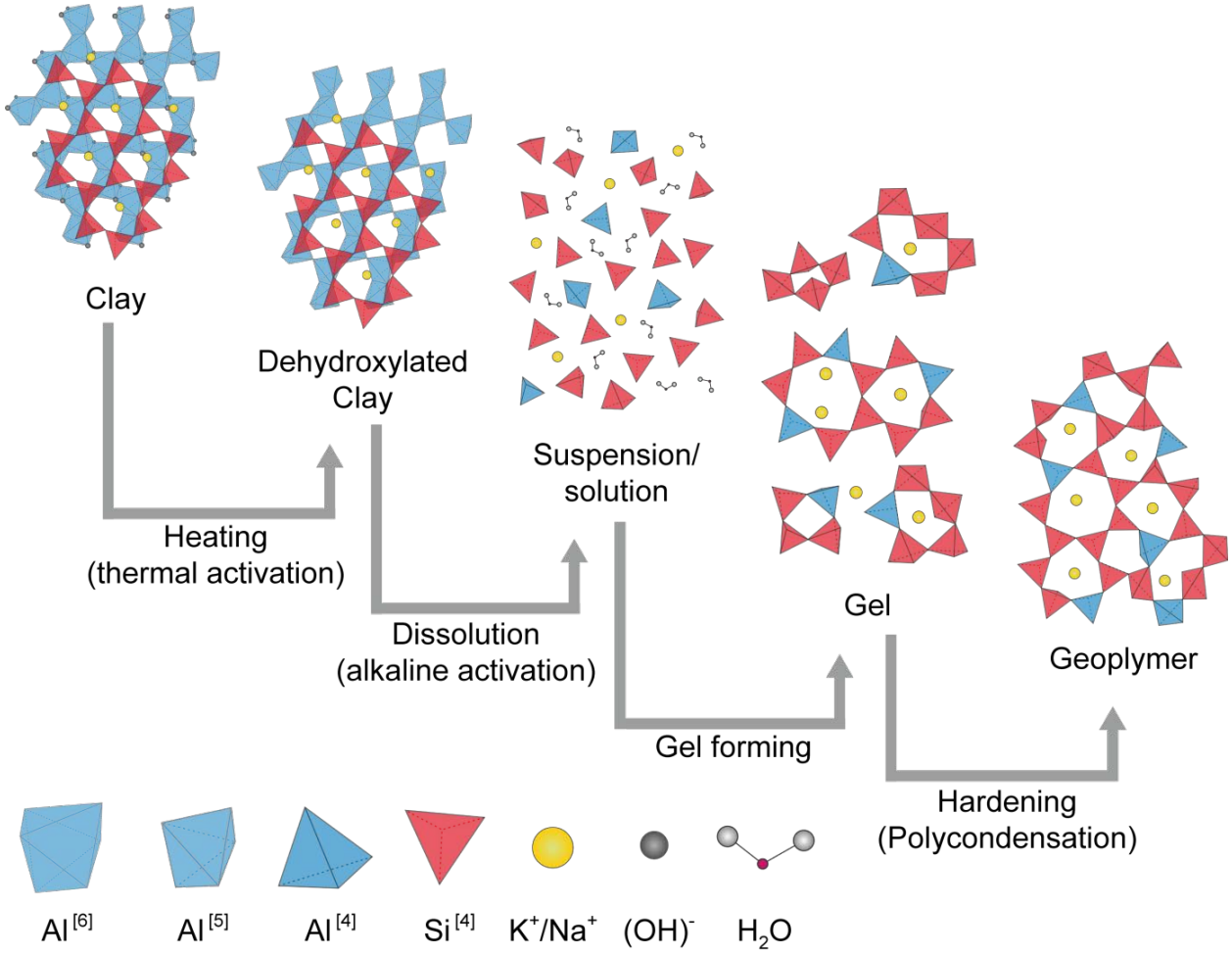

Figure 1.1. Simplified scheme illustrating the process of clay based GP formation. Clay is heated in order to increase the amount of Si and Al dissolved by alkaline solution. Supersaturation leads to aggregation and gelatinisation forming a gel phase that creates a GP while hardening. Typical reactions are shown here, although a GP can also form directly from solution without gelinisation and some reverse reactions may occur.

Because mineral phases in calcined clay are selectively dissolved and only a proportion of the Si and Al is released into solution, the activated binder material forms either a thick suspension or viscous slurry. The dissolved Si and Al occur as species in the suspension (mostly monomeric, Duxson *et al.*, 2007c) in the form of either single tetrahedra or smaller rings or other groups made up of several Si and Al tetrahedra (Figure 1.1). As more and more Si and Al are dissolved, supersaturation is reached

simultaneous with aggregation and gelatinisation, which results in formation of a gel phase (Duxson *et al.*, 2007c). However, some systems do not form gels but their Si and Al concentrations oscillate far from equilibrium (Faimon, 1996; Duxson *et al.*, 2007c).

The joining together of monomers to form oligomers in suspension (Figure 1.2a) and eventual condensation of the oligomers forms more complex structural networks characteristic of GP binders (Figure 1.1 and Figure 1.2b, after Cioffi *et al.*, 2003; Duxson *et al.*, 2007c). In this reaction step additional Si is often needed that may be provided by quartz or by adding silica fume. Adding silica fume, furnace slag or Na/K-silicate solution ("water glass") is a very common procedure when using metakaolin as a precursor because it is easy to dissolve and promotes strong polymerisation resulting in higher compressive strengths of the GP. However, "water glass" is an expensive product with a poor CO_2 footprint, thus offsetting the advantage of potentially low carbon GP cement (Duxson *et al.*, 2007d).

Additional ingredients like naphthalene sulfonate, working as a plastifier that increases workability and delays hardening, may be added (Rangan, 2010). By evaporation of the fluid (water), the gel hardens forming a strong 3D inorganic GP network (Figure 1.1; Duxson *et al.*, 2007c; Rangan, 2010). The process of gelatinisation and hardening can be regarded as a polycondensation reaction, similar to that in organic chemistry. Si and Al act as a network builder, while alkali and alkaline earth ions act as a network modifier that equalise charges (Duxson & Provis, 2008). Some of the water released by hardening remains in the pores of the GP (Duxson *et al.*, 2007c) or is incorporated in the GP structure (e.g. Sun *et al.*, 2004). All these reaction steps may occur simultaneously and additional preparation steps like grinding may be necessary to increase reactivity, depending on the precursor used (Duxson *et al.*, 2007c). The reaction steps involved also strongly depend on the solution chemistry whereby systems with a Si:Al ratio $\geq$ 3 contain no free $[Al(OH)_4]^-$ species due to a fast GP reaction that immediately consumes the dissolved Al species (Sagoe-Crentsil & Weng, 2007). Hence, Al species promote and accelerate condensation, while Si species condense much slower. The condensation stage can therefore be divided into a first, fast reaction due to condensation of Al and Si species and a second, slower step characterised by condensation of only silicate species (Sagoe-Crentsil & Weng, 2007).

The structure of GP has similarities to that of glass, containing 4-fold coordinated Si and Al (e.g. Brew & MacKenzie, 2006), although some authors consider that GP can be crystalline at higher temperatures (150-200 °C; Rangan, 2010). The GP phase can be described as a zeolite-like composition with an amorphous microstructure (Rangan, 2010) mainly being composed of three types of molecular species, poly-sialates (PS), poly-sialate-siloxo (PSS), and poly-sialate-disiloxo (PSDS) (Table 1.1; Sun *et al.*, 2004). Which type occurs depends among others on the Si:Al molar ratio. High Si:Al molar ratios >>3 result in cross linking of polysilicate chains or sheets linked with sialate in two or three dimensions (Davidovits, 1999). It may be that crystallites that formed at higher temperatures are caused by crystallisation of zeolites from the glassy matrix (geopolymer) in a high alkaline environment at elevated temperatures (40-200 °C), which are the typical formation conditions, for example, analcime, phillipsite, clinoptilolite,

or faujasite in natural environments (Hay, 1986). Some authors (e.g. Rangan, 2010) refer to these crystallisation products also as GPs, although they are not X-ray amorphous, and can be identified as zeolite phases. The water added while mixing increases the "water-to-geopolymer solids ratio", which is the mass ratio of the sum of water in the hydroxide solution and if used the silicate solution or additional water, and the sum of all solid precursors and all dissolved solids in the hydroxide and silicate solutions. This ratio plays an important role in determining the properties of the GP cement (Rangan, 2010). A higher water-to-geopolymer solids ratio leads to a better workability of the GP before hardened, but results in a lower compressive strength of the hardened GP. This effect is very similar to that occurring in OPC (Rangan, 2010).

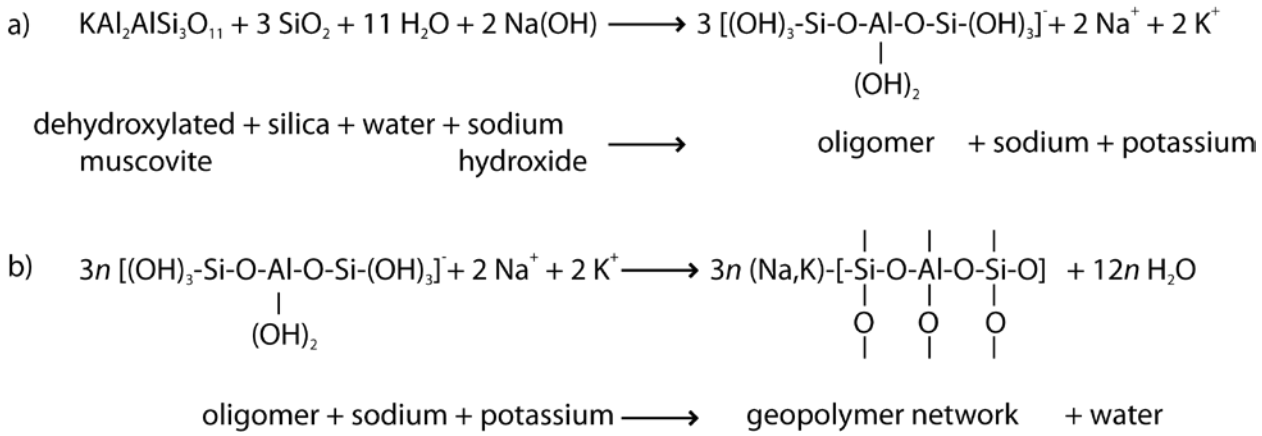

Figure 1.2: Simplified chemical reactions of the condensation of monomers to dimers (a) to a GP network (b). Oligomer structure taken over from Cioffi *et al.*, 2003.

A typical metakaolin recipe is 35% w/w metakaolin, 19% w/w silica fume, 17% w/w K(OH), and 29% w/w water, with a "water-to-geopolymer solids ratio" of 0.4 (Rickard, 2013, pers. comm.). The molarity of the Na or K hydroxide solution is typically between 8 mol/L and 12 mol/L and maybe as high as 16 mol/L because higher molarities increases the reactivity and thus the compressive strength of the product (Rangan, 2010; Rickard, 2013, pers. comm.). This results in optimal element concentrations with a stoichiometric ratio $K_2O:Al_2O_3:SiO_2:H_2O$ of 1:1:4:11 for a K-based GP binder (Si:Al molar ratio of 2, Duxson *et al.*, 2007c; Bell *et al.*, 2009), which maximises its reactivity.

Curing the samples at elevated temperatures (between 30 °C and 80 °C) is a common procedure to accelerate the GP reactions that results in higher compressive strengths. Using curing times of one or more days also increases polymerisation and thus the compressive strength (Rangan, 2010). After Rangan (2010), the compressive strength rises slowly after about 24 hours at elevated temperatures, hence, curing times at elevated temperatures should be least 24 hours long. Nevertheless, hardening at room temperature (or below) and even under wet conditions (in water vapour) is possible, but such conditions may significantly reduce compressive strength (Rangan, 2010).

Table 1.1. Type of species that primarily GPs are composed of. (modified after Sun *et al.*, 2004)

Types of species	Abbreviations	Si:Al molar ratio
Poly(sialate) $R_n - (-Si - O - Al - O -)_n -$	R-PS	1
Poly(sialate-siloxo-) $R_n - (-Si - O - Al - O - Si - O -)_n -$	R-PSS	2
Poly(sialate-disiloxo-) $R_n - (-Si - O - Al - O - Si - O - Si - O -)_n -$	R-PSDS	3

To make a GP with a high compressive strength and low water permeability, a suitable precursor material must be chosen. Precursors for a suitable GP production should have the following properties (Table 1.2):

Table 1.2. Precursor requirements for a suitable GP production with high compressive strength, low shrinkage, and low permeability. ([1)] Xu & van Deventer, 2003; [2)] Brew & MacKenzie, 2006; [3)] Heller-Kallai & Lapides, 2007; [4)] Duxson *et al.*, 2007c; [5)] Duxson & Provis, 2008, [6)] MacKenzie *et al.*, 2008; [7)] Duxson, 2009; [8)] Wang *et al.*, 2010)

Properties	Effect	Consequent GP properties
High Si and Al content [2), 3), 4), 5)]	Forming the GP as network builders; with a higher Si and Al content, more GP phase is created; Al-O-Si bonds break up faster than Si-O-Si bonds [5)]	High compressive strength, chemically resistant
Appropriate Si:Al ratio (similar to GP phase) [3), 4)]	Better connectivity, faster reaction, higher materials conversion, less undesirable phases created	High compressive strength, less inhomogenities
Suitable content of alkali and alkaline earth elements [1), 5)]	As network modifiers they equalise charges in the GP network and promote dissolution of glassy precursors [5), 7)]	High compressive strength, depending on the element and its concentration [1)]
Higher content of alkali than alkaline earth elements [5)]	Bigger alkaline earths cause more damage to the structure of the glass while being removed by dissolution; alkaline earths benefit disordering (i.e. Al-O-Al-bonds), which is less reactive [5)]	High compressive strength, depending on the element and its concentration [1)]
Amorphous or poorly crystalline [5)]	Good solubility and high reaction rates	Homogeneous, high compressive strength, low permeability
Round particles [5)]	Less water consumption [5)]	Low porosity [5)]
Intact surface [5)]	Less water consumptions [5)]	Low porosity [5)]
High content of 5-fold coordinated Al [6), 8)]	Easier and more complete Al solubility, high reaction rates	Homogeneous, high compressive strength, low permeability

The element ratios used have an important role in determining the rate and degree of dissolution and the mechanical properties of the resulting GP. Too high a Si content (without a proper Si:Al and e.g. Si:Na ratio) leads to a higher viscosity of the solution/gel, which results in less mixing and less reacted particles. Unreacted particles can significantly decrease the mechanical strength of the GP (Duxson *et al.*, 2007c). Variation in the Si:Na (or K) ratio also influences the degree of polymerisation of the dissolved species (Duxson *et al.*, 2007c). The type of alkali or alkaline earth element used additionally plays a role in the dissolution process. Na(OH) was determined to increase the solubility of silicate and aluminate monomers more than K(OH) (Duxson *et al.*, 2007c). But Na^+ tends to form zeolites much more easily than other alkali elements, possibly due to the small cation radius combined with a high charge density and high mobility in the gel/solution (Duxson *et al.*, 2007c).

The most common precursor materials used are fly ash, slag, "silica fume" (also as an additive to metakaolin), pozzolan, and "metaclays" (Brew & MacKenzie, 2006). The most common clay used for GPs, kaolin, is calcined before usage to obtain a higher reactivity due to structure breakdown associated with dehydroxylation (see section 1.4). Davidovits (1991) used calcination temperatures of 750 °C for 6 hours, while Zhang *et al.* (2005) used 750 °C for 12 hours. Cioffi *et al.* (2003) investigated different calcination temperatures and different calcination times and concluded the optimum to be 650 °C for 2 hours. Although the calcination temperatures and durations used vary, they all indicate that a complete dehydroxylation is necessary (heating for at least 2 hours above 600 °C). The temperatures should be also chosen carefully to prevent recrystallisation of high temperature phases, such as spinel (no heating above 900 °C). These requirements should also kept in mind using 2:1 layer silicates.

In contrast to kaolin, the applicability of 2:1 layer silicates as a GP binder material is poorly studied. He at al. (1995) investigated illite as a pozzolan/mortar with an 83% w/w pure illite 1Mt sample calcined at 650 °C, 790 °C, and 930 °C for 100 minutes, respectively. These authors studied activation of the heated illitic material using Na(OH) and $Ca(OH)_2$ curing at 40 °C. The Si and Al solubility as well as the pozzolanic activity increased with increasing calcination temperature, but the 930 °C sample was the only one that attained a pozzolan property with a compressive strength 79% that of OPC and 65% that of metakaolin based GP (He *et al.*, 1995). Hence, not only dehydroxylation, but also further structure breakdown seems to be important for obtaining a suitable binder material. MacKenzie *et al.* (2008) investigated the suitability of pyrophyllite and concluded that no stable GP can be formed from this material, maybe due to the TOT (tetrahedral-octahedral-tetrahedral) unit structure. Sperberga *et al.* (2011) investigated an illitic clay of Quaternary age and made two types of test series. First, one set of samples was not activated by an alkaline solution while another one was activated with 2 mol/L K(OH), afterwards they calcined both clays at 700 °C, 800 °C, and 900 °C. For the second series, clay was activated with 4 mol/L, 6 mol/L, and 8 mol/L, respectively and then calcined at 20 °C, 100 °C and 700 °C. They concluded that untreated clay and clay heated to 100 °C, both activated with 6 mol/L K(OH) produced GPs with the highest compressive strengths. This is in contrast to Buchwald *et al.* (2009) who investigated the suitability of Friedland clay, for producing a GP by heating between 550 °C and 950 °C in 100 °C steps

and activated with 6 mol/L Na(OH) solution. They concluded that the highest compressive strength is reached by calcinating the clay to 850 °C or 950 °C. Therefore the results on illitic clays are somewhat contradictory and the driving factors of producing GPs with high compressive strengths are still largely unknown.

1.3 Clay mineral interstratifications – a short summary

Clay mineral interstratifications, also called mixed-layered structures, are not only physical mixtures of two or more components, but structures in which two or more layer types of layer silicates occur vertically stacked within the same crystallite or X-ray scattering domain (Brigatti *et al.*, 2013). There are different types of interstratifications, depending on the probability of layer occurrence and the degree of ordering (Figure 1.3). They can be subdivided into (1) disordered, (2) with increasing long range order and (3) ordered structures (Reynolds, 1980; Meunier, 2005).

The degree of long-range of ordering can be expressed by a parameter called “Reichweite” (German word for reach back), *R*. This value was defined from Jagodzinski (1949) as an expression for the extent of the influence of a layer A on the probability on the nature of its adjacent layers (A or B) (Ufer *et al.*, 2012a; Brigatti *et al.*, 2013). If layers are stacked randomly, the nature of a certain layer does not influence the nature of adjacent layers, the *R* value is zero (*R*0). If the nature of one layer only influences the directly neighboured layer, the *R* value is stated as *R*1. *R*2 equally means that two preceding layers have to be considered to specify the nature of the following layer. The occurrence of *R*3 requires considering the three preceding layers to specify the nature of the following layer. In the literature, only Reichweite values of *R*0, *R*1, *R*2, and *R*3 have been reported for I-S interstratifications (Ufer *et al.*, 2012a). The changes between *R* values and even between degrees of ordering are transitional in nature. The *R* value is a statistical parameter and in the case of an individual sequence, different *R* values may fit (Brigatti *et al.*, 2013).

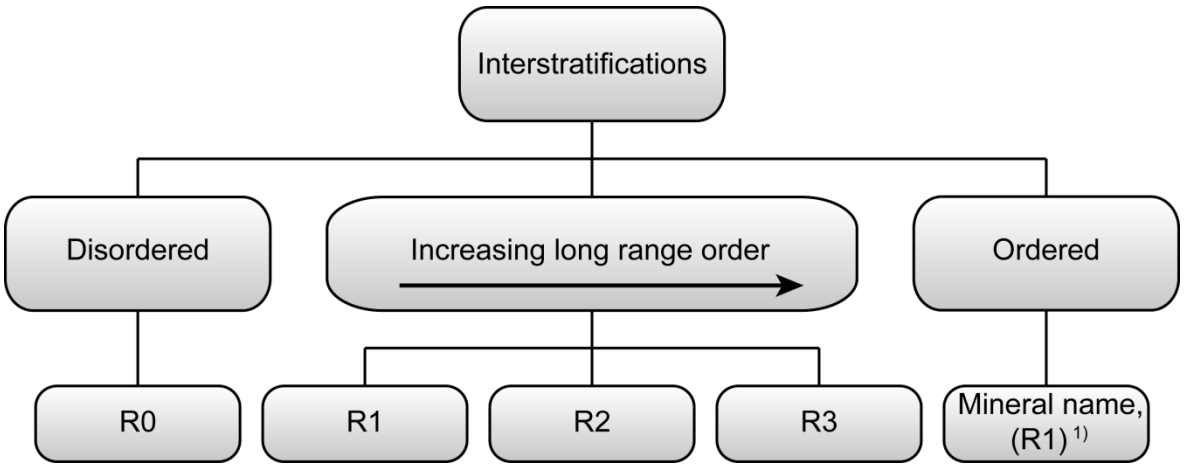

Figure 1.3. Schematic classification of interstratifications. 1) Ordered structures are described mathematically as *R*1, but because being allocated an own mineral name, no *R*-value will be stated.

For description of the probability of layers, parameters are defined. The junction probability is defined as *p*, hence, the probability of, for example, an illitic layer (I) is followed by a smectitic layer (S) is defined as *pSI*, S followed by S is denoted as *pSS*, I followed by I is *pII*, and I followed by S is *pIS*. The amount of a certain layer type (e.g. I) within an interstratification is denoted as *wI*, and in a two-component system of illite and smectite, *wI* + *wS* = 1. These parameters are necessary for the quantitative description of interstratifications (Ufer *et al.*, 2012a).

The different degrees of ordering are described in more detail as follows:

(1) Disordered or irregular stacked interstratification means that stacking of the involved layer types is random. These structures show irrational basal reflections and diffraction effects that do not follow the Bragg equation because of the disordered stacking of illitic and smectitic layers and the inhomogeneous hydration state of the interlayer cations (Ufer *et al.*, 2012a; Brigatti *et al.*, 2013). Randomly stacked interstratifications are named after the single components separated by a hyphen (Brigatti *et al.*, 2013). The component with a lower (d_{001}) value is stated first and, if known, the content of the first layer type can be noted in brackets (e.g. ***R*0 I(0.3)-S**). The probabilities (*pSI*, *pII*, *pIS*, *pSS*) are, for the layers being randomly interstratified, also random and depend on the amount of I in the system (*pII* = *wI*) (Figure 1.4). Hence, only *wI* must be refined.

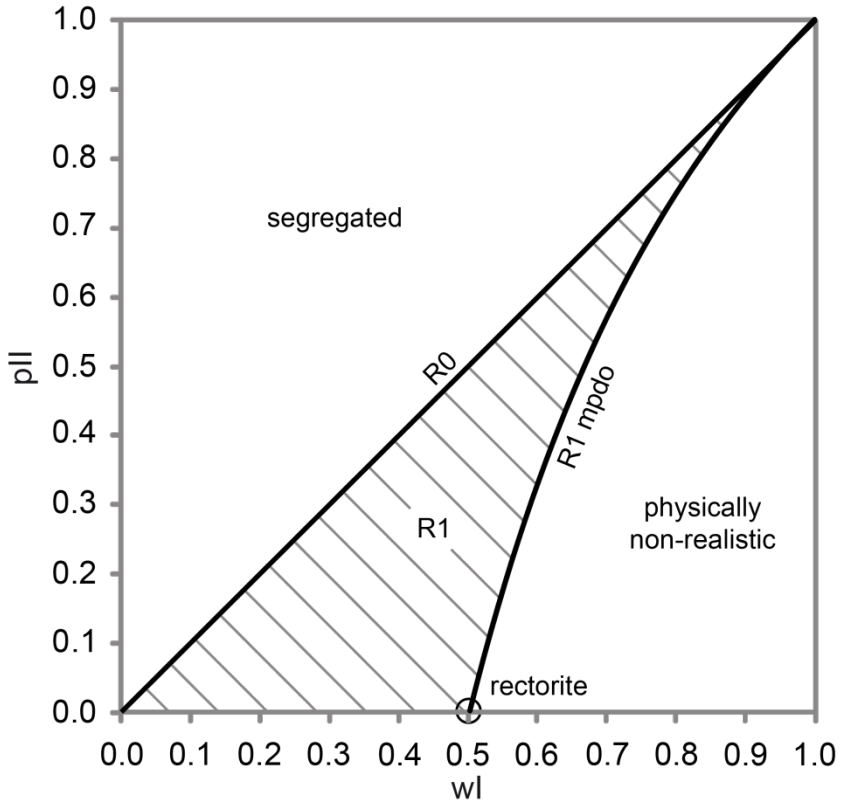

Figure 1.4. Junction probability diagram for *R*0/*R*1 that shows variation of composition (*wI*) versus layer arrangement (*pII*) for I-S interstratifications (modified after Bethke *et al.*, 1986).

(2) If ordering increases, higher *R* values are reached. *R*1 refers to short range order, while *R*3 refers to long range order, based on illite (Meunier, 2005). These interstratifications are named similarly to the disordered ones (e.g. ***R*0 I(0.6)-S**), or ***R*3 I(0.8)-S**). Because *pII* is no longer equal to *wI* for *R*1 ordering, the parameter *pII* needs to be additionally refined (Drits & Tchoubar, 1990). Refining *wI* and *pII*, the other probabilities can be calculated (e.g. *wSI* = (*wI*− *wI*×*pII*)/*wS*, Figure 1.4, Ufer *et al.*, 2012a). If there are not enough illitic layers for a certain *pII* value (or p*III* or *pIIII* depending on the Reichweite), segregation occurs.

Some sets of values of *wI* and *pII* are forbidden because both, the probabilities *p*, and the amount of layers *w* cannot become <0 or >1, and a certain amount of illitic layers *wI* (if *wI* > 0.5) requires a certain value of *pII* (or p*III* or *pIIII* depending on the Reichweite), simply because of the higher probability of illitic layer occurrence. This is expressed as "physically non-realistic" in the junction probability diagram because *pII* or *wI* values <0 or >1 would occur. The extreme case *pII* = 1 describes the occurrence of a physical mixture of illite and smectite (Bethke *et al.*, 1986). The limiting case *pSI* = 1 expresses that every S is followed by I and no S can be followed by another S, which is called the maximum possible degree of ordering (mpdo, Figure 1.4; Ufer *et al.*, 2012a). In the case of *R*1 with mpdo and an amount of illitic layers *wI* = 0.5, this leads to perfect ordering (...ISISIS...) and the phase would be called rectorite (see (3)).

Increasing *pII* to, e.g., 0.1 while the amount of illitic layers *wI* remains 0.5 leads to an *R*1 I-S interstratification with 50% illitic layers that is not allocated an own mineral name (Figure 1.3, Figure 1.4). Hence, in the case of *R*1, mpdo need not implicitly occur, while in stacks with higher degrees of long range ordering (*R*2 and *R*3) the mpdo case for *R*1 parameter seems to be very common (Bethke *et al.*, 1986; Ufer *et al.*, 2012). Further increasing the long range ordering requires the definition of more probability parameters such as *pIII*, *pIIS*, *pISI*, *pISS*, *etc.* (*R*2), or *pIIII*, *pIIIS*, etc. (*R*3; Ufer *et al.*, 2012a). Assuming mpdo, the number of parameters is reduced because the junction SS need not to be considered. The junction probability diagrams for both cases are displayed in Figure 1.5 and Figure 1.6. *R*2 I-S interstratifications seem to be seldom, but Inoue *et al.* (2005) described such an ordering in a natural sample. An example of a *R*3 I-S interstratification is shown in Figure 1.7A.

(3) Ordered structures have a regular stacking that results in a supercell along the c* direction, hence, diffraction occurs in a rational basal reflection series from repeating (d_{00l}) values equal to the sum of the thickness of each layer type (Brigatti *et al.*, 2013). If these structures show a coefficient of variation (CV) <0.75 regarding at least 10 (00*l*) reflections with similar peak breadths (full width at half maximum, FWHM), they are allocated an own mineral name and are not named after the involved layer types (Bailey, 1982; Guggenheim *et al.*, 2006). Although these minerals can be mathematically described as perfectly ordered *R*1 structures, no *R*-values will be stated, but instead their mineral name. Rectorite is defined as a regularly interstratified 2:1 layer silicate, composed of dioctahedral mica with dioctahedral smectite, replacing the name allevardite (Caillère & Henin, 1950) as a synonym. The prefix Na-rich, K-rich or Ca-rich describes the dominant cation present in

the mica interlayer (Guggenheim *et al.*, 2006, based on the work of Bailey, 1982). The probabilities (*pSI*, *pII*, *pIS*, *pSS*) are well defined because of the mpdo (*pII* = 0, *pSI* = 1). As described above, in the case of *R*1 with mpdo and *wI* = 0.5, this leads to a perfectly regularly ordered interstratification (...ISISIS...), which would be called K-rich rectorite (Figure 1.4, Figure 1.7 B).

A more detailed description of all parameters needed for a quantitative description of I-S interstratifications is given in Drits & Tchoubar (1990).

There are two different ways to describe interstratifications: (1) The pile of different layers are stacked in one single "crystallite" which acts as a coherent scattering domain, known as the MacEwan-crystallite (MacEwan, 1958, Figure 1.7 A). (2) All neighboured illitic layers are described as one fundamental particle that are separated by smectitic interlayer cations occurring on their outer surface (McHardy *et al.*, 1982 and Nadeau *et al.*, 1984a,b, Figure 1.7 A). Both theories can explain the observed scattering effects of X-rays observed in nature clay mineral samples.

(1) The MacEwan model was derived from X-ray diffraction (XRD) results of dispersed clay samples and assumes illitic and smectitic layers are combined in large crystallites (MacEwan crystallite) (Reynolds, 1980). The layers are divided through the centre of the octahedral sheet (Moore & Reynolds, 1997). The I:S ratio and ordering is controlled by the proportion and sequence of illitic and smectitic layers, respectively. Following this model, illitisation (smectite to illite transformation) is envisaged to occur by an in-situ solid-state transformation process (layer-by-layer; SST). Indications of this mechanism are provided from the retention of morphology and polytypism during illitisation. As the two separate phases (illite and smectite) are distributed within one crystallite (TOT layer), this arrangement does not comply with thermodynamic models (Moore & Reynolds, 1997), but is best viewed as having a metastable state (Essene & Peacor, 1995).

(2) The fundamental particle model was derived from transmission electron microscopy (TEM) observations, interpreting XRD patterns of I-S interstratifications as the effect of interparticle diffraction (McHardy *et al.*, 1982 and Nadeau *et al.*, 1985). In this model, 10 Å units envisaged as stacked together making up fundamental particles and therefore form relatively small crystallites. These particles may expand by adsorbing water or organic molecules on both surfaces of the particle. Illite particles being 200 Å thick are described as two individual units each 10 Å thick, bound together by the interlayer cations (Moore & Reynolds, 1997). The layers in this model are divided through the centre of the interlayer space and do not grow together epitaxially, but are stacked into groups of particles that diffract X-rays coherently. (Moore & Reynolds, 1997). Following this model, illitisation occurs by direct precipitation as a dissolution-crystallisation (DC) mechanism. Support for this mechanism comes from the changes of morphology and polytypism during illitisation. In this model the disordered part of I-S is considered to be composed of two separate phases whereas the ordered part consists of a single phase (Nadeau, 1984a).

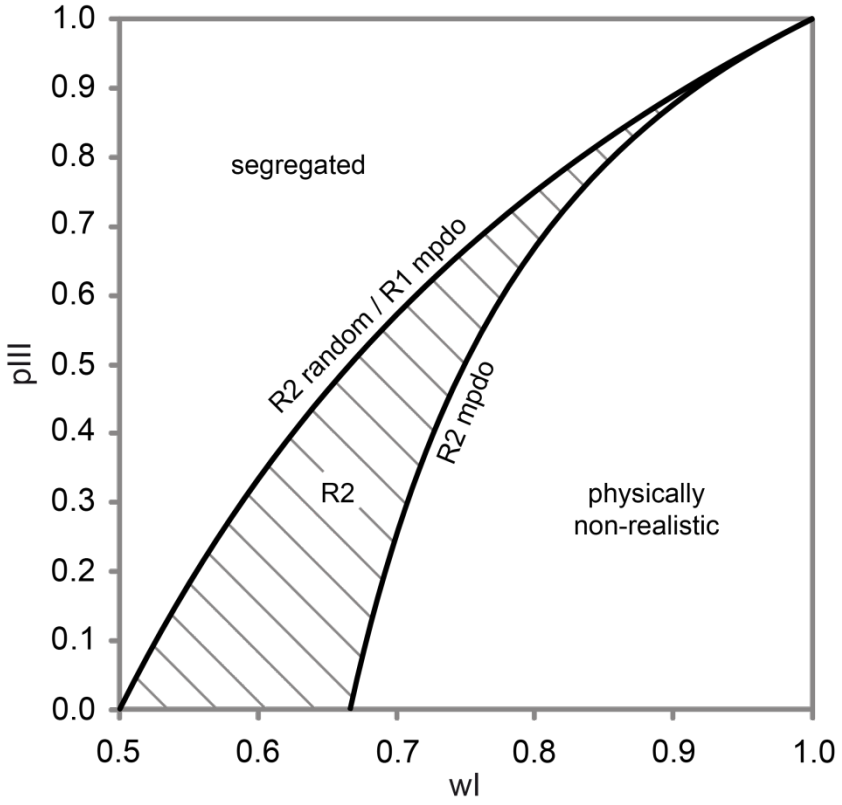

Figure 1.5. Junction probability diagram for *R*2 that shows variation of composition (*wl*) versus layer arrangement (*pIII*) for I-S interstratifications (modified after Bethke *et al.*, 1986).

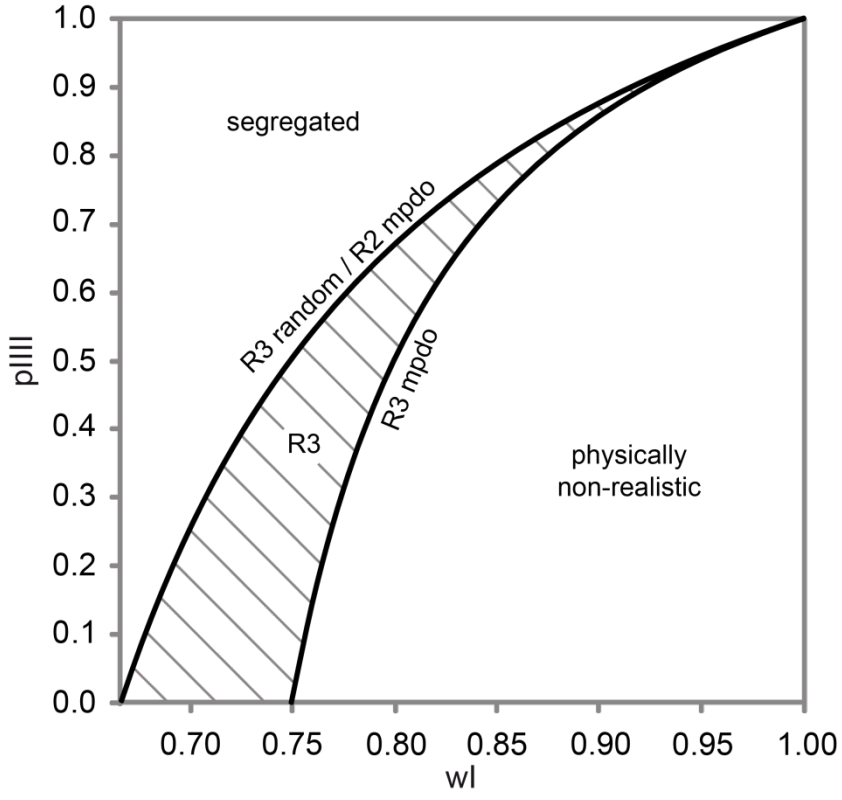

Figure 1.6. Junction probability diagram for *R*3 that shows variation of composition (*wl*) versus layer arrangement (*pIIII*) for I-S interstratifications (modified after Bethke *et al.*, 1986).

The existence of thin sheeted particles each with a thickness of integral multiples of about 10 Å, was shown based on HRTEM imaging after an extensive ultrasonic treatment of the samples (e.g. Środoń *et al.*, 1990). The sheets are stacked together in packets of, for example, *N* = 3 to *N* = 7 layers which were interpreted as fundamental particles. The number of stacked layers *N* related to the amount of smectite in the interstratification. The amount of illite is equal to (*N*−1), therefore a layer packet of *N* = 2 is equivalent to 50% smectite content [I(0.5)-S] and *N* = 5 a 20% smectite content [I(0.8)-S] (Figure 1.7). For X-rays having a larger penetration depth, the diffraction effects are an average resulting from large numbers of *N* (*N* = 10^6....10^9), which may look like MacEwan crystallites (Moore & Reynolds, 1997). This is accordance to Nadeau *et al.* (1984b and 1985) who made physical mixtures of 10 Å particles resulting in an XRD pattern similar like that expected in the MacEwan model with a number of layers *N*>20.

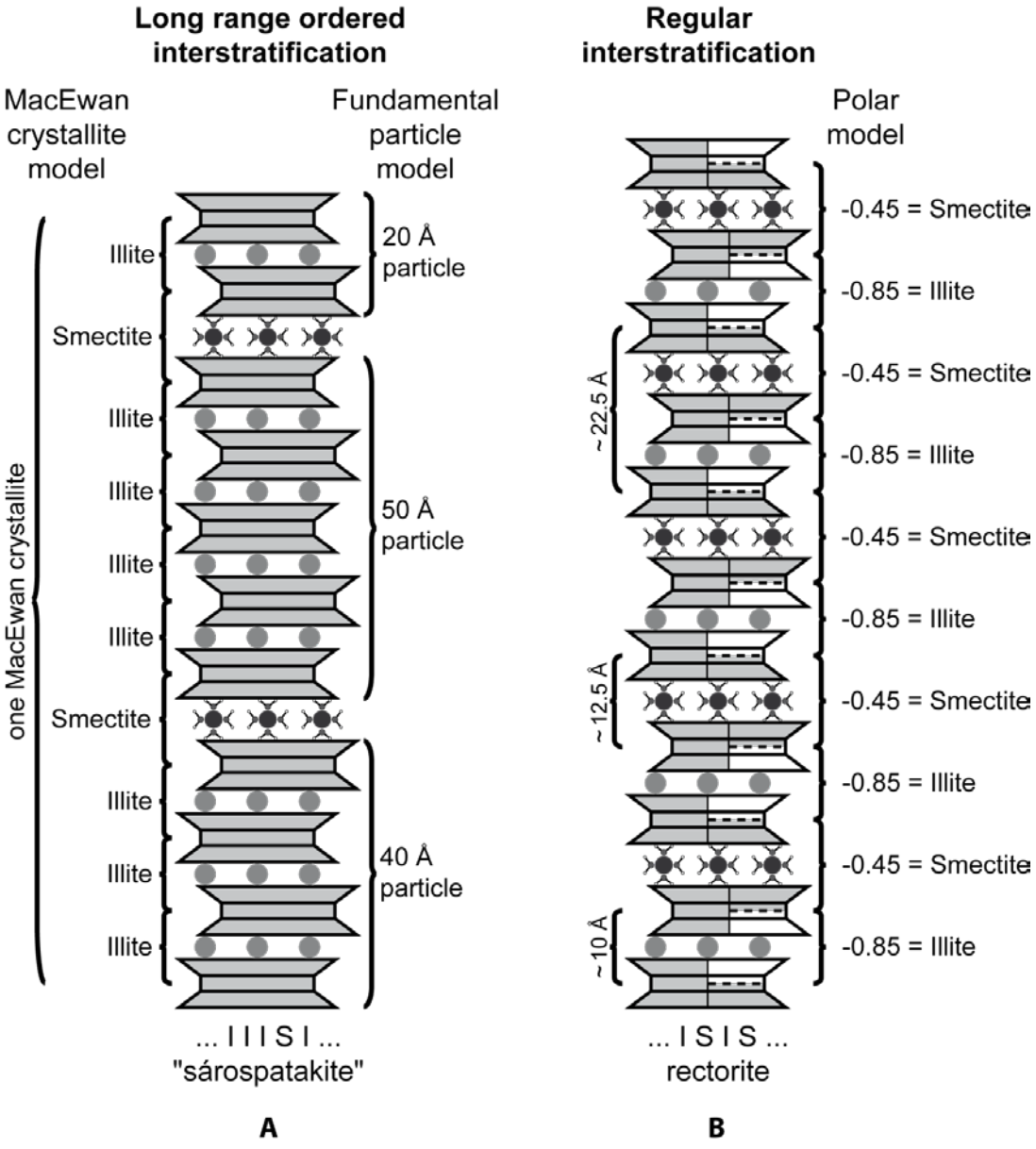

Figure 1.7. Scheme showing a *R*3 (left) and a regular I-S interstratification (right) and different models describing interstratifications. The MacEwan and fundamental particle model (both left) and the polar model (right, average layer charge surrounding the interlayer given). (Modified after Altaner & Ylagan, 1997 and Brigatti *et al.*, 2013)

Altaner & Ylagan (1997) proposed two models for describing non-polar and polar 2:1 layers. In the non-polar model, the layers are chemically homogeneous while the polar model has an illite charge on the one side and a smectite charge on the other (Figure 1.7 B). Hence, a fundamental particle in this model with a thickness of, e.g., 50 Å contains tetrahedral sheets with illite composition sandwiched between two tetrahedral sheets with smectitic composition on the edge (top and bottom). For the crystal structure of I-S interstratifications, a polar model was assumed for the non-polar model has difficulties explaining the occurrence of collapsed interlayers (illitic). Hence, for illitisation of I-S several reactions are possible. Changes in ordering, polytype, chemical composition, crystallite size and shape may occur gradually as in the SST model or as crystal growth events as in the DC model (depending on the rate-controlling step). Even the coarsening of the crystals by surface-controlled Ostwald ripening (OR) by dissolving the smallest crystals is conceivable. Brigatti *et al.* (2013) states that the SST seems to be the best model for illitisation of solids-dominated systems like bentonite, whereas DC describes better illitisation in fluid-dominated systems like sandstones or hydrothermal environments. Both models have been applied extensively to shales (see references in Brigatti *et al.*, 2013).

Natural interstratifications are often considered to represent metastable transitions between two separate phases and therefore are not thermodynamically stable. Their formation requires low activation energies because their composition and structures are similar to that of the educts such as smectite or feldspar phases (Galán & Ferrell, 2013). They are often formed by illitisation of smectite (typically between 60 °C and 120 °C) or by hydrothermal activity above 50 °C in the presence of water related to plutonic or volcanic activity whereby newly formed mineral phases replace existing phases or fill pore space (Eberl & Środoń, 1988; Inoue *et al.*, 1988; Christidis, 1995; Nieto *et al.*, 1996; Środoń, 2010; Galán & Ferrell, 2013). However, other formation mechanisms such as K^+ diffusion in bentonites from enclosing sediments over a long period of time (Galán & Ferrell, 2013) or K^+ fixation in soils (Środoń, 2010) have been proposed.

During the illitisation of I-S interstratifications, the interlayer water content decreases and the interlayer cations are exchanged by K^+, resulting in more parallel layers and a higher degree of ordering (compare amount of illite *wI* and Reichweite parameter *R*). The (00l) reflections become progressively sharper as the mean thickness of the scattering domains increases (Brigatti *et al.*, 2013). Additionally there is a decrease in disordering of the layers , including defect density or lattice strain effects with the increasing illitisation process, hence, a disordered $1M_d$ particle may evolve into a better ordered 1M particle (Cuadros, 2010; Peacor, 1992) and eventually to an even better ordered $2M_1$ mica (Galán & Ferrell, 2013). The overall evolution of dioctahedral 2:1 layer silicates during diagenesis can be represented as

$$smectite \rightarrow R0\ I\text{–}S \rightarrow R1\ I\text{–}S \rightarrow R3\ I\text{–}S \rightarrow 1M_d\ illite \rightarrow 1M\ illite \rightarrow 2M_1\ muscovite,$$

in the case of a higher K^+ than Na^+ activity (Cuadros, 2010; Peacor, 1992; Galán & Ferrell, 2013). This illitisation process considered to involve a layer-by-layer transformation (SST) (Bethke & Altaner, 1986).

The process of illitisation by transformations in I-S interstratifications clearly depends on the chemical composition of educts, fluids and surrounding rocks and is driven by many parameters such as time, temperature, pressure and pH values, the activity of alkali and alkaline earth elements, Al^{3+} for Si^{4+} substitution and interlayer hydration (Brigatti *et al.*, 2013). I-S Interstratifications are especially formed in an intermediate temperature and pH region (<300 °C) with high activities of K^+, Ca^{2+} and Mg^{2+} (Meunier, 2005). The K^+ needed is often provided by alteration of K^+-feldspars or white micas (Furlan *et al.*, 1996).

Illitisation and I-S formation is commonly used as a palaeogeothermometer for diagenetic and hydrothermal alterations (Dudek & Środoń, 2003; Galán & Ferrell, 2013; Brigatti *et al.*, 2013). Additionally it is still used for calibration of geophysical borehole data for estimating palaeotemperatures and the geothermal gradients of sedimentary basins worldwide (Pevear, 1999; Jeans *et al.*, 2005; Kemp *et al.*, 2005; Merriman, 2005; Aróstegui *et al.*, 2006; Środoń, 2010). In oil exploration, I-S interstratifications are highly important for a correlation between the smectite content in the interstratification and the depth of oil generation in source rocks (Drits *et al.*, 1997; Weaver, 1979). The illitisation process during burial diagenesis is correlated with the hydrocarbon formation during maturation of organic matter and therefore the appearance of *R*1 I-S coincides with the “oil window” and the transition from shallow to deep diagenetic zones (Galán & Ferrell, 2013). Moreover, I-S may play an important role in polymetallic repository exploration and can be used as a geothermometer and an indicator for hydrothermal alteration. In the Cabo de Gata province, Spain, I-S interstratifications were associated with native gold in veins indicating formation temperatures below 200 °C (Carrillo-Rosua *et al.*, 2009).

Nieto *et al.* (1996) described two different I-S interstratifications in a diagenetic environment (*R*1 I(0.5)-S and *R*>3 I(>0.9)-S) together with chlorite and calcite over distances of <1000 Å by TEM, and concluded most of the phases not to be in thermodynamic equilibrium with the formation conditions. This is in contradiction to the fundamental particle theory, whereby the illitisation was originally described as a process of Ostwald ripening (Morse & Casey, 1988, Galán & Ferrell, 2013). Eberl *et al.* (2011) states that a similarly occurrence of *R*1 and *R*0 I-S interstratifications in XRD patterns can be interpreted as a single phase. As a result of crystal growth, variable thickness distributions of the smectite and illite fundamental particles may occur and irregular stacking of single smectite layers with illite particles. In this case interparticle diffraction effects lead to the appearance of two separate interstratification phases (Galán & Ferrell, 2013). However, the formation mechanism for I-S interstratifications remains an open debate, whether they are formed by a dissolution-crystallisation process or a solid-state transformation, as discussed extensively by Meunier (2010).

1.4 Thermal behaviour of clay mineral phases – state of the art

Due to their ability to adsorb water on their surface, clay mineral phases lose this loosely bonded water when heated. More strongly bonded water in the interlayer space (for example in the case of smectitic layers) is released at slightly higher temperature by the endothermic reaction of dehydration. Dehydration occurs, depending on the mineral phase, crystal chemistry, or degree of disordering at temperatures up to ca. 300 °C.

The structurally bonded hydroxyl groups ($(OH)^-$) that are bonded more stronger than water molecules, are located in the octahedral sheets of clay mineral phases. Hence, these $(OH)^-$-groups are released at even higher temperatures by condensation (equations 1.3-1.6) resulting in an another endothermic reaction, known as dehydroxylation, which occurs typically between 450 °C and 850 °C (Emmerich, 2011). The thermal strength of bonding of the $(OH)^-$-groups depends on the corresponding metal ion. The strength, and thus dehydroxylation temperature increases from Fe-(OH) to Al-(OH) to Mg-(OH) (Köster, 1993).

$$2\ (\mathrm{OH})^- \rightarrow H_2O \uparrow + O_R^{2-} \qquad 1.3$$

This chemical equation is a simplified version exemplary for clay minerals containing structurally bonded $(OH)^-$-groups because the condensation of $(OH)^-$-groups to form water and residual oxygen (O_R) is equivalent. However, the amount of released water per formula unit (F.U.) differs for clay minerals. In formula 1.4-1.6 a chemical equation for dehydroxylation of kaolinite (equation 1.4), montmorillonite (equation 1.5), and muscovite (equation 1.6) is given.

$$\underset{\text{kaolinite}}{\mathrm{Al_2Si_2O_5(OH)_4}} \rightarrow \underset{water}{2\ H_2O} \uparrow + \underset{metakaolinite}{Al_2Si_2O_7} \qquad 1.4$$

$$\underset{\text{montmorillonite}}{\mathrm{Na_{0.3}(Al,Mg)_2[Si_4O_{10}(OH)_2]} \times \mathrm{n}\ H_2O} \rightarrow \underset{water}{\mathrm{n}+1\ H_2O} \uparrow + \underset{metamontmorillonite}{\mathrm{Na_{0.3}(Al,Mg)_2Si_4O_{11}}} \qquad 1.5$$

$$\underset{\text{muscovite}}{\mathrm{KAl_2[Si_3AlO_{10}(OH)_2]}} \rightarrow \underset{water}{H_2O} \uparrow + \underset{metamuscovite}{\mathrm{KAl_2[Si_3AlO_{11}]}} \qquad 1.6$$

The residual oxygen remains in the structure and is responsible for the 5-fold coordination of Al ($Al^{[5]}$) in the dehydroxylated clay mineral phases (e.g. Drits *et al.*, 1995). Decomposition and structure breakdown takes place as a result of the highly disturbed and disordered structures, resulting in a weak endothermic reaction to form amorphous silicates (Emmerich, 2011). 5-fold coordination in most cases is a metastable condition, hence, 4-fold coordination is favoured. A more stable condition is achieved at high temperatures by forming, for example, spinel or mullite phases during an exothermic recrystallisation reaction (Emmerich, 2011). The temperature required to form these thermodynamically stable phases differs for most clay minerals.

Brindley & Nakahira (1959a,b) investigated the dehydroxylation behaviour of kaolinite. By dehydroxylation of kaolinite, the phase "metakaolinite" forms containing $Al^{[5]}$ together with the release of water:

$$\begin{matrix} 6\,Al_2Si_2O_5(OH)_4 \rightarrow\ 12\,H_2O\uparrow +6\,Al_2Si_2O_7 \\ \text{kaolinite} \rightarrow\ 2\,water\uparrow +metakaolinite \end{matrix} \quad 1.7$$

By further heating to 925 °C the excessive oxygen atoms are thereby expelled together with silicon forming SiO_2 and a closely packed defect spinel phase with $Al^{[4]}$ is formed from the original kaolinite structure (Brindley & Nakahira, 1959a,b).

$$\begin{matrix} 6\,Al_2Si_2O_7 \rightarrow 3\,SiO_2 + 3\,Al_3Si_4O_{12} \\ \text{metakaolinite} \rightarrow\ amorphous\ silica + spinel \end{matrix} \quad 1.8$$

At even higher temperatures (above 1075 °C) most of the spinel phase is converted to 3:2 mullite by forming additional SiO_2, and the amorphous silica crystallises as cristobalite (Brindley & Nakahira, 1959b).

$$\begin{matrix} SiO_2 + 3\,Al_3Si_4O_{12} \rightarrow 6\,SiO_2 + 2\,Al_6Si_2O_{13} \\ amorphous\ silica + spinel \rightarrow\ cristobalite + mulite \end{matrix} \quad 1.9$$

The peak dehydroxylation temperature of kaolinite lies typically between 500 and 600 °C, depending on crystallite size, the degree of ordering or "crystallinity". Small crystallites and a high degree of disordering will result in a lower dehydroxylation temperature and vice versa (Smykatz-Kloss, 1974; Guggenheim & Koster van Groos, 2001; Emmerich, 2011).

Smectites are a group of expandable 2:1 layer silicates that have the ability to adsorb large amounts of water in the interlayer as hydration shells around interlayer cations. This water is released during dehydration leading to a collapse of the layers (Emmerich, 2011). First, the outer hydration shell is released and later the stronger bound inner hydration shell water molecules. Both steps are mainly controlled by diffusion of water parallel to the layers which is hindered by the attraction force of the interlayer cations (Bray & Redfern, 1999). The dehydration temperature depends among others on the type of interlayer cation and the amount and location of the layer charge, but often is between 130-160 °C (Bray & Redfern, 1999; Steudel, 2008; Emmerich, 2011). In XRD, the collapse of the interlayers can be recognised by lowering of the d-value of the (001) reflections towards ≈10 Å. Micaceous minerals (in this case true micas and interlayer deficient micas), without the ability to intercalate water, only show a weak dehydration, mostly below 100 °C (Emmerich, 2011). Dehydroxylation of both mineral groups occurs at elevated temperatures, usually between 450 °C and 850 °C for interlayer deficient micas and smectite, and 850-920 °C for true micas and strongly depends on a number of parameters such as di-/tri-octahedral character, trans-/cis vacancy (in the case of

dioctahedral sheets), crystal chemistry (Fe/Mg content; predominant interlayer cation), and other features (Smykatz-Kloss, 1974; Tsipursky & Drits, 1984; Emmerich, 2011). Dehydroxylation temperatures decrease for dioctahedral, instead of trioctahedral sheets, a higher trans- (tv) than cis-vacancy (cv) content (for dioctahedral sheets), and higher Fe- than Al or Mg contents (Köster, 1993; Drits *et al.*, 1995; Emmerich, 2011). Dehydroxylation of cv sheets occurs at about 700 °C, which is 150-200 °C higher than dehydroxylation of tv sheets (Drits *et al.*, 1995). During the dehydroxylation of cv sheets, Al migrates to cis positions which requires more energy and thus higher degrees of heating (Emmerich, 2011). Hence, all dioctahedral sheets are tv following dehydroxylation. This discrepancy allows us to estimate the tv/cv ratio by studying the dehydroxylation temperature (Drits *et al.*, 1998; Wolters & Emmerich, 2007; Emmerich, 2011). Interlayer deficient micas mostly occur as dioctahedral, tv varieties, hence, dehydroxylation is most always between 500 °C and 580 °C, while dioctahedral smectites often occurs as cv varieties (Cole, 1955; Drits *et al.*, 1999; Emmerich, 2011). Dehydroxylation of mica can be recognised by the decreasing intensity of the 10 Å reflection and increasing intensities of the (020) and (110) reflections (Jiang *et al.*, 2008). Decomposition (breakdown of the structure) and thereafter recrystallisation (often as enstatite, spinel or mullite) follows dehydroxylation at 700-1050 °C (Smykatz-Kloss, 1974; Michael & McWhinnie, 1989). Jiang *et al.* (2008) investigated dehydroxylation and structural breakdown of illite and found a temperature window between 1093 °C and 1100 °C where the layered structure of illite is lost and an amorphous phase is formed before recrystallisation of mullite starts. This temperature window could be of high potential for making precursor clays for GP production.

The thermal behaviour of interstratifications may differ from that of their pure components. Smykatz-Kloss (1974) investigated an irregular I-S interstratification and found the dehydration to be complete by 205 °C, dehydroxylation occurred at 533 °C, 557 °C, and 680 °C, respectively, and was followed by decomposition at 763 °C, then recrystallisation at 808 °C and 897 °C. Hence, peak temperatures of irregular interstratifications, except dehydration, appear to lie between those of the pure components, similar to Méring´s principle for the (00l) reflections in the XRD method (Smykatz-Kloss, 1974; Méring, 1949). Similar finding were reported by Grim & Rowland (1942) who studied rectorite from Garland County, Arkansas who found dehydration to be finished by 200 °C and dehydroxylation occurred between 450 °C and 630 °C. Rectorite from Pakistan investigated by Komada (1966) revealed dehydration endothermic reactions at 140 °C and 200-205 °C. Here the dehydroxylation temperature was found to occur at 570 °C and decomposition/recrystallisation with an exothermic peak at 960 °C and 1030 °C.

Minerals of the chlorite group show almost no dehydration peak because they are not expandable and are only able to adsorb minor amounts of water on particle surfaces. Dehydroxylation occurs in two steps. Dehydroxylation of the interlayer octahedral sheet is followed at ca. 700 °C by dehydroxylation of the 2:1 layers (Villieras *et al.*, 1994; Emmerich, 2011). Because dehydroxylation of the interlayer octahedral sheet releases about 6 times more water than dehydroxylation of the 2:1 layers, the latter is often hardly recognisable without evolved gas analysis (Emmerich, 2011). The first step of

dehydroxylation can be recognised by XRD because the (001) reflection increases while (002) disappears and (003) and (004) decrease and (005) remains constant. Depending on the chlorite mineral a 27 Å and a 9 Å peak may occur. The second dehydroxylation steps leads to a structural collapse and the long-range atomic periodicity is lost (Villieras *et al.*, 1994; Zhan & Guggenheim, 1995). Identification of different chlorite is possible with STA because an increased Fe content leads to lower dehydroxylation temperatures for both steps (860 °C for Mg-chlorites and <700 °C for Fe-chlorites; e.g. Smykatz-Kloss, 1974; Zhan & Guggenheim, 1995; Emmerich, 2011). The dehydroxylated chlorite has a so-called "modified chlorite structure" (MCS) which is very stable, even under water (Brindley & Ali, 1950), and can be identified by a 2-5 times higher intensity of the 14 Å-reflection, in contrast to the lower intensities of the other (00l) reflections (Zhan & Guggenheim, 1995). The MCS mostly produces a 27 Å-spacing, whereby the peak width of l = odd (00l) reflections are different from l = even (00l) reflections and the (001) peak is not exactly an integer multiple of the 14 Å-reflection (Brindley & Chang, 1974). Zhan & Guggenheim (1995) attributed this feature to the topotactically intergrow of a poorly crystalline 27 Å phase with a better crystalline 14 Å phase. The MCS is created independently of the Fe content or oxidation/reduction atmosphere, but depends on water fugacity, polytypism, and the di-/trioctahedral character (Zhan & Guggenheim, 1995). Decomposition, which strongly depends on water fugacity (Bai *et al.*, 1993) and recrystallisation of spinels, forsterite, enstatite, or other phases, usually occurs at temperatures between 850 °C and 930 °C (Smykatz-Kloss, 1974; Villieras *et al.*, 1994).

Heated clays are widely used in industry. Kaolin and kaolinite rich clays, such as "china clay" or "fire clay" are heated to produce fire bricks or pottery, such as stoneware, earthenware or porcelain (Harvey & Lagaly, 2013). Especially earthenware is very common in private use as plate, tiles, flower pots or even sculptures. "Ball clays", which are micaceous kaolins are also used for fire brick, stoneware and earthenware production (Harvey & Lagaly, 2013). Heated illitic and bentonitic clays, such as Friedland clay, are used to produce wall constructions or shield tunnelling in the building industry and for the purpose of water filtration (Harvey & Lagaly, 2013). A new field of heated clay usage is GP production. Kaolin is currently used to industrially produce fire- and acid-resistant GP products, as well as coatings, fibre composites, paint, and concrete in many countries including Australia, Germany, the United Kingdom, the United States of America, France, and India (www.geopolymer.org/about/business-fellows).

2 Materials

A range of different illitic clays containing an important amount of I-S interstratification were used to characterise the nature of dehydration, dehydroxylation and structural breakdown during thermal activation. The behaviour of three main types of interstratifications was studied (see section 1.3). i) a disordered interstratification, the Eocene clay from Friedland, Northern Germany, containing an irregular stacked I-S interstratification, ii) a regular interstratification (Rectorite) from North Little Rock, Arkansas, USA, and iii) a long distance ordered I-S interstratification ("sárospatakite") from Füzérradvány, Hungary.

2.1 Eocene illitic clay from Friedland, Mecklenburg-Vorpommern, Germany

Samples of Friedland clay were provided from the Mineralische Rohstoffmanagement GmbH – Blautonwerk Friedland (MRG), which were industrially milled and dried. The Friedland clay deposit is located about 150 km north of Berlin near Neubrandenburg, NE Germany (Figure 2.1).

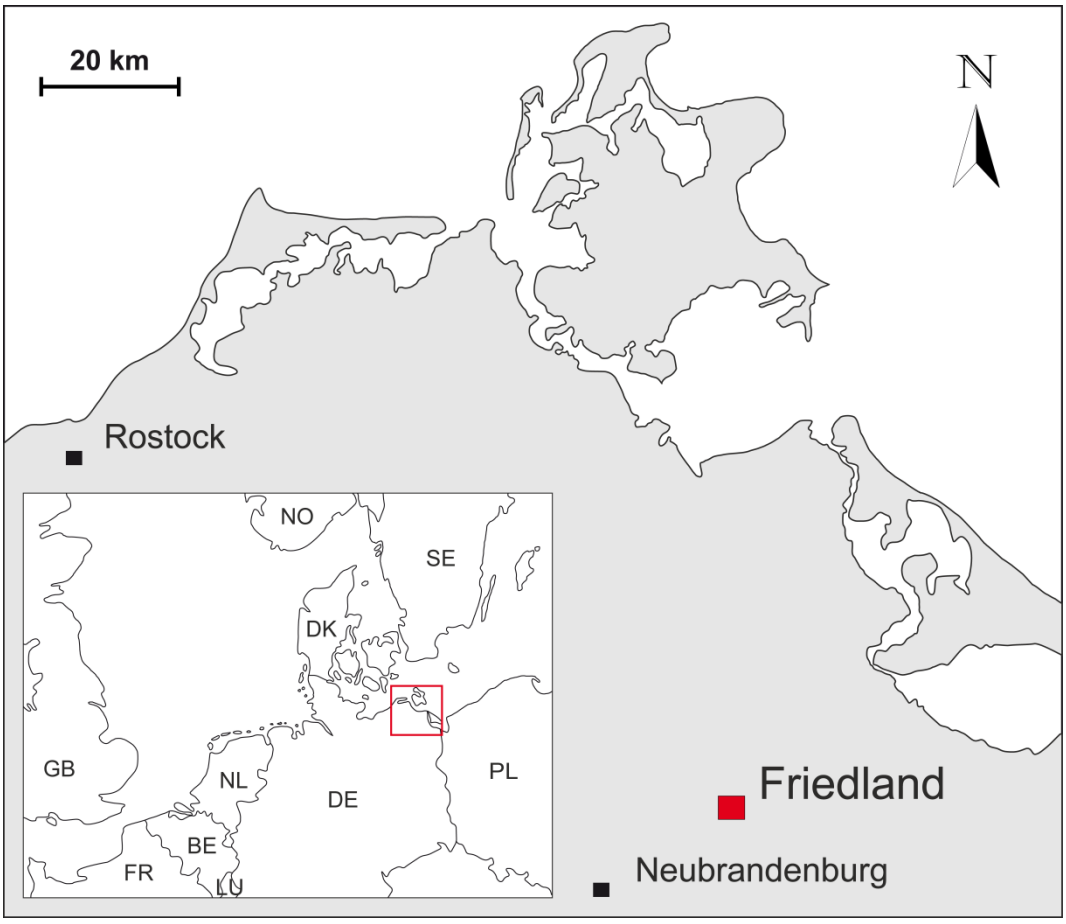

Figure 2.1. Map of northeastern Germany showing the location of Friedland.

It is a bluish grey (Figure 2.2) allochthonous sedimentary clay deposited during the Lower Eocene (Ypresian) about 47.8 – 56.0 million years ago (Henning & Kasbohm, 1998, Karnland, 2006, Cohen *et al.*, 2013). A marine transgression, active since the Upper Palaeocene (Thanetian, 59.2 – 56.0 Ma, Cohen *et al.*, 2013), progressed to the south and during the Eocene (56.0 – 33.9 Ma, Cohen *et al.*, 2013; Henning, 1968) to the east resulting in sedimentation of fluvial and subaerial weathering products derived from the Scandinavian Shield and the Bohemian Massive (Henning & Kasbohm, 1998; Katzung, 2004). It is a slack-water deposition of the north eastern Germany area, formed in a pelagic-marine facies of an epicontinental sea (Henning & Kasbohm, 1998; Katzung, 2004). Detrital mineral phases like muscovite, kaolinite and chlorite as well as quartz and feldspars occur were sedimented during the Ypresian, which partially makes up the mineralogy of today's clay formation. Eventual uplift of the surrounding continents during orogenic activity (for example formation of the Alps) and halokinetic (salt tectonic) processes eventually led to a regression of the sea until today's coast line shape was attained (Henning & Kasbohm, 1998). The sedimented material was affected by early diagenesis still under marine conditions leading to the neoformation of authigenic mineral phases, namely I-S interstratifications, apatite (with organic material as "phosphorite" concretions), pyrite (disperse and as concretions), or carbonates such as siderite, calcite, and dolomite occurring in dispersed and concretional form (Henning & Kasbohm, 1998). Due to diagenesis and compaction, dewatering occurred resulting in the lower porosity and permeability of the clay deposit. With the appearance of glacial tectonics during the Middle and Upper Pleistocene (0.0117 – 0.781 Ma, Cohen *et al.*, 2013), the movement of overlying ice led to imbrication of the clay deposit (Richter, 2000). Sulphates like gypsum or jarosite were most likely formed recently by oxidation of pyrite (Henning & Kasbohm, 1998). Today´s clay deposit is a weakly hardened bluish to greenish grey material with siderite, pyrite, and "phosphorite" concretions (Börner, 2013). The complex mineralogy of the clay mineral assemblage reflects the complex genesis of this sedimentary deposit (Henning & Kasbohm, 1998).

Figure 2.2. Photograph of the Friedland clay deposit in May 2011 (viewing direction northeast) (A) and a typical mining place with bluish-grey Friedland clay (B).

Henning (1968) investigated Friedland clay and some of its size fractions and concluded the interstratification is an irregularly stacked smectite-dominated muscovite-montmorillonite interstratification with about 60-70% smectitic layers (I(0.3-0.4)-S). Additional to the I-S interstratification (44% w/w) he found muscovite (12% w/w), kaolinite (11% w/w), glauconite (1% w/w), chlorite (traces), quartz (24% w/w), minor feldspar and carbonates (2% w/w) as well as pyrite (1% w/w)

occurring in the Friedland clay. Henning (1968) considered that the smectitic layers did not originate by alteration of volcanic material but formed by weathering of feldspars and micas. Henning & Kasbohm (1998) concluded Friedland clay contains an irregular I-S interstratification with 40-60% smectitic layers. About 50-70% w/w of the bulk material is located in the clay fraction <2 µm. A cation exchange capacity (CEC) of 54 cmol(+)/kg was measured for the bulk material. Pusch (1998, 2001) also characterised Friedland clay and determined its grain size distribution. He concluded that clay-sized particles <2 µm make up 57% w/w of the material. Additionally he determined the CEC of Friedland clay to be 40 cmol(+)/kg and concluded that adsorbed cations are dominated by K (66%) and Na (21%). The I-S interstratification present in the sample was estimated to I(0.45)-S.

Carlson (2004) extensively characterised Friedland clay and found it to consist mainly of an I-S interstratification, quartz, kaolinite, chlorite, illite, feldspars, and pyrite. In the size fraction >62 µm the author found quartz, siderite, pyrite, K-feldspar, plagioclase, kaolinite, and chlorite in decreasing abundance. In all size fractions, no pure smectite was found. Additionally, the content of total carbon (0.59% w/w) was determined where 0.57% w/w is bound as carbonates. The CEC was determined by leaching with $BaCl_2$ solution, LiCl solution, and using the ammonium acetate (NH_4-Ac) and the copper triethylenetetramine (Cu-trien) method resulting in values of 37 cmol(+)/kg, 38 cmol(+)/kg, 35 cmol(+)/kg, and 42 cmol(+)/kg, respectively. These results were later confirmed by Koskinen (2012) who determined the CEC using the Cu-trien method to be 32 cmol(+)/kg. Karnland *et al.* (2006) also determined the CEC value with the Cu-trien method and measured 22 cmol(+)/kg for the bulk sample and 34 cmol(+)/kg for the clay fraction which is significantly lower than measured by earlier authors. Furthermore they determined the exchangeable cations in the bulk material concluded that Friedland clay is dominated by Na (76%) with minor amounts of Mg (14%), K (7%), and Ca (4%). The measured LOI (loss on ignition) of 7.6% w/w of the bulk material increased to 9.5% w/w for the clay fraction (<2 µm). Karnland *et al.* (2006) determined a total amount of carbon of 0.6% w/w in the bulk material according to Carlson (2004), but found it was all organically bound, not in carbonates. The measured sulphur (0.5%) occurred as sulphate (17-33%) and sulphide (67-83%). Karnland *et al.* (2006) determined the grain size distribution of Friedland clay bulk material and concluded that about 50% w/w of the material is related to particles with a size <1 µm in diameter while only <15% w/w of the particles are >10 µm. The specific surface area (A_S) was determined by BET (Brunauer-Emmett-Teller) techniques to be 50-65 m^2/g. The I-S interstratification was estimated to have about 28% illitic layers and can be written as I(0.28)-S which is significantly lower than reported by Pusch (1998).

Kumpulainen & Kiviranta (2010) extensively characterised Friedland clay found, according to Karnland *et al.* (2006), that the bulk material is dominated by Na (58-76%) as the main exchangeable cation, followed by Ca (4-20%), Mg (13-17%) and some minor K (5-6%). The CEC was determined as 26 cmol(+)/kg (Cu-trien), 31 cmol(+)/kg (NH_4Cl), or 40 cmol(+)/kg (NH_4-Ac) which is in accordance to earlier reported data. The Fe^{2+}/Fe^{3+} ratio was determined for both, the bulk material and the Na-exchanged <2 µm fraction to be 0.65 and 0.47, respectively. The amount of carbon existing as minerals

was measured to be 2.40% w/w while organically bound carbon was 0.31% w/w, which is significantly higher than the values determined by Carlson (2004).

Typical results of chemical analyses for Friedland clay are shown in Table 2.1.

Table 2.1. Chemical analyses of Friedland clay bulk material by Pusch (1998), Carlson (2004), Karnland *et al.* (2006), and Kumpulainen & Kiviranta (2010). Values normalised to 100.00% w/w.

Component/ Element	Unit	Pusch (1998)	Carlson (2004)	Karnland *et al.* (2006)	Kumpulainen & Kiviranta (2010)
SiO_2	% w/w	57	62.52	60.77	57.97
TiO_2	% w/w	—	1.07	0.90	0.91
Al_2O_3	% w/w	18	19.00	17.27	16.53
$FeO + Fe_2O_3$	% w/w	5.5	7.09	6.39	6.77
MnO	% w/w	—	0.03	—	—
MgO	% w/w	2	2.02	1.90	1.85
CaO	% w/w	0	0.40	0.40	0.46
Na_2O	% w/w	0.9	1.07	1.10	1.04
K_2O	% w/w	3.1	3.19	3.09	2.81
SO_4+S(other)	% w/w	—	0.49	0.50	0.88
P_2O_5	% w/w	—	0.09	0.10	—
105 °C	% w/w	—	3.03	—	3.84
LOI 1050 °C	% w/w	—	—	7.58	6.94
Sum	% w/w	100.0	100.00	100.00	100.00

Quantitative phase analyses were made by different authors. Some of the results are summarised in Table 2.2.

Structural formulas were determined by Karnland *et al.* (2006) and Kumpulainen & Kiviranta (2010) per 2 F.U. But because none of these authors used a monomineralic sample, these structural formulas are unlikely to accurately constrain the formula for the I-S interstratification present in the sample. The impurity of these measurements is supported by calculation of the CEC values from these formulas that do not fit to analytically measured values.

$$(Na_{0.90})(Al_{1.75}Fe^{3+}_{1.26}Mg_{0.90}Ti_{0.19})[(Si_{7.49}Al_{0.51})O_{20}|(OH)_4] \quad \text{(Karnland } et\ al.\text{, 2006)}$$

$$(Na_{0.71})(Al_{2.22}Fe^{3+}_{1.09}Mg_{0.59}Fe^{2+}_{0.18})[(Si_{7.80}Al_{0.20})O_{20}|(OH)_4] \quad \text{(Kumpulainen \& } Kivirana\text{, 2010)}$$

Although this material was extensively investigated, the amount of the I-S interstratification present as well as mica, kaolinite and other minerals in the Friedland clay do appear to vary significantly from sample to sample due to strong material heterogeneities within the deposit. Hence, a characterisation of the sample material used in this work was considered necessary, rather than to rely of published information.

Table 2.2. Results of quantitative phase analyses of Friedland clay from Pusch (1998), Carlson (2004), Karnland *et al.* (2006), Kumpulainen & Kiviranta (2010), and Koskinen (2012). Values normalised to 100% w/w.

Mineral phases	Unit	Pusch (1998)	Carlson (2004)	Karnland *et al.* (2006)	Kumpulainen & Kiviranta (2010)	Koskinen (2012)
Clay minerals	% w/w	**69**	**45-55**	**74.2**	**66.3**	**77.4**
Smectite	% w/w	—	—	—	19.2	33.3
I-S interstratification	% w/w	45	10-15	33.2	—	—
White mica (illite-muscovite)	% w/w	13	<5	30.3	37.4	36.2
Kaolinite	% w/w	11	30-35	10.7	9.7	7.9
Chlorite	% w/w		—	—		—
Framework silicates	% w/w	**29**	**45-60**	**21.3**	**29.0**	**17.8**
Quartz	% w/w	24	35-40	20.2	28.5	14.9
Potassic Feldspar	% w/w	5	5-10	0.0	—	1.4
Plagioclase	% w/w		5-10	1.1	0.5	1.5
Others	% w/w	**2**	**traces**	**4.5**	**4.7**	**4.8**
Siderite	% w/w		traces	0.4	2.7	2.0
Dolomite	% w/w	2	—	—	—	—
Calcite	% w/w		—	0.1	—	0.1
Anatase+Rutile	% w/w	—	—	0.6	—	0.6
Goethite+Lepidocrocite	% w/w	—	—	0.5	—	0.2
Pyrite	% w/w	—	1	1.2	0.7	1.7
Hematite+Magnetite	% w/w	—	—	0.6	0.1	—
Gypsum	% w/w	—	—	0.7	1.2	0.2
Cristobalite+Tridymite	% w/w	—	—	0.4	—	—
Sum	% w/w	**100**	**100**	**100.0**	**100.0**	**100.0**

2.2 Rectorite from North Little Rock, Arkansas, USA

The North Little Rock (Figure 2.3) rectorite used for the study was obtained from the clay mineral collection of the Ernst-Moritz-Arndt-University Greifswald. The sample occurred as soft aggregates of rectorite and cookeite foliae together with quartz crystals according to Brown & Weir (1963) and Miser & Milton (1964) (Figure 2.4).

As the ancient continents Laurussia and Gondwana collided (Carboniferous, 258.9-303.7 million years, Cohen *et al.*, 2013) to form the new supercontinent Pangaea, the ocean between both continents closed (McFarland, 2004). During the late state of this closure (Lower Pennsylvanian, Bashkirian, 323.2-315.2 million years, Cohen *et al.*, 2013), increasing amounts of terrestrial sediment was deposited at a depth between 1.500 to 2.500 m as turbidites in submarine-fans, which is today preserved as the Jackfork sandstone (McFarland, 2004, Stone & Lumsden, 1984). The ongoing collision caused deformation and uplift of the sandstone formation, forming the Big Rock syncline, a part of the Ouachita fold-and-thrust belt (McFarland, 2004). During the late Pennsylvanian-Early Permian Ouachita orogeny (307.0-290.1 million years, Cohen *et al.*, 2013), silica-rich hydrothermal veins (<350 °C) formed during structural dilation (Richards *et al.*, 2002). These veins are generally dominated by quartz, but may contain significant amounts of rectorite, cookeite, calcite or other mineral phases (Richards *et al.*, 2002).

In Arkansas, rectorite localities generally occur along or close to the north margin of the vein quartz belt, mainly, but not exclusively in the Jackfork sandstone (Miser & Milton, 1964, Richards *et al.*, 2002).

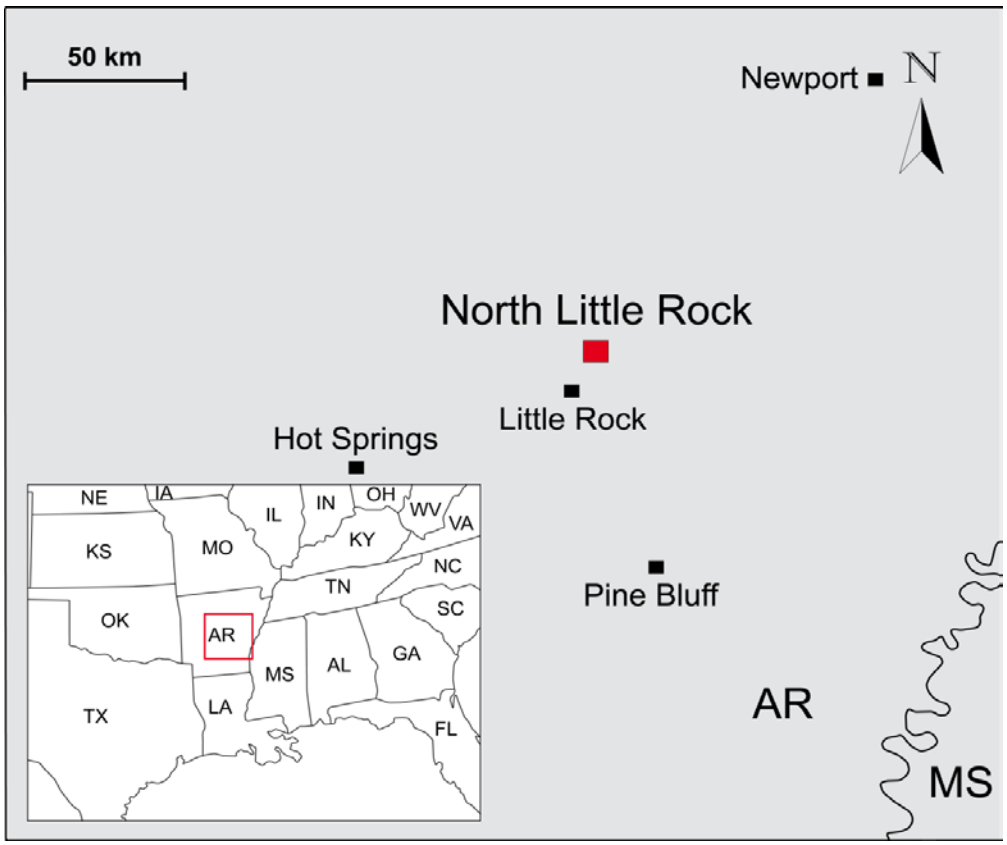

Figure 2.3. Map of Arkansas showing the location of North Little Rock.

In the Jeffrey quarry, Arkansas, the rectorite is associated with quartz, cookeite aggregates and various sulphides (pyrite, sphalerite, galena), as well as carbonates and rutile. These vertical veins are some meters long and about half a meter wide. Rectorite forms a gel-like substance, surrounding quartz crystals, with a high viscosity due to uptake of seepage water within these veins, especially in the lower part of the quarry. On drying, the semiliquid substance forms yellowish flexible plasters of rectorite (Figure 2.4). This generally seldom occurring mineral is abundant in the Jeffry Quarry, Arkansas (Miser & Milton, 1964). Altogether, there are about 11 locations of rectorite in Arkansas (Miser & Milton, 1964) and maybe another 8 main localities described worldwide (e.g. Kitagawa, 1997; Matsuda *et al.*, 1997). Rectorite mainly occurs in hydrothermal alterations, but has also been described in altered bentonites and as alterations of muscovite formed during shale diagenesis (Anthony *et al.*). Rectorite from North Little Rock, Arkansas, is a well known and extensively described material because it is one of the best examples of rectorite found in hydrothermal veins (<350 °C).

Numerous studies have been made on the geology, mineralogy and chemistry of hydrothermal Na-rich rectorite. Bracket and Williams (1891) first investigated material from Garland County, Arkansas and named it rectorite. Bradley (1950) investigated rectorite from Arkansas by XRD and thermal analysis (TA) and described it as a regular interstratification of pyrophyllite and vermiculite or montmorillonite. In

contrast, Brown & Weir (1963) who investigated this rectorite by XRD, electron microscopy, infrared (IR) spectroscopy, chemical analysis, and cation exchange measurements by measuring the difference in Mg content of Na- and Mg-saturated material considered the non-swelling 2:1 layers of the rectorite from Arkansas to be micaceous instead of pyrophyllite and found a CEC of 54 cmol(+)/kg. The micaceous and montmorillonite-like 2:1 layers were identified as dioctahedral. Additionally he stated that rectorite and allevardite is the same mineral. Miser & Milton (1964) characterised this material from different quarries in Arkansas by XRD and chemical analyses and concluded rectorite to be made up of pyrophyllite and vermiculite or montmorillonite-like layers. In contrast, Barron *et al.* (1985a and b) and Klimentidis & Mackinnon (1986) considered the non-swelling 2:1 layers of the rectorite from Arkansas to be micaceous instead of pyrophyllite. Klimentidis & Mackinnon (1986) concluded from high resolution transmission electron microscope (HRTEM) and XRD investigations that rectorite "is a regularly interstratified I-S with *R*1 ordering and 50% illite layers". More specifically, using solid state nuclear magnetic resonance spectroscopy (NMR), XRD, total chemical dissolution, and cation exchange, Jakobsen *et al.* (1995) considered the micaceous 2:1 layers to be paragonite with an exceptional high degree of tetrahedral substitution. These authors described this mineral as an ideally ordered interstratification of 50% paragonite and 50% smectite.

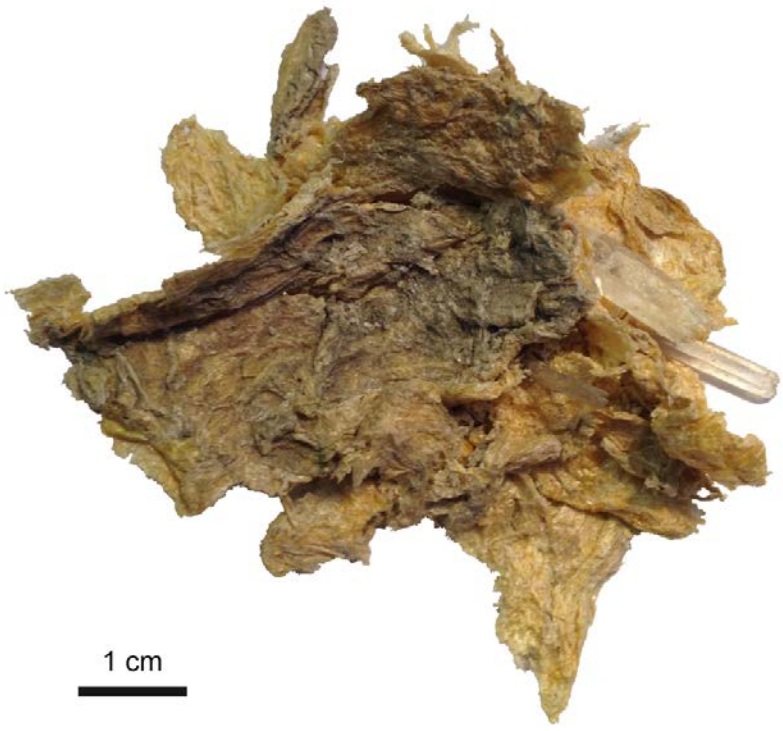

Figure 2.4. Photograph of a typical yellowish rectorite aggregate intergrown with cookeite and with large quartz crystals from North Little Rock, Arkansas.

Studies on rectorites from different locations other than Arkansas also considered rectorite (allevardite) to consist of pyrophyllitic (Brindley, 1956) or micaceous and smectitic layers either without specification of the mica or smectite-type (Brown & Weir, 1963) or by considering the smectite to be montmorillonite (Gradusov *et al.,* 1968). Similar to Jakobsen *et al.* (1995), Kodama (1966) described rectorite from

Pakistan as an ordered mixture of non-swelling paragonite-like layers and swelling beidellitic and montmorillonitic layers. Kodama (1966) noticed endothermic reactions related to dehydration (140 °C, 200-205 °C) and dehydroxylation (570 °C) and endothermic (960 °C) and exothermic (1030 °C) peaks both related to mullite formation. Today, rectorite is defined as a regularly interstratified 2:1 layer silicate, composed of dioctahedral mica and dioctahedral smectite, replacing the name allevardite (Caillère & Henin, 1950) as a synonym. The prefix Na-rich, K-rich or Ca-rich describes the dominant cation present in the mica interlayer (Guggenheim *et al.*, 2006, based on the work of Bailey, 1982). Typical X-ray fluorescence spectroscopy (XRF) results for rectorite from North Little Rock, Arkansas are shown in Table 2.3.

Table 2.3. Chemical analyses of rectorite from North Little Rock, Arkansas by Brackett & Williams (1891), published by Brown & Weir (1963) after correction for 12.5% w/w dickite, Brown & Weir (1963), and Miser & Milton (1964). Values normalised to 100.00% w/w.

Component/ Element	Unit	Brackett & Williams (1891)	Brown & Weir (1963)	Miser & Milton (1964)
SiO_2	% w/w	56.51	55.57	46.80
Al_2O_3	% w/w	38.31	38.96	33.54
FeO + Fe_2O_3	% w/w	0.30	0.59	0.02
MnO	% w/w	—	—	0.01
MgO	% w/w	0.61	—	0.52
CaO	% w/w	0.55	0.33	1.09
Na_2O	% w/w	3.41	4.43	3.48
K_2O	% w/w	0.31	0.11	0.12
LOI 1050 °C	% w/w	—	—	14.42
Sum	% w/w	100.00	100.00	100.00

Structural formulas were determined according to Stevens (1946) without using layer charge measurements according to Lagaly & Weiss (1971) from data published by Brackett & Williams (1891) (data re-published by Brown & Weir, 1963 after correction for 12.5% w/w dickite), Brown & Weir (1963), Miser & Milton (1964), and Jakobsen *et al.* (1995) per 2 F.U.:

$$(Na_{0.78}Mg_{0.10}Ca_{0.06}K_{0.04})\left(Al_{4.02}Fe^{3+}_{0.02}\right)[(Si_{6.68}Al_{1.32})O_{20}|(OH)_4] \quad \text{(Brackett \& } Williams, 1891)$$

$$(Na_{1.02}Ca_{0.04}K_{0.02})(Al_{4.02}Fe^{3+}_{0.06})[(Si_{6.60}Al_{1.40})O_{20}|(OH)_4] \quad \text{(Brown \& } Weir, 1963)$$

$$(Na_{0.94}Ca_{0.16}Mg_{0.10}K_{0.02})(Al_{4.00})[(Si_{6.50}Al_{1.50})O_{20}|(OH)_4] \quad \text{(Miser \& } Milton, 1964)$$

$$(X_{0.24}Na_{0.98}Ca_{0.02})(Al_{4.00}Fe^{3+}_{0.06}Mg_{0.02})[(Si_{6.52}Al_{1.48})O_{20}|(OH)_4] \quad \text{(Jakobsen } et\ al., 1995)$$

Despite the numerous studies of rectorite, the precise crystal chemistry of this mineral continues to remain controversial and the type of micaceous and the smectitic layers are still not unambiguously determined.

2.3 "Sárospatakite" from Füzérradvány, Hungary

The "sárospatakite" sample studied was obtained from the clay mineral collection of the Ernst-Moritz-Arndt-University Greifswald. The "sárospatakite", although being an interstratification is sometimes also called "Füzérradvány illite" or "Zempleni illite". It is named after a larger town of Sárospatak, although occurring next to the clay deposit of Füzérradvány, which is located in the northeastern part of the Tokaj mountain range (= Zempleni Mountains) in northeastern Hungary (Figure 2.5, Viczián, 1997; Viczián *et al.*, 2004).

Figure 2.5. Map of northeastern Hungary showing the location of Füzérradvány and Sárospatak.

As the African and the Eurasian plate collided at the end of Mesozoic to Tertiary times (100-10 million years, Cohen *et al.*, 2013), the former ocean basins of Tethys were partly preserved within an accretionary prism. The following continental-continental collision process resulted in an orogeny forming the alpine orogenic belt including the Carpathian Mountains (Pécskay *et al.*, 2006). As a part of the Western Carpathians, the Northern Hungarian Mountains includes the Tokaj Mountains. The Tokaj Mountains mainly consist of an Early Palaeozoic metamorphic rock basement (gneiss, amphibolite, mica schist) overlain by Upper Miocene sediments (9.3-5.3 million, Cohen *et al.*, 2013; Viczián *et al.*, 2004). These marine clays are overlain by pumice tuffs and tuffite formed by eruptions initiated by Pannonian Basin subsidence during Middle Miocene times (15.0-9.3 million, Cohen *et al.*, 2013; Pécskay *et al.*, 1986, 2006) which are covered by a high siliceous lacustrine sequence (Mátyás, 1974; Ilkeyné Perlaky & Pentelényi, 1968; Gyarmati, 1977; Csongrádi *et al.*, 1996). These acidic (rhyolitic) rocks provided the

starting material for hydrothermal alteration, dated to 10-15 million years by K/Ar isotope study (Pécskay *et al.*, 1986; Viczián, 1997; Molnár *et al.*, 1999 cited in Bajnóczi *et al.*, 2000). Towards the end of the intermediate volcanism during Lower Miocene (14.8-9.3 million years, Cohen *et al.*, 2013; Pécskay *et al.*, 1986, 2006), hydrothermal activities of a low sulphidation type epithermal environment occurred in that region forming today´s Füzérradvány clay deposit (Pécskay *et al.*, 1986; Viczián *et al.*, 2004). This clay crystallised from hydrothermal fluids within a short period of time as all size fractions of the illite fundamental particles have very similar K-Ar ages within analytic uncertainties and supposedly a constant temperature indicated by $\delta^{18}O$ values (Clauer *et al.*, 1997; Clauer, 2006). The hydrothermal alteration fluids were proved to be acidic and silica-rich resulting in an intense silicification of clastic sediments (Viczián *et al.*, 2004).

This standard material for illite/I-S interstratification (Figure 2.6) has been described by many authors since the 1930´s (Viczián *et al.*, 2004). It was used in the porcelain industry in the early 20th century (Viczián *et al.*, 2004). Maegdefrau & Hofmann (1937) first investigated this material by XRD and XRF concluding to be composed of a mineral with a muscovite-like structure and compared it to illite from Illinois, U.S.A. Based on structural formula determinations they concluded only 1.41 K and Ca cations are present per formula unit and supposed that the other 0.59 positions are occupied by water molecules. Subsequent heating of the material revealed that most water expelled during dehydroxylation is lost within 400-500 °C. Hofmann *et al.* (1941) and Beutelspacher & van der Marel (1968) investigated this material with electron micrograph and described it as “perfectly crystallised thin plates and laths”. Grim & Brandley (1948, 1952) first noticed the sample to consist of illitic and montmorillonitic layers as an interstratification. Kiss & Takáts (1963) investigated this clay using XRD and heating of the sample and concluded that the clay did not consist of an interstratification, but a discrete illite phase, although they noticed dehydroxylation occurs at temperatures that are typical for illites (550-600 °C) and for montmorillonite (700 °C). Henning & Störr (1986) described this “sárospatakite” as an irregular I-S interstratification with lath-like particle shape. Nemecz & Varju (1970) noticed the heterogeneity of the samples and recognised the interstratification because XRD results revealed a basal reflection (001) of 10.1-11.1 Å that split upon ethylene glycol intercalation. The amount of expandable layers was estimated to <10-26%. Nemecz & Varju (1970) found a good correlation between layer charge and equivalent K content and recognized the 1M polytype of this material. Patzkó & Szántó (1983) concluded the finest fraction of this sample to contain only pure illite without any interstratification by peptisation methods. This was supported by Dódony (1985) who observed stacks of several micaceous layers each rotated on their (001) plane by HRTEM.

Środoń (1984) investigated this illitic material and concluded to be dominated by I-S with ISII ordering and a smectite content of 17%. Szegedi (1988) concluded that about 10-13% expandable layers exist with an ordering type of ISII. Similar results were later published on the basis of XRD by Ahn & Buseck (1990) (18% smectite content), Veblen *et al.* (1990) (17% smectite content determined by XRD, 25% determined by HRTEM), Reynolds (1992) (16% smectite content), and Środoń *et al.* (1992) (16% smectite

content determined by XRD, 21% and 32% determined by transmission electron microscopy (TEM), respectively), each of them observing *R*3 ordering. Środoń *et al.* (1992) additionally found that no NH_4 exists in this sample. Ahn & Buseck (1990) also investigated the material by HRTEM and found 1M polytypic order interrupted by stacking faults while XRD results indicated a $1M_d$ polytype. Veblen *et al.* (1990) considered this material to be typical for *R*>1 ordering of I-S interstratifications and described the particle shape as elongated lath-like crystallites. Based on electron diffraction they concluded the ordering type to be ISIIISII where 2-6 illite packets are separated by one smectitic layer. Clauer *et al.* (1997) who investigated the smectite content of this material as a function of the particle size concluded that the average content of expandable layers varies between 11% and 18% and increases with decreasing particle size.

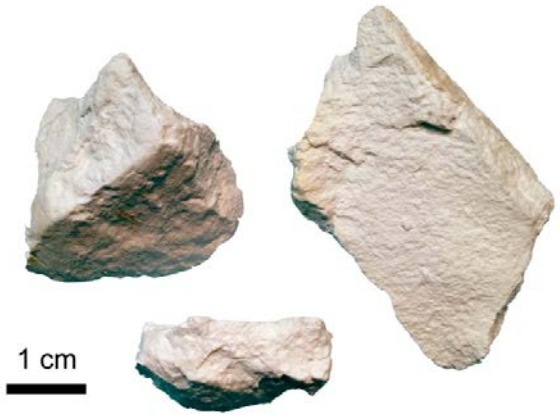

Figure 2.6. Photograph of a three pieces of the white, homogeneous "sárospatakite" sample from Hungary.

Ferrari & Gualtieri (2006) and Gualtieri & Ferrari (2006) investigated a sample from Füzérradvány, Hungary by XRD, temperature dependent X-ray diffraction (TXRD), XRF, simultaneous thermal analysis (STA), scanning electron microscopy (SEM), and TEM and described the material as consisting of 62% w/w illite, 27% w/w quartz, 6% w/w I-S, 5% w/w K-feldspar, and traces of goethite. The interstratification was not investigated further. Dehydroxylation of the clay minerals occurred in two steps, one between 813-823 °C, and a second one between 933-943 °C indicating both trans-vacant (tv) and cis-vacant (cv) layers. Additionally, they reported that the material melts at about 1200 °C. Gualtieri *et al.* (2008) characterised a sample from northern Hungary by XRD, SEM, and TEM and concluded from WILDFIRE, NEWMOD, and DIFFaX simulations that this sample contains 10% expandable layers and an amount of 30% cis-vacant layers. The illitic layers were described as dioctahedral mica with K dominated interlayer (80% site population) and a prevalence of 1M over $2M_1$ polytype. The rotational disorder was described as "limited" (*p0* = 0.75). The material was called illite, although the presence of smectitic layers was recognised using XRD. They described the crystal habit as lath-like, according to Beutelspacher & van der Marel (1968), Henning & Störr (1986), and Veblen *et al.* (1990). Furthermore they measured a total weight loss (1000 °C) of 8.04% w/w which is higher than measured by Mátyás (1972, Table 2.4).

Zumsteg & Puzrin (2012) determined the CEC using the Cu-trien method to be 9 cmol(+)/kg and the N_2-BET value to be 34 m²/g. Ufer *et al.* (2012a,b) investigated the material to develop a structural model for interstratifications. They concluded the sample to contain exclusively an *R*3 ordered dioctahedral I-S interstratification except for 4% w/w quartz. The structural refinement of the I-S interstratification compared to XRF results revealed low very Fe contents (0-0.06), an occupancy of K of about 0.70-0.76 derived from Rietveld refinement and 0.79 derived from XRF (all per F.U.), and an amount of smectitic layers of 13-15%. The amount of cv layers was refined to be 53%. *p0* was refined to be 63% indicating a medium disordered polytype between 1M and $1M_d$.

Typical XRF results for the "sárospatakite" are shown in Table 2.4.

Table 2.4. Chemical analyses of "sárospatakite" by Mátyás (1972) using XRF, Veblen *et al.* (1990) using electron microprobe analysis, and Ferrari & Gualtieri (2006) and Gualtieri & Ferrari (2006), both using XRF. Values normalised to 100.00% w/w.

Component/ Element	Unit	Mátyás (1972)	Veblen *et al.* (1990)	Ferrari & Gualtieri (2006)	Gualtieri & Ferrari (2006)	Ufer *et al.* (2012a,b)
SiO_2	% w/w	49.10	54.14	57.76	50.19	51.86
TiO_2	% w/w	0.04	0.08	0.11	0.08	0.10
Al_2O_3	% w/w	31.64	33.87	26.37	30.39	27.68
FeO + Fe_2O_3	% w/w	0.51	0.11	0.49	0.33	0.60
MnO	% w/w	—	0.02	—	0.01	0.00
MgO	% w/w	1.88	2.23	1.16	3.45	2.51
CaO	% w/w	1.77	0.76	0.33	0.24	0.60
Na_2O	% w/w	0.10	0.00	0.26	0.17	0.00
K_2O	% w/w	7.95	8.78	8.49	7.03	7.32
SO_3	% w/w	0.06	—	—	—	—
P_2O_5	% w/w	—	—	—	0.07	—
LOI 1050 °C	% w/w	6.94	—	5.02	8.04	9.33
Sum	% w/w	100.00	100.00	100.00	100.00	100.00

Structural formulas were determined by Veblen *et al.* (1990) using electron microprobe, Gualtieri *et al.* (2008), and Ufer *et al.* (2012a,b) both using XRF (per 2 F.U.):

$$(K_{1.38}Ca_{0.10})(Al_{3.62}Fe^{3+}_{0.02}Mg_{0.42})[(Si_{6.68}Al_{1.32})O_{20}|(OH)_4] \quad \text{(Veblen } et\ al.\text{, 1990)}$$

$$(K_{1.56}Ca_{0.04}Na_{0.04})(Al_{3.38}Fe^{3+}_{0.04}Mg_{0.68})[(Si_{6.70}Al_{1.30})O_{20}|(OH)_4] \quad \text{(Gualtieri } et\ al.\text{, 2008)}$$

$$(K_{1.34}Ca_{0.12})(Al_{3.46}Fe^{3+}_{0.06}Mg_{0.52})[(Si_{6.82}Al_{1.18})O_{20}|(OH)_4] \quad \text{(Ufer } et\ al.\text{, 2012a).}$$

Although this material has been extensively characterised, there is still no consistent description whether this material consists of illite containing some minor expandable layers (<<5%) or an illite-rich I-S interstratification (>5% expandable layers; definition based on Środoń & Eberl, 1984 and Moore & Reynolds, 1997).

3 Sample preparation and analytical methods

3.1 Sample preparation

3.1.1 Pre-treatments

For characterization and investigation of the dehydroxylation behaviour, the I-S interstratification of each sample was concentrated by particle size fractionation. The <0.1 µm fraction was chosen for being highly enriched in I-S material.

In the case of rectorite, large quartz crystals were first picked out by hand. Rectorite and "sárospatakite" were gently milled in an agate mortar to obtain a powder (Figure 3.1). All three samples were separated by disaggregation by ultrasonic treatment for 15 minutes and dispersed in deionised water and subsequently allowed to stand overnight to hydrate. The next day, the size fractioning was started (see section 3.1.2). Friedland clay was selected for investigating the size fractions in more detail, whereby the following size fractions were separated (Table 3.1).

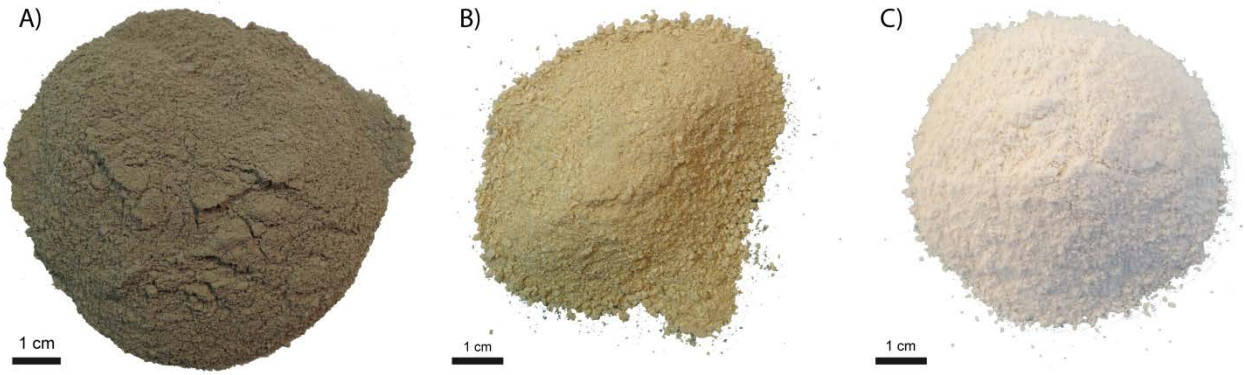

Figure 3.1. Powdered samples of A) Friedland clay, B) rectorite, and C) "sárospatakite" bulk material.

Table 3.1. Particle sizes separated for Friedland clay, the method used, and the expected mineral phase content.

Size fraction separated	Method	Expected minerals and mineral groups
>10 µm	Sedimentation	Large clay minerals, e.g. 2M mica, kaolinite, framework silicates, oxides, sulphides, sulphates, carbonates
10-2 µm	Sedimentation	Large and medium clay minerals, e.g. 2M mica, kaolinite, framework silicates, oxides, sulphides, sulphates, carbonates
2-0.2 µm	Centrifugation	Medium and small clay minerals, e.g. interstratification, 1M and 2M micas, kaolinite, some framework silicates
<0.2 µm	Centrifugation	Small clay minerals, e.g. interstratification, 1M mica
<0.1 µm	Centrifugation	Small clay minerals, e.g. interstratification, 1M mica

3.1.2 Particle Size Separation

Settling times of particles can be calculated using Stokes´ law (equation 3.1) after Moore & Reynolds (1997). This equation assumes ideally round particles (spheres) without any interactions between the particles or between a particle and the bottle. Additionally, this equation is only valid for laminar streaming (Reynolds numbers <1), which is equal to a maximum particle size of about 100.8 µm in water at a temperature of 20 °C. Here, the equation was applied only for particle sizes about up to 20 µm in order to fulfil these requirements. As spherical particles are assumed, the separated particle sizes are "equivalent diameters" only. Clay mineral particles are rarely spherical, and most often platy, rod- or tubular in shape and sometimes spiral in form; as a result they have more complex settling behaviour during grain size separation. Additionally, the assumed average density of the material may differ widely as a result of swelling phases, i.e. smectite, which can adsorb a high content of water and thus drastically reduce the particle density. The large differences in density of the different phases separated directly influences the settling rate and the size fractions separated. Stokes´ law is given as:

$$t = \frac{18 \times \eta_0}{(\rho - \rho_0) \times g} \times \frac{(h - h_0)}{d^2} \qquad 3.1$$

t …. Settling time [s]

η_0 …. Viscosity of water (1.0020 g/m×s at 20 °C, Kestin *et al.*, 1978)

ρ …. Density of the sample [g/cm³]

ρ_0 …. Density of water (0.9982336 g/cm³ at 20 °C, Kestin *et al.*, 1978)

g …. Force of gravity (~9.814×10² cm/s² at Greifswald)

h …. Filling level of the suspension [cm]

h_0 …. Height were suspension is removed [cm]

d …. Equivalent sphere diameter [mm]

By using a centrifuge, the gravity force is changed and hence, the equation for calculation the settling time must be adjusted (equation 3.2, after Tributh & Lagaly, 1986). The main term remains and parameters influencing the gravity force like namely distances within the centrifugal device or the rotational speed are added.

The boundary conditions mentioned above such as interactions between particles, laminar streaming, assuming spherical particles, or density variations are in the centrifuge method equally valid. Additionally, the acceleration and deceleration time when the centrifuge is not at its selected rotational speed needs to be considered. Turbulence effects were reduced by using a high accelerating speed and a low brake force.

$$t = \frac{18 \times \eta_0 \times \ln(\frac{r}{r_0})}{(\rho - \rho_0) \times 4\pi^2 \times d^2 \times f^2} \quad 3.2$$

t …. Settling time [s]

η_0 …. Viscosity of water (1.0020 g/m×s at 20 °C, Kestin *et al.*, 1978)

r …. Distance between rotation axis and removal point [cm]

r_0 …. Distance between rotation axis and suspension surface [cm]

ρ …. Density of the sample [g/cm³]

ρ_0 …. Density of water (0.9982336 g/cm³ at 20 °C, Kestin *et al.*, 1978)

d …. Equivalent sphere diameter [mm]

f …. Rotational speed [1/s]

Procedure

Particle size separations were made using two different methods: Atterberg sedimentation for particle sizes ≥2 µm using a glass cylinder, and centrifugation for particle sizes <2 µm using an Eppendorf Centrifuge 5810 R device. The parameters used for size separations are listed in Table 3.2.

Table 3.2. Methods and parameters used for particle size separations.

Size fraction separated	Method	Temperature	Time	Rotations per minute	Sedimentation height	Rotary length
<10 µm	Sedimentation	20 °C	30 min	—	15 cm	—
<2 µm	Centrifugation	20 °C	29 min	340 min^{-1}	15 cm	18 cm
<0.2 µm	Centrifugation	20 °C	30 min	3,350 min^{-1}	15 cm	18 cm
<0.1 µm	Centrifugation	20 °C	79 min	4,000 min^{-1}	15 cm	18 cm

First, the loose sample powder was placed into a beaker and dispersed in distilled water by ultrasonic treatment for 15 minutes and afterwards allowed to stand overnight in order that the clay swelled as was fully hydrated. The following day, the samples were again ultrasonically treated for 15 minutes before pouring the suspensions into the Atterberg cylinders or centrifuge tubes. After the given settling period or centrifugation time, size fractioning was achieved by removing the suspension containing the required particle size fraction and the remaining sediment resuspended in distilled water and the procedure repeated until most particles of that size fraction were removed. The prepared size fraction suspensions were concentrated by evaporation at 50 °C until it became a dry powder and homogenised by hand using an agate mortar.

3.1.3 Milling

Milling was used in this study 1) to reduce micro-absorption effects during XRD analyses and having similar grain sizes for each phase present in the clay size fractions (micronising mill), 2) to break up large sintered aggregates obtained by heating, and 3) to activate the clay material mechanically. For the latter purpose, a range of different mills were used and tested.

Planetary balls mills are named after the movement inside the mill while grinding, similar to the movement of planets in the solar system. The grinding beakers move around the rotation axis in the middle of the mill with constant or varying velocity. The beakers themselves rotate around their own axis in the opposite direction to swing motion of the wheel. Within the beakers, balls (commonly agate, steel of wolfram carbide) move at different velocities due to differences in the ball weight, and movements of beaker and wheel. These ball movements guarantee a consistent milling process of the sample by shearing and friction as well as by direct impact and deviatoric pressure. To reduce spalling of the balls, the beakers should be filled with as much sample powder to cover the grinding balls. An important factor in this type of milling is the ratio between amount of sample and grinding ball weight (e.g. Hamazaoui *et al.*, 2015). Additionally, the ground material, the number, size, and size distribution of the balls, and ball hardness all play an important role in the milling process.

Disc mills are composed of a larger grinding container (basin) typically made of steel or agate in which a set of rings are placed. The sample is placed between the rings and during shaking the rings collide and grind down the intervening powder. Due to the high weight of the grinding set there is a high energy of transmission and therefore this method is generally faster and more aggressive in terms of milling treatment. As in the ball mill, the sample is ground and homogenised by friction, impacts, and pressure. However, the disc mill has the disadvantage that there is a relatively high amount of contamination of the grinding set material (e.g. by steel). In this study, the contamination was not considered to be of relevance as the material was not ground for the purpose of chemical analyses.

Procedure

Grinding the clay in order to activate the material mechanically was undertaken using two planetary ball mills: A Retsch PM4 and a Fritsch Pulverisette, and a disc mill MSL 2 from the VEB Bergbau- und Hüttenkombinat Freiberg. The grinding conditions are listed in Table 3.3.

For reducing micro-absorption effects during XRD analyses, 3 ml of the dry sample powder (except the <0.1 fraction samples) were ground using a McCrone micronising mill for 8 minutes in 10 ml ethanol which served as a cooling agent (see section 3.2.1).

To break up large sintered aggregates, the heat-treated clays were milled with a Retsch PM 4 using agate balls (ball:clay ratio 7.6) at 300 rpm for 2 hours.

Table 3.3. Methods and parameters used for particle size separations.

Type of mill	Manufacturer, model	Grinding set	Rotational speed	Sample amount	Duration of milling
Planetary ball mill	Retsch PM 4	Agate balls (94 g) in an agate jar	300 min^{-1}	70 g	10 h
Planetary ball mill	Fritsch Pulverisette 7	Steel balls (74 g) in a tungsten carbide jar	400 min^{-1}	30 g	2 h 11 h 16 h
Disc mill	VEB Bergbau- und Hüttenkombinat Freiberg, Type MSL 2	Hardened steel	930 min^{-1}	20 g 20 g 20 g 40 g 40 g 50 g	5 min 30 min 1 h 1 h 2 h 3 h

3.2 Qualitative and quantitative phase analysis

3.2.1 Powder X-Ray Diffraction (XRD)

The powder XRD method uses characteristic X-ray radiation of a certain wavelength depending on the anode (here Co). By using a suitable filter material (e.g. Fe for Co radiation), the k_β radiation can be reduced resulting in an almost monochromatic k_α radiation. Here, a Fe foil was used that adsorbs about 99.5% of the k_β radiation. By irradiation of the powdered sample, several effects occur, namely emission of fluorescent characteristic X-rays (used in X-ray fluorescence) or electrons (e.g. Auger electrons), heating of the sample or scattering of the X-rays. Compton effects (inelastic/incoherent scattering) are negligible and in XRD, scattering without any modification of the primary X-ray (elastic/coherent scattering) dominants. The impinging X-rays cause periodic swinging of the inner electrons of the sample atoms for having similar radii compared to atomic radii and atomic plane distances (10^{-9} – 10^{-11} m). Due to the regular array of atoms within a single domain (presence of atomic planes), interferences occur. Braggs´ law describes the diffraction of these X-rays by atomic planes and at which angle of 2θ constructive interferences occur (equation 3.3, Bragg & Bragg, 1913).

$$n \times \lambda = 2 \times d \times \sin(\theta) \qquad 3.3$$

n …. Integer number

λ …. Wavelength [Å]

d …. Spacing between adjacent atomic planes [Å]

θ …. Scattering angle [°θ]

Figure 3.2 shows a schematic outline of the variables in Braggs´ law. Using monochromatic radiation, for every d-spacing a constructive interference occurs at a certain scattering angle θ. Having a powdered sample with (almost) no preferred orientation and enough crystallites (grain statistics), every possible scattering angle occurs. Hence, a certain atomic plane family (*hkl*) of a mineral phase diffracts with a certain order *n* at a defined scattering angle θ. By moving the tube and detector constantly with identical angle velocities on the goniometer circle around the sample, an X-ray pattern can be recorded for the sample surface being on a tangent to the focusing circle.

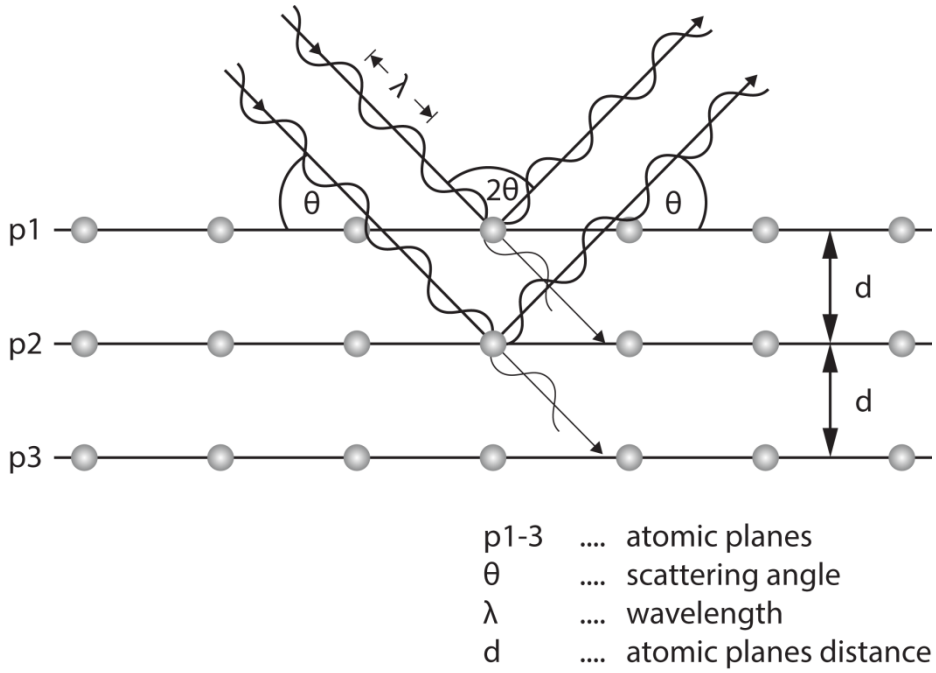

Figure 3.2. Schematic outline of Braggs´ law. The incoming parallel X-ray beam is diffracted at adjacent atomic planes (p1-3). For a defined d-spacing, at a certain angle, constructive interferences occur.

By calculation of d-spacings from the diffraction angles and considering intensity ratios, interpretations of the unit cell like symmetry or size can be made that are used for mineral phase identification in the sample.

For quantification purposes the program BGMN (Bergmann *et al.*, 1998) was used, which applies the Rietveld method of Rietveld (1967, 1969). This is a whole pattern fitting method that uses structure models for every single crystal structure present in the sample. For every phase in a mixture, a theoretical diffraction pattern is calculated and summed to a theoretical pattern for the whole mixture. By variation of the structural parameters described below, the theoretical pattern is fitted to the measured one. Every single data point in the pattern is a summation of intensities of all phases and the background at this data point. Kleeberg & Bergmann (2002) translated it to the following mathematical formula:

$$Y_i = \sum_p \left[S_p \sum_k \left[L_k P_k H_k |F_k|^2 G(\Delta\Theta_{ik}) Po_k \right] \right] + y_{bi} \,. \qquad 3.4$$

Y_i …. Intensity at data point i

S_P …. Scale factor (proportional to the scattering volume of the phase)

L_k …. Lorentz factor

P_k …. Polarisation factor

H_k …. Multiplicity factor (area frequency)

$|F_k|^2$ …. Squared structure factor

K …. Line k

$G(\Delta\Theta_{ik})$ …. Profile function

Po_k …. Preferred orientation correction

Y_{bi} …. Intensity of the background

By varying structural parameters such as lattice parameters or occupation factors and profile analyses for micro strain or crystallite size broadening, the calculated diffraction pattern can be fitted to the measured. The phase contents of all phases can be calculated because the peak area of a single phase related to the sum of peak areas of all phases is proportional to the phase content (in volume-%). Including the volume of the unit cell and the calculated X-ray density of each phase, the % w/w of every single phase can then be calculated (equation 3.5, Kleeberg & Bergmann, 2002).

$$X_p = \frac{S_p \rho_p V_p^2}{\sum_j S_j \rho_j V_j^2} \qquad 3.5$$

X …. Mass fraction

S …. Rietveld scaling factor

ρ …. Calculated X-ray density

V …. Volume of the unit cell

p …. Phase p

j …. Number of phases

After reaching the best possible fit, the goodness-of-fit can be verified by both visually examining a difference curve or by mathematically calculating the least square sum (equation 3.6, Kleeberg, 1996).

$$R_{wp} = \sqrt{\frac{\sum_i [w_i (y_i - y_{ic})^2]}{\sum_i [w_i y_i^2]}} \quad 3.6$$

and

$$w_i = \frac{1}{y_i} \quad 3.7$$

R_{wp} …. Weighted least square sum (goodness of fit)

w_i …. Weighting factor

y_i …. Observed intensity at data point i

y_{ic} …. Calculated intensity at data point i

The weighting factor refers to the statistical background noise. If the peak/background ratio is low ("less noise"), the weighting factor is low and vice versa.

The coefficient of variation (CV) is a factor that describes the regularity of alternation within interstratifications and can be calculated for rectorite from the ethylene glycol saturated sample pattern. A CV of <0.75 qualifies a regularly stacked interstratification to be allocated a mineral name, such as rectorite or corrensite (Bailey, 1982; Guggenheim *et al.*, 2006). At least three orders of basal reflections including two odd orders must be considered and for a reliable CV value at least ten (00*l*) values should be used (Bailey, 1982; Guggenheim *et al.*, 2006). Additionally, all peaks utilised should have similar peak breadths (full-width-at-half-maximum, FWHM). The CV is calculated according to equation 3.8 (after Bailey, 1982):

$$\mathrm{CV} = \frac{100 \times \sigma}{\overline{X}} \quad 3.8$$

where the standard deviation σ is defined as:

$$\sigma = \sqrt{\frac{\sum (X_i - \overline{X})^2}{n - 1}} \; . \quad 3.9$$

X_i …. Observed l×(00*l*) value

$\overline{X}$ …. Arithmetic mean of all X_i

n …. Number of observed (00*l*)-reflections

The FWHM parameter was determined using the measurement method of the Kübler index after stripping $k_{\alpha 2}$ and correcting for angular-dependent broadening.

Analytical procedure

XRD was applied for qualitative and quantitative phase analysis of both, clay- and non-clay minerals. Before preparation for XRD study, a volume of 3 mL of every dry powder sample (except <0.1 µm fraction samples) was milled for 8 minutes in a McCrone micronising mill with ethanol as a cooling agent for reducing micro absorption effects and to produce similar grain sizes of each phase present in the clays (see section 3.1.3). Two different sample preparation techniques were used: (1) Random powders were prepared by frontloading of an Al-cuvette for identification on mineral phases and for quantification purposes. (2) Preferred oriented samples were prepared by using a small amount of clay from the tip of a spatula and dispersing it with 3 mL 0.01 mol/L ammonium hydroxide solution (NH_4OH) for 10 minutes by ultrasonic treatment. Afterwards the suspension was tipped on a glass slide for sedimentation of particles until it dried under room condition (ca. 1.5 mg/cm²). For diagnostic reasons, the samples were measured in air dried condition, after ethylene glycol ($C_2H_6O_2$) saturated (20 hours at 60 °C) and after heating to 550 °C. These preferred oriented specimens were only used for characterisation and qualitative phase analyses, not for quantification purposes.

A Bruker D8 Advance θ-θ diffractometer was used with Fe-filtered CoKα radiation ($K\alpha_1$ = 1.78897 Å; $K\alpha_2$ = 1.79285 Å) generated at 40 kV and 30 mA, equipped with a 0.499° divergence slit, an 8 mm antiscatter slit, 2.5° primary and secondary soller collimator and a 1D LynxEye detector that includes 14 strips each with a height of 0.075 mm. Scans were ran with a step size of 0.02° 2θ (rounded) between 3 and 100° 2θ with an angle velocity of 0.5 °/min (rounded) for randomly oriented powders and 2.5 to 80° 2θ with an angle velocity of 3 °/min (rounded) for preferred oriented samples.

Qualitative phase analyses were made with the aid of Brindley & Brown (1984) and the program Diffrac^{plus} Evaluation Package "EVA" Version 14.0 by Bruker AXS with the PDF database PDF-2, Release 2008. Quantification of both, clay and non-clay mineral phases, and crystallographic modelling of the I-S samples were carried out with the program BGMN 4.2.20 (Bergmann *et al.*, 1998) and modified structure models of I-S interstratifications after Ufer *et al.* (2012a,b). Because rectorite is a regularly stacked interstratification, and in this case additionally Na dominated, the structure model of Ufer *et al.* (2012a, b) had to be modified extensively according to Ufer (2014, pers. comm.). The I-S structure model published by Ufer *et al.* (2012a,b) consist of two separate models, one calculating the basal series and one calculating the non-basal reflections, that are connected by globally defined parameters such as the scale factor, degree of preferred orientation, content of K^+ in the interlayer (*pK*) and Fe content of the octahedral sheet (*pFe*). The atomic position starting values of both models are based on Drits (2006). The non-basal model considers and refines the possibilities of *n*×60°/*n*×120° rotations and the proportion cis- and trans-vacant octahedral sheets as well as its stacking vectors (Table 3.4).

To determine the illite content of I-S interstratifications, two different methods were used to check for consistency. First, a Rietveld refinement was made using the BGMN program based on random powder measurements as well as analysis of patterns determined on preferred oriented samples in the air dried

and ethylene glycol saturated condition. These three independently determined values of illite contents were compared to the results of the Moore & Reynolds (1997) method which is based on NEWMOD (Reynolds, 1985) calculations. This method uses simulated XRD patterns of the (00l) series of ethylene glycol saturated sample and lists the d-values of the (001) or (002), (002) or (003), and (002)−(003) reflection for illite contents between 10% and 90% relative abundance, respectively. Comparing these values with the d-values determined from preferred oriented samples, one can estimate the illite content within the I-S interstratification. This method is based on Mérings´ principle which states that X-ray interferences of interstratifications lie between those of the pure components (Méring, 1949). The maximum peak position can be used to estimate the relative content of the components. The method after Moore & Reynolds (1997) is limited to two-component systems with K as an interlayer cation of micaceous layers. Rietveld refinement is assumed to be more reliable because it is based on a refinement process instead of calculation of theoretical patterns and because different conditions (air dried/different water saturations, ethylene glycol saturated, and, if necessary, others) of preferred oriented samples as well as powdered samples can be used, even if other phases are involved which may superimpose the reflections of interstratifications. Additionally, different cation occupancies in the interlayer can be considered (e.g. K-rich rectorite vs. Na-rich rectorite) and determination of contents of three-component systems is possible.

Using the Rietveld program BGMN (Bergmann *et al.*, 1998) and the structure models published by Ufer *et al.* (2012a,b), a number of structural parameters important for structural characterisation of the I-S interstratification can be determined (Table 3.4). The probabilities *p60*, *p180*, *p300*, and *p120*, *p240* were calculated from the refined parameters *p0* and *p60120* (Table 3.4). The standard deviation σ calculated by BGMN refers to an estimated standard deviation derived from the correlation matrix and is given to 1 σ which equals 68% confidence level (except when a refinement limit was reached), and the identical number of decimals of the refined parameters was stated, according to Ufer *et al.* (2012b). If the estimated standard deviation is in the same magnitude as the refined/calculated value, this may indicate that the phase is not present in the sample or the structural model applied fits not properly (BGMN handbook, 2004). However, the standard deviation and the number of decimals given do not reflect the estimated accuracy of measurements based on experiences of the Reynolds Cup mixed samples (e.g. McCarty, 2002; Kleeberg, 2005, 2009; Omotoso *et al.*, 2006), but just the calculated error of the refinement process (Ufer *et al.*, 2008). For typical clay mixtures and estimated accuracy of about 2% w/w at the 95% confidence level for each clay mineral phase can be achieved by using BGMN (e.g. Kleeberg, 2009; Kaufhold *et al.*, 2012). If interstratifications are involved the accuracy may be much higher because they are noticeably more difficult to refine and quantify. The accuracy then strongly depends on the type and amount of additionally involved phases and the similarity of their structure to the interstratification. If phases are structurally similar (e.g. different dioctahedral smectites such as montmorillonite and nontronite), it is very difficult or impossible to distinguish them. Hence, a dioctahedral I-S interstratification mixed with illite and muscovite may be very difficult to refine and

quantify. However, the errors of groups of phases with similar structures is still low, as in mixtures with similar and very different structures (e.g. *R*3 I(0.8)-S, illite, kaolinite, quartz, clinochlore, and calcite) the error of the interstratification may be up to 10% w/w but the error of the group interstratification + illite can be estimated to be still 2-5% w/w.

Table 3.4. Table explaining some selected parameters assumed to be important for structural characterisation, used for Rietveld refinement of I-S interstratifications (BGMN program). Some of the parameters are stated for just one type of sample preparation, powder patterns or preferred oriented specimens because, e.g., parameters for the non-basal model cannot be refined on the basis of a preferred oriented specimen. (According to Ufer *et al.*, 2012a,b)

Parameters	Explanation
***R*-values**	
*R*wp (%)	Parameter expressing the goodness of fit; calculated by least square sum
*R*exp (%)	Smallest possible Rwp value; calculated from the measurement data
Global parameters	
p(Fe)	Content of Fe in the octahedral sheet; refined between 0.1 and 0.7 as one parameter for both models, the basal and the non-basal model
p(K)	Content of K/Na in the interlayer of the micaceous layers; refined between 0.6 and 1.0 as one parameter for both models, the basal and the non-basal model
Non-basal model	
a (Å)	Lattice parameter a; parameter b was calculated by $b = a \times \sqrt{3}$
$-t_x$(cv)	Stacking vector to compensate the monoclinic offset for cis-vacant layers; refined between 0.26 and 0.32
$-t_x$(tv)	Stacking vector to compensate the monoclinic offset for trans-vacant layers; refined between 0.38 and 0.44
p0	Probability of 0° rotation; refined between 1/3 (maximum disorder, all rotations are equiprobable ≙ $1M_d$) and 1 (maximum order, no non-0° rotations ≙ 1M)
p60120	Probability ration of *p60*/*p120* rotational disordering; refined between 0 and 1
p60, p180, p300	Probability of *n*×60° rotations; calculated from *p0* and *p60120* by *p60*=(1−*p0*) ×*p60120*/3; *p180* = *p300* = *p60*
p120, p240	Probability of *n*×120° rotations; calculated from *p0* and *p60120* *p120*=(1−*p0*) × (1-*p60120*)/2; *p240* = *p120*
pcv	Probability of cis-vacant layers; refined between 0 and 1
Basal model	
t_S(1w) (Å)	Thickness of a “one water layer”; refined between 12.5 and 12.85
t_S(2w) (Å)	Thickness of a “two water layer” ; refined between 14.3 and 15.51
p(Ca)	Content of Ca/Na in the interlayer of the smectitic layers; refined between 0.1 and 0.3 for divalent cations and 0.2 to 0.6 for monovalent cations as one parameter for both, the basal and the non-basal model
wI (*R*0-*R*3)	Proportion of micaceous layers influencing the *R* value; refined between 0 and 1
p1w	Probability of a smectite layer being in the “one water” state; refined between 0 and 1. *p2w* = 1-*p1w*.
pII (*R*1)	Probability that an illitic layer is followed by another illitic layer; the highest possible value is called mpdo indicating a higher *R*-value or an ordered interstratification
pIII (*R*2)	Probability that two illitic layers are followed by another illitic layer; the highest possible value is called mpdo indicating a higher *R*-value or an ordered interstratification
pIIII (*R*3)	Probability that three illitic layers are followed by another illitic layer; the highest possible value is called mpdo indicating a higher *R*-value or an ordered interstratification

3.3 Chemical analysis of solids and liquids

3.3.1 X-ray Fluorescence (XRF)

An introduction into XRF spectroscopy including historical background and topics about analytical precision and accuracy, the measurement principle as well as quantitative analysis and others is given by Beckhoff *et al.* (2006).

Analytical procedure

To obtain major element compositions of the Friedland clay bulk sample and the <0.1 µm fractions of the purified interstratification clay minerals used to determine structural formulas (except for Friedland clay), a Philips PW 2404 XRF device with a PW2540 vrc sample changer was used. An X-ray anode material of Rh was excited at 3.0 kW. Calibration was made on the basis of international standard materials that were chosen with similar elemental concentrations to the samples (e.g. USGS standards MAG-1 and G-2, NBS standard 98, and NRCC standards BEST-1 and MESS -2). The general measurement conditions for the main elements are listed in Table 3.5.

Table 3.5. General measurement conditions of main elements.

Element	Line	Crystal	Collimator	Detector	kV	mA
Si	Kα	PE 002-C	300 µm	Flow	30	100
Ti	Kα	LiF 200	300 µm	Flow	30	100
Al	Kα	PE 002-C	300 µm	Flow	30	100
Fe	Kα	LiF 200	300 µm	Duplex	60	50
Mn	Kα	LiF 200	300 µm	Duplex	60	50
Mg	Kα	PX1	700 µm	Flow	30	100
Ca	Kα	LiF 200	300 µm	Flow	30	100
Na	kα	PX1	700 µm	Flow	30	100
K	Kα	LiF 200	300 µm	Flow	30	100
P	Kα	LiF 200	300 µm	Flow	30	100

800 mg of dry powdered sample was weighed, and again after heating at 105 °C (20 hours) and 1050 °C (1 hour) to determine the loss-on-ignition (LOI). The remaining sample was melted with a flux mixture of 2 g lithium metaborate (Alfa Aesar Spectroflux, $LiBO_2$) and 1.932 g di-lithium tetraborate (Merck Spectromelt A 10, $Li_2B_4O_7$) at about 1100 °C to prepare a fusion tablet. Additionally, a small amount of di-iodine pentoxide p.a. (Merck, I_2O_5) was added, to prevent cracking of the tablet.

3.3.2 Flame Atomic Absorption Spectroscopy (Flame-AAS)

The principles of flame-AAS spectroscopy can be referred at García & Báez (2012).

Analytical procedure

Concentrations of Si and Al in an 5 mol/L K(OH) solution, dissolved from heated Friedland clay, were measured by flame-AAS, using an Analytik Jena contrAA 300 device with high pressure xenon gas discharge lamp and nitrous oxide-acetylene flame. The absorbance was measured at 251.61 nm for Si and 396.15 nm for Al. 3 g heated Friedland clay was stirred with 30 g of 5 mol/L K(OH) solution then left for 24 hours to leach Si and Al without shaking the bottles. Shaking was not used so as to simulate the same conditions as used during preparation of the GP cements.

3.3.3 Inductively Coupled Plasma - Optical Emission Spectroscopy (ICP-OES)

The principles of ICP-OES can be referred at Boss & Fredeen (1997).

Analytical procedure

For structural formula determinations of rectorite and CEC determination of the Friedland clay <0.1 µm, 5 mL of the solutions with exchanged cations (CEC method see section 3.5.4) were pipetted into vials and analysed by ICP-OES. A Perkin Elmer Optima 8300 DV spectrometer operating at 40 MHz and 1,400 W equipped with an echelle-based polychromator and two solid-state Segmented-array Charge-coupled Device (SCD) detectors was used. The sample was nebulised with a Burgener Mira Mist nebuliser into a cyclone nebuliser chamber (12.0 L/min). Argon, used as a protective and as a nebuliser gas, was adjusted to 0.5 L/min each. The sample was taken at a rate of 1 mL/min with a flexible-tube pump. The wavelengths used for analysing the exchanged elements are given in Table 3.6.

Table 3.6. Wavelengths used for ICP-OES measurements of the elements listed.

Element	Wavelength [nm]
Mg	279.533
Ca	317.933
Na	589.592
K	766.490

3.4 Thermal analysis (TA)

3.4.1 Simultaneous Thermal Analysis coupled with Mass Spectrometer (STA-MS)

For characterisation of dehydration, dehydroxylation and recrystallisation processes, STA-MS measurements were made. Simultaneous Thermal Analysis (STA) refers to the combination of at least two TA methods. In this case thermogravimetry (TG) and differential scanning calorimetry (DSC) were combined. Additionally, coupling with a mass spectrometer (MS) results in a multi-component STA (Emmerich, 2011). TA methods are used for investigation of temperature-dependent processes like variation of mass (TG) or temperature (DTA, DSC that can be converted into enthalpy) due to changing physical and/or chemical properties of the sample. Such methods allow investigation of e.g. adsorbed and absorbed water (water on smectite surface and water in the interlayer of smectite), structural bonded “water” (hydroxyl groups in the octahedral sheet of smectite) or activation energy and a range of other reaction kinetic parameters.

TG as part of the STA-MS device is used to detect weight changes of the sample within a given temperature-time range in a defined atmosphere (Hemminger & Cammenga, 1989). These weight changes may result from the release of water (e.g. interlayer water of smectite) or degassing as a result of decomposition (e.g. in the case of sulphates or carbonates) or oxidation reactions upon heating (Figure 3.3 A). The mass changes are measured electro-magnetically because changing of mass induces a voltage that is proportional to the mass change. For further interpretation of the TG signal, it can be differentiated against the time used to obtain the derivative thermogravimetry curve (DTG, Figure 3.3 B). This can be useful because the resolution of TG curve is improved (Emmerich, 2011) and information about the type of reaction is provided.

DTA and DSC measure the temperature difference between the sample and a reference (Hemminger & Cammenga, 1989), such as an empty Pt crucible. The temperature difference is measured by thermocouples (here “type S”, Pt/10%Rh-Pt) using the electric voltage. With the DSC method the measured signal can be calibrated to reaction heat flows, which allows determination of specific heat capacities and the reaction type (Hemminger & Cammenga, 1989, Emmerich, 2011). The temperature is increased constantly with a defined heating rate ($\Delta T/\Delta t$) and heats both sample and reference. A suitable reference material should be used that does not show any effects upon heating in the temperature interval applied. As long as the sample does not react, the temperature difference is equal to zero. As soon as endothermic or exothermic reaction occur, the sample absorbs (endothermic, e.g. interlayer water loss of smectite) or releases energy (exothermic, e.g. crystallisation of mullite out of kaolinite) resulting in a detectable temperature difference between sample and reference (Figure 3.3 A). For a further interpretation of the DTA or DSC signal it can be differentiated against time obtaining the derivative differential thermal analysis curve (dDTA, Figure 3.3 B). This can be useful because the resolution of DTA curve is improved further and small overlapping reactions can be more easily resolved.

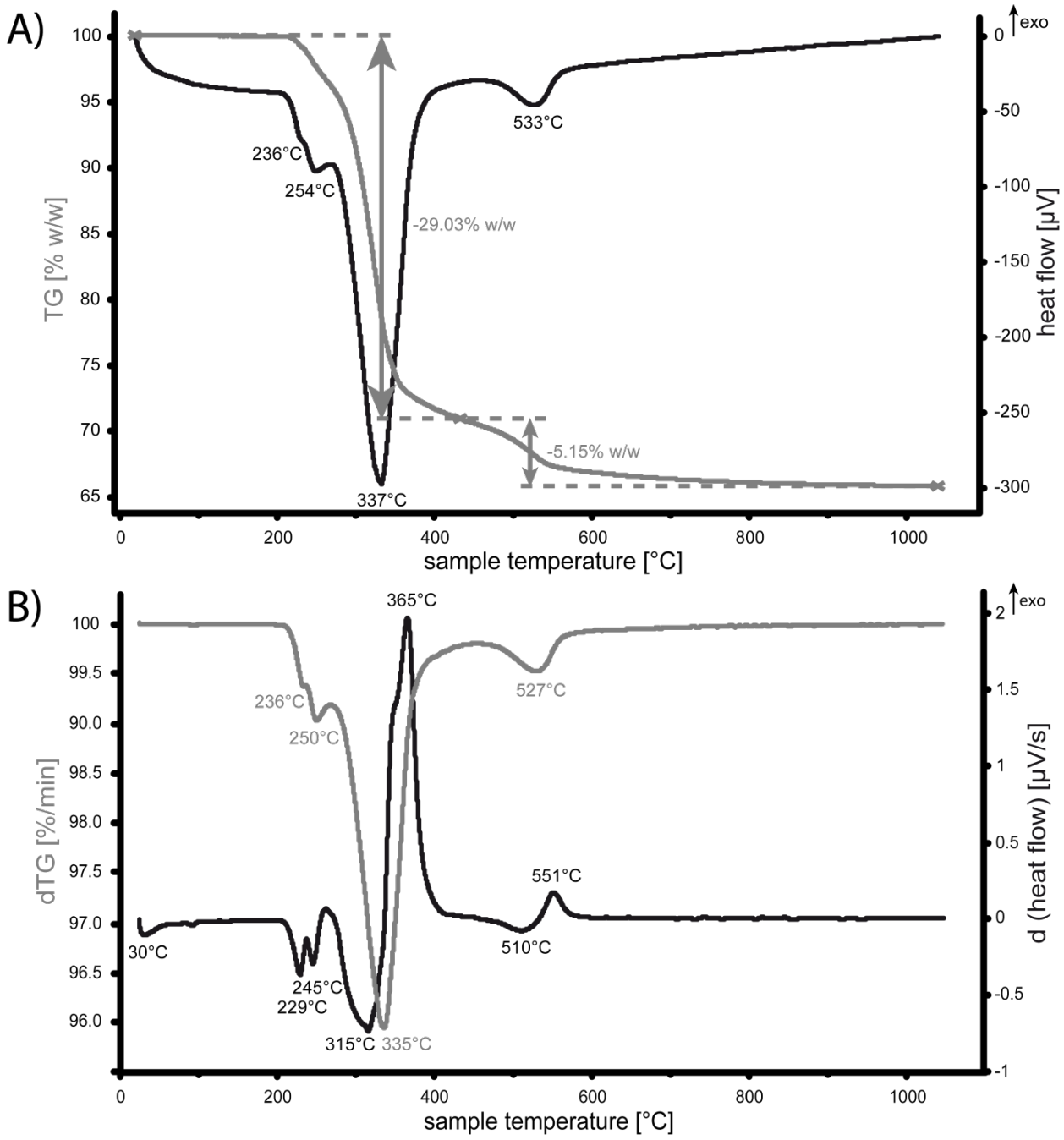

Figure 3.3. STA curves of a gibbsite sample showing the TG (upper, grey) and heat flow (HF, upper, black) curves and its derivations dTG (lower, grey) and dHF (lower, black). Some of the gibbsite transforms into boehmite during dehydroxylation (230-400 °C) resulting in another endothermic peaks due to boehmite dehydroxylation around 530 °C. TG starting value 100.00% w/w, sample amount 100 mg

The MS can be used to detect and quantify evolving gases like H_2O, CO_2 or SO_2 according to their charge/mass ratio (evolved gas analysis, EGA, Emmerich, 2011). This can be useful for differentiating parallel occurring, processes such as oxidation of organic matter (exothermic, CO_2, SO_2, ... release) and dehydration or dehydroxylation of clay minerals (endothermic, H_2O release), which are opposite in regards to their energy consumption/release.

There are a large number of parameters influencing the results of STA measurements, some of them are listed below. With increasing

a) heating rate, more intense but broader peaks appear, which are shifted to higher temperatures because both energy and evolving gases cannot be transported fast enough.
b) thermal conductivity of the sample, the sharper peaks shift to lower temperatures because energy can be released/absorbed sufficiently fast enough. The thermal conductivity is also influenced by e.g. package density.
c) package density, the sharper peaks shift to lower temperatures because heat can be transported very fast (Smykatz-Kloss, 1974). If the sample evolves significant quantities of gas during the reaction process that cannot escape fast enough from available pore space, then higher pressures may result, which can led to bursting of the sample.
d) amount of sample, the higher is the temperature gradient within the sample leading to broader peaks that shift to higher temperatures (Smykatz-Kloss, 1974).
e) concentration of reactive phases in the sample, more intense peaks occur because phase concentrations are proportional to integral intensity of the peak.
f) particle size, the lower is the surface area resulting in faster gas and energy evolving, but similarly a higher temperature gradient within the particle leads to opposing effects. Sharp peaks shifted to lower temperatures result from increasing evolving rates and broader peaks shifted to higher temperature occur due to higher temperature gradients. Which effect prevails depends on sample properties such as the heat capacity, thermal conductivity, and a number of other factors.
g) gas flow rate, the sharper peaks become, which are shifted to lower temperatures because the streaming gas promotes release of gases (Smykatz-Kloss, 1974). If, for example, water vapour is not removed by a dry gas flow, further reactions releasing water are delayed or prevented due to increasing partial water pressure. Additionally, very high gas flow rates can lead to physical disturbances of the scaling unit.
h) gas pressure of the atmosphere, the broader peaks result, which are shifted to higher temperature due to hindering of gaseous release. On the other hand, phase transitions occurring at elevated pressures can be promoted leading to decreasing peak temperatures.

Additionally, the type of atmosphere used can greatly influence the measurement. The purge gas and protective gas (prevents corrosion of the weighing mechanism by evolved gases) merge in the furnace chamber and form the atmosphere (Emmerich, 2011). Using synthetic air can promote oxidation while the usage of nitrogen prevents it. If high amounts of organic compounds are present, the DTA/DSC-curve may have totally different shapes due to strong exothermic reactions that occur while using synthetic air and that is absent or minimised by using nitrogen.

To avoid or minimise the mentioned effects that lead to fluctuations in STA measurements, all parameters should be held as constant as possible. A standardised heating rate of 10 K/min is the most commonly used (Emmerich, 2011), in combination with uncompacted to slightly compacted samples of constant weight (100 mg). If other sample amounts are used, a PA-curve should be applied in order to extrapolate the sample amount to 100 mg. The effects of grain size did not play an important role in the investigations made here because the clay minerals have very similar particle size distributions. To simplify data comparison of STA measurements, Emmerich (2011) suggested reporting the used measurement conditions as noted in Table 3.7.

Analytical procedure

In this study, a STA 449C Jupiter device (NETZSCH-Gerätebau GmbH) equipped with a TG/DSC sample holder coupled with a quadrupole mass spectrometer (403 C Aëolos, InProcess Instruments 10 (IPI)/NETZSCH-Gerätebau GmbH) was used, based at the Karlsruhe Institute of Technology (KIT), Germany. EGA was used to detect H_2O (*m/z* = 18), CO_2 (*m/z* = 44) and SO_2 (*m/z* = 64). However, the mass/charge-relation is detected, therefore an inaccuracy exists for H_2O having the same ratio as, for example, NH_3 (*m/z* = 18). But because degassing of NH_3 in these samples is negligible, the values of H_2O can be used. Additionally, a Setaram TG-DTA 92 device was used for further investigations equipped with a TG/DTA unit without EGA. The specific temperature-time-path as well as the STA measurement conditions used for all measurement on both devices is shown in Table 3.7.

Table 3.7. STA measurement conditions of both used STA devices.

	Netzsch 449C Jupiter with Netzsch 403 C Aëolos, InProcess Instruments 10	**Setaram TG-DTA 92**
Housing of equipment	Karlsruher Institute of Technology (KIT), Germany	University Greifswald, Germany
Equipment	TG/DSC/MS	TG/DTA
Sample amount	100 mg (43 mg for rectorite, PA curve recorded)	100 mg
Grain size	Powder	Powder
Packing density	Loosely packed, no pressing	Loosely packed, no pressing
Reference material	Empty Pt/Rh crucible with lid	Empty Pt crucible with lid
Furnace atmosphere (furnace + carrier gas)	50 mL/min air + 20 mL/min N_2	50 mL/min Ar + 20 mL/min N_2
Crucibles	Pt/Rh with lid (Ø 5 mm, height 5 mm)	Pt with lid (100 µL)
Thermocouples	Pt/Pt90Rh10, type S	Pt/Pt90Rh10, type S
Temperature range	Isothermal: 10´ 35 °C Dynamic: 35-1100 °C Isothermal: 30´ 1100 °C	Isothermal: 10´ 35 °C Dynamic: 35-1100 °C Isothermal: 30´ 1100 °C
Heating rate	10 K/min (50 K/min for one Friedland clay and one rectorite measurement)	10 K/min

Although studies on the classification of dioctahedral smectites and interlayer deficient micas (Wolters & Emmerich, 2007) have based on sample amounts of typically 100 mg, only 43 mg of the rectorite

sample could be filled in the crucible without compaction due to the low bulk density of the sample. Hence, sample amount dependency curves (so called PA-curves after Smykatz-Kloss, 1967) were used to make appropriate corrections. PA-curves display the shift of the maximum peak temperature during mineral decomposition that is dependent on sample amount or changing concentration of the mineral in any given mixture (Smykatz-Kloss, 1967). As reference samples, the PA-curves of a mainly trans-vacant Fe-rich smectite (Valdol, Wolters & Emmerich, 2007), a mainly trans-vacant illite (Arginotec NX), a mainly cis-vacant smectite (Bentonite P) and a cis-vacant smectite (Volclay, Wolters & Emmerich, 2007) were measured using several sample amounts between 5 and 100 mg. These results were used to check if the temperature of the peak maxima in the STA curves of the rectorite appears plausible (see Appendix i). The slope of the PA-curves obtained from STA analysis in a log plot flattened with decreasing iron content. Due to very low Fe contents of rectorite, the maximum peak temperature of the dehydroxylation peaks of rectorite for a sample weight of 100 mg results in a negligible shift and no shift of the tv/cv ratio.

Normalisation of the measured TG-values is required because interlayer water does not belong to the stoichiometric formula of clay minerals as it depends on ambient conditions. The measured TG curves most commonly starts with values lower than 100% w/w because when the sample is placed in the oven, some humidity enters the system, which must be removed first by flushing with a constant dry gas stream that is also used during measurements. When placed in a vacuum and purged with gas with significantly lower water content, some water adsorbed on the surface of the sample evaporates that was acquired while stored at ambient relative humidity. This results in a TG starting value lower than 100% w/w. The TG starting value is noted in every figure caption. All TG-values are given in both in their measured and normalised form. The normalised values were used for theoretical calculations. TG-values are normalised to the dry state of the sample.

The cis- and trans-vacant character of the octahedral sheet of rectorite <0.1 µm fraction, Friedland clay <0.1 µm fraction and “sárospatakite” <0.1 µm fraction was determined by peak decomposition of the mass spectrometer curve of evolved water (m/z = 18) using PeakFit (Version 4.12; SeaSolve Software, Framingham, Massachusetts, USA). Decomposition was achieved by using the least number of symmetrical peaks to achieve the best possible fit. The relative areas of all peaks with maxima below 600 °C and above 600 °C were summed and the ratio of both areas reflects the number of trans- and cis-vacant octahedral sheets (Drits *et al.* 1998, Wolters & Emmerich 2007, Wolters *et al.*, 2009).

3.4.2 Temperature X-ray Diffraction (TXRD)

To further characterise dehydration, dehydroxylation and recrystallisation processes and investigate structural transformation of mineral phases present in Friedland clay, TXRD patterns were recorded.

Analytical procedure

For temperature dependent X-ray diffraction, a TC-basic MRI Physikalische Gerätebau GmbH (now Bruker AXS GmbH) temperature chamber equipped with an inductively heated Pt heater and a Pt/Pt10%Rh type S thermocouple (30-1750 °C), which was controlled by a TCPU1 Temperature Control and Power Unit (Bruker AXS, 2005). The chamber was mounted onto a Bruker D8 Advance θ-θ diffractometer (see section 3.2.1) and samples irradiated with Fe-filtered CoKα radiation ($K\alpha_1$ = 1.78897 Å; $K\alpha_2$ = 1.79285 Å) generated at 40 kV and 30 mA. The beam was modified using a 0.499° divergence slit (Friedland clay bulk sample) or an automatic divergence slit to produce a constant irradiated sample length of 12 mm (Friedland clay size fractions). The diffracted beam passed through a 0.499° antiscatter slit, 2.5° primary and secondary soller collimators until reaching a 1D LynxEye detector comprised of 14 strips, each with a height of 0.075 mm. Scans were ran with a step size of 0.02° 2θ (rounded) between 6 and 80° 2θ, using an angle velocity of 1.5 °/min (rounded) for bulk samples and 2 °/min (rounded) for size fractions. XRD measurements of Friedland clay bulk samples were carried out under air atmosphere with a heating rate of 10 K/s and a dwell time of about 20 minutes between 30 °C and 1500 °C and for Friedland clay size fractions the temperature range of 30 °C and 950 °C was used.

The diffraction patterns were analysed qualitatively, not quantitatively using the information of Brindley & Brown (1984) and the program Diffrac^{plus} Evaluation Package “EVA” Version 14.0 by Bruker AXS with the PDF database PDF-2 (Release 2008).

Because the thermocouple is located beneath the heating band while the powdered samples were loosely spread on top of the flexible heater, a temperature gradient exists that increases to the surface of the sample. As X-ray scattering is more influenced by the material close to the sample surface, the amount (thickness) of the specimen used is of importance. When using too much sample, a temperature gradient of several 10´s or even 100´s °C may exist, especially at elevated temperatures. A temperature calibration was tested by using the temperature dependence of corundum lattice parameters. An amount of powdered corundum sample similar to the clay samples was loosely spread onto the heating band. TXRD patterns were measured at each of the selected temperatures to determine the lattice parameters *a* and *c* and the cell volume *V* of the corundum: both of which depend on the temperature. These values were compared to a data set of Fiquet *et al.* (1999) who determined the temperature dependent lattice parameters of corundum. The cell volume was not stated by Fiquet *et al.* (1999), but was calculated from the given lattice parameters. The lattice parameters were determined with the help of the program Topas 4.2 by Bruker AXS and the corundum data set of ICDD number 00-43-1484. The data of Fiquet at al. (1999) as well as both data sets obtained from own measurements are shown in Table 3.8 and graphically in Figure 3.4. The TXRD patterns are included in the Appendix ii - Appendix iii.

Both calibration tests made (in 2012 and 2013) produced consistent results with very similar values, especially at low temperatures (correlation coefficients $r > 0.995$ for a, c, and V). A discrepancy rises

with increasing temperature. Compared to the data of Fiquet *et al.* (1999) the values generally fit well (correlation coefficients 0.964 < *r* < 0.987 for a, c, and V measured in 2012, and 0.944 < *r* < 0.991 for a, c, and V measured in 2013), although the published results varies more than the data present in this study. The temperature measured by the thermocouple seems to be very close to the temperature present in the sample, as long as the material is spread thinly on the heater. However, with increasing temperature the gradient increases resulting in an overestimation of the actual sample temperature. Hence, up to about 700-800 °C, the temperature error is estimated to be several degrees up to 10´s of degree, while at higher temperature (above 900 °C) the error can reach several 10´s of degrees and further increases with increasing temperature. The highest temperature reached in the experiment (1493 °C) may have an error of more than 100 °C.

Table 3.8. Lattice parameters a and c and cell volume V of corundum determined by Fiquet *et al.* (1999) compared to own measurements for the purpose of checking the temperature calibration of TXRD.

	Fiquet *et al.* (1999)			Calibration test 2012			Calibration test 2013		
T [°C]	a [Å]	c [Å]	V [cm³/mol]	a [Å]	c [Å]	V [cm³/mol]	a [Å]	c [Å]	V [cm³/mol]
25	4.758	12.996	25.571	4.761	12.998	25.516	4.761	12.997	25.511
134	4.763	13.019	25.670	4.764	13.006	25.564	4.764	13.006	25.565
221	4.767	13.025	25.726	4.767	13.014	25.609	4.767	13.014	25.606
310	4.764	13.041	25.732	4.769	13.021	25.650	4.770	13.024	25.660
421	4.770	13.059	25.825	4.773	13.034	25.716	4.774	13.036	25.726
514	4.773	13.061	25.867	4.776	13.044	25.769	4.778	13.048	25.792
611	4.778	13.046	25.897	4.781	13.056	25.841	4.782	13.061	25.868
746	4.783	13.071	25.998	4.786	13.074	25.936	4.789	13.081	25.976
920	4.793	13.081	26.126	4.791	13.087	26.014	4.793	13.096	26.055
1051	4.797	13.105	26.213	4.753	13.102	26.091	4.803	13.127	26.228
1184	4.813	13.107	26.395	4.800	13.115	26.164	—	—	—
1306	4.824	13.116	26.528	4.805	13.131	26.257	—	—	—

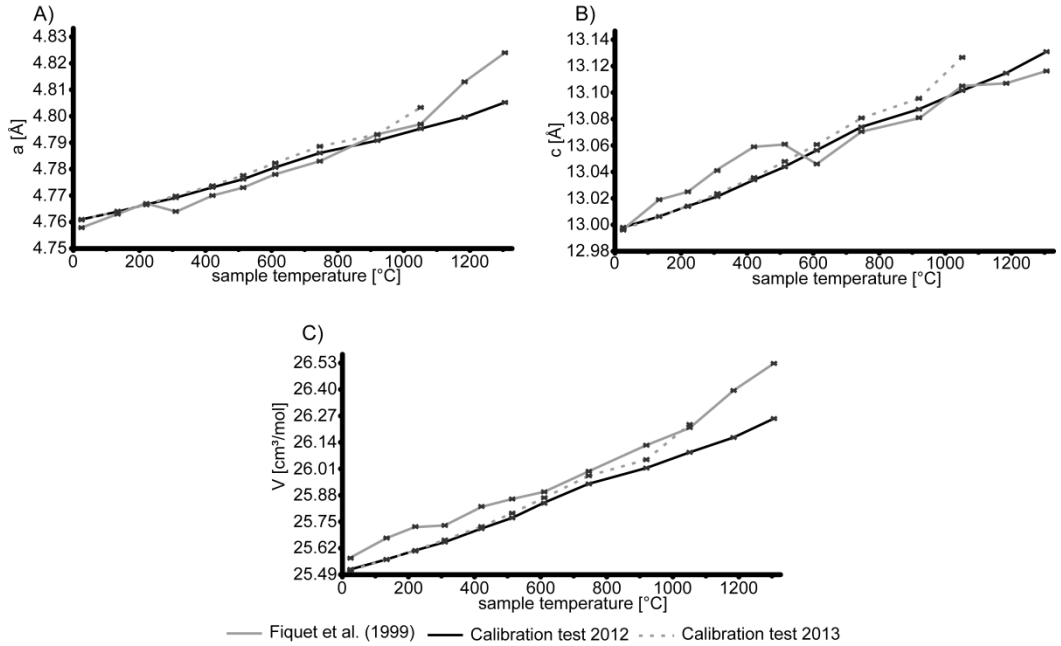

Figure 3.4. Lattice parameters a (A) and c (B), and cell volume V (C) of corundum determined by Fiquet *et al.* (1999, grey solid line) compared to own measurements from 2012 (black solid line) and 2013 (grey dashed line) for the purpose of checking the temperature calibration of TXRD.

3.5 Other methods

3.5.1 Specific Surface Area (A_S) and Pore Size Distribution

The specific surface area (A_S) was determined for heated Friedland clay samples after the method of Brunauer, Emmett, and Teller (BET, Brunauer *et al.*, 1938), and the pore size distribution measurement after Barrett, Joyner, and Halenda (BJH, Barrett *et al.*, 1951). The basics described below are extracted from Langmuir (1918), Brunauer *et al.* (1938), Barrett *et al.* (1951), and Carter *et al.* (1986).

Every solid material has the ability to physically adsorb gas molecules on the surface. This ability mainly depends on the surface area of the sample, temperature and gas pressure. During gas adsorption the temperature is held constant (here at T = 87.4 K, the temperature of liquid argon), hence, the volume of adsorbed gas is a function of gas pressure. Adsorbing gas physically on the surface of a solid is due to van der Waals forces between gas and solid. These forces are very weak, hence, while adsorbing gas molecules some desorption occurs. Increasing gas pressure leads to increasing coverage of the sample surface until the entire surface is covered by a monomolecular layer of gas. Knowing the required area of a single gas molecule and measuring the numbers of molecules adsorbed in the monolayer, the surface area of the solid can be calculated. Brunauer, Emmett and Teller (1938) derived an equation considering the existence of multilayers of the adsorbed gas (equations 3.10 and 3.11):

$$\frac{P}{N \times (P_0 - P)} = \frac{(C-1) \times P}{N_{mono} \times C \times P_0} + \frac{1}{N_{mono} \times C} \qquad 3.10$$

and

$$\mathrm{C} = exp^{\frac{E_1 - E_2}{R \times T}} \ . \qquad 3.11$$

P …. Partial pressure of adsorbate gas at equilibrium with material surface [Pa]

P_0 …. Saturation pressure of adsorbate gas [Pa]

N …. Amount of adsorbed gas molecules at STP (standard temperature and pressure)

N_{mono} …. Amount of adsorbed gas molecules in a monolayer at STP

E_1 …. Heat required for adsorption of a monolayer [kJ/mol]

E_2 …. Heat of condensation [kJ/mol]

R …. Gas constant (~8.314 $\frac{\mathrm{J}}{mol*K}$)

T …. Absolute temperature (−273.15 K)

The number of adsorbed gas molecules (N) was calculated at seven points of P/P_0, respectively, within the BET range (7-point method). Subsequently, the BET value (equation 3.12) was plotted versus P/P_0 in

the range of 0.05 < P/P_0 < 0.31 ("BET range") obtaining a linear function with its slope (equation 3.13) and its intercept (equation 3.14).

$$BET\ value = \frac{1}{N \times (\frac{P_0}{P} - 1)} \quad 3.12$$

$$slope = \frac{(C-1)}{N_{mono} \times C} \quad 3.13$$

$$intercept = \frac{1}{N_{mono} \times C} \quad 3.14$$

The slope and intercept can be combined to calculate N_{mono} which is the amount of adsorbed gas in a monolayer (equation 3.15).

$$N_{mono} = \frac{1}{slope + intercept} \quad 3.15$$

The A_S of a solid material [in m²/g], which is defined as the surface area related to sample weight, can be calculated by multiplication of the amount of molecules in the monolayer (N_{mono}) with the required area for one molecule (A_{CS}) and some constants (equation 3.16).

$$A_S = N_{mono} \times A_{cs} \times \frac{N_A}{M_{Ar}} \quad 3.16$$

A_s …. Specific surface area [m²/g]

N_{mono} …. Amount of adsorbed gas molecules in the monolayer

A_{cs} …. Molecular cross section of one adsorbed gas molecule [Ar: 14.2 Å² ≙ 14.2×10^{-20} m²]

N_A …. Avogadro´s constant [mol^{-1}]

M_{Ar} …. Molecular mass of Ar (39.95 $\frac{g}{mol}$)

After building up a monomolecular layer on the adsorbate, the pressure is further increased and used for the BJH method. This leads to condensation of the gas within the pore space, whereby small pores are filled first. The volume of gas needed can be measured, and after reaching the saturation point (all pores are filled with condensed gas), gas pressure is decreased step by step. Desorption occurs because gas evaporates again, whereby large pores are emptied first. Plotting the adsorbed/desorbed gas

volume versus gas pressure (p/p_0), hysteresis occurs, which yields information about pore size, volume and area.

To calculate the pore sizes, two main assumptions are made. First, the pores are assumed to be cylinders and secondly, the amount of adsorbate that is in equilibrium with the gas phase is retained by the adsorbent by physical adsorption on the pore walls, and capillary condensation in the inner capillary volume.

The pore space can then be calculated by:

$$\mathrm{V_{p_1}} = V_{k_1} \times \frac{r_{p_1}^2}{r_{k_1}^2} \ . \qquad 3.17$$

V_p …. Pore volume [Å³]

V_k …. Capillary volume [Å³]

r_p …. Pore radius [Å]

r_k …. Radius of the inner capillary within the physically adsorbed layer [Å]

By lowering p/p_0, desorption occurs and the desorbed gas volume ΔV can be measured for each desorption step. The thickness of the adsorbed layer (t_1) is lowered by Δt_n each step. Considering the occurrence of more than one pore in the adsorbent, and generalising the equation to represent any step of desorption, the pore volume can be calculated according to equation 3.18.

$$\mathrm{V_{p_n}} = \mathrm{R_n} \times \Delta \mathrm{V_n} - \mathrm{R_n} \times \Delta \mathrm{t_n} \times \sum_{j=1}^{n-1} A_{\mathrm{c_j}} \qquad 3.18$$

and

$$R_n = \frac{{r_{p_n}}^2}{(r_{k_n} + \Delta t_n)^2} \qquad 3.19$$

V_p …. Pore volume [Å³]

r_p …. Pore radius [Å]

r_k …. Radius of the inner capillary within the physically adsorbed layer [Å]

Δt_n …. Change in thickness of adsorbed layer on the surface while desorption [Å]

ΔV_n …. Volume of desorbed gas [Å³]

A_{C_j} …. Average area from which physically adsorbed gas is desorbed [Å²]

A_{C_j} is not constant, but decreases with every decreasing step of p/p_0. Assuming that all capillaries emptied have an average radius $\overline{r_p}$, A_c can be calculated from the pore area A_p by determining the factor c (equation 3.20).

$$A_c = A_p \times \frac{\overline{r_p} - t_{\overline{r}}}{\overline{r_p}} = A_p \times c \qquad 3.20$$

A_c …. Average area from which physically adsorbed gas is desorbed [Å²]
A_p …. Pore area [Å²]

$\overline{r_p}$ …. Average radius of emptied capillary [Å]

$t_{\overline{r}}$ …. Thickness of the physically adsorbed layer [Å]

Using this assumption, equation 3.18 can be written as:

$$\mathrm{V_{p_n}} = \mathrm{R_n} \times \Delta \mathrm{V_n} - \mathrm{R_n} \times \Delta \mathrm{t_n} * \sum_{j=1}^{n-1} \mathrm{c_j} \times A_{\mathrm{p_j}} \qquad 3.21$$

and

$$R_n = \frac{{r_{p_n}}^2}{(r_{k_n} + \Delta t_n)^2} \quad \wedge \quad c = \frac{\overline{r_p} - t_{\overline{r}}}{\overline{r_p}} \; . \qquad 3.22$$

V_p …. Pore volume [Å³]

r_p …. Pore radius [Å]

r_k …. Radius of the inner capillary within the physically adsorbed layer [Å]

Δt_n …. Change in thickness of adsorbed layer on the surface while desorption [Å]

ΔV_n …. Volume of desorbed gas [Å³]

$\overline{r_p}$ …. Average radius of emptied capillary [Å]

$t_{\overline{r}}$ …. Thickness of the physically adsorbed layer [Å]

A_p …. Pore area [Å²]

This equation (equation 3.21) can be used for determining pore sizes at any desorption step p/p_0 because r_k can be easily calculated from the classical Kelvin equation (equation 3.23).

$$\log\left(\frac{p}{p_0}\right) = \frac{-2 \times \sigma \times V}{R \times 2.303 \times T \times r_k} = \frac{-4.29}{r_k} \qquad 3.23$$

σ …. Surface tension of liquid argon (0.01253 N/m at 87.3 K, Lemmon & Penoncello, 1994)

V …. Liquid molar volume of nitrogen (2.863×10^{-5} m³/mol at 87.3 K)

r_k …. Radius of capillary [Å]

T …. Temperature (87.3 K)

R …. Gas constant (8.314 J/mol×K)

Analytical procedure

A known mass of the powdered sample is put into the sample carrier (here 0.138-0.232 g). Before measurements were made, the surface was cleared of all gases adsorbed by storage in a vacuum, heating to 105 °C for 12 h (heated Friedland clay 775-900 °C, except 875 °C), 24 h (untreated Friedland clay), and 72 h (heated Friedland clay 875 °C) respectively, and then purging with an inert gas (here Ar). After cleaning the mineral surfaces from adsorbed gases, the device was evacuated again. Three samples were chosen to determine the pore space distribution using the BJH method. For both methods, argon absorption was carried out using a Quantachrome Instruments Autosorb 1-MP device located at the Karlsruhe Institute of Technology (KIT), Germany.

3.5.2 Solid-state Nuclear Magnetic Resonance Spectroscopy (NMR)

NMR spectroscopy was used to investigate the role of 5-fold coordinated Al for the process of GP hardening. A short introduction to solid state NMR spectroscopy is given below and more detailed descriptions are available in Fitzgerald & DePaul (1999) or Freude & Haase (2014). Atoms are built up by electrons surrounding a nucleus. This nucleus itself consists of protons (p^+) and neutrons (n), and these protons and neutrons consist of quarks. A proton is built up by two up-quarks (u) and one down-quark (d), while a neutron is built up by one up-quark and two down-quarks. For up-quarks, having a charge of +2/3 and a spin of 1/2, and down-quarks having a charge of −1/3 and a spin of ½, protons are electrically charged (uud: charge $p^+ = 2 \times \frac{2}{3} + 1 \times -\frac{1}{3} = +1$), while neutrons are not (udd: charge $\mathrm{n} = 1 \times \frac{2}{3} + 2 \times -\frac{1}{3} + = \pm 0$). But all quarks (u and d) have the spin ½ and arrange oppositely (one spin up ↑, next upside down ↓, next up ↑). As quarks are not distributed homogenously, by spinning of protons and neutrons electric dipoles (quarks) are moving, which induces a magnetic field after Maxwell's equations and a magnetic moment is created. Transitions between spin states are measured by NMR spectroscopy. Hence, not all isotopes are NMR active (can be measured by NMR spectroscopy). If there is an even number of protons, the quarks spins compensate each other because of alternating arrangement (↑↓), having a resultant spin of 0 (a spin quantum number *I* = 0). The same effect occurs with neutrons. This means, only those isotopes are NMR active, that do not have an even number of protons and an even number of neutrons, resulting in *I* = 0 and therefore no dipole moment, due to anti-parallel spins (e.g. ^{56}Fe). All other isotopes are NMR active, having either an odd number of protons or neutrons (e.g. ^{27}Al) or both (e.g. ^{14}N).

Initially there is a degeneracy of the spin states in the sample during which the energy states are equal (Figure 3.5, time 1). After placing the sample in a homogenous magnetic field (B_0), the magnetic field aligns the spins of the sample parallel and antiparallel to B_0 and lifts the degeneracy of the spin state (Figure 3.5, time 2). The higher the magnetic field strength, the higher is the energy difference between the states (Zeemann effect).

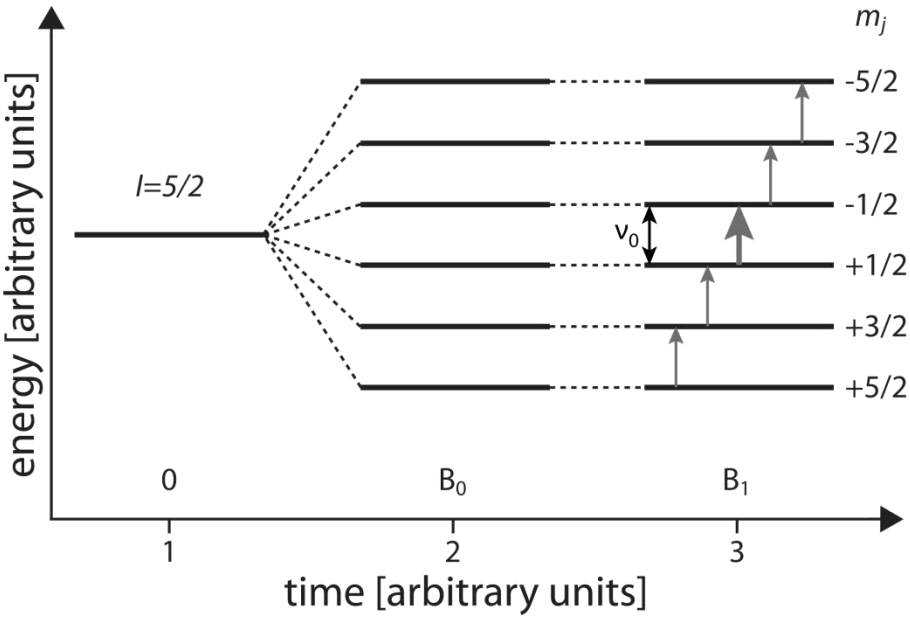

Figure 3.5. Spin energy level diagram showing the initial state of energy states for ^{27}Al (time 1), splitting due to the Zeemann effect while applying a magnetic field B_0 (time 2) and some possible transitions between the split states while absorbing energy from B_1, including main transition between ½ -> –½.

For NMR spectroscopy, measuring these very small energy differences (transition between the states), B_0 should be as strong as possible and as homogenous as possible. In thermal equilibrium, there is a small excess of spins in the up state compared to the down state. Therefore, a macroscopic magnetization can be calculated by summing up all spin states. This magnetization is aligned along the magnetic field B_0. Some energy has to be inserted into the system to stimulate the transition, which is done by an electromagnetic wave (which induces a high frequency electromagnetic field (B_1) perpendicular to the main magnetic field B_0). If the energy of this wave is equal to the energy difference between the two states (ν_0), the energy is absorbed by the nuclear spin (Figure 3.5, time 3). By inducing this second magnetic field for just a few microseconds, the macroscopic magnetization is now aligning parallel to B_1. After the short impulse, the magnetisation regenerates equilibrium orientation parallel to B_0 again, which is called relaxation. But while relaxation occurs, an electric voltage is induced in the coil that is detected. The detector measures one signal point each time interval whereas the time interval is called “dwell time”. This remission of the NMR signal is called free induction decay (FID) (Figure 3.6).

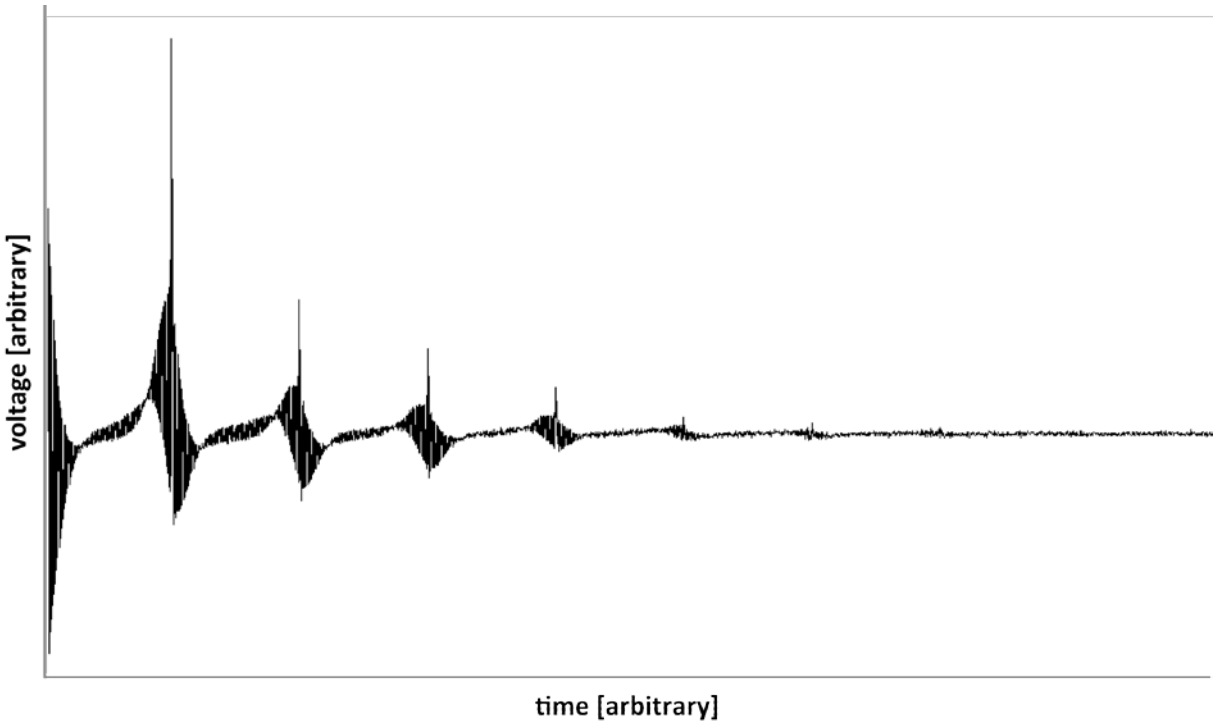

Figure 3.6. FID graph of ^{27}Al in the untreated Friedland clay sample.

By Fourier transformation, the signal can be converted into a graph of intensity over frequency. Every peak at a certain frequency means a different electric field surrounding the nucleus (coordination sphere, Figure 3.7), for coordination leads to a different magnetic field and a shift of the energy states of the nucleus.

That means a higher electron density induces a magnetic field anti-parallel to the external field, shielding the nucleus. The energy differences between the states therefore are getting smaller. These shifts are called “chemical shift” δ with the unit part per million (ppm) for being normalised to the shift of a reference sample (equation 3.24).

$$\delta = \frac{(\nu_m - \nu_{Ref})}{\nu_{Ref}} \qquad 3.24$$

δ …. Chemical shift [ppm]

ν_m …. Frequency measured [Hz]

$\nu_{A,\text{Ref.}}$ …. Frequency of the reference sample [Hz]

In the case of ^{27}Al, the highest electron density (6-fold coordinated) leads to the highest shielding and therefore the lowest shift:

6-fold coordination: −2-22 ppm; 5-fold coordination: 22-43 ppm; 4-fold coordination: 43-80ppm (according to Rocha & Klinowski, 1990).

The peak position in the NMR spectrum (chemical shift) is used for identification of isotopes and their electric environment and the intensity of the peak can be used for quantification purposes for it is proportional to the amount of nuclei with a specific environment.

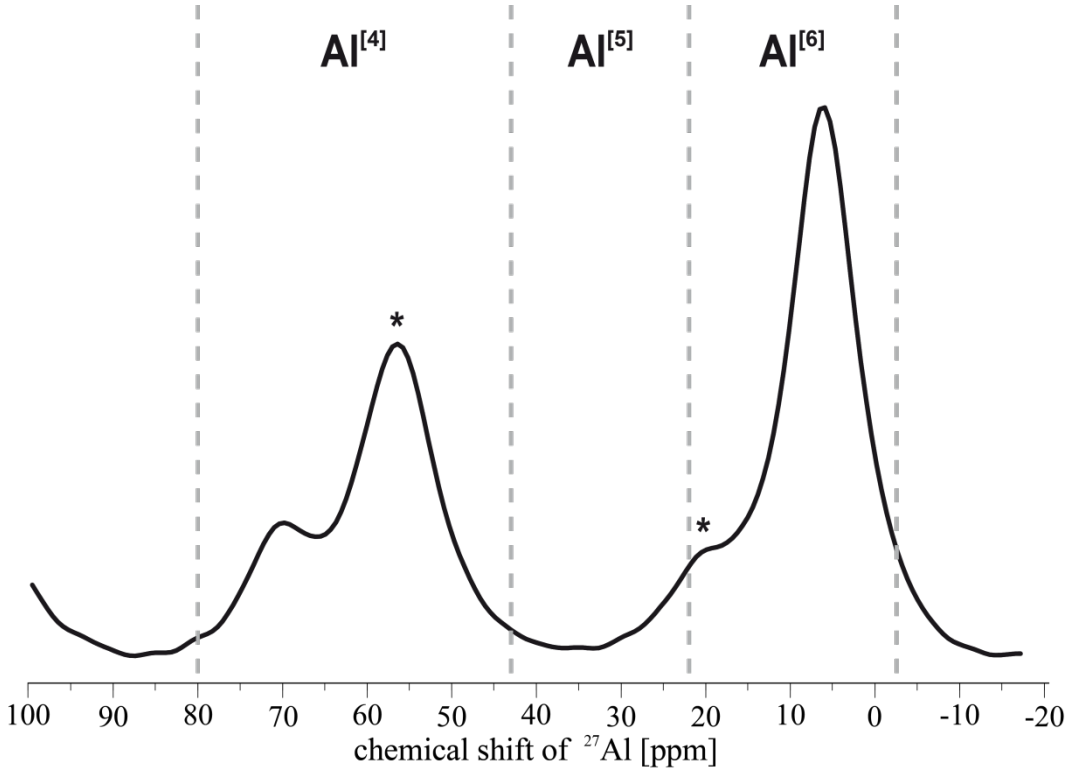

Figure 3.7. NMR spectrum of ^{27}Al in the untreated Friedland clay sample showing two different coordination spheres of Al - 4-fold and 6-fold coordinated expressed by different chemical shifts. * Rotational sidebands

Analytical procedure

NMR spectroscopy was performed using a Bruker Avance 750 spectrometer with a resonance frequency of 195.2 MHz (magnetic field strength 17.6 T) for ^{27}Al, using a 2.5 mm Magic-Angle-Spinning (MAS) probe and a spinning frequency of 20 kHz. This equipment is housed at the institute for physics at the University Leipzig, Germany. The powder samples were filled into the sample holder and slightly densified. The untreated Friedland clay sample (FT_NT) and the 600 °C heated one was measured using a 4 mm MAS probe and a spinning frequency of 10 kHz. The recycle delay was 200 ms and the excitation pulse length 0.5 µs. 4-fold coordinated Al gave a resonance between 43-80 ppm, whereas 6-fold coordinated Al at −2-22 ppm. 5-fold coordinated Al lies in between at 22-43 ppm, according to Rocha & Klinowski (1990). The chemical shifts of ^{27}Al were referenced to a 1 mol/L $Al(NO_3)_3$ solution. The different Al coordinations were quantified by integration of the NMR spectra with the program DMfit vs 2009 (Massiot *et al.*, 2002).

3.5.3 Transmission Electron Microscopy (TEM)

TEM images and selected area electron backscattering images (SAED) were recorded for morphological descriptions of the clay particles and to check the crystalline state of milled clays and whether or not the clay mineral structure was transformed to an electron amorphous character. The high resolution connected with a focused electron beam allows measurement of single particles instead of bulk samples as in XRD. Hence, a material which appears completely X-ray amorphous in XRD may still yield SAED patterns from some particles indicating only a certain percentage of particles to be X-ray amorphous. The principles about electron microscopy are well described by Buseck, (1992), Hawkes & Spence (2007), Pennycook & Nellist (2011), Warr & Grathoff (2012), or Nieto & Arroyo (2013).

Analytical procedure

Investigations were carried out with a TEM Jeol JEM 1210 device with a 30 mm² Oxford Pentafet Link EDX spectroscopy system and selected area electron diffraction (SAED). All analyses were made using a LaB_6 filament and an accelerating voltage of 120 kV. Images were captured at magnifications between 2,000× and 2,500× (rectorite) and 2,000 and 50,000 (Friedland clay) using a GATAN Digital Micrograph Orius SC200 CCD camera with a pixel resolution of 2.000 × 2.000.

For sample preparation, a small amount of clay from the tip of a spatula was dispersed by ultrasonic treatment for 15 minutes in distilled water. The resulting suspension was thinned until no blur was observed and one drop of the suspension was put on a carbon-coated Cu grid. The particles sedimented until water vaporised. With this method a representative mixture of the sample and mostly single clay particles without aggregation and a minimum of contamination are obtained.

3.5.4 Cation Exchange Capacity (CEC)

Clay minerals are able to adsorb cations in the interlayer and on their edges whereby the amount of exchanged cations is referred to as the CEC. While interlayer adsorption is reversible and does not depend on the pH value, edge adsorption strongly depends on the pH. Low pH values lead to positively charged edges, resulting in rejection of cations and hence, underestimation of the CEC value. Consequently alkaline solutions lead to attraction of cations resulting in overestimation of the CEC. At a pH of 7, the CEC of smectite can be attributed to as much as 20% edge adsorption (Lagaly, 1981). By exchanging the initially bound cations by Cu-trien (Figure 3.8 left) or ammonium (Figure 3.8 right), the CEC value can be determined. A more detailed description of both methods is given in Steudel & Emmerich (2013).

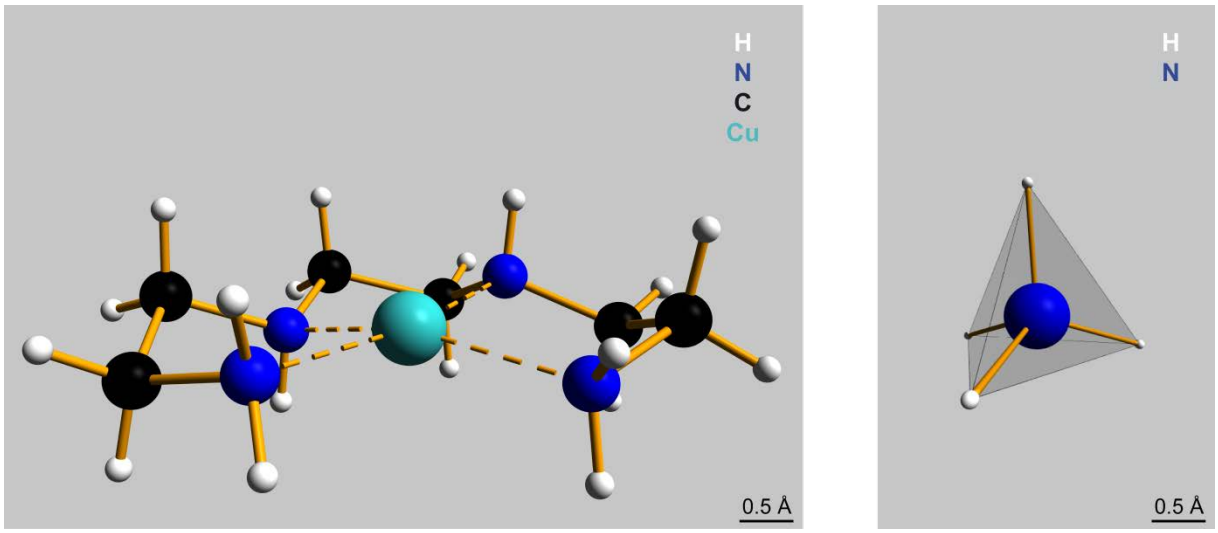

Figure 3.8. Left: Structure model of a planar copper triethylenetetramine (Cu-trien) complex (data from Liu *et al.* (2010), CCDC # 683103).; Right: Polyhedral model of the NH_4^+ (ammonium) ion (data from Seisenbaeva *et al.* (2013), CCDC # 915222).

Because a known volume of Cu-trien solution with a known concentration is used for the Cu-trien exchange method, after measuring the concentration of the supernatant solution, the amount of adsorbed Cu-trien can be calculated (equations 3.25 and 3.26). Therefore, the dry weight of the sample must be determined by oven drying or STA measurements, because the CEC value refers to the dry weight.

$$CEC = \frac{2 \times [(c_{Cu,0} \times V_{Cu} - c_{Cu} \times \left(\frac{V_{Cu} + V_{H_2O}}{1000}\right) \times 100]}{m_{dry}} \quad 3.25$$

and

$$c_{Cu} = a \times A_{\lambda} \quad 3.26$$

CEC …. Cation exchange capacity [cmol(+)/kg]

$c_{Cu,0}$ …. Concentration of Cu-trien in the initial solution (0.01 mol/L used) [mol/L]

V_{Cu} …. Volume of Cu-trien solution (5 mL used)

c_{Cu} …. Concentration of Cu-trien in the supernatant [mol/L]

V_{H_2O} …. Volume of water (10 mL used)

m_{dry} …. Mass of dried sample [g]

a …. Slope of the photometric calibration curve

A_{λ} …. Absorbance measured photometrically

For the NH_4-Ac method, the sample was NH_4^+ saturated and then washed with ethanol. The NH_4^+ exchanged material was diluted with deionised water and Na(OH) solution for Na replacing ammonium (NH_4^+) in the interlayer, which is transformed into ammoniac (NH_3) that is captured in a flask. The amount of NH_3 is determined by H_2SO_4 titration. The CEC value can be calculated using equations 3.27 and 3.28.

$$CEC = \frac{V_{H_2SO_4} \times n_{H_2SO_4} \times 100}{m_{dry}} \quad 3.27$$

and

$$V_{H_2SO_4} = V_{sample} - V_{blank} \quad 3.28$$

CEC …. Cation exchange capacity [cmol(+)/kg]

$V_{H_2SO_4}$ …. Volume of consumed sulphuric acid [mL]

$n_{H_2SO_4}$ …. Molarity of sulphuric acid (0.0067 mol used) [mol]

m_{dry} …. Mass of dried sample [g]

V_{sample} …. Volume of sulphuric acid used for the sample [mL]

V_{blank} …. Volume of sulphuric acid used for the blank sample [mL]

Analytical procedure

For determination of the cation exchange capacity (CEC), two different methods were applied: (1) Intercalation of copper triethylenetetramine (Cu-trien) (after Meier & Kahr, 1999) and (2) Intercalation of ammonium acetate (NH_4-Ac, CH_3COONH_4) (after Schollenberger & Dreibelbis, 1930, Mackenzie, 1951). The NH_4-Ac method was used as a reference method for the rectorite sample, as when high charged layers are present, the Cu-trien methods yielded values that are often too small (Steudel *et al.*, 2009). The exchanged cations of the Friedland clay and the rectorite samples were subsequently analysed in the supernatant by ICP-OES (see section 3.3.3) to assess the saturation of the interlayer. For both methods a Heraeus/Kendro Multifuge 3S-R centrifuge and a Thermo Genesys 10UV UV-VIS spectrometer was used housed at the Karlsruhe Institute for Technology (KIT), Germany.

After storing the sample over $Mg(NO_3)$ (53% r.h.) for several days, 50 mg of the sample dispersed in 10 mL deionised water was shaken with 5 mL 0.01 mol/L Cu-trien solution for three hours. Thereafter, the suspension was centrifuged and the clear blue supernatant with the remnant Cu-trien solution measured photometrically at a wavelength of 580 nm. A calibration curve was measured before, which is needed for the CEC calculation. Additionally, two bentonites with known CEC values (Volclay and Calcigel) were measured at the same time as the standard materials.

For the NH_4-Ac method, 200 mg of the sample was shaken in 1 mol/L NH_4-Ac solution for 24 hours and afterwards centrifuged. This procedure was repeated four times and subsequently, the samples were washed four times with ethanol and the supernatant solutions collected and then dried at 90 °C for all exchange and washing steps. The solid was dissolved in 3 mL HNO_3 and deionised water and measured by ICP-OES (see section 3.3.3). The NH_4^+ exchanged material was diluted with 30 mL deionised water and mixed with 2 mL Na(OH) solution. The ammonium (NH_4^+) in the interlayer is replaced by Na^+ and transformed into ammoniac (NH_3), which is distilled and poured into a beaker containing 2 mL boric acid (H_3BO_3) and the indicator for determination of NH_3 by H_2SO_4 titration. The solution was titrated until the colour changed from blue to red. Additionally, one blank solution and two bentonites with known CEC values (Volclay and Calcigel) were measured at the same time as standard reference materials.

The dry weight of the samples were determined by oven drying (105 °C for 24 hours in the case of Friedland clay <0.1 fraction) or STA measurements (in the case of rectorite <0.1 fraction).

3.5.5 pH measurements

The functional principle of the pH electrode has been extensively described and tested against a standard glass electrode by Kahlert *et al.* (2004). The pH values are calculated from the measured potential using the following equation (Kahlert, pers. comm., according to Kahlert *et al.*, 2004):

$$pH = \frac{E - 0.48028}{-0.05716} \quad . \qquad 3.29$$

E …. Potential [V]

The standard deviation was determined by Kahlert *et al.* (2004) to be ± 4 mV (± 0.07 pH).

Analytical procedure

In this study, a quinhydrone electrode for pH measurements was used developed by Kahlert *et al.* (2004). The advantage of this electrode in contrast to an “ordinary” glass electrode is the possibility to measure pH values in soil systems with low water content without calibration. pH values were made on untreated Friedland clay bulk sample, and samples heated to different temperatures between 775 °C and 925 °C (in steps of 25 °C). For analysis, 2 g of (heated) clay was mixed with 2 g deionised water to form a paste. Preliminary tests showed that equilibration of the system needed some time hence, the first value was read of after 20 minutes, followed by 80 minutes, and 140 minutes.

3.5.6 Compressive Strength Tests

During testing of the compressive strength of a material, the stress is increased gradually until the structure of the material cannot absorb any more energy, which leads to fracturing and eventually brittle failure (assuming no plastic behaviour). In the standard testing procedure for hardened concrete (based on OPC), defined and described by the DIN standard DIN EN 12390-3 (German Industry Standard), issue July 2009, the applied force at the point of failure of the material is read off and divided by the initial area the force was applied to (equation 3.30).

$$\sigma_e = \frac{F}{A_0} \qquad 3.30$$

σ_e …. Engineering stress (= compressive strength) [N/m², often in MN/m² or N/mm²]

F …. Force applied at failure of the material [N]

A_0 …. Area at which force is applied at the beginning [m²]

Analytical procedure

Compressive strength was measured with the help of a modified vice. Cylindrical samples of either 25 mm or 45 mm in diameter and 8 mm thickness were used. The sample with a smooth surface was carefully fixed into the vice by slight pressing against a pair of conical sections with defined areas (50 mm², 7.98 mm diameter). For measuring force, a torque handle was fixed to the vice, which was turned to increase the force uniformly. The maximum force value that led to complete failure of the sample was used for evaluation. This testing device was calibrated with 15 OPC samples to a standard testing machine located at the Institute for Buildings and Environment Friedland, Germany, operating after DIN EN 12390-3. Calibration was carried out with samples having exactly the same dimension as the GP samples measured. The thickness of a sample has a large influence of the absolute value of the compressive strength measured (Figure 3.9).

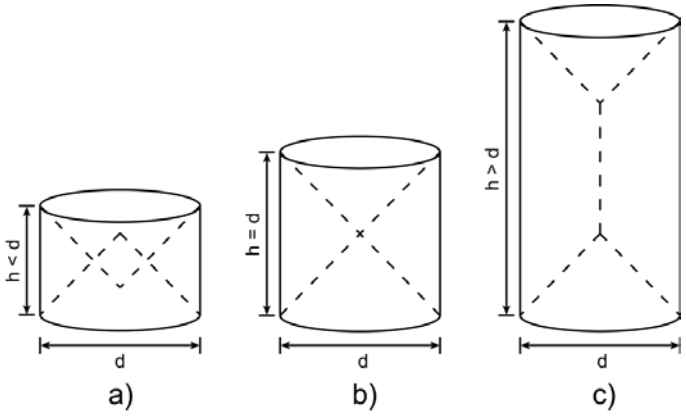

Figure 3.9. Failure modes with specimen geometry. A) Showing samples with a too low height/diameter ratio resulting in failure by crushing, b) showing the right ratio of 1, and c) showing a too high height/diameter ratio resulting in failure by cracking (modified after Kim & Yi, 2002).

A sample diameter:sample thickness ratio of maximal 1:1 should be used according to DIN EN 206-1 with a sample thickness of 150 mm (cube) or 300 mm (cylinder with 150 mm diameter). If the diameter of the testing area is lower than the sample diameter, the testing area diameter must be used for calculation. If another than the recommended 1:1 ratio is used, the determined compressive strength must be divided by a factor, called a shape factor (Table 3.9, Figure 3.10).

Table 3.9. Calculation of the shape factor (after Kühn, 2014).

Sample height	Diameter	Height/diameter ratio	Shape factor
10	15	0.67	1.12
12	15	0.80	1.07
14	15	0.93	1.02
15	15	1.00	1.00
16	15	1.07	0.98
18	15	1.20	0.94
20	15	1.33	0.91
22	15	1.47	0.89
24	15	1.60	0.87
26	15	1.73	0.86
30	15	2.00	0.85

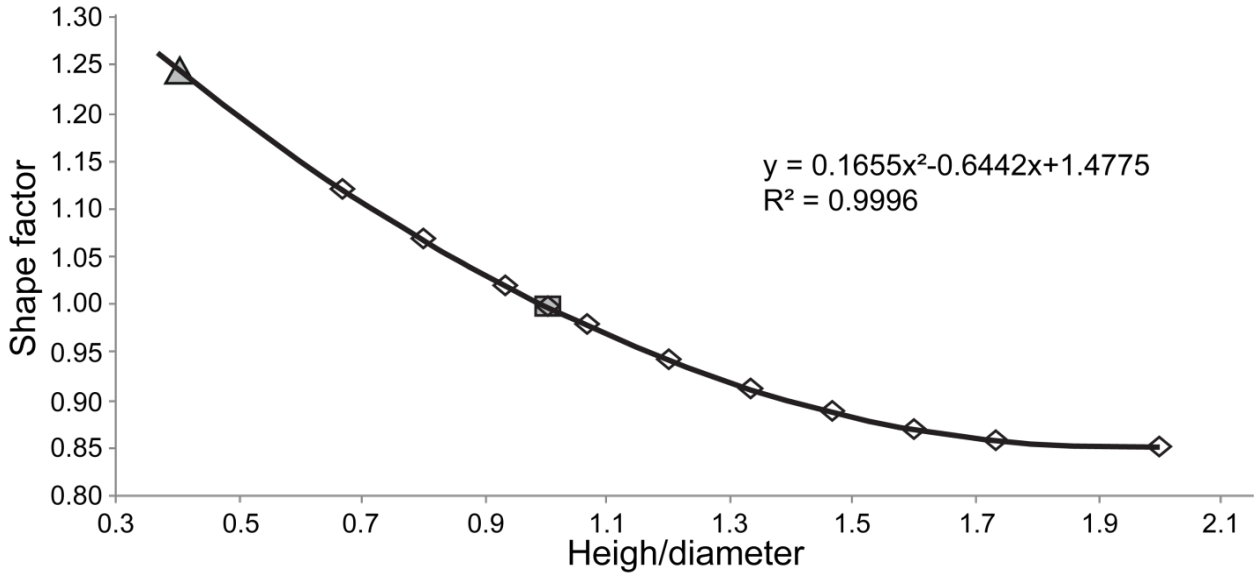

Figure 3.10. Calculation of the shape factor from the height/diameter ratio (trapezium data points from Kühn, 2014). The calculated function was interpolated to lower ratios until 0.40 (triangle: data point of calibrating machine). The rectangle marks the ratio of our self-built testing machine.

At constant diameter, this factor decreases with increasing sample thickness. Because a sample thickness of 8 mm was used, the conic sections with 7.98 mm diameter have a ratio of 1:1. Hence, a shape factor of 1 was chosen resulting in no shift of the measured compressive strength value occurring for the self-built testing machine. The testing machine needed for calibration purposes had conic sections with a diameter of 20 mm and used a load increase of 2400 N/s. Hence, a shape factor of 1.25 was used for this device. However, due to the small sample dimensions such as thickness, compressive strength values show increased errors due to the higher effects of sample heterogeneities. Additionally,

the smaller sample dimensions resulted in a larger influence of friction between the testing plates and the sample during deformation and failure. Hence, the smaller the sample thicknesses, the higher the compressive strength measured. These compressive strength values could be corrected by a factor of 0.875 (approximated value, according to Städtke, Institute for Buildings and Environment Friedland, 2014, pers. comm.). The estimated errors involved in this method are summarised in Table 3.10.

Table 3.10. Estimated errors for the compressive strength measurements.

Compressive strength [N/mm²]	Estimated error [N/mm²]
10-20	4
20-30	5
30-40	7
40-50	8
50-60	9

The calibration curve of the self-made testing device is shown in Figure 3.11.

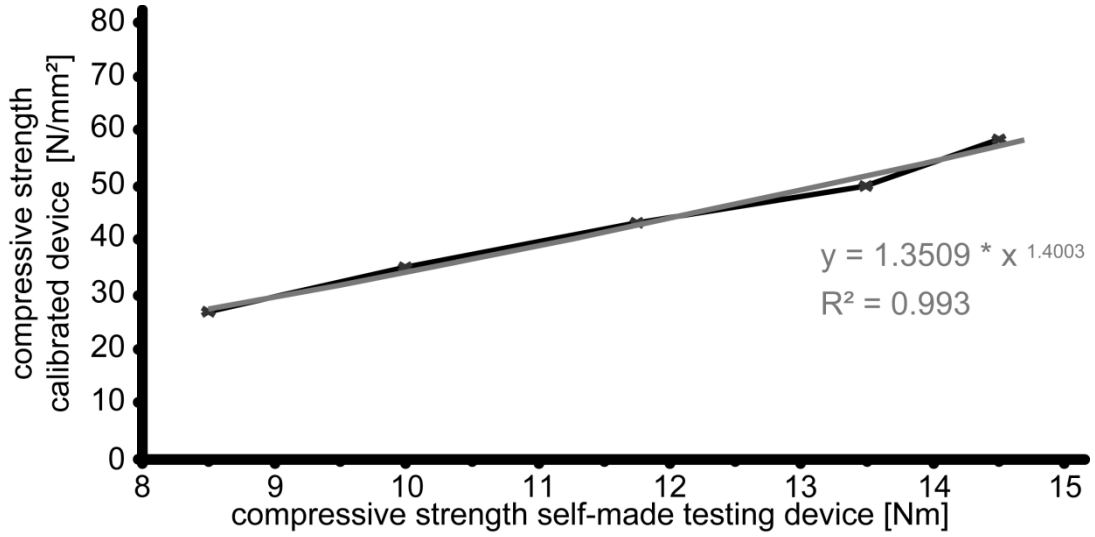

Figure 3.11. Calibration curve of the self-made testing device to the standard testing machine working after DIN EN 12390-3. The function of the regression curve (grey) was used to convert the measured compressive strength values. Displayed values are not corrected for sample shape.

4 Results

4.1 Characterisation

4.1.1 Eocene clay of Friedland

XRD

For mineralogical characterisation such as qualitative and quantitative phase analysis and determination of structural parameters a combination of analytical methods was used. Qualitative and quantitative phase analysis was undertaken using XRD and the Rietveld program BGMN. A BGMN fit of an XRD random powder pattern of the bulk sample is shown in Figure 4.1. According to several earlier authors (e.g. Henning, 1968; Pusch, 1998, 2001), the Friedland clay bulk sample is a complex mixture mainly composed of a smectite-rich irregular I-S interstratification, quartz, white mica and kaolinite (Table 4.1). The white mica can be subdivided into at least two phases, a well crystalline muscovite and an illitic mica based on the profile shape of the, e.g. 10 Å reflection. However, for quantification purposes, both phases were grouped as white mica. Kaolinite seems to occur with a bimodal crystallite size distribution, as indicated by the profile shape. However, the kaolinite content in the sample was summed together. Because the Friedland clay deposit is notably heterogeneous, the phase contents are expected to vary from sample to sample (Kasbohm, 2013, pers. comm.). However, the qualitative and quantitative data presented here only applies to the samples, whereby the contents of the interstratification, quartz, mica and kaolinite may vary up to 10% w/w, and the accessory minerals show sporadic occurrence. The quantitative results presented are compared to the literature (e.g. Pusch, 1998) whereby differences may reveal the heterogeneity of the clay as well as errors involved in the quantification methods. For example, some authors (Kumpulainen & Kiviranta, 2010; Koskinen, 2012) reported smectite in Friedland clay samples but no chlorite: results which could not be confirmed in this study.

Identification of the clay mineral phases was made using preferred oriented specimens (Figure 4.2). The I-S interstratification was determined to be smectite-rich (about 66% smectite content) with a Reichweite *R*0 (randomly stacked; see Table 4.3 - Table 4.4). Chlorite, as well as kaolinite and white mica are recognisable, and quartz and feldspar phases were the most abundant non-layer silicate phases. The gypsum present in bulk rock powders was detected in these measurements and was removed by dissolution during preparation of the preferred oriented specimens. To determine the type of smectitic layers present in the I-S, a test according to Hofmann & Klemen (1950) and Greene-Kelly (1952) without Li saturation was undertaken. The Na-saturated, 875 °C heated sample showed no swelling behaviour under ethylene glycol saturation indicating montmorillonitic instead of beidellitic layers (Appendix iv).

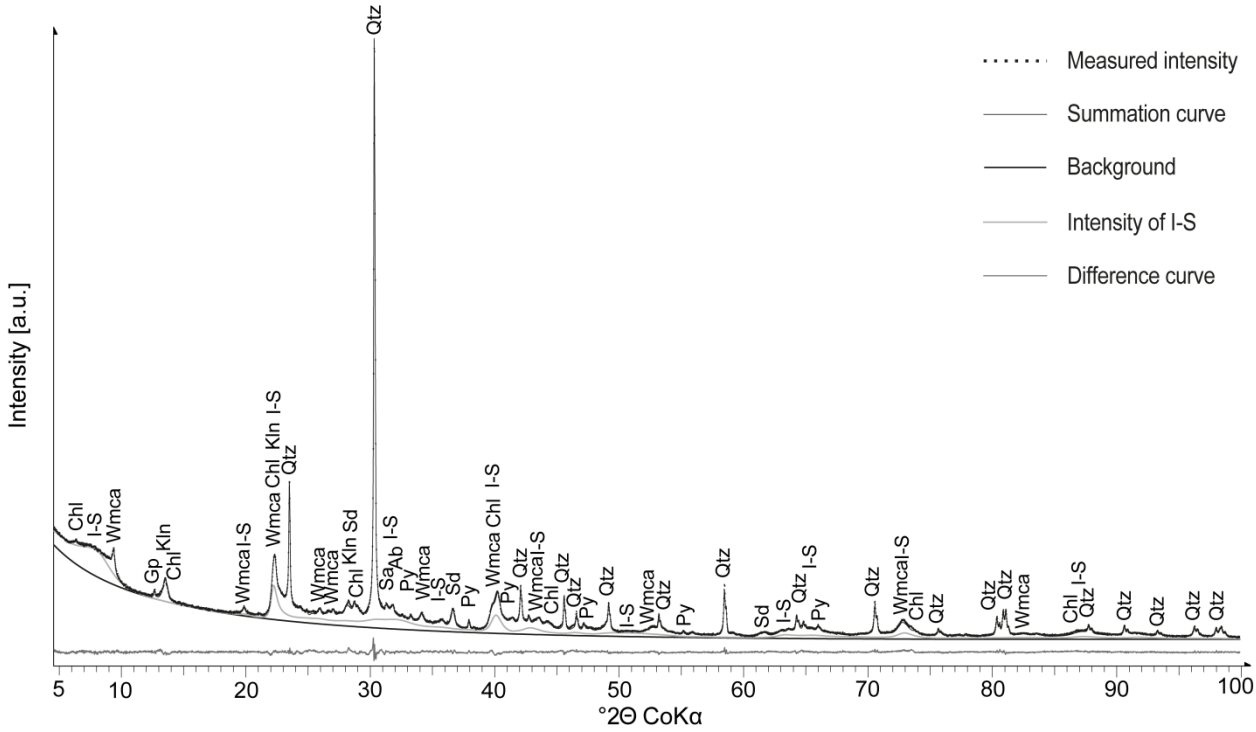

Figure 4.1. BGMN fit of the XRD pattern of the random powder Friedland clay bulk sample. The major phases are marked and the calculated diffraction pattern for I-S shown as a curve. Chl: chlorite, I-S: illite-smectite interstratification, Wmca: white mica, Gp: gypsum, Kln: kaolinite, Qtz: quartz, Sd: siderite, Sa: sanidine, Ab: albite, Py: pyrite; *R*wp = 2.02%, *R*exp = 1.10%

Table 4.1. Generic qualitative and quantitative phase analyses of Friedland clay bulk sample using BGMN program (*R*wp = 2.02%, *R*exp = 1.10%).

Mineral phases	% w/w
Clay minerals	**65.2**
*R*0 I(0.3)-S interstratifications	30.0
White mica (illite-muscovite)	19.8
Kaolinite	11.8
Chlorite, tri	3.6
Framework silicates	**29.3**
Quartz	23.0
Potassic Feldspar	5.1
Na-rich Plagioclase	1.2
Others	**5.5**
Siderite	1.6
Anatase	1.0
Pyrite	0.9
Gypsum	1.2
Rutile	0.8
Sum	**100.0**

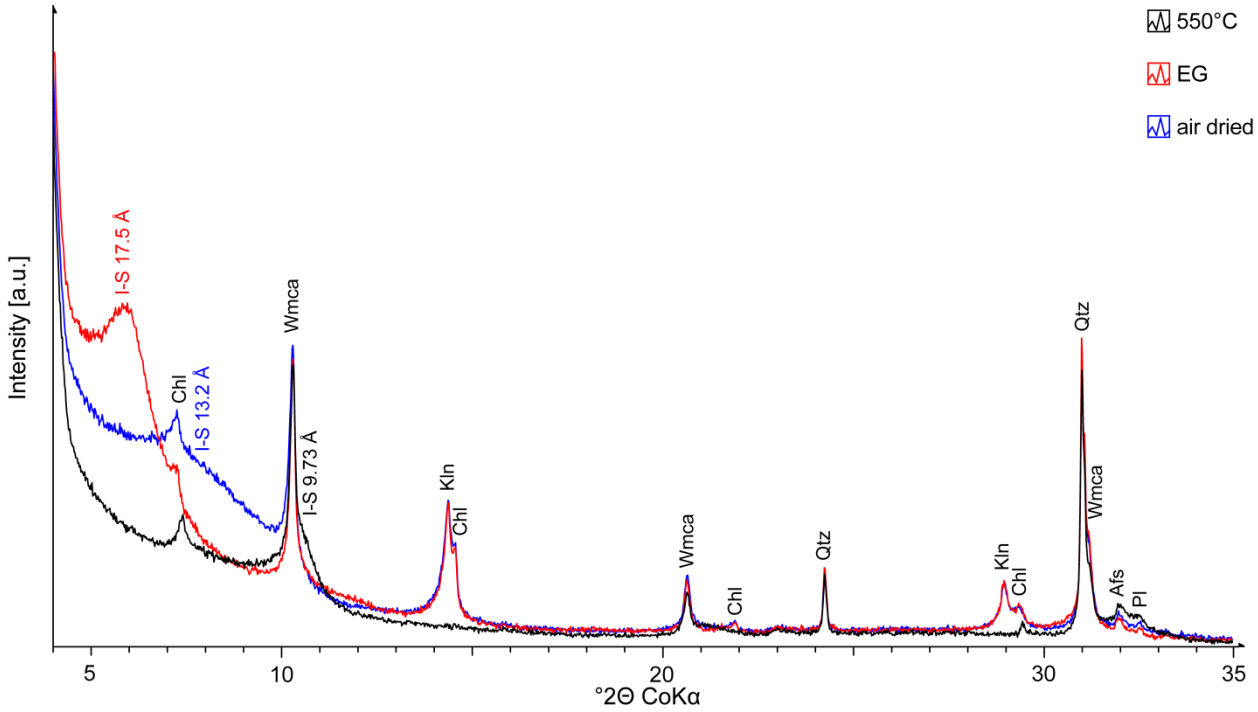

Figure 4.2. XRD patterns of preferred oriented specimens of the Friedland clay bulk sample. The major phases are marked. I-S: illite-smectite interstratification, Chl: chlorite, Wmca: white mica, Kln: kaolinite, Qtz: quartz, Afs: alkali feldspar, Pl: plagioclase

Random XRD pattern and preferred oriented specimen patterns were studied for the different size fractions (<0.1 µm; <0.2 µm; 0.2-2 µm; 2-10 µm; >10 µm) of the Friedland clay (Figure 4.3 - Figure 4.5, Appendix v - Appendix viii). With decreasing particle size the content of the non-clay minerals, such as framework silicates (esp. quartz and plagioclase) and accessory minerals (esp. siderite and pyrite) strongly decreases from 91.8% w/w to only traces, whereas the bulk clay mineral content (esp. I-S and kaolinite) increases from 8.2% w/w (dominated by white mica and kaolinite) to almost 100.0% w/w (dominated by I-S, white mica, and kaolinite). The white mica behaves differently, depending on its polytypism. Muscovite ($2M_1$) is strongly enriched in the fractions between 0.2 µm and 10 µm (14-15% w/w each) and its content decreases with decreasing particle size. No $2M_1$ muscovite was detected in the <0.1 µm fraction. In contrast, muscovite/illite ($1M_d$) was found to occur in all fractions in similar contents (3-5% w/w) but is strongly enriched in the <0.1 µm fraction (17% w/w). Hence, $2M_1$ white mica occurs as larger, better crystallised particles than $1M_d$ white mica. Chlorite mainly occurs in the coarser sized fractions 0.2-10 µm with equal contents (1-2% w/w) but is almost lacking in the >10 µm fraction, indicating a similar particle size distribution related to $2M_1$ white mica. Feldspars are distributed over a large size fraction range but are most abundant in the 2-10 µm fraction (9.6% w/w) and lacking in the <0.1 µm fraction. Anatase and rutile are distributed homogeneously (0.8-1.4% w/w and 0.5-0.9% w/w, respectively) in size fractions, except the <0.1 µm fraction. Both pyrite and siderite are enriched in size fractions >2 µm indicating large particles. Pyrite made up about 1-2% w/w in these coarse fractions and then strongly decreasing with decreasing particle size whereas siderite almost exclusively exists in the >10 µm fraction (10.7% w/w) with only traces (<0.6% w/w) in size fraction <10 µm.

Because the I-S interstratification is strongly enriched in the <0.2 µm fraction, the <0.1 µm fraction was separated to further concentrate it for structural characterisation purposes. A random powder XRD pattern as well as a preferred oriented specimen pattern is shown in Figure 4.4 and Figure 4.5, respectively. The phase content of I-S interstratification was increased to about 71% w/w in the <0.1 µm size fraction (Table 4.2). Kaolinite is assumed to be underestimated because it occurs as small and highly disordered particles, possibly having halloysite-like properties such as a larger d-spacing of the basal reflections (>7.2 Å) and a high degree of disordering, resulting in broad reflections that cannot be fitted correctly. These broad peaks were best fitted using high degrees of crystallite size- and microstrain-induced broadening. The phase content of white mica is assumed to be overestimated because of its strong overlap with the I-S and kaolinite reflections and the underestimation of kaolinite. The BGMN fits are displayed in the Appendix ix - Appendix xv.

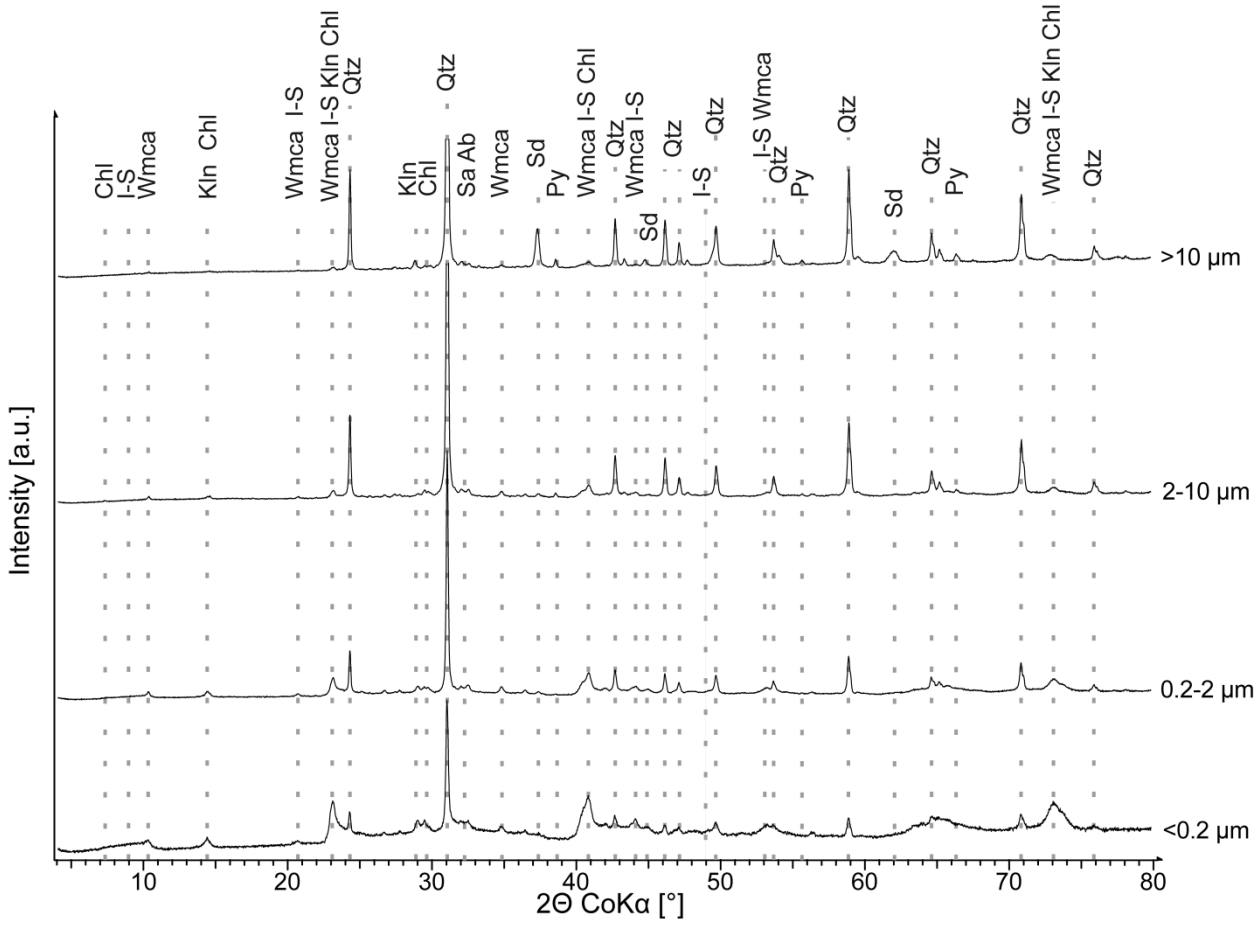

Figure 4.3. XRD patterns of Friedland clay size fractions. Lower: <0.2 µm, lower middle: 0.2-2 µm, upper middle: 2-10 µm, upper: >10 µm. The major phases are marked. Chl: chlorite, I-S: illite-smectite interstratification, Wmca: white mica, Kln: kaolinite, Qtz: quartz, Sa: sanidine, Ab: albite, Sd: siderite, Py: pyrite

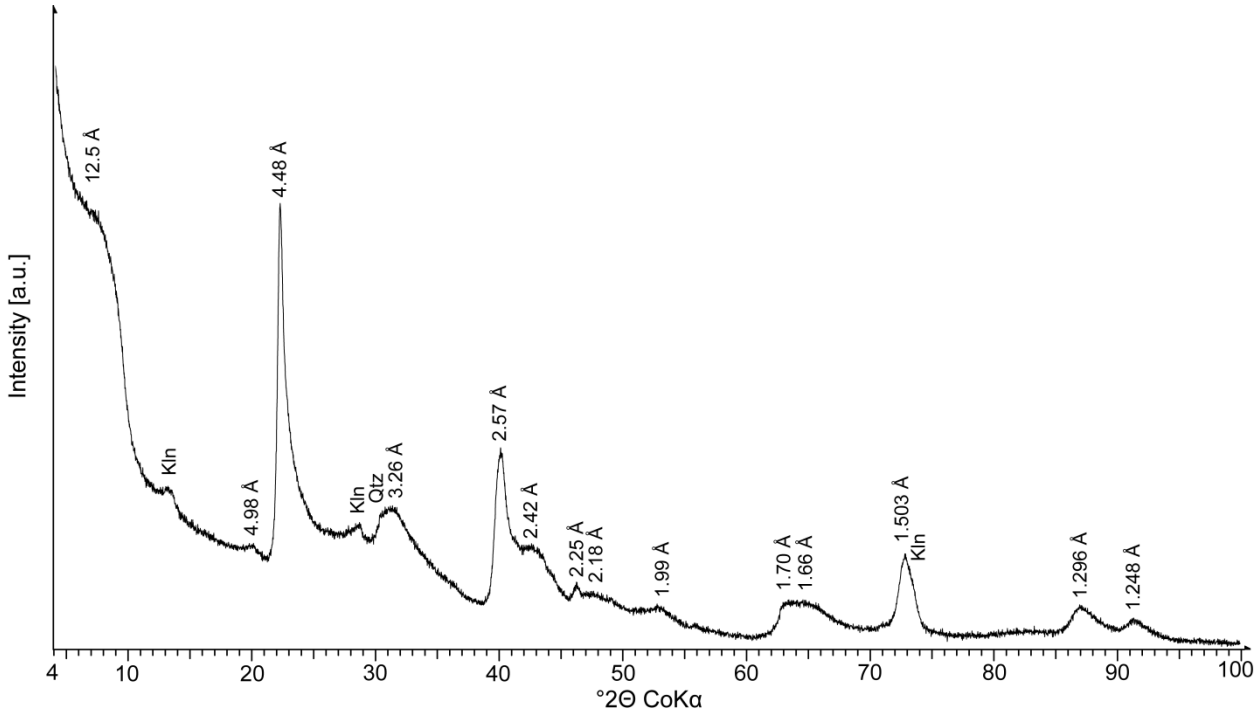

Figure 4.4. XRD pattern of a random powder of the Friedland clay <0.1 µm fraction. The sample is highly enriched in the I-S interstratification. The d-values given belong to the I-S interstratification. Kln: kaolinite, Qtz: quartz

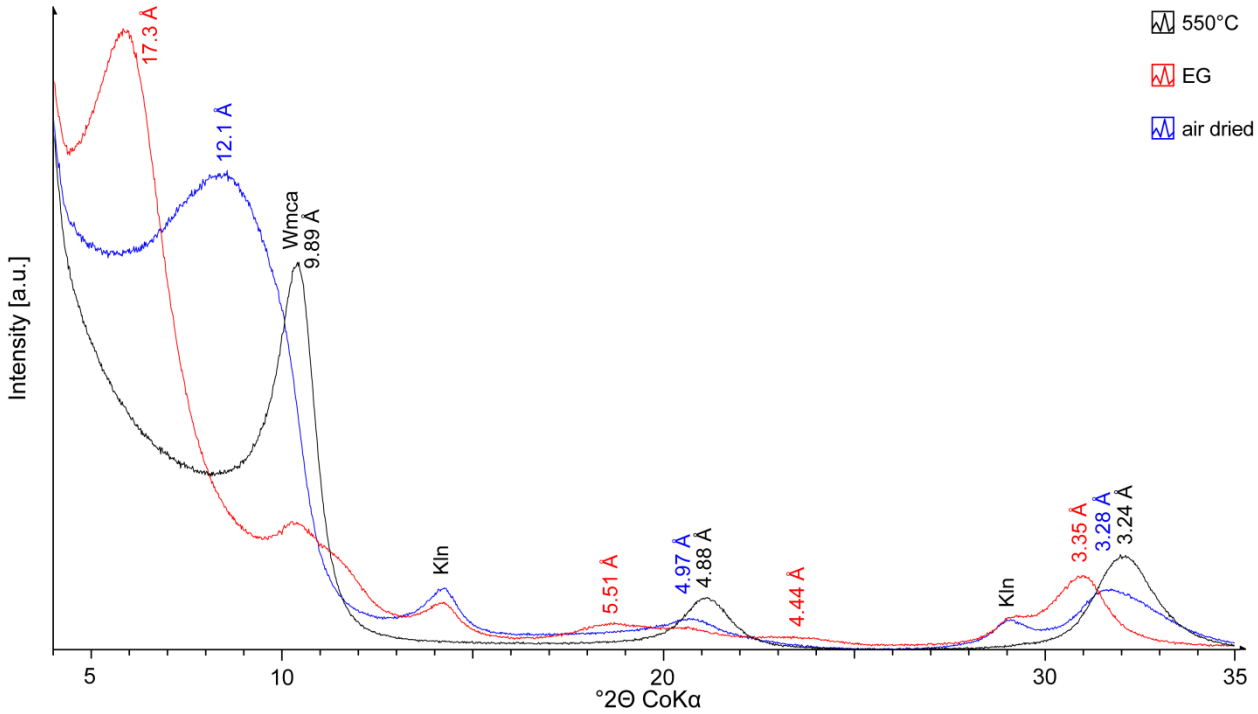

Figure 4.5. XRD patterns of preferred oriented specimens of the Friedland clay <0.1 fraction. The d-values given belong to the I-S interstratification. Wma: white mica, Kln: kaolinite

Table 4.2. Qualitative and quantitative phase analyses of the Friedland clay size fractions using BGMN program (Fits and *R*-values are given in the Appendix ix - Appendix xv).

Mineral phases	Size fractions [% w/w]				
	>10 µm	2-10 µm	0.2-2 µm	<0.2 µm	<0.1 µm
Clay minerals	**8.2**	**26.2**	**65.5**	**84.3**	**100.0**
*R*0 I(0.3)-S interstratification	traces	traces	33.0	60.3	71.2
White mica (illite-muscovite)	6.8	19.4	18.0	9.6	17.0
Kaolinite	1.4	5.7	12.3	13.6	11.8
Chlorite, tri	traces	1.1	2.2	0.8	—
Framework silicates	**78.0**	**70.3**	**32.6**	**13.9**	**—**
Quartz	70.9	60.7	26.9	8.6	traces
Potassic feldspar	4.5	7.2	3.8	3.4	—
Na-rich plagioclase	2.6	2.4	1.9	1.9	—
Others	**13.8**	**3.5**	**1.9**	**1.8**	**—**
Siderite	10.7	0.6	0.3	0.1	—
Anatase	0.8	1.0	1.4	1.1	—
Pyrite	1.8	1.0	0.2	traces	—
Rutile	0.5	0.9	traces	0.6	—
Sum	**100.0**	**100.0**	**100.0**	**100.0**	**100.0**

Determination of the illite content in I-S by Rietveld refinement and the Moore & Reynolds method (see section 3.1.1) produced consistent results considering the errors of determination (Table 4.3). In agreement with literature (e.g. Henning, 1968; Henning & Kasbohm, 1998; Pusch 1998, 2001), the interstratification can be well described as a *R*0 I(0.3)-S with montmorillonitic layers. The refinement of the powdered sample resulted in a slightly lower value for illitic layers than indicated by Moore & Reynolds (1997), presumably caused by the strong peak overlap and an overestimation of white mica. In the case of the air dried specimen, the illite content is slightly higher than determined from the ethylene glycol saturated specimen probably due to the occurrence of collapsed or partially collapsed smectite layers caused by industrial drying of the wet clay pit sample. The d-spacings of these collapsed layers are quite similar to the d-spacings of the illitic layers, resulting in higher errors. Intercalating ethylene-glycol leads to a more homogeneous expansion of the partially collapsed smectite layers to ≈17 Å and a reduction of refined parameters required to fit complex water distribution in the smectitic interlayer, which yields a more reliable value with lower error.

Table 4.3. Determination of the illite content in the I-S interstratification using Rietveld refinement of powdered and preferred oriented samples of the Friedland clay <0.1 µm fraction using BGMN program. Both, powder patterns as well as preferred oriented specimens were independently refined (Fits are given in the Appendix ix - Appendix xv). Additionally, the method after Moore & Reynolds (1997) of simulated oriented patterns was applied.

Method used	Rietveld refinement			Moore & Reynolds (1997)
Sample	Powdered	Preferred oriented		Preferred oriented
Condition		Air dried	Ethylene glycol saturated	Ethylene glycol saturated
Illite content in I-S interstratification [%]	32	38	33	35

Using the Rietveld program BGMN (Bergmann *et al.*, 1998) and the structure models published by Ufer *et al.* (2012a,b), the structural parameters of the *R*0 I-S interstratification were determined (Table 4.4). Only some of the refined parameters, important for structural characterisation of the interstratification, are shown here.

The I-S interstratification was highly enriched in the <0.1 µm fraction with only about 17% w/w white mica (1M) and 12% w/w kaolinite present, whereby white mica is considered to be overestimated, and the kaolinite underestimated. The high octahedral iron content of the Friedland clay I-S interstratification of 1.25 per F.U. (0.625 is per half F.U.) is consistent with the high Fe content measured by XRF and with structural formulas of I-S determined by Karnland *et al.* (2006) and Kumpulainen & Kiviranta (2010). The interlayer K content for micaceous layers reached with 0.6 the lower refinement limit, indicating strongly interlayer deficient layers (illitic). This is consistent with Ferrage *et al.* (2007) who states that the layer charges of different layers in an interstratification should not differ too much. Interlayer deficient micaceous layers interstratifying with high charged smectitic layers are considered more likely than high charged micaceous layers interstratifying with very low charged smectitic layers (Ferrage *et al.*, 2007; Emmerich, 2011).

The stacking vector for cv layers reached the lower refinement limit (0.26), whereas the stacking vector for tv layers reached the upper refinement limit (0.44). The *p0* value reached also the lower refinement limit, indicating a highly disordered structure. The high degree of disordering indicates micaceous layers more similar to $1M_d$ than 1M. The accuracy of the cv layer content in this case is estimated to be low due to the number of overlapping reflections, especially in the case of the illitic mica. Further characterisation of I-S, kaolinite, and white mica is necessary to improve the structural parameters for these phases. The amount of cv layers vary by using different structural models for kaolinite and illitic mica but is estimated to be about 42%, which is lower than the content of smectitic layers. Assuming illitic layers in this interstratification are dominated by tv layers, the smectitic layers should be cv dominated, although tv layers exist. The Na content of smectitic layers in the I-S interstratifications also reached the upper refinement limit suggestive of high charged layers, which appears plausible as described for the micaceous layers. The calculated content of illitic layers (*wI*) is discussed above (Table 4.3) and lies close to the values reported in the literature (e.g. Henning & Kasbohm, 1998).

The fit was best using an R0 structural model, which is according to the commonly used *R*-value for this material in the literature (*R*0, e.g. Henning & Kasbohm, 1998). In the *R*0 structural model, *pII* is defined to be equal to *wI*. The refined parameters obtained from ethylene glycol saturated preferred oriented sample were quite similar compared to the air dried condition, while the values of *p*K and *p*Na differed for air dried preparation. The air dried sample is much more difficult to refine due to the variable water content in the smectitic interlayers, as well as varying cations in the interlayer of both smectitic and micaceous layers. By using ethylene glycol solvation, some of these parameters are eliminated (e.g. water content) or are of negligible influence (e.g. interlayer cations) resulting in XRD patterns that can

be more reliably refined and produce a result consistent with those obtained by refinement of the powdered sample. In general, the refined result obtained from a random powder pattern seems most reliable because of the larger amount of information that can be resolved from the XRD pattern concerning the 3D structure of the interstratifications. This is in contrast with the one dimensional patterns of preferred oriented samples, where the overlapping peaks of white mica and kaolinite are more difficult to resolve.

Table 4.4. Quantitative phase analysis and results of Rietveld refinement of the I-S interstratification from Friedland clay <0.1 µm fraction using BGMN program. Both, powder patterns as well as preferred oriented specimens were independently refined (Fits are given in the Appendix ix - Appendix xv). σ standard deviation, [1] minimum reached, [2] maximum reached, mpdo maximum possible degree of ordering

	Friedland clay <0.1 µm fraction					
	powder		preferred oriented			
			untreated		glycolated	
	result	σ	result	σ	result	σ
***R*-values**						
*R*wp (%)	3.16		3.58		2.32	
*R*exp (%)	1.02		0.97		0.97	
Global parameters						
I-S (% w/w)	71.20	0.75				
White mica (% w/w)	17.05	0.68				
Kaolinite (% w/w)	11.75	0.37				
p(Fe)	0.625	0.017	0[1]		0.070	0.013
p(K)	0.6[1]		1.00000	0.00031	0.6[1]	
Non-basal model						
a (Å)	0.52123	0.00018				
$-t_x$(cv)	0.26[1]					
$-t_x$(tv)	0.44[2]					
p0	0.333[1]					
p60120	0.544	0.011				
p60, *p180*, *p300*	0.1208	0.0024				
p120, *p240*	0.1522	0.0036				
*p*cv	0.419	0.014				
Basal model						
t_l (Å)	10.105	0.0044	12.117	0.018		
t_S(1w) (Å)	12.85[2]		12.117	0.018		
t_S(2w) (Å)	15.101	0.028	14.809	0.046		
p(Na)	0.5[2]		0.1[1]			
wl	0.322	0.021	0.379	0.023	0.3322	0.0047

XRF

Using XRF for bulk chemistry analysis of the Friedland clay, the water loss (105 °C) and the loss on ignition (LOI, 1050 °C), as well as major and trace elements were determined (Table 4.5). The main components are SiO_2 (49-56%), Al_2O_3 (17-19%), Fe_2O_3 (7-9%) and minor K_2O (2-3%), MgO (2%), and Na_2O (1-2%). The higher Fe_2O_3 content is in agreement with the Rietveld refinement, which considered the interstratification to have high tetrahedral Si and octahedral Fe contents combined with low tetrahedral

and octahedral Al contents. The Si:Al molar ratio in the bulk sample is about 2.80 (SiO_2:Al_2O_3 weight ratio = 3.30), and of the <0.1 µm fraction about 2.15 (SiO_2:Al_2O_3 weight ratio = 2.53). The chemical composition of the bulk material is consistent with those reported in the literature (e.g. Pusch, 1998; Carlson, 2004; Karnland *et al.*, 2006). The difference between the bulk sample and the <0.1 µm fraction shows similarities between both samples, except for, e.g. SiO_2 which is enriched in the bulk sample, due to higher contents of quartz and feldspar, and Al_2O_3, Fe_2O_3, MgO, and Na_2O, which are depleted due to a lower clay mineral content in the bulk sample, especially I-S that contains high amounts of Fe (tetrahedral and octahedral), Mg (octahedral and some interlayer) and Na (smectitic interlayers).

Table 4.5. Bulk chemistry analyses of Friedland clay bulk sample and its <0.1 µm fraction by XRF analysis.

Component/Element	Unit	Friedland clay bulk sample	Friedland clay <0.1 µm fraction	Difference bulk - <0.1 µm fraction
SiO_2	% w/w oxide	55.58	49.22	6.36
TiO_2	% w/w oxide	0.88	0.29	0.59
Al_2O_3	% w/w oxide	16.86	19.44	-2.58
Fe_2O_3	% w/w oxide	6.51	8.63	-2.12
MnO	% w/w oxide	0.03	0.01	0.02
MgO	% w/w oxide	1.79	2.42	-0.63
CaO	% w/w oxide	0.37	0.12	0.25
Na_2O	% w/w oxide	0.93	1.91	-0.98
K_2O	% w/w oxide	2.84	2.38	0.46
P_2O_5	% w/w oxide	0.09	0.03	0.06
LOI 1050 °C	% w/w	6.61	8.25	-1.64
H_2O 105 °C	% w/w	5.74	6.38	-0.64
Sum	% w/w	98.23	99.08	-0.85
Ba	ppm	296	81	215
Ce	ppm	71	48	23
Co	ppm	16	12	4
Cr	ppm	117	162	-45
Cu	ppm	<100	<50	<50
Ga	ppm	23	30	-7
Hf	ppm	6	<5	>1
La	ppm	40	27	13
Mo	ppm	<3	<3	0
Nb	ppm	20	7	13
Nd	ppm	22	<20	>2
Ni	ppm	47	35	12
Pb	ppm	27	21	6
Rb	ppm	147	140	7
Sc	ppm	18	24	-6
Sr	ppm	188	56	132
Ta	ppm	<5	<5	0
U	ppm	4	<4	>0
V	ppm	187	325	-138
W	ppm	<5	<5	0
Y	ppm	30	18	12
Zn	ppm	87	196	-109
Zr	ppm	187	91	96

TEM

TEM observation showed some anhedral opaque grains, identified as quartz (Figure 4.6 A) and minor feldspar, often between 0.2 µm and 10 µm in size. Translucent kaolinite occurs as platy and euhedral crystal shapes that are similar in size, which are sometimes intergrown and often pseudohexagonal and fragmented (Figure 4.6 A; according to Henning & Störr, 1986; Buatier *et al.*, 1992). Smaller kaolinite particles (<1 µm) are sometimes xenomorphous, indicating a poorly ordered kaolinite (Henning & Störr, 1986). These results confirm XRD observations implying a bimodal crystallite distribution. Other large (0.5-10 µm) thin platy crystals, mostly euhedral in shape and frequently broken are presumably muscovite (Figure 4.6 B). The large particle sizes and broken appearance of both kaolinite and muscovite grains is taken to indicate a detrital origin, according to Henning & Kasbohm (1998).

Most small grains (<0.5 µm) occur as fine anhedral flakes with irregular outlines (irregular nepheloid shape) with particle sizes <1 µm. Some minor lath-shaped particles with regular or irregular ends also occur. These particles are interpreted as I-S interstratifications (primarily flaky/nepheloid shaped; Figure 4.6 A,B) and as illite (Figure 4.6 A; primarily lath shaped), according to Henning & Störr (1986) and Henning & Kasbohm (1998). Buatier *et al.* (1992) described these anhedral flakes as typical for smectite in marine sediments. However, for hydrothermal I-S Inoue *et al.* (1987, 1988) described both, flakes and lath-like habits occurring in irregularly interstratified I-S material, in which with increasing illite content a general transition from flaky (with some minor laths), through more thin laths, to dominantly wider laths and some hexagonal plates occurs. Additional TEM images are given in the appendix (Appendix xvi).

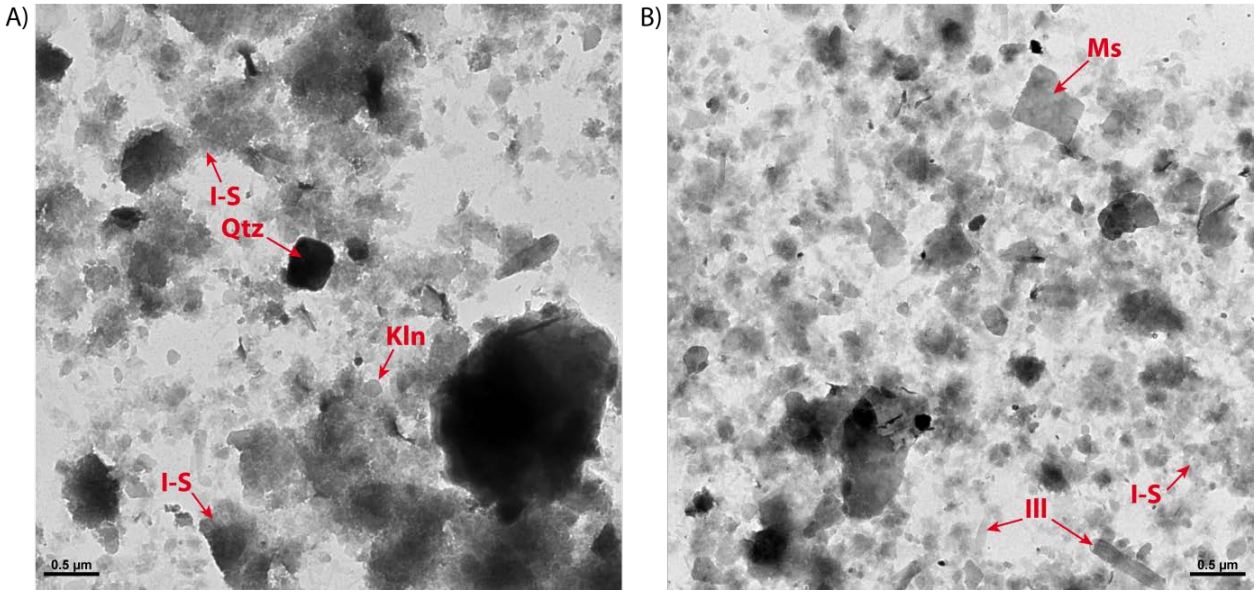

Figure 4.6. TEM image of Friedland clay showing A) anhedral opaque grains, interpreted as quartz (Qtz), pseudohexagonal shapes, interpreted as kaolinite (Kln), and flaky grains, interpreted as I-S interstratification (I-S), and B) flaky clay minerals (I-S), laths, interpreted as illite particles (Ill), and larger euhedral, often broken grains, interpreted as detrital muscovite (Ms).

CEC

The CEC of the Friedland clay <0.1 µm fraction as well as the exchanged cations in solution were determined by the Cu-trien method and ICP-OES, respectively, to better characterise the I-S interstratification (Table 4.6). Th elevated CEC value results from the high content of smectitic layers (according to Henning & Kasbohm, 1998). The high Na content indicates most of the smectitic layers are Na-dominated. Both, the CEC value and the clay being Na-dominated are consistent with published data where the measured CEC value mostly varied between 40 cmol(+)/kg and 54 cmol(+)/kg (e.g. Henning & Kasbohm, 1998; Pusch, 1998, 2001; Carlson, 2004; Karnland *et al.*, 2006).

Table 4.6. CEC of Friedland clay <0.1 µm fraction, determined by Cu-trien method and the appropriate ICP-OES data of the exchanged cations in solution.

Sample	CEC value [cmol(+)/kg]	Ø CEC [cmol(+)/kg]	Exchanged cations Mg [%]	Ca [%]	Na [%]	K [%]
Friedland clay <0.1 µm	47.3 46.5	47	4.7	4.8	86.8	3.7

A_S and pore size distribution

The A_S and pore size distribution of untreated Friedland clay were characterised by BET and BJH measurements (see section 3.5.1) for comparison with the heat-treated "metaclay" (Table 4.7). The "BJH-porosity" (micro- to macropores) was determined from the measured pore volume and bulk density of the clay. The relatively high A_S reflects the high amount of smectite-rich interstratification and is slightly lower than measured by Karnland *et al.* (2006) who determined the A_S to be 50-65 m²/g. This probably reflects a lower white mica and a higher quartz and feldspar content in this sample. However, because no fresh solid clay but a dry clay powder was used, which was industrially milled and dried (see section 2.1), the pores are not all natural but artificially formed during drying and grinding.

Table 4.7. A_S, pore size distribution and porosity of Friedland clay bulk sample.

Sample	A_S [m²/g]	Micropores (<20 Å) [%]	Mesopores (20-500 Å) [%]	Macropores (>500 Å) [%]	"BJH-Porosity" [% V/V]
Friedland clay bulk	45.5	13.3	20.1	66.6	6.0

STA-MS

The STA-MS curves were recorded for both the bulk sample and the <0.1 µm fraction of Friedland clay. In Figure 4.7 the STA-MS curves of the bulk sample (A-D) and the <0.1 µm fraction (E-H) is displayed. The STA-MS curve of the bulk sample shows an overall mass loss of 10.12% w/w (normalised 11.58% w/w), from which 3.82% w/w (normalised 4.88% w/w) is attributable to water loss (Figure 4.7 B) during dehydration of the clay minerals (complete by 200 °C), 5.15% w/w (normalised 5.41% w/w) of water loss (Figure 4.7 B) related to their dehydroxylation (finished at 800 °C) and about 1.15% w/w (normalised 1.28% w/w) corresponding to SO_2 loss (Figure 4.7 D) during destruction of at least one sulphate phase at higher temperature (about 890 °C). The DSC (heat flow) curve shows two main endothermic reactions belonging to dehydration (20-300 °C) and dehydroxylation (400-800 °C) of the clay mineral phases including the I-S interstratification, as well as white mica, kaolinite and chlorite. As these separate phases have different dehydration and dehydroxylation temperatures, the overall DSC curve is therefore a summation curve showing different slopes.

Another small minimum is located at about 892 °C caused by the structural breakdown of at least one sulphate phase, but this region is overlapped by an exothermic reaction and thus, the minimum is shifted to lower temperatures. Gypsum was identified in XRD as a sulphate, being transformed to γ-anhydrite up to 240 °C without SO_2 loss (Emmerich, 2011). The destruction of anhydrite is not seen here as it occurs at higher temperatures (beginning peak at 1100 °C in Figure 4.7 D). The endothermic reaction at about 890 °C accompanied by a loss of SO_2 reflects destruction of a thermally stable sulphate phase newly formed by the reaction of evolving SO_2 formed by pyrite oxidation (407 °C and 479 °C) with the solid sample or alternatively minor traces of barite possibly present in the sample.

The simultaneous H_2O, CO_2, and SO_2 removal (Figure 4.7 B-D) at lower temperature (finished at 400 °C) is interpreted as destruction of organic matter primarily associated with clay minerals. This reaction is exothermic but cannot be seen in the DSC curve due to the overlap by the more strongly endothermic reactions related to dehydration and the onset of clay mineral dehydroxylation. The decomposition of siderite causes the CO_2 loss between 450 and 600 °C. Calcite and dolomite were not detected in this sample, confirming the XRD results, as no decompositions between 700 and 900 °C are evident (Smykatz-Kloss, 1974). An exothermic reaction at about 956 °C is attributed to the recrystallisation of former kaolinite as it is the first clay mineral phase in this assemblage to show this effect (Emmerich, 2011).

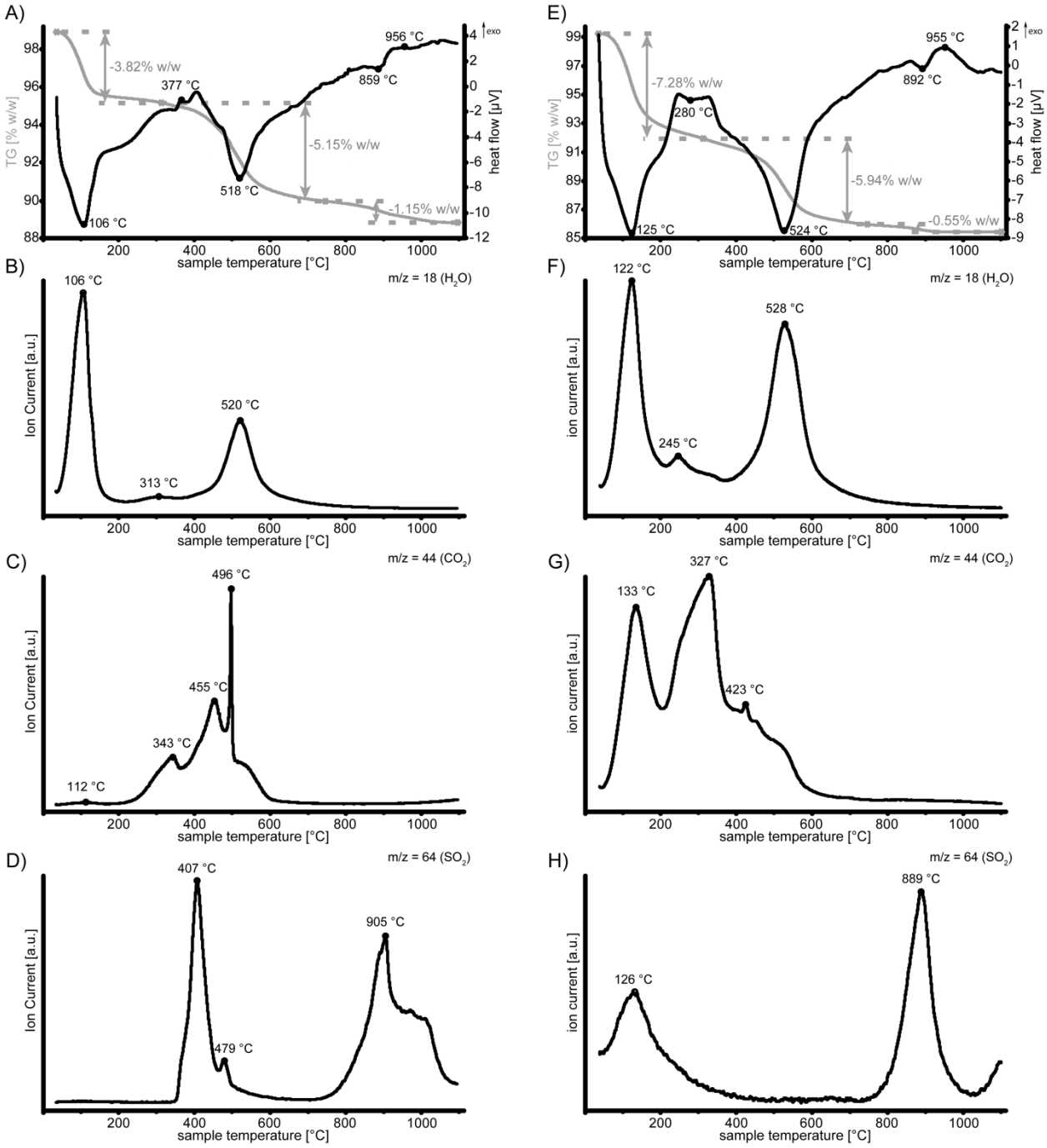

Figure 4.7. STA-MS curves of the Friedland clay bulk sample (A-D) and the <0.1 µm fraction (E-H). A) TG (grey) and DSC (heat flow, black) curve of the bulk sample; B) Water ion current of the bulk sample; C) CO_2 ion current of the bulk sample; D) SO_2 ion current of the bulk sample; E) TG (grey) and DSC (heat flow, black) curve of the <0.1 µm fraction; F) Water ion current of the <0.1 µm fraction; G) CO_2 ion current of the <0.1 µm fraction; H) SO_2 ion current of the <0.1 µm fraction. TG starting value bulk 98.94% w/w, sample amount 103 mg; TG starting value <0.1 µm fraction 99.23% w/w, sample amount 101 mg

The STA-MS curves of the <0.1 µm fraction of Friedland clay produces similar results compared to the bulk sample. The overall mass loss of 13.77% w/w (normalised 15.15% w/w) as well as mass loss related to dehydration (20-200 °C, normalised 8.05% w/w) and dehydroxylation (400-800 °C, normalised 6.46% w/w) are higher than that of the whole rock fraction due to the higher amount of clay minerals (Figure 4.7 E and F) as seen in the XRD patterns. The higher ratio of dehydration to dehydroxylation

weight loss in the <0.1 µm fraction indicates a higher amount of adsorbed surface water and water intercalated in the interlayer. This seems plausible because a more purified I-S interstratification is present with a higher A_S, which contains a relatively higher amount of adsorbed water caused by an increased proportion of expandable (smectitic) layers than the bulk sample, and a lower mean particle size increasing the outer surface area.

The intensity of both dehydration and dehydroxylation in the <0.1 µm fraction DSC curve is also higher than that of the bulk sample confirming a higher clay mineral content as indicated by Rietveld quantification. Some minor organic compounds are decomposed at about 300-350 °C as described for the bulk material (Figure 4.7 E-G). Decomposition of different carbonate phases such as siderite (Figure 4.7 G) is of less intensity according to XRD results. Recrystallisation of kaolinite as indicated by an exothermic reaction at about 955 °C is similar to that observed in the bulk sample (Emmerich, 2011, Figure 4.7 E).

The amount of stable sulphate phase indicated by the mass loss accompanied by SO_2 outgassing and an endothermic peak in the DSC curve (Figure 4.7 E and H) is considerably lower (decomposing at 860-900 °C, normalised 0.64% w/w) than in the bulk sample. Similar to that described for the bulk material measurement, the traces of sulphates are newly formed by reactions with evolving SO_2 released during oxidation of organic molecules (Figure 4.7 H). In this sample no pyrite oxidation was detected, confirming the XRD results.

Peak decomposition of the MS water curve of the <0.1 µm fraction was applied to determine the octahedral cis- and trans-vacant character of the I-S interstratification (Figure 4.8). As both kaolinite and illitic mica occur in the sample as indicated by Rietveld quantification, one dehydroxylation peak for kaolinite and illitic mica was subtracted, respectively. One peak with maximum at 521 °C was attributed to kaolinite and another with a maximum at 538 °C to illitic mica. Both peak areas were selected according to the theoretical dehydroxylation peak area assuming 11.8% w/w kaolinite and 17.0% w/w illitic mica based on the Rietveld refinement (see equations 4.1 – 4.5).

$$m_{kaol}[\%\, w/w] = 100 - m_{2:1} \qquad 4.1$$

and

$$m_{2:1} = 100 \times \frac{\Delta m_{meas} - \Delta m_{kaol,meas}}{\Delta m_{2:1,theor}} \qquad 4.2$$

and

$$\Delta m_{kaol,meas} = \frac{\Delta m_{kaol,theor} \times A_{kaol}}{100} \quad 4.3$$

m_{kaol} …. Mass fraction of kaolinite [% w/w]

$m_{2:1}$ …. Mass fraction of all 2.1 layer silicates [% w/w]

Δm_{meas} …. Measured mass loss of all phases during dehydroxylation [6.46% w/w]

$\Delta m_{kaol,\ meas}$ …. Measured mass loss of kaolinite during dehydroxylation [% w/w]

$\Delta m_{kaol,\ theor}$ …. Estimated theoretical mass loss of kaolinite during dehydroxylation [13.96% w/w]

A_{kaol} …. Peak area of kaolinite dehydroxylation peak [15.52%]

For kaolinite, this leads to the following equation:

$$m_{kaol}[\%\ w/w] = 100 - 100 \times \left(\frac{\Delta m_{meas} - \frac{\Delta m_{kaol,theor} \times A_{kaol}}{100}}{\Delta m_{2:1,theor}} \right) \quad 4.4$$

$$= 100 - 100 \times \left(\frac{6.46 - \frac{13.96 \times 15.52}{100}}{4.80} \right) = 10.64\%\ w/w$$

For illitic mica, the following equation must be regarded:

$$m_{illite}[\%\ w/w] = 100 - m_{kaol} - 100 \times \left(\frac{\Delta m_{meas} - \Delta m_{kaol,meas} - \frac{\Delta m_{illite,theor} \times A_{illite}}{100}}{\Delta m_{I-S,theor}} \right) \quad 4.5$$

$$= 100 - 10.64 - 100 \times \left(\frac{6.46 - 2.17 - \frac{4.67 \times 16.66}{100}}{4.84} \right) = 16.68\%\ w/w$$

m_{illite} …. Mass fraction of illite [% w/w]

m_{kaol} …. Mass fraction of kaolinite [% w/w]

Δm_{meas} …. Measured mass loss of all phases during dehydroxylation [6.46% w/w]

$\Delta m_{kaol,\ meas}$ …. Measured mass loss of kaolinite during dehydroxylation [% w/w]

$\Delta m_{illite,\ theor}$ …. Estimated theoretical mass loss of illitic mica during dehydroxylation [4.67% w/w]

A_{illite} …. Peak area of illitic mica dehydroxylation peak [16.66%]

$\Delta m_{I\text{-}S,\ theor}$ …. Estimated theoretical mass loss of I-S during dehydroxylation [4.84% w/w]

Both values (10.6% w/w kaolinite, 16.7% w/w illitic mica) are consistent with Rietveld refinement results (11.8% w/w kaolinite, 17.0% w/w illitic mica). After subtracting both peaks, the remaining peaks were assumed to exclusively represent the I-S interstratifications and the peak area ratio (<600 °C / >600 °C) expressed as a percent. About 89% peak area of peaks with a maximum below 600 °C were attributed to tv sheets (Drits *et al.*, 1998; Wolters & Emmerich, 2007; Wolters *et al.*, 2009) and 11% above 600 °C to cv layers which is significantly lower than determined by the Rietveld method (42% cv layers). The differences can be explained by considering the high Fe contents of the interstratification as indicated by XRD and XRF (Table 4.4) that lead to a lower maximum peak temperature of dehydroxylation of I-S (Smykatz-Kloss, 1974; Drits *et al.*, 1995; Emmerich, 2011) and hence in this context the calculated amount of tv layers is overestimated. Additionally, Rietveld quantification indicates overestimation of mica and underestimation of kaolinite. Assuming a higher kaolinite content would result in less peak area <600 °C attributed to tv I-S dehydroxylation. Hence, an increasing content of kaolinite would result in less I-S tv layers. Hence, decomposition of the MS water curve underestimates the cv layer content in the case of this sample, while the Rietveld method in this case is assumed to overestimate the cv value. Therefore, the "true" cv layer content for this interstratification cannot be accurately determined and can only be estimated to lie between 11% (indicated by STA-MS) and 43% (indicated by XRD). However, the conclusion that tv-layers dominate in this sample is considered plausible, because it is commonly assumed that high Fe contents in dioctahedral clay minerals increases the amount of tv layers (e.g. Tsipurski & Drits, 1984), which is here the case. Assuming a relatively low Al content in both, octahedral and tetrahedral positions (<1.55 and <0.35 per F.U., respectively), as indicated by XRD and XRF, also leads to a prevalence of tv layers, according to Drits & Zviagina (2009).

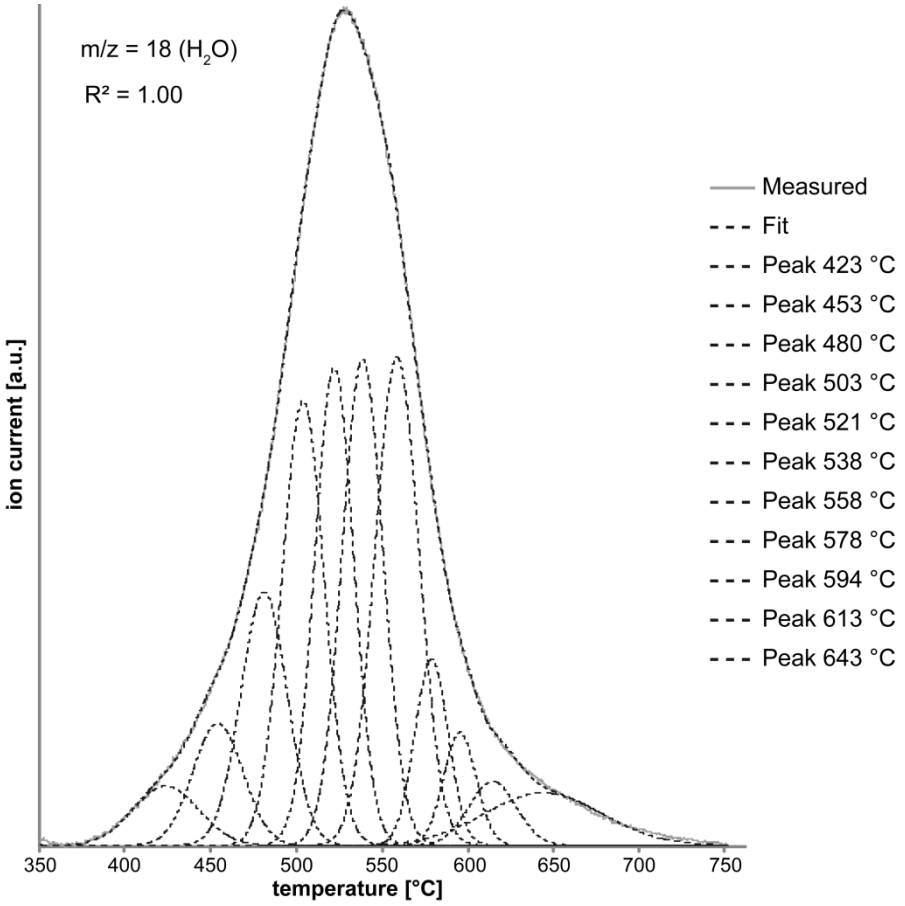

Figure 4.8. MS water curve of Friedland clay <0.1 µm. Curves with maximum above 600 °C represent the amount of cv-layers.

NMR

The coordination state of ^{27}Al in the bulk sample was investigated for it is assumed to be an important indicator of reactivity (see section 1.2), whereby the 5-fold coordinated Al ($Al^{[5]}$) is considered to be the most reactive species of the heated clay. The untreated sample was measured to be compared with heated samples. In the untreated clay only 4- and 6-fold coordinated Al exists (Figure 4.9). Hence, all $Al^{[5]}$ present in the heated samples must be formed by the heating process and is not previously present in the sample. The 4-fold coordinated Al ($Al^{[4]}$) is present in the tetrahedral sheet of the clay minerals, replacing Si, and in framework silicates like quartz and feldspars. In contrast, the 6-fold coordinated Al ($Al^{[6]}$) is exclusively located in the octahedral sheet of the clay minerals, often together with some Fe or Mg. The spectrum is similar to that recorded by Buchwald *et al.* (2009), although they did not quantify the amount of the different Al species. The amount of tetrahedral and octahedral coordinated Al was determined here to be 18% and 82%, respectively, which is similar to Rietveld quantification results (≈19% tetrahedral and ≈81% octahedral Al), assuming 10% Al for Si substitution for clay minerals and octahedral Al contents as refined by BGMN.

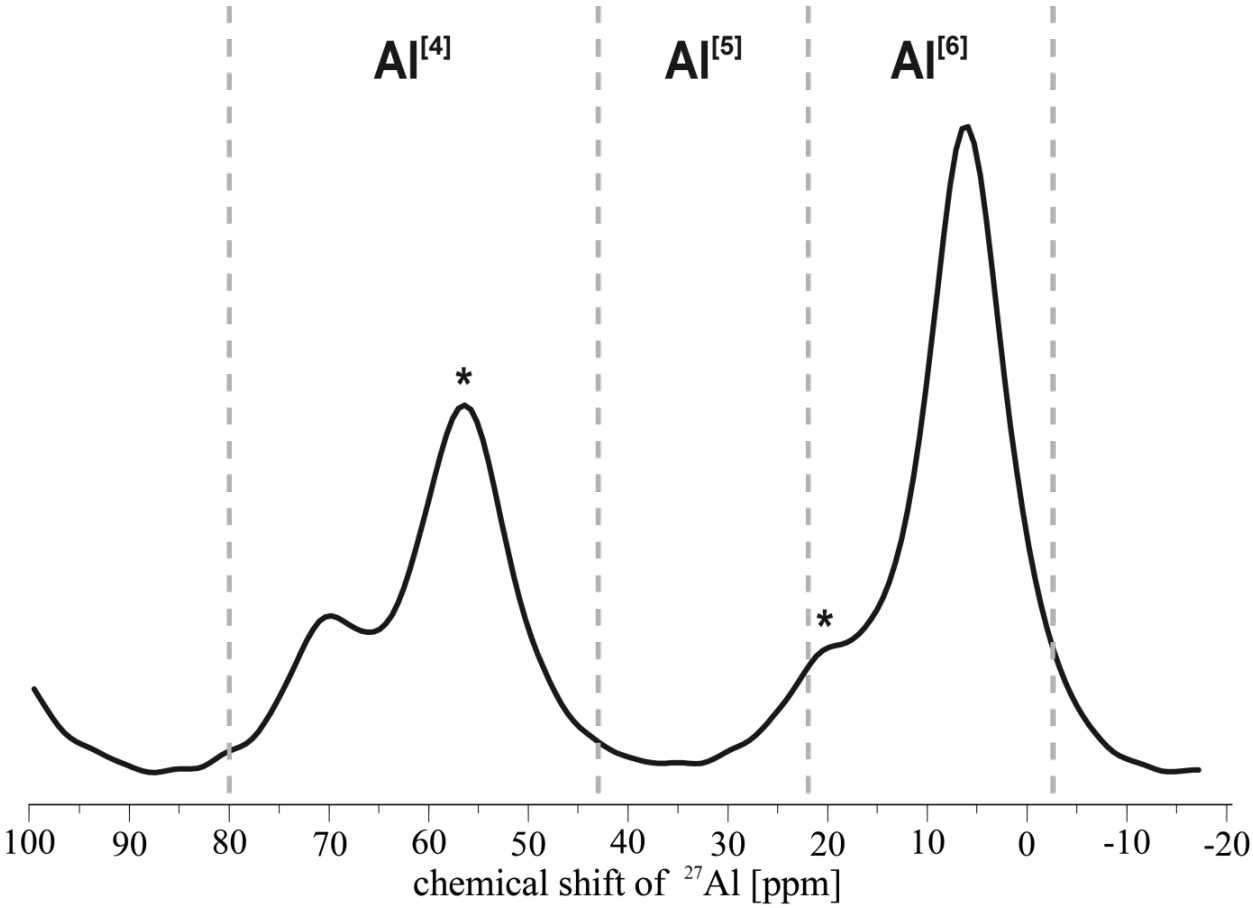

Figure 4.9. NMR spectrum of ^{27}Al of the untreated Friedland clay bulk sample. 6-fold coordinated Al is dominating over 4-fold coordinated Al. 5-fold coordinated Al does not exist here. * Rotational side bands

4.1.2 Rectorite from Arkansas

Some of following results concerning the characterisation of rectorite are published by Dietel *et al.* (2015).

XRD

Qualitative phase analysis was undertaken using XRD with the help of the Rietveld program BGMN to check the purity of rectorite. The raw material was a mixture, dominated by rectorite and quartz with significant impurities of a (di, tri)-chlorite (cookeite) and traces of white mica. These results are in agreement with Miser & Milton (1964) who described rectorite, quartz, and cookeite in this material. Quantification was not possible due to the lack of a rectorite and a cookeite structural model. Although in the course of this study an improved model for rectorite has been developed (according to Ufer, 2014, pers. comm.), a structural model for a (di, tri)-chlorite is still missing. To further enrich rectorite, the <0.1 µm fraction was separated. A random powder XRD pattern as well as a pattern of the preferred oriented specimen is shown in Figure 4.10 and Figure 4.11, respectively. Only small impurities of quartz (0.6% w/w) and traces of cookeite, detected in the preferred oriented sample could be identified here. With the help of the improved structural model for rectorite, quantification was applied and structural parameters relevant for characterisation were determined. The small amounts of cookeite were ignored. The random powder XRD pattern marked with rectorite Miller indices is shown in Appendix xvii.

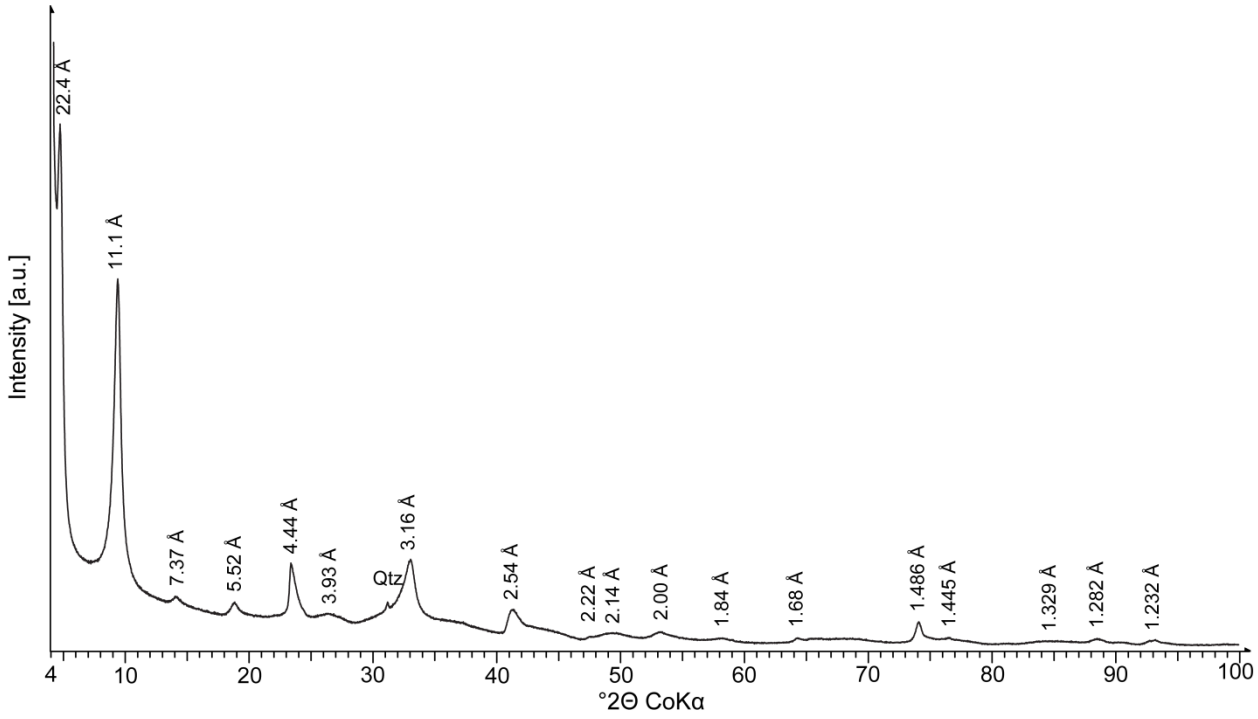

Figure 4.10. XRD pattern of a random powder of the rectorite <0.1 µm fraction. The sample contains small impurities of quartz. The d-values given belong to the I-S interstratification. Qtz: quartz

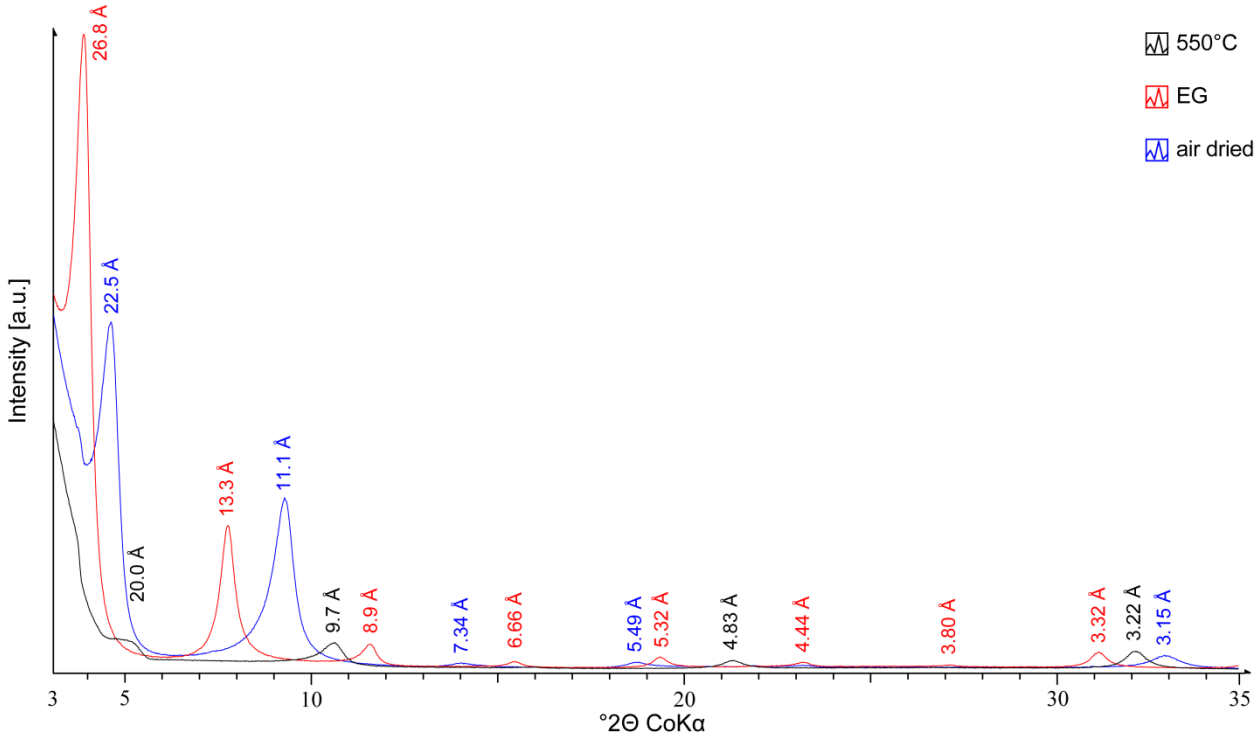

Figure 4.11. XRD patterns of preferred oriented specimens of the rectorite <0.1 fraction. The d-values given belong to the I-S interstratification.

The determination of the content of micaceous layers in the I-S interstratification using the Moore & Reynolds method could not be applied because the patterns were not calculated for regular interstratifications. But with the help of the CV, the regularity and thus, indirectly the content of micaceous layers can be estimated. Rectorite is defined as a regularly interstratified 2:1 layer silicate, composed of dioctahedral mica with dioctahedral smectite, replacing the name allevardite (Caillère & Henin, 1950). The prefix Na-rich, K-rich or Ca-rich describes the dominant cation present in the mica interlayer (Guggenheim *et al.*, 2006, based on the work of Bailey, 1982). The CV was calculated using peak positions from the ethylene glycol saturated preferred oriented sample (see Appendix xviii). The CV value of 0.19 with similar FWHM values between 0.28 °2θ and 0.46 °2θ confirms the regular interstratified 2:1 layer silicate as rectorite (Figure 4.12).

Hence, the interstratification is confirmed as a rectorite having a content of micaceous layers of 50%, although small variations are possible, which is consistent with published data (e.g. Brown & Weir, 1963; Miser & Milton, 1964; Klimentidis & Mackinnon, 1986). To further characterise the rectorite and to determine a more exact proportion of micaceous layers, the Rietveld program BGMN (Bergmann *et al.*, 1998) and the improved structure model for rectorite (original model published by Ufer *et al.*, 2012a,b) were used. The structural parameters of this rectorite were determined (Table 4.8), but only some of the refined parameters important for structural characterisation, were selected to be shown here (BGMN fits shown in the Appendix xix - Appendix xxi).

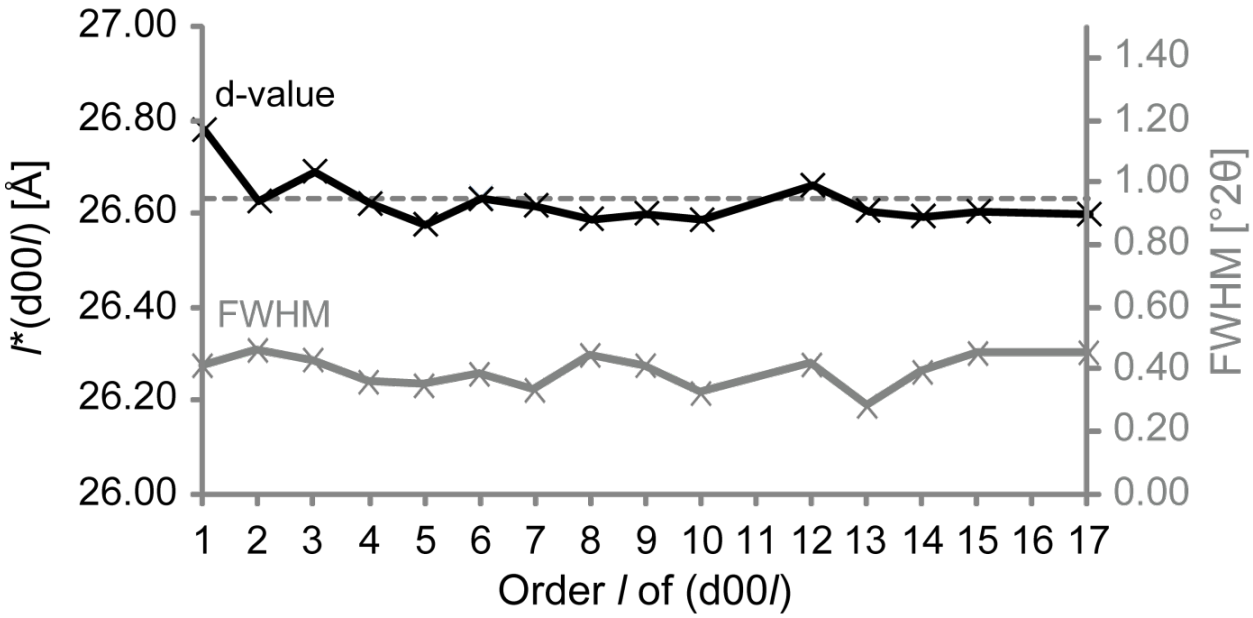

Figure 4.12. Measured d-values (black) and its mean (dashed line) used for CV value calculation of rectorite. All values determined from an XRD pattern of an ethylene glycol saturated, preferred oriented sample of the rectorite <0.1 fraction. FWHM: Full width at half maximum (grey)

Although the structural model for this regular interstratification has been improved by adding turbostratic disordering of smectitic layers (according to Ufer, 2014, pers. comm.), replacing the interlayer cations as Na, and changing the structure of illitic layers to brammallitic layers, it is still not completely satisfactory. Whereas a number of the parameters seem to be reliable, such as a low Fe content, a low content of cis-vacant layers (≈12%), or a high Na content for smectitic layers and a content of micaceous layers nearby 50%, others appear less accurate. Notably the Na content of micaceous layers is not consistent with structural formula determinations made (see below). In the case of the powdered sample the *pII* value is also not equal to the mpdo simply because of a slightly high content of micaceous layers in the calculation. However, calculated *pII* values are allowed to vary within a small range (Bethke *et al.*, 1986). This structural model does generally reflect an ordered interstratification, but further refinement of the structural parameters is required to attain a crystal-chemistry fully compatible with the compositional constraints. When reducing the number of parameters using preferred oriented samples, a more reliable structural model is attained with a significantly lower interlayer Na content for the micaceous layers and the mpdo was reached. However, even these models require some further refinement because the Na content of smectitic layers appears to be still unrealistically low.

Table 4.8. Results of Rietveld refinement of the rectorite <0.1 µm fraction using BGMN program. Both, powder patterns as well as preferred oriented specimens were independently refined (Fits are given in the Appendix xix - Appendix xxi). σ standard deviation, [1] minimum reached, [2] maximum reached, mpdo maximum possible degree of ordering

	Rectorite <0.1 µm fraction					
	powder		preferred oriented			
			untreated		glycolated	
	result	σ	result	σ	result	σ
***R*-values**						
*R*wp (%)	3.41		12.28		12.35	
*R*exp (%)	1.28		2.21		2.22	
Global parameters						
p(Fe)	0[1]		0.03 (fix)		0.03 (fix)	
p(Na)	0.9554	0.0070	0.868	0.017	0.6[1]	
Non-basal model						
a (Å)	5.1551	0.00017				
$-t_x$(cv)	0.485	0.0086				
$-t_x$(tv)	0.3136	0.0014				
*p*cv	0.1169	0.0086				
Basal model						
t_S(1w) (Å)	12.4665	0.0053	12.3722	0.0038		
t_S(2w) (Å)	14.1360	0.0086	15.506	0.020		
p(Na)	0.6[2]		0.1[1]			
wI	0.5459	0.0016	0.50711	0.00082	0.50597	0.00032
pII (*R*1)	0.2485	0.0038	0.0280 (mpdo)	0.0032	0.0236 (mpdo)	0.0013

XRF

Using XRF for bulk chemistry analysis, the water loss (105 °C) and the loss on ignition (LOI, 1050 °C), as well as major and trace elements were determined (Table 4.9). The main components are SiO_2 (45%), Al_2O_3 (31%), and Na_2O (4%). The Si:Al molar ratio is about 1.22 (SiO_2:Al_2O_3 weight ratio = 1.44). These data are very similar to that reported by several authors before (e.g. Brackett & Williams, 1891; Brown & Weir, 1963; Miser & Milton, 1964).

The structural formula of this illite rich I-S interstratification was determined from the results of the XRF data according to Stevens (1946) without measuring layer charge according to Lagaly & Weiß (1971). Low contents of Fe, Mg, Ca, K, Ba, and Sr were included in the calculation whereby Ba and Sr were not included due to their low contents. Traces of Ti, Mn, and Zn, detected by XRF were excluded from structural formula determination as these elements are not considered to be incorporated in the structure. Traces of quartz in the sample, detected and quantified by XRD with the help of the Rietveld method, were subtracted from the compositional analyses and the results normalised to the dry state without water. The spherules that occur on the clay surfaces (Figure 4.14) are considered not to influence structural formula determination because even if they contain Fe, these nanoparticles are not abundant enough to influence the calculation. The structural formula of this rectorite was determined

as follows, which is according to the literature (Brackett & Williams, 1891; Brown & Weir, 1963; Miser & Milton, 1964; Jakobsen *et al.*, 1995):

$$(Na_{1.05}Ca_{0.06}Mg_{0.06}K_{0.03})\ (Al_{3.93}Fe^{3+}_{0.11}Mg_{0.02})\ [(Si_{6.52}Al_{1.48})\ O_{20}|(OH)_4]$$

Table 4.9. Bulk chemistry analyses of the rectorite <0.1 µm fraction using XRF method. n.d. not detectable

Component/Element	Unit	Rectorite <0.1 µm fraction
SiO_2	% w/w	44.98
TiO_2	% w/w	0.02
Al_2O_3	% w/w	31.21
Fe_2O_3	% w/w	0.99
MnO	% w/w	0.09
MgO	% w/w	0.39
CaO	% w/w	0.36
Na_2O	% w/w	3.69
K_2O	% w/w	0.17
P_2O_5	% w/w	0.00
LOI 1050 °C	% w/w	13.16
H_2O 105 °C	% w/w	4.81
Sum	% w/w	99.87
Ba	ppm	643
Ce	ppm	<24
Co	ppm	36
Cr	ppm	62
Cu	ppm	<50
Ga	ppm	22
Hf	ppm	<5
La	ppm	<20
Mo	ppm	3
Nb	ppm	4
Nd	ppm	<20
Ni	ppm	37
Pb	ppm	13
Rb	ppm	10
Sc	ppm	<5
Sr	ppm	387
Ta	ppm	<5
U	ppm	n.d.
V	ppm	74
W	ppm	<5
Y	ppm	21
Zn	ppm	215
Zr	ppm	7

As the interlayer cations are dominated by Na based on XRF and ICP-OES results, this rectorite sample is considered to be a Na-rich rectorite. The layer charges per 2 formula units of −1.48 for tetrahedral sheets and +0.16 for octahedral sheets are according to Brown & Weir (1963), Kodama (1966) and

Jakobsen *et al.*, (1995). Data from all authors led to slightly positive octahedral charges, except Miser & Milton (1964) who calculated no octahedral charge (Table 4.10). Figure 4.13 graphically shows the charge distribution of different rectorite sample compared with that from North Little Rock, Arkansas, analysed in the present study.

Table 4.10. Comparison of results with published data for the charge distribution in the tetrahedral and octahedral sheet and the interlayer of the rectorite (per 2 F.U.). The charges of the proposed beidellitic and brammallitic layers are also given (per 1 F.U. each).

Worker	Phase	Charges		
		Tetrahedral	Octahedral	Interlayer
Present work	Beidellitic layer (1 F.U.)	−0.64	+0.16	+0.48
	Brammallitic layer (1 F.U.)	−0.84	0.00	+0.84
	Rectorite (2 F.U.)	*−1.48*	*+0.16*	*+1.32*
Brown & Weir (1963)	*Rectorite (2 F.U.)*	*−1.32*	*+0.12*	*+1.20*
Miser & Milton (1964)	*Rectorite (2 F.U.)*	*−1.50*	*0.00*	*+1.50*
Kodama (1966)	*Rectorite (2 F.U.)*	*−1.58*	*+0.24*	*+1.34*
Jakobsen *et al.* (1995)	*Rectorite (2 F.U.)*	*−1.48*	*+0.22*	*+1.26*

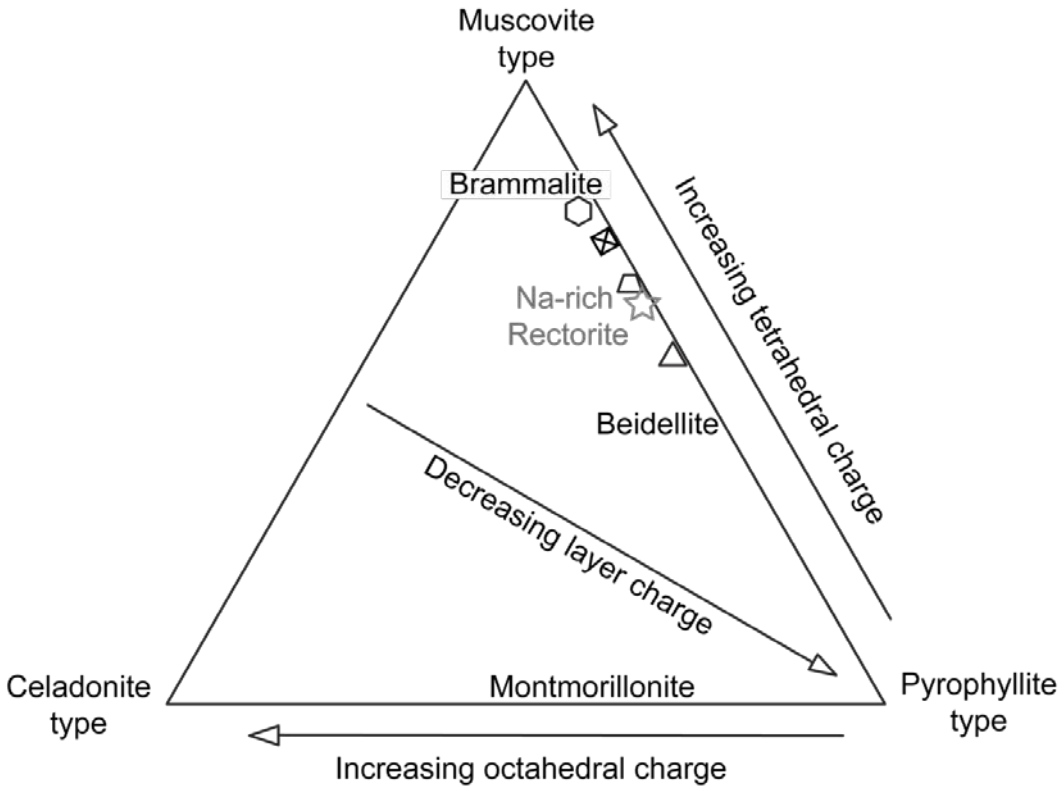

Figure 4.13. Triangle diagram showing the charge distribution of rectorite from North Little Rock, Arkansas, analysed in the present work (star), which are compared with rectorites from Baluchistan, Pakistan (Kodama, 1966; hexagon), from Allevard, France (Brindley, 1956; square), and from North Little Rock (cross), Garland County (trapezium), Saline County (triangle), all located in Arkansas (Miser & Milton, 1964). Paragonite is located in the edge of muscovite. (after Moore & Reynolds, 1997)

In the case that all divalent interlayer cations are present in the smectitic layers as indicated by CEC measurements and confirmed by ICP-OES data of exchanged cations (Table 4.11), the average composition of the smectitic layers is

$$(Na_{0.24}Ca_{0.06}Mg_{0.06})\ (Al_{1.93}Fe^{3+}_{0.11}Mg_{0.02})\ [(Si_{3.36}Al_{0.64})\ O_{10}|(OH)_2].$$

For the micaceous layers remains an average composition of

$$(Na_{0.81}K_{0.03})\ Al_{2.00}[(Si_{3.16}Al_{0.84})\ O_{10}|(OH)_2].$$

Layer charges of both layer types are 0.48 per F.U. for smectitic, and 0.84 per F.U. for micaceous layers, respectively. As most of the charges are located in the tetrahedral sheet, the smectitic layers can be considered to be beidellitic. This interpretation was confirmed with a test according to Hofmann & Klemen (1950) and Greene-Kelly (1952) without Li saturation. The Na-saturated, 875 °C heated sample showed a distinct swelling behaviour under ethylene glycol saturation indicating beidellitic instead of montmorillonitic layers (Appendix xxii). For smectite being defined between 0.2 (low charged) and 0.6 (high charged) per F.U. (Guggenheim *et al.*, 2006; Emmerich *et al.*, 2009), the calculated value fits well as medium charged smectite layers. The non-swelling layers seem to be interlayer deficient (0.84 per F.U., Rieder *et al.*, 1998; Guggenheim *et al.*, 2006) and Na-dominated and thus called brammallitic, which appears plausible assuming similar compositions of the Na-dominated interstratifications as K-dominated interstratifications composed of illitic rather than muscovitic layers. The tetrahedral substitution of Al of 18.5% is according to Barron *et al.* (1985b) who found 17% by NMR and XRF. However, the Al distribution was determined differently. Using XRF, Barron *et al.* (1985b) concluded 25% tetrahedral Al substitution occurs on the micaceous layers and 10% in the smectitic layers, which is in agreement with the data presented in this study (21% for micaceous and 16% for smectitic layers). In contrast, using NMR spectroscopy, Barron *et al.* (1985b) determined 31% tetrahedral Al substitution for micaceous layers and 3% for smectitic layers).

Although the oxidation state of Fe was not determined here, a chemical study of Arkansas rectorite has shown that only <12% of the total Fe is present in the Fe^{2+} state (Bishop *et al.*, 2011). A higher Fe^{2+} content would result in a lower positive octahedral charge. The XRF results gave a slightly higher Mg content than seen in the ICP-OES data used for CEC measurements. Therefore some fixed Mg is considered to occur in the octahedral position in addition to the Mg in the interlayer.

Based on the compositional constraints, this rectorite is best described as a regular interstratification consisting of brammallitic and beidellitic layers. This interpretation is consistent with Brown & Weir (1963) whose results indicated the existence of brammallitic layers (Środoń, 2013), and the presence of such interlayer deficient mica layers is generally consistent with the nature of illitic interstratifications. This result differs, however, from the interpretation of Komada (1966) and Jakobsen *et al.* (1995) who considered the Na-rich mica to be either paragonite-like or paragonite sensu stricto. But Jakobsen *et al.´*s (1995) structural formula determination based in part on NMR spectroscopy is not considered to be more reliable than calculations based primarily on XRF results, because there are not enough constrained parameters in both approaches. The calculated layer charge of paragonite with its high degree of tetrahedral substitution, as proposed by Jakobsen *et al.* (1995) is not supported by other

published results (e.g. Ahn *et al.*, 1985 or Comodi & Zanazzi, 1997, 2000). But because the layer charge of the micaceous layers in this rectorite sample lie close to the defined phase boundary between paragonite and brammallite (0.85 charges per F.U.), these different mica compositions reported may simply reflect some degree of sample heterogeneity in the materials studied or may also fall within the range of analytical errors.

TEM

TEM observation showed thin elongated laths of rectorite, partially overlying each other (Figure 4.14). Some of the lath plates are kinked, folded or broken. These observations are similar to the particle shapes for rectorite described from Allevard (Kitagawa, 1997 and Brown & Weir, 1963), Dagestan, Baluchistan, and Arkansas (Brown & Weir, 1963; Henning & Störr, 1986) as well as other I-S interstratifications with about 50% expandable layers (Inoue 1987, 1988). On some of the particles, dark spots were observed with a diameter between 65 and 125 nm, which may represent Fe- or Mn oxides or hydroxides. These nanoparticles were too small for compositional determinations. More images as well as electron diffraction patterns are attached in the Appendix xxiii - Appendix xxiv.

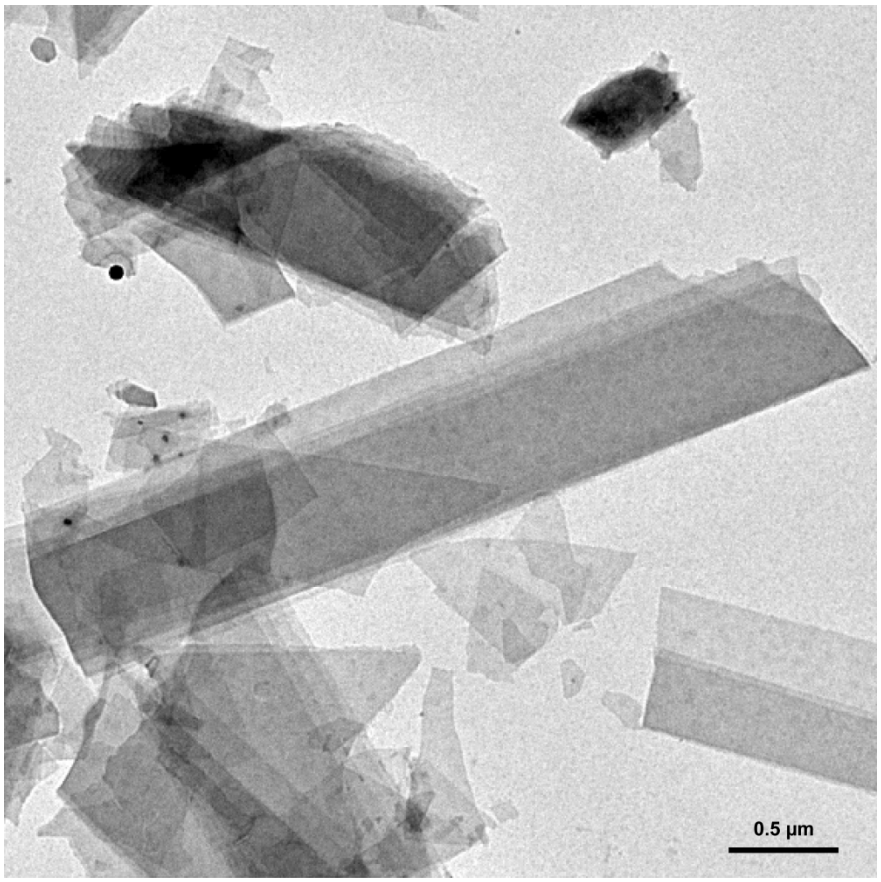

Figure 4.14. TEM image of rectorite showing typical laths and fragments that partially overlay each other. Small black spherules (left side of image) may represent Fe or Mn oxides/hydroxides.

CEC

The CEC of the rectorite <0.1 µm fraction was determined by both, the NH_4Ac and the Cu-trien method for a better characterisation (Table 4.11). Intercalation of NH_4^+ resulted in a higher CEC value than intercalation of Cu-trien, the latter probably reflecting incomplete intercalation in the presence of divalent cations in high-charged smectitic layers (Steudel *et al.*, 2009). These results are according to those reported by Brown & Weir (1963).

Table 4.11. CEC of the rectorite <0.1 µm fraction determined by the ammonium acetate (NH_4-Ac) and copper-triethylenetetramine method (Cu-trien). Both CEC values were determined twice and the mean used for further calculations.

Sample		Intercalation complex	CEC [cmol(+)/kg]	Ø CEC [cmol(+)/kg]	ICP-OES data of exchanged cations [%]			
					Na	Mg	Ca	K
Rectorite <0.1 µm	(1)	NH_4Ac	60.2	60	78.3	13.9	7.3	0.5
		NH_4Ac	60.6					
	(2)	Cu-trien	50.2	50	77.6	15.5	6.6	0.3
		Cu-trien	49.8					

To verify the structural formula determined above, a theoretical CEC value calculation was undertaken as follows. The structural formula determined according to Stevens (1946) without measuring layer charge according to Lagaly & Weiss (1971) tends to overestimate layer charge of expandable 2:1 layer silicates and thus CEC (Wolters *et al.*, 2009, Kaufhold *et al.*, 2011). As in the case of I-S interstratifications direct measurement of layer charge of the smectitic layers is not possible, it is therefore considered important criteria that the calculated CEC value matches well the measured CEC data.

$$CEC = \frac{\xi}{M} \times 100{,}000 \qquad 4.6$$

CEC …. Cation exchange capacity

ξ…. Layer charge [0.48 mol(+)/mol]

M …. Molar mass of the I-S interstratification [376.37 g/mol]

As only smectitic layers are assumed to contain exchangeable cations, the layer charge of the smectitic layers was used for CEC calculations. As rectorite is a regular interstratification of micaceous and smectitic layers, two F.U. of rectorite must be used in the calculation:

$$CEC = \frac{0.48\ {}^{mol(+)}/_{mol}}{752.73\ {}^{g}/_{mol}} \times 100{,}000 = 64\ \frac{cmol(+)}{kg}\ . \qquad 4.7$$

The calculated CEC value of 64 cmol(+)/kg is slightly higher than measured by the NH_4Ac method, which is typical applied to high charged layers (Steudel *et al.*, 2009).

STA-MS

The STA-MS curves were recorded for the rectorite <0.1 µm fraction (Figure 4.15 A-D). The dehydration of this rectorite occurs at 118 °C, seen as a strong endothermic reaction (Figure 4.15 A) that is accompanied by a mass loss of 5.70% w/w (normalised 6.76% w/w) (Figure 4.15 A) and water release (Figure 4.15 B, finished at 200 °C). This occurs at slightly lower temperatures than reported by Kodama (1966). Dehydroxylation of rectorite results in another endothermic reaction accompanied by a water release, and a mass loss of 4.39% w/w (normalised 4.76% w/w, finished at 650 °C; Figure 4.15 A-B), which is consistent with Kodama (1966). Organic molecules that are part of the original sample and not introduced during separation, are oxidised during STA and detected by an exothermic peak at 316 °C in the DSC curve, with a mass loss of 0.88% w/w (normalised 0.94% w/w), and two small peaks of released H_2O and CO_2 in the MS curves (Figure 4.15 A-C). As the organic matter is low in abundance and there is no indication of complexation in the interlayer space from the measured d-values determined by XRD, the presence of organics is considered to have a negligible effect on the structure determination. The organic matter is clearly oxidised by heating during STA measurements prior to dehydroxylation of the rectorite and, hence has no influence on the trans/cis -vacancy determination.

Dehydroxylation occurred in two steps with peak maxima at 470 °C and 588 °C. The mass loss with respect to the dry solid weight of 4.76% w/w was slightly lower than the stoichiometric value of 4.79% w/w (equation 4.3). The deviation is explained by the uncertainty in determining the onset of dehydroxylation due to the superimposing oxidation of the organic material. The mass loss of 0.35% w/w (normalised 0.40% w/w) at even higher temperatures above 700 °C may caused by dehydroxylation of the trioctahedral sheet of cookeite, detected by XRD as an impurity in the <0.1 µm fraction. Trioctahedral sheets commonly dehydroxylate at higher temperature than dioctahedral sheets (Emmerich, 2011). However, the weight loss of 0.40% w/w would be equivalent to a cookeite content of about 5-6% w/w in the sample, which is much too high, considering XRD patterns. Hence, the weight loss accompanied with water loss is high likely a combination of dehydroxylation of some minor cookeite and evaporating water, trapped during dehydroxylation of rectorite. Na-rich clay minerals tend to form spheres during dehydroxylation, because Na serve as a flux reducing the melting temperature dramatically (Mackenzie, 1964; Emmerich, 2011). By partial melting of the clay minerals during dehydroxylation, some water is trapped in these spheres. Heating to higher temperature, the pressure in these sphere increases due to water evaporation until the sphere blasts, releasing the water suddenly which can be recorded by the MS (Emmerich, 2011). A small SO_2 loss at 894 °C (Figure 4.15 D) with negligible mass loss belongs to destruction of a sulphate phase, an impurity present in very low concentrations. An exothermic peak at 1056 °C indicates recrystallisation.

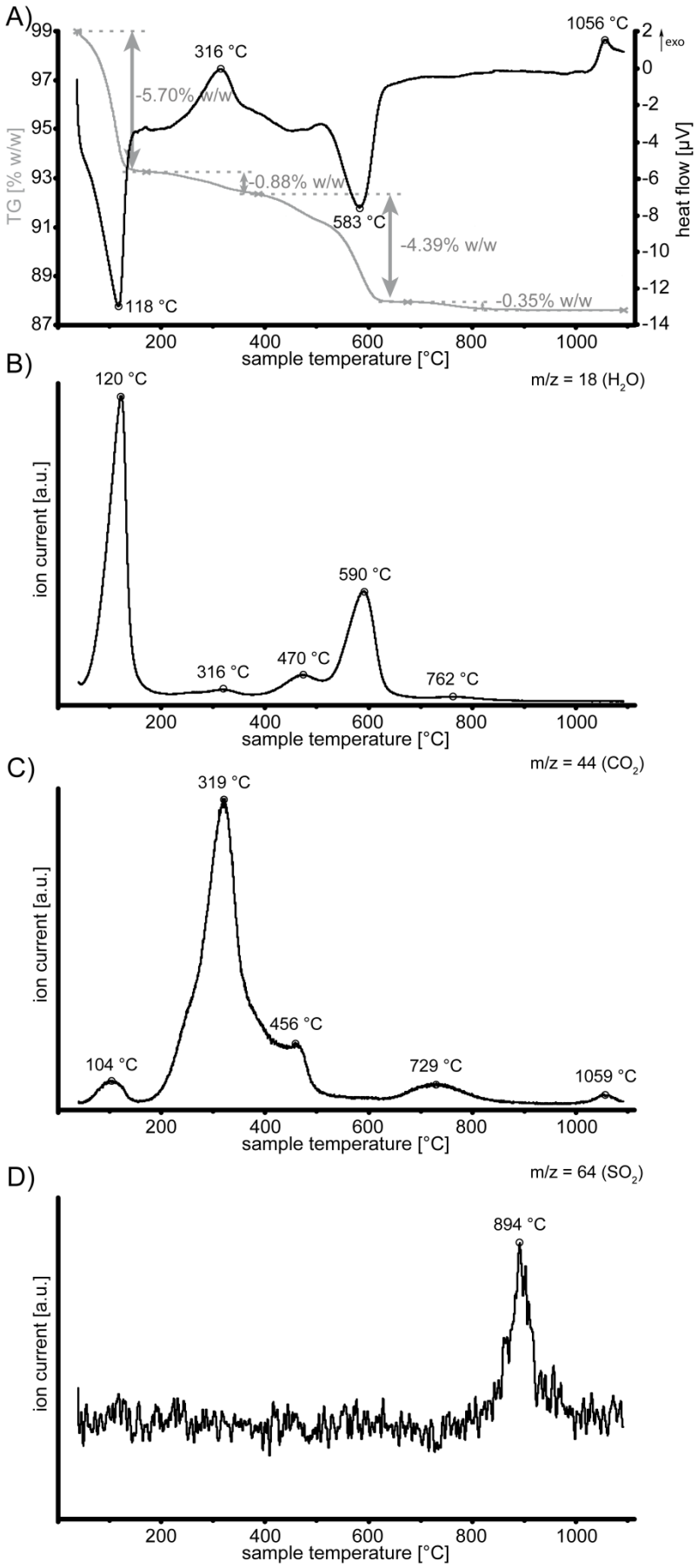

Figure 4.15. STA-MS curves of the rectorite <0.1 µm fraction. A) TG (grey) and DSC (heat flow, black) curve; B) Water ion current; C) CO_2 ion current; D) SO_2 ion current. TG starting value 98.94% w/w, sample amount 43 mg

$$\Delta m_{rectorite,DHX} = \frac{n \times M_{H_2O}}{M_{rectorite}} \times 100 = 4.79\%\ w/w \qquad 4.8$$

$\Delta m_{\text{rectorite, DHX}}$ …. Mass loss of rectorite during dehydroxylation [% w/w]

n …. Number of water molecules released during dehydroxylation [1]

M_{H_2O} …. Molar mass of water [18.016 g/mol]

$M_{\text{rectorite}}$ …. Molar mass of rectorite [376.37 g/mol]

Decomposition of the MS water curve revealed an ≈80% peak area below 600 °C, which corresponds to tv layers in rectorite (Drits *et al.*, 1998) and ≈20% above 600 °C that is attributable to cv layers (Figure 4.16). Decomposition was achieved by using the least number of symmetrical peaks to achieve the best possible fit.

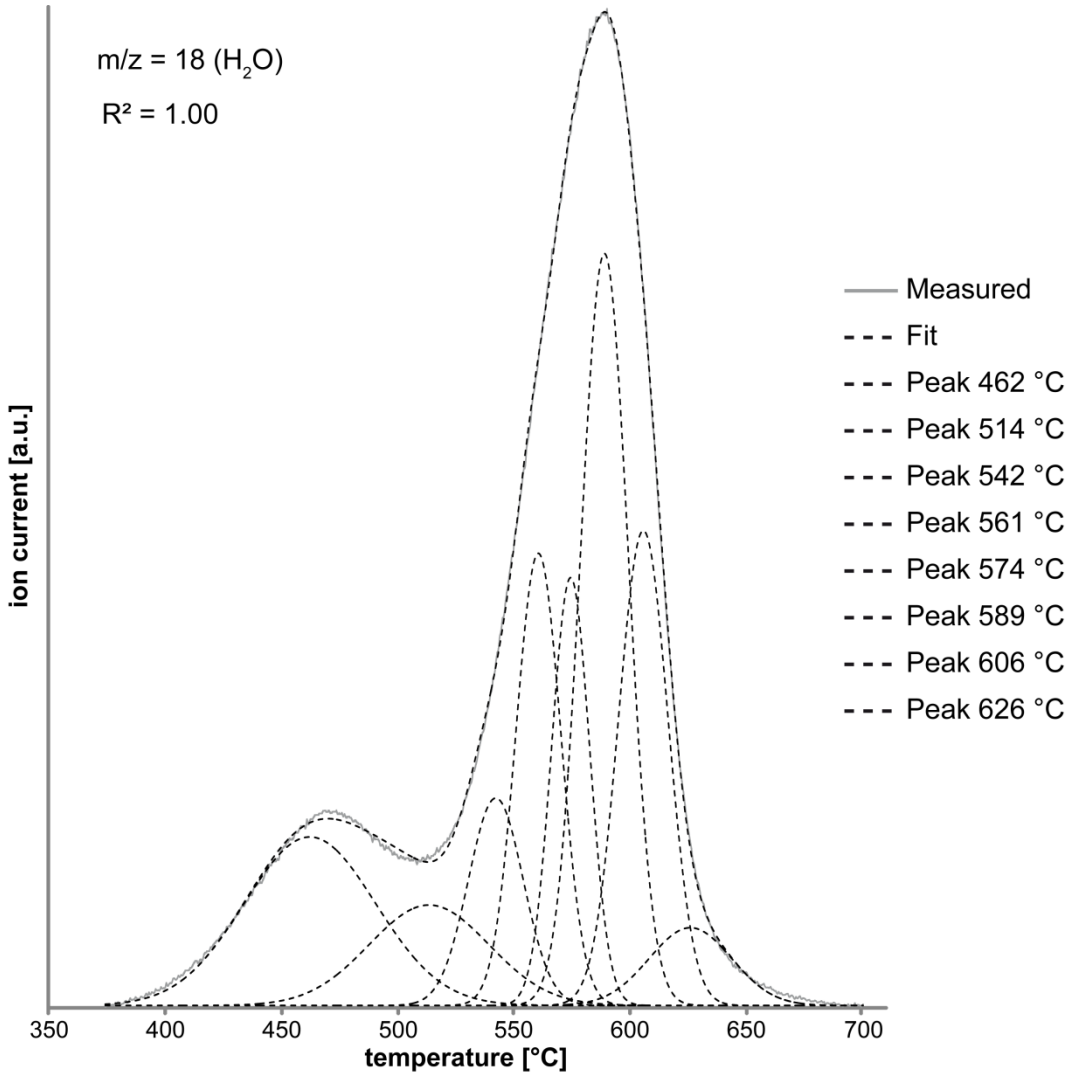

Figure 4.16. MS water curve of rectorite <0.1 µm fraction. Curves with maximum above 600 °C represent the amount of cv-layers.

The ratio of tv and cv layers determined from peak decomposition seems to be plausible for a regular interstratification of brammallite and beidellite and is according to that determined by the Rietveld method (≈12% cv layers) considering the error of both methods. Assuming beidellitic layers are mainly tv (Tsipursky & Drits, 1984; Lantenois *et al.*, 2008), the brammallitic layers should contain both tv and cv sites in the octahedral sheet. This is similar to that of Drits & Zviagina (2009) who described a prevalence of cv layers in usually tv-dominated illites and illite fundamental particles within I-S interstratifications when the Al content in the octahedral and tetrahedral sheets are >1.55 and >0.35 per F.U., respectively. Because these criteria fit well with the data obtained for the assumed brammallitic layers of Arkansas rectorite, the increased amount of cv´s in the brammallitic layers appears to be a realistic model. The existence of interstratified tv/cv mica is also in agreement with the tendency of Al-rich 1M cv illite to be more stable than 1M tv illite formed during low-temperature diagenesis or hydrothermal conditions (Drits & Zviagina, 2009).

4.1.3 "Sárospatakite"

XRD

Qualitative and quantitative phase analysis was undertaken using XRD and the Rietveld program BGMN to quantify the purity of the interstratification and to determine structural parameters, important for characterisation. The raw material was almost monomineralic, only containing some feldspar (1.9% w/w, Appendix xxv). To further enrich the interstratification, the <0.1 µm fraction was separated. A random powder XRD pattern as well as a pattern of the preferred oriented specimen is shown in Figure 4.17 and Figure 4.18, respectively in which no impurities could be identified.

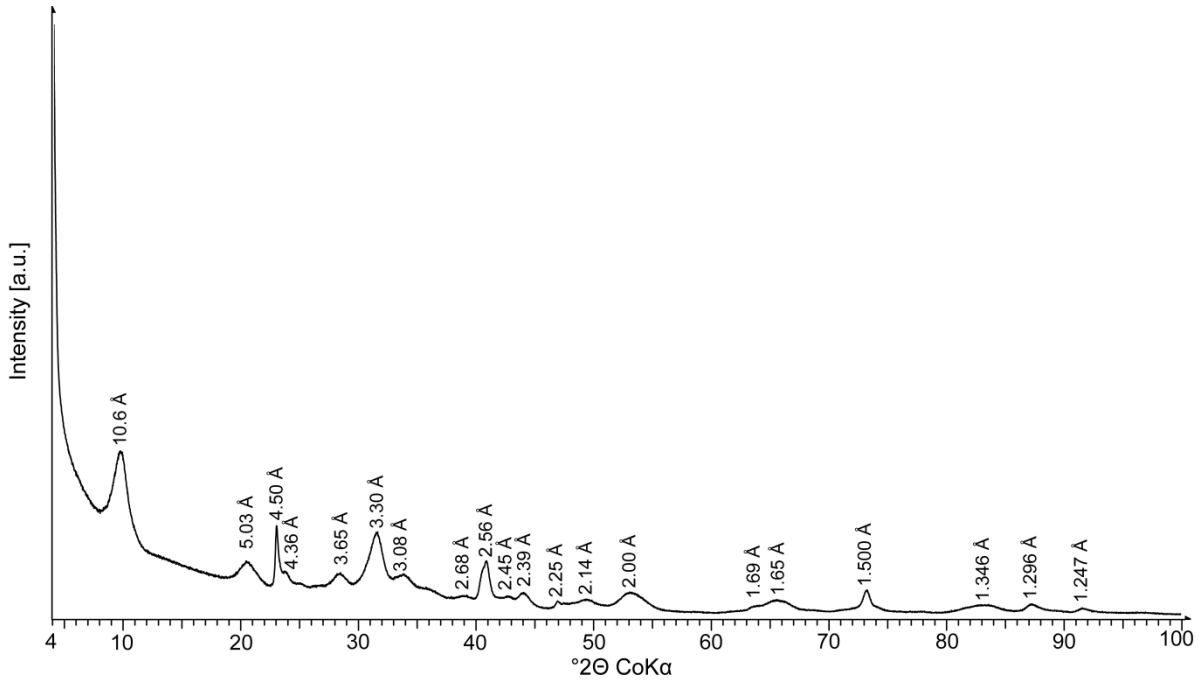

Figure 4.17. XRD pattern of a random powder of the "sárospatakite" <0.1 µm fraction. The sample is monomineralic. The d-values given belong to the I-S interstratification.

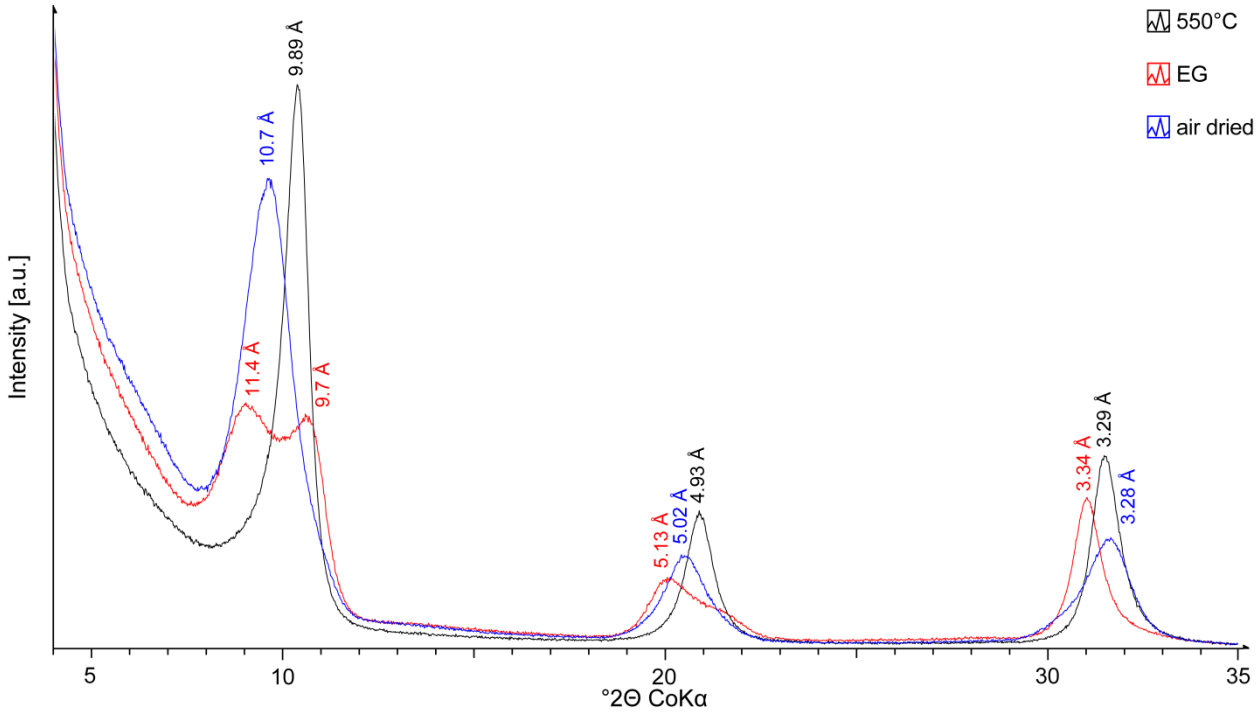

Figure 4.18. XRD patterns of preferred oriented specimens of the "sárospatakite" <0.1 µm fraction. The d-values given belong to the I-S interstratification.

Determination of the illite content in the I-S interstratification using Rietveld refinement and Moore & Reynolds method resulted in very similar illite contents considering the errors of both methods (Table 4.12). Hence, the interstratification can be stated as a *R*3 I(0.84)-S interstratification. This is according to Clauer *et al.* (1997) who investigated the smectite content as a function of the particle size and concluded that the average content of expandable layers varies between 11% and 18%, and increased with decreasing particle size. Ahn & Buseck (1990) concluded this interstratification also has 18% expandable layers whereas Ufer *et al.* (2012a,b) described it as an *R*3 ordered dioctahedral I(0.86)-S interstratification.

Table 4.12. Determination of the illite content in the I-S interstratification using Rietveld refinement of powdered and preferred oriented samples of the "sárospatakite" <0.1 µm fraction using BGMN program. Both, powder patterns as well as preferred oriented specimens were independently refined. Additionally, the method after Moore & Reynolds (1997) of simulated oriented patterns was applied.

Method used	**Rietveld refinement**			**Moore & Reynolds (1997)**
Sample	**Powdered**	**Preferred oriented**		**Preferred oriented**
Condition		**Air dried**	**Ethylene glycol saturated**	**Ethylene glycol saturated**
Illite content in I-S interstratification [%]	84	83	86	85

Using the Rietveld program BGMN (Bergmann *et al.*, 1998) and the structure models published by Ufer *et al.* (2012a,b), the structural parameters of the I-S interstratification were determined (Table 4.13). Only some of the refined parameters, important for structural characterisation of the interstratification,

are shown here (BGMN fits shown in the Appendix xxvi - Appendix xxviii). Results obtained from Rietveld refinement in this study are in agreement with that reported by Ufer *et al.* (2012b), differences are discussed.

The octahedral iron content of this I-S interstratification appear to be very low (0.03 per F.U.) and the K content for micaceous layers is calculated to be 0.75, indicating interlayer deficient layers (illitic). The stacking vector for cis-vacant layers reached the lower refinement limit of 0.26. Ufer *et al.* (2012b) calculated a value of 0.263 for this vector indicating a still plausible result. The intermediate p0 value of 0.57 determined indicates a medium disordered structure with a very low content of n×60° rotations and a higher content of n×120° rotational disordering. The content of cis-vacant layers is estimated to be about 46%, which indicates that assuming most of the smectitic layers are cv (according to Wolters & Emmerich, 2007; Wolters *et al.*, 2009; Emmerich, 2011), even the micaceous layers must contain a significant amount of cv layers. This is in agreement with Drits & Zviagina (2009) who described a prevalence of cv layers in usually tv dominated illite fundamental particles in I-S interstratifications when the Al content in the octahedral and tetrahedral sheets are >1.55 and >0.35 per F.U., respectively. The existence of a cv/tv interstratification of micaceous layers is additionally supported by the tendency of Al-rich 1M cv illite to be more stable than 1M tv illite formed during low-temperature diagenesis or hydrothermal conditions (Drits & Zviagina, 2009).

The Ca content of smectitic layers reached the upper refinement limit indicating high charged layers in contrast to Ufer et al (2012b) who calculated 0.1 (lower refinement limit). Although this value is inaccurate, according to Ufer *et al.* (2012b), the tendency of smectitic layers to be medium or high-charged layers is more realistic. Because the transition from smectite to illite is a continuous reaction (Rieder *et al.*, 1998; Emmerich *et al.*, 2009), both types of layers are very similar and differ only in small variations in layer charge (Ferrage *et al.*, 2007, Emmerich, 2011).

The calculated content of illitic layers (*wI*) is considered to be reliable (Table 4.12) and the *R*-value *R*3 is in accordance with the commonly used *R*-value for this material in the literature (e.g. Ufer *et al.* 2012b). The refined results obtained from preferred oriented samples (air dried and ethylene glycol saturated) are similar, but not identical. These show the limits of the models used which could be improved further. Nevertheless all refined results are plausible and not contradictory. The refined results obtained from a random powder pattern seems the more reliable, maybe due to the higher content of information about the interstratification included in the XRD pattern for regarding the 3D structure, in contrast to the one dimensional information given by the preferred oriented samples. However, some uncertainties remain because the refined *pIIII* values are slightly too high for the refined *wI* value considering the junction probability diagram of Bethke *et al.* (1986; see section 1.3). Although *pII* may vary within a small range (Bethke *et al.*, 1986), this indicates tendencies towards segregation of the micaceous units.

Table 4.13. Results of Rietveld refinement of the I-S interstratification from "sárospatakite" <0.1 µm fraction using BGMN program. Both, powder patterns as well as preferred oriented specimens were independently refined (Fits are given in the Appendix xxvi - Appendix xxviii). *σ* standard deviation, [1] minimum reached, [2] maximum reached, mpdo maximum possible degree of ordering

	"Sárospatakite" <0.1 µm fraction					
	powder		preferred oriented			
			untreated		glycolated	
	result	*σ*	result	*σ*	result	*σ*
***R*-values**						
*R*wp (%)	5.19		3.41		6.21	
*R*exp (%)	1.41		1.48		1.54	
Global parameters						
p(Fe)	0.0149	0.0057	0.1344	0.0021	0.2167	0.0027
p(K)	0.7499	0.0032	0.6[1]		0.6[1]	
Non-basal model						
a (Å)	5.19528	0.00055				
$-t_x$(cv)	0.26[1]					
$-t_x$(tv)	0.4352	0.0013				
p0	0.5739	0.0040				
p60120	0.4198	0.0078				
p60, *p180*, *p300*	0.0596	0.0012				
p120, *p240*	0.1236	0.0021				
*p*cv	0.4636	0.0044				
Basal model						
t_S(1w) (Å)	12.5658	0.0070	12.8426			
t_S(2w) (Å)	15.449	0.016	15.6823			
p(Ca)	0.3[2]		0.3[2]			
wI	0.8446	0.0011	0.8294	0.00047	0.85795	0.00070
pII (*R*1)	0.8161 (mpdo)	0.0015	0.79430 (mpdo)	0.00069	0.83444 (mpdo)	0.00094
pIII (*R*2)	0.7746 (mpdo)	0.0023	0.7410 (mpdo)	0.0011	0.8016 (mpdo)	0.0014
pIIII (*R*3)	0.8408	0.0026	0.77437	0.00079	0.7892	0.0016

XRF

Using XRF for bulk chemistry analysis, the water loss (105 °C) and the loss on ignition (LOI, 1050 °C), as well as major and trace elements were determined (Table 4.14). The main components are SiO_2 (49-50%), Al_2O_3 (26-27%), K_2O (7%), and MgO (3%) for both the bulk and the <0.1 µm fraction sample. The Si:Al molar ratio in the bulk sample is about 1.58 (SiO_2:Al_2O_3 weight ratio = 1.86), and of the <0.1 µm fraction about 1.59 (SiO_2:Al_2O_3 weight ratio = 1.88). These chemical data are in agreement with published results (e.g. Mátyás, 1972; Veblen *et al.*, 1990; Ferrari & Gualtieri, 2006).

The structural formula of this illite rich I-S interstratification is similar to that that reported by Veblen *et al.* (1990) and Ufer *et al.* (2012a,b):

$$(K_{1.31}Ca_{0.10}Na_{0.02})(Al_{3.36}Fe^{3+}_{0.02}Mg_{0.68})[(Si_{6.97}Al_{1.03})O_{20}|(OH)_4]\,.$$

The layer charges per 2 formula units of −1.03 for tetrahedral sheets and −0.50 for octahedral sheets is also similar to Ufer *et al.* (2012a) who calculated −1.18 for tetrahedral sheets and −0.40 for octahedral sheets. The octahedral Fe content of 0.02 per 2 F.U. is in satisfactory agreement with that calculated by Rietveld refinement (0.06 per 2 F.U).

Table 4.14. Bulk chemistry analyses of the "sárospatakite" bulk sample and the <0.1 µm fraction using XRF method. n.d. not detectable

Component/Element	Unit	"Sárospatakite" bulk sample	"Sárospatakite" <0.1 µm fraction
SiO_2	% w/w	49.71	49.16
TiO_2	% w/w	0.05	0.03
Al_2O_3	% w/w	26.66	26.18
Fe_2O_3	% w/w	0.16	0.22
MnO	% w/w	0.01	0.01
MgO	% w/w	2.95	3.23
CaO	% w/w	0.49	0.68
Na_2O	% w/w	0.04	0.07
K_2O	% w/w	7.38	7.24
P_2O_5	% w/w	0.02	0.02
LOI 1050 °C	% w/w	5.98	6.73
H_2O 105 °C	% w/w	3.88	4.93
Sum	% w/w	97.45	98.70
Ba	ppm	115	412
Ce	ppm	<24	0
Co	ppm	<5	<5
Cr	ppm	20	25
Cu	ppm	<50	<50
Ga	ppm	50	52
Hf	ppm	<5	5
La	ppm	<20	<20
Mo	ppm	4	6
Nb	ppm	8	7
Nd	ppm	<20	<20
Ni	ppm	n.d.	n.d.
Pb	ppm	6	7
Rb	ppm	511	515
Sc	ppm	12	17
Sr	ppm	24	25
Ta	ppm	<5	<5
U	ppm	n.d.	n.d.
V	ppm	57	64
W	ppm	<5	<5
Y	ppm	30	17
Zn	ppm	16	30
Zr	ppm	73	11

The structural formula is calculated assuming the presence of 84% micaceous layers and 16% smectitic layers as refined by BGMN program (Table 4.12, Table 4.13) and that all interlayer K^+ and some minor Ca^{2+}/Na^+ is present in the micaceous interlayers according to Brigatti & Guggenheim (2002), maybe due to locally expandable layers or widened edges. As muscovite/illite charges being mainly located in the tetrahedral sheet (Rieder *et al.*, 1998), the entire tetrahedral Al substituting Si is assumed to be located in the micaceous layers to minimise octahedral charge. Hence, the structural formula of the micaceous layers is

$$(K_{0.78}Ca_{0.01}Na_{0.01})(Al_{1.73}Fe^{3+}_{0.01}Mg_{0.29})[(Si_{3.39}Al_{0.61})O_{10}|(OH)_2]\,.$$

For the smectitic layers remains an average composition of

$$(Ca_{0.29})(Al_{1.41}Mg_{0.59})[(Si_{4.00})O_{10}|(OH)_2].$$

Layer charges of both layer types are 0.80 per F.U. for micaceous, and 0.58 per F.U. for smectitic layers, respectively. As most of the charge is located in the octahedral sheet, the smectitic layers can be considered to be montmorillonitic. This interpretation was demonstrated with a test according to Hofmann & Klemen (1950) and Greene-Kelly (1952) without Li saturation. The Na-saturated, 875 °C heated sample showed no swelling behaviour under ethylene glycol saturation indicating montmorillonitic instead of beidellitic layers (Appendix xxix).

For smectite being defined between 0.2 (low charged) and 0.6 (high charged) per F.U. (Guggenheim *et al.*, 2006; Emmerich *et al.*, 2009), the calculated value indicates high charged smectite layers (between 0.426-0.600 per F.U., Emmerich *et al.*, 2009). This is in agreement with the Rietveld refinement (0.3 Ca per F.U., upper limit reached). The non-swelling layers are interlayer deficient (0.81 per F.U., Rieder *et al.*, 1998) and K-dominated and best referred to as illitic, which appears plausible as compositions are similar to other interstratifications composed of illitic rather than muscovitic layers. The Rietveld refinement also indicates interlayer deficient mica (illitic) layers, however, with a lower K^+ content (0.75 per F.U.). The charges of both smectitic and illitic layers are quite close when calculated from the composition measured. Assuming no Ca^{2+}/Na^+ in the illitic layers would result in a lower layer charge of illitic layers and a higher layer charge of the smectitic layers. That both layer charges are close is considered to be plausible because the transition from high-charged smectite (≤ 0.6 per F.U.) to an illite with a low layer charge (≥ 0.6 per F.U.) occurs as a continuous change (Rieder *et al.*, 1998; Emmerich *et al.*, 2009). Decreasing the layer charge of illite decreases the attractive forces (Ferrage *et al.*, 2007) and thus increases expandability (Emmerich, 2011). A model of similar types of layers differing only by a small difference in the layer charge that determines the expandability and cation occupancy makes more sense than interstratifications of two very different layer types.

CEC

The CEC of the "sárospatakite" <0.1 µm fraction was determined by the Cu-trien method for a better characterisation of this long-range ordered I-S interstratification (Table 4.15). The high CEC value of 22 cmol(+)/kg of the present sample is due to the very high interstratification content including smectitic layers. Zumsteg & Puzrin (2012) and Zumsteg *et al.*, (2013a,b) determined the CEC of an highly illitic sample from the same location to be 9 cmol(+)/kg, but this bulk sample had only 64% w/w illite or I-S together with 27% w/w K-feldspar and 9% w/w quartz, which dramatically reduce the overall CEC value.

Table 4.15. CEC of the "Sárospatakite" <0.1 µm fraction, determined by the Cu-trien method.

Sample	CEC value [cmol(+)/kg]	Ø CEC [cmol(+)/kg]
"Sárospatakite" <0.1 µm	25.0 19.9	22

To verify the structural formula determined above, theoretical calculation of the CEC value were undertaken as shown in equation 4.9. As smectitic layers are assumed to provide the majority of exchangeable cations, the layer charge of the smectitic layers was used for CEC calculations. As the smectite content is about 16 mol-%, the layer charge must be multiplied with 0.16:

$$CEC = \frac{0.16 \times 0.59 \ {}^{mol(+)}/_{mol}}{387.86 \ {}^{g}/_{mol}} \times 100{,}000 = 24 \ \frac{cmol(+)}{kg} \ . \qquad 4.9$$

CEC …. Cation exchange capacity

ξ…. Layer charge [0.59 mol(+)/mol]

M …. Molar mass of the I-S interstratification [387.86 g/mol]

The calculated CEC value of 24 cmol(+)/kg is slightly higher than measured by Cu-trien method, which is typical for high charged layers (Steudel *et al.*, 2009).

STA-MS

The STA-MS curves recorded for the "sárospatakite" <0.1 µm fraction (Figure 4.19 A-D) show dehydration occurs at 119 °C, represented by a strong endothermic reaction and accompanied by a mass loss of 2.41% w/w (normalised 3.00% w/w) (Figure 4.19 A) with a discrete phase of water release (Figure 4.19 B, finished at 200 °C). The low mass loss during dehydration indicates only a minor amount of smectitic layers are present (Emmerich *et al.*, 2015). Dehydroxylation of 2:1 layers occurs in two separate steps each represented by distinct endothermic reactions accompanied by the release of water. First, trans-vacant layers dehydroxylate at ≈550 °C, accompanied with a mass loss of 3.07% w/w (normalised 3.21% w/w; Figure 4.19 A-B; Emmerich *et al.*, 2009). At ≈690 °C cv layers dehydroxylate with a mass loss of 1.52% w/w (normalised 1.64% w/w; Figure 4.19 A-B; Emmerich *et al.*, 2009). Very similar dehydroxylation temperatures were reported before by Kiss & Takáts (1963), however, Ferrari & Gualtieri (2006) and Gualtieri & Ferrari (2006) produced much higher dehydroxylation temperatures (813-823 °C and 933-943 °C) for these stages, probably reflecting the fast heating rate and different amount of sample used.

The small mass loss of 1.26% w/w (normalised 1.30% w/w) occurring between the dehydration and dehydroxylation of the trans-vacant layers, which is accompanied by some release of H_2O and a multiphase CO_2 peak observed in the MS curve (Figure 4.19 B-C), probably reflects either oxidation of organic molecules and/or decomposition of carbonates such as aragonite that is present as an impurity. The release of some water during oxidation of these impurities does slightly influence the trans/cis-vacancy determination artificially increasing the tv amount. The dehydroxylation occurs in two steps with peak maxima at ≈550 °C and ≈690 °C. The mass loss with respect to the dry solid weight of 4.84% w/w was higher than the stoichiometric value of 4.65% w/w (equation 4.10) because of the strong overlap of mass loss from impurities (300-600 °C) and the 2:1 tv layers dehydroxylation (400-600 °C). The small SO_2 loss at ≈878 °C (Figure 4.19 D) with negligible mass loss is attributed to the destruction of a sulphate phase, an impurity present in very low concentrations. The endothermic peak at 958 °C represents the structural breakdown of the 2:1 layers of "sárospatakite" and the exothermic peak at 1011 °C indicates recrystallisation.

$$\Delta m_{sárospatakite,DHX} = \frac{n \times M_{H_2O}}{M_{sárospatakite}} \times 100 = 4.65\%\ w/w \qquad 4.10$$

$\Delta m_{\text{sárospatakite, DHX}}$ …. Mass loss of "sárospatakite" during dehydroxylation [% w/w]

n …. Number of water molecules released during dehydroxylation [1]

M_{H_2O} …. Molar mass of water [18.016 g/mol]

$M_{\text{sárospatakite}}$ …. Molar mass of "sárospatakite" [387.77 g/mol]

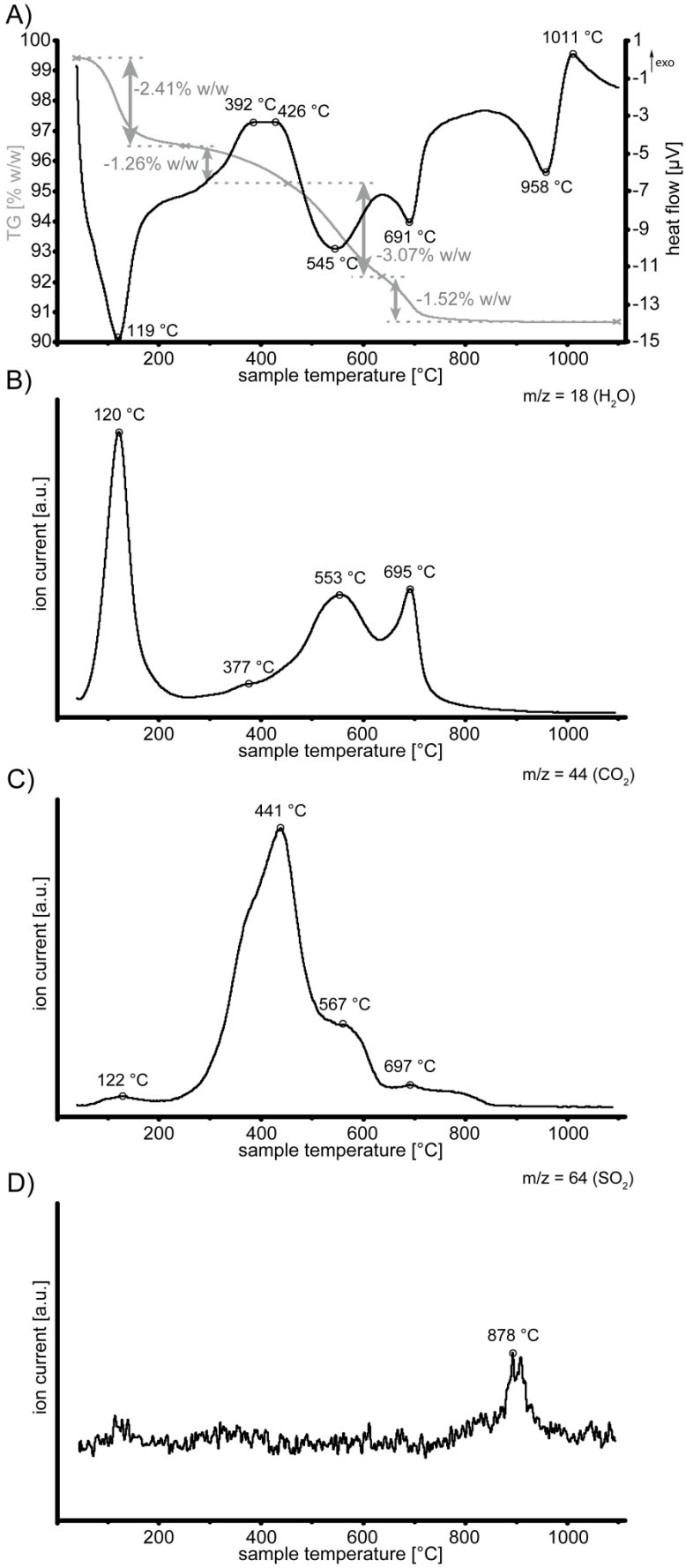

Figure 4.19. STA-MS curves of the "sárospatakite" <0.1 µm fraction. A) TG (grey) and DSC (heat flow, black) curve; B) Water ion current; C) CO_2 ion current; D) SO_2 ion current. TG starting value 99.40% w/w, sample amount 104.3 mg

Decomposition of the MS water curve revealed ≈57% peak area below 600 °C, which corresponds to tv layers in this I-S interstratification (Drits *et al.*, 1998) and ≈43% above 600 °C attributable to cv layers (Figure 4.20). This is in agreement with results obtained from Rietveld refinement (46% cv layers), considering the errors of both methods and thus, confirming the interpretation of cv containing illitic layers due to high tetrahedral and octahedral Al content according to Drits & Zviagina (2009). Ufer *et al.* (2012a,b) used Rietveld refinement and concluded the cv amount is about 53%, which is slightly higher than that calculated here.

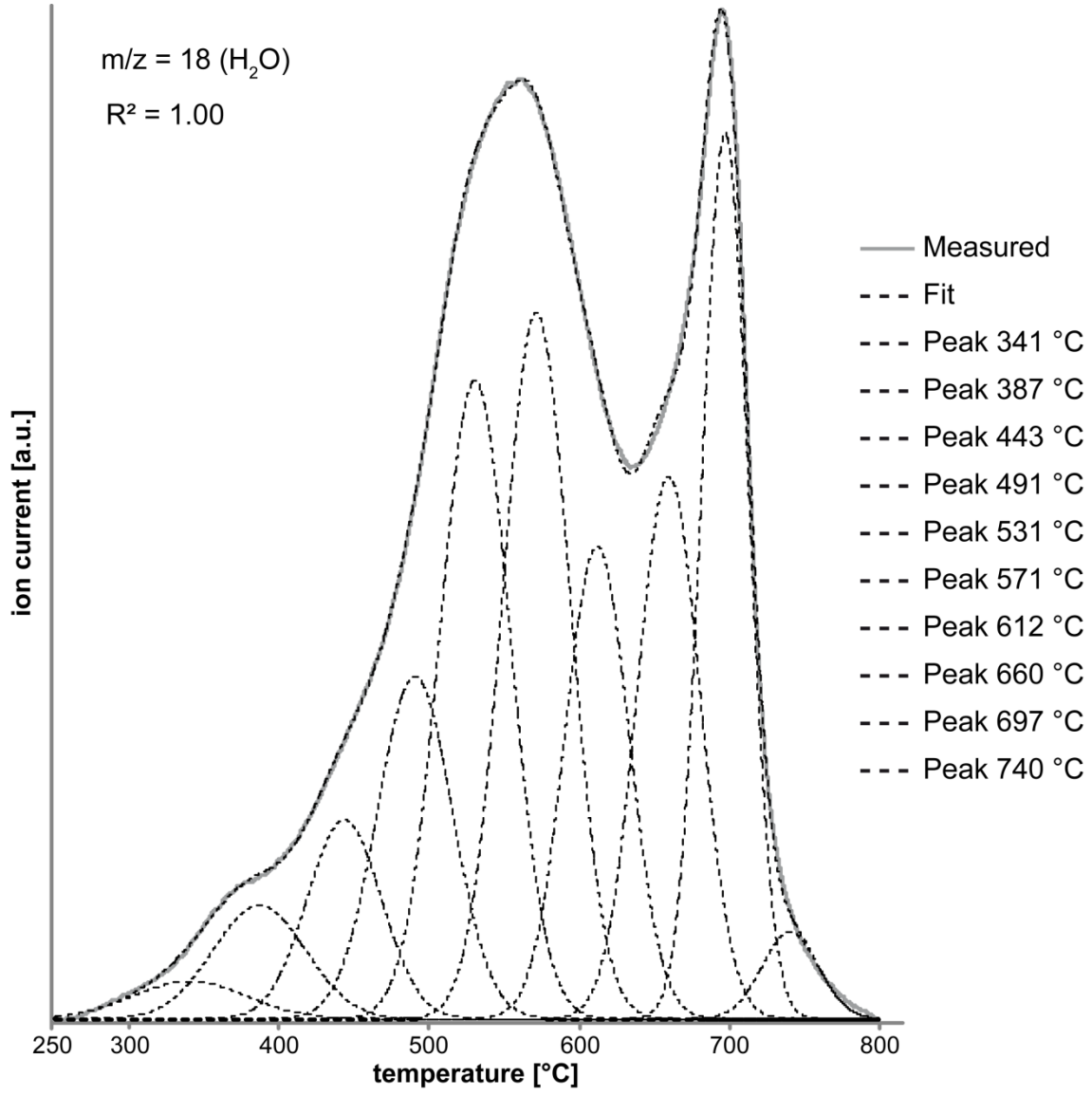

Figure 4.20. MS water curve of "sárospatakite" <0.1 µm fraction. Curves with maximum above 600 °C represent the amount of cv-layers.

4.1.4 $Al(OH)_3$ source

The $Al(OH)_3$ source was obtained from the clay mineral collection (Prof. M. Störr) of the Ernst-Moritz-Arndt-University Greifswald and occurred as a loose powder sample of unknown origin.

Considering Si:Al ratios of Friedland clay bulk material and <0.1 µm fraction, calculated from XRF results and measured by flame-AAS, a source of Al can be added to the clay to decrease the Si:Al ratio and reach the optimal value for GPs. $Al(OH)_3$ was found to be a successful candidate for its purity and high solubility in alkaline solution. The Al source used was characterised mineralogically by XRD and STA measurements.

XRD

The $Al(OH)_3$ was examined by XRD for identification of the mineral phases and to check the purity of the sample. In Figure 4.21 the XRD pattern is displayed showing a highly purified gibbsite (γ-$Al(OH)_3$) without any impurities of other $Al(OH)_3$ polymorphs like bayerite, doyleite, or nordstrandite or other contaminations. Heated to 1200 °C in a muffle oven, the gibbsite transforms to corundum (Figure 4.21).

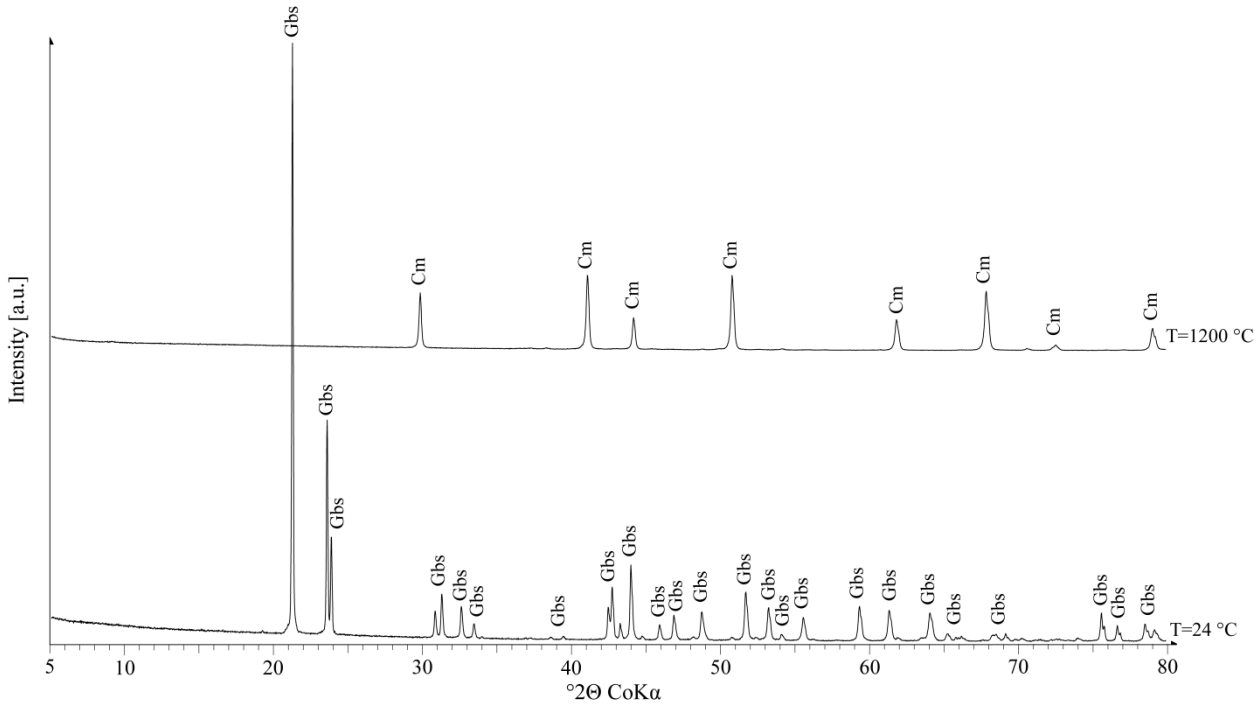

Figure 4.21. XRD pattern of a random powder of the $Al(OH)_3$ source (lower pattern). No other phases could be detected than gibbsite. Heated to 1200 °C, gibbsite transforms to corundum (upper pattern). Gbs: gibbsite, Cm: corundum

XRF

Using XRF for bulk chemistry analysis, the water loss (105 °C) and the loss on ignition (LOI, 1050 °C), as well as major and trace elements were determined (Table 4.16). The main component is Al_2O_3 (64%). Minor impurities of SiO_2 (0.26% w/w) and Na_2O (0.16% w/w) are present. The LOI of 33.78% w/w (normalised 34.47% w/w) is slightly lower than the theoretical value of 34.64% w/w (equation 4.2), caused by partial rehydration of the sample and the crucible when removed from the oven prior to weighting.

Table 4.16. Bulk chemistry analyses of the $Al(OH)_3$ source using XRF method. n.d. not detectable

Component/Element	Unit	Number
SiO_2	% w/w	0.26
TiO_2	% w/w	0.01
Al_2O_3	% w/w	63.53
Fe_2O_3	% w/w	0.07
MnO	% w/w	0.00
MgO	% w/w	n.d.
CaO	% w/w	0.01
Na_2O	% w/w	0.16
K_2O	% w/w	0.01
P_2O_5	% w/w	0.01
LOI 1050 °C	% w/w	33.78
H_2O 105 °C	% w/w	0.14
Sum	% w/w	97.99
Ba	ppm	21
Ce	ppm	<24
Co	ppm	<5
Cr	ppm	<5
Cu	ppm	<50
Ga	ppm	34
Hf	ppm	<5
La	ppm	<20
Mo	ppm	5
Nb	ppm	3
Nd	ppm	<20
Ni	ppm	n.d.
Pb	ppm	<5
Rb	ppm	n.d.
Sc	ppm	5
Sr	ppm	4
Ta	ppm	<5
U	ppm	n.d.
V	ppm	<12
W	ppm	<5
Y	ppm	<3
Zn	ppm	32
Zr	ppm	8

STA

The gibbsite (γ-$Al(OH)_3$) was examined by STA for identification of possible trace mineral phases not detectable by XRD and to examine the temperature behaviour of the sample. In Figure 4.22 the STA curves including TG and heat flow curve are displayed. Four endothermic reactions, each accompanied by a mass loss could be detected.

Dehydroxylation of gibbsite occurs between 220 °C and 350 °C resulting in evaporation of water and χ-Al_2O_3 as the remaining solid (see equation 4.11; Smykatz-Kloss, 1974; Kloprogge *et al.*, 2002; Pareira *et al.*, 2009).

$$2\,Al(OH)_3 \rightarrow\ 3\,H_2O\uparrow + Al_2O_3 \qquad 4.11$$

Assuming complete dehydroxylation of gibbsite, the mass loss can be calculated as:

$$\Delta m\ [\%\ w/w] = \frac{3 \times M_{H_2O}}{2 \times M_{Al(OH)_3}} \times 100\ . \qquad 4.12$$

Δm …. Mass loss of the sample [% w/w]

M_{H_2O} …. Molar mass of water [18.016 g/mol]

$M_{Al(OH)_3}$ …. Molar mass of $Al(OH)_3$ [78.0036 g/mol]

Hence, the theoretical value is Δm = 34.64% w/w, but the TG curve shows only 29.03% w/w mass loss, which is about 83.80% of the theoretical value. Some of the gibbsite therefore must be transformed into another phase, which is dehydroxylated at higher temperatures (533 °C, Figure 4.22). Depending on the crystal size and the heating conditions, gibbsite can transform into boehmite as an intermediate phase (Yusihami & Gilkes, 2012). The theoretical mass loss for boehmite during dehydroxylation (15.02% w/w using equation 4.6; molar mass of boehmite M_{AlOOH} = 59.988 g/mol) is almost exactly the mass loss of the 533 °C dehydroxylation peak (15.07% w/w, see equation 4.13).

$$\Delta m\ [\%\ w/w] = \frac{\Delta m_2}{\Delta m_1 + \Delta m_2} \times 100 \qquad 4.13$$

Δm_1 …. Mass loss of the sample below 440 °C [29.03% w/w]

Δm_2 …. Mass loss of the sample above 440 °C [5.15% w/w]

The overall mass loss of the sample is with 34.18% w/w, slightly lower than the calculated one (34.64% w/w), which is in good agreement considering possible minor amounts of impurities such as corundum and the analytical errors.

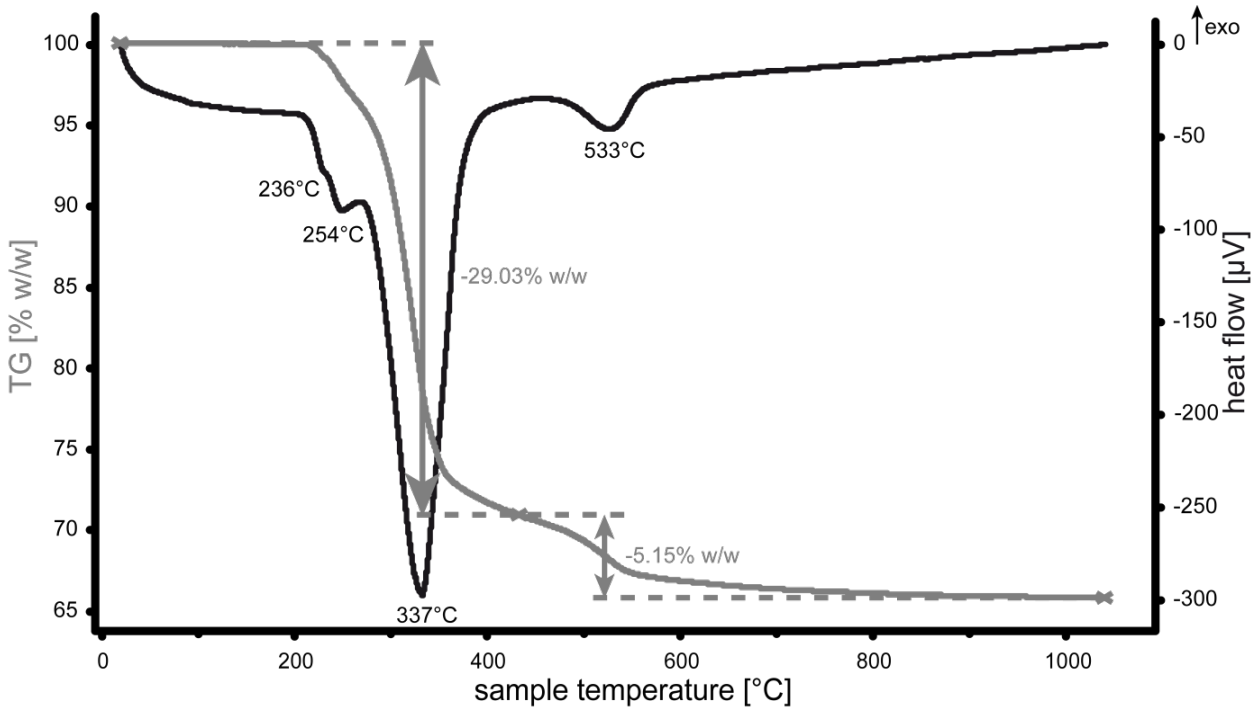

Figure 4.22. STA curves of a gibbsite sample showing the TG (grey) and heat flow (black) curves. Some of the gibbsite transforms into boehmite during dehydroxylation (230-400 °C) resulting in another endothermic peaks due to boehmite dehydroxylation around 530 °C. TG starting value 100% w/w, sample amount 100 mg

The actual chemical reaction taking place while heating can be described as:

$$92\ Al(OH)_3 \xrightarrow{337\ °C} 134\ H_2O \uparrow + 42\ Al_2O_3 + 8\ AlO(OH)$$

$$gibbsite\ (100\%) \xrightarrow{337\ °C} water\ (72\%) \uparrow + corundum\ (23\%) + boehmite\ (4\%) \qquad 4.14$$

$$8\ AlO(OH) \xrightarrow{533\ °C} 4\ H_2O \uparrow + 4\ Al_2O_3$$

$$boehmite\ (4\%) \xrightarrow{533\ °C} water\ (2\%) \uparrow + corundum\ (2\%)\ .$$

Gibbsite is mainly transformed into a corundum variety at low temperatures (<400 °C) and because Al_2O_3 is very thermally and chemically resistant, a significantly lower amount of Al would be available for the GP reaction (according to XRD results). Gibbsite as a raw material is therefore not thermally activated together with the clay sample, but instead is added to the heated clay product.

4.2 Activation of the clay

As many silicate minerals are build up of stable octahedral and tetrahedral coordination´s of Al and Si they generally show low reactivity and solubility at room temperature and pressure. Therefore in order to create reactive Al and Si species (see section 1.2), partial destruction of the network without full reorganisation of the structure appears to be the best way to form a metastable precursor for GP reactions. This type of activation is achieved in two different ways. Thermally, by dehydroxylation resulting in partial destruction of the clay mineral structure (due to removal of hydroxyl groups), and mechanical grinding that causes kinking and rupturing of the clay mineral particles, which increases the proportion of broken crystal edges where reactive Al and Si species are preferentially complexed and pass into solution.

Thermal heating causes dehydroxylation of clay minerals, which leads to reorganisation of the structure. At very high temperatures, a complete reorganisation or even recrystallisation takes place, resulting in even more stable phases, such as mullite or various types of spinel. Hence, a temperature window exists where dehydroxylation is almost complete, but recrystallisation has not yet occurred. Because of Na^+ in the clay acts as a flux, the range of the suitable temperature window may decrease.

Mechanical treatment of the clay mineral particles may also be a suitable activation method because high energy grinding is known to cause delamination, rupturing of layers and unit structures, and structural breakdown (Číčel & Kranz, 1981; Perrin-Sarazin *et al.*, 2009). Because the surface of clay mineral particles is covered with oxygen atoms, the majority of Al and Si is dissolved at crystal edges, where these Al and Si cations are exposed. At a later stage, amorphisation of the structure occurs, leading to Mg- and aluminosilicates (Perrin-Sarazin *et al.*, 2009; Yariv & Lapides, 2000). Hence, these mechanically-activated materials are considered suitable for a GP production because similar steps of change occur like structural breakdown and amorphisation.

Thermal and mechanical activation experiments were carried out with Friedland clay because this is the cheapest most abundant material used in this study and thus more economically suitable for GP production.

4.2.1 Thermal-activation

The temperature behaviour of Friedland clay was determined by a combination of in-situ and ex-situ measurements. The dehydration and dehydroxylation behaviour as well as the structural breakdown was investigated by STA-MS (see section 4.1.1) and TXRD analysis (both in-situ), while NMR spectroscopy (ex-situ) was used to further investigate the structural breakdown by determination and quantification of the amounts of 4-, 5-, and 6-fold coordinated Al.

Additionally, two separate ways of heating were tested. Heating clay in a laboratory oven (“static”) was used to investigate the structural breakdown and properties of the heated clay with ex-situ methods.

"Dynamic" heating was used to investigate whether or not different ways of heating require different heating conditions such as temperature and time. Additionally, this experiment was used to test the possibility of upscaling the laboratory conditions to industrial dimensions.

TXRD

TXRD measurements were carried out to investigate structural changes of the clay mineral phases with temperature. Both bulk samples as well as size fraction samples except for the <0.1 µm fraction were investigated (Figure 4.23 and Appendix xxx - Appendix xxxiii). TXRD measurements of size fraction samples were interpreted in Podlech (2013, unpublished). The major phases initially occurring in the samples including the I-S interstratification, white mica (grouped), kaolinite, chlorite, quartz, feldspar (grouped), siderite, and pyrite changed differently with increasing temperature, but almost all d-values of every single phase increased with increasing temperature due to volume expansion.

By heating from almost room temperature (30 °C) to 250 °C, dehydration of the expandable clay mineral layers (in this case smectite) occurs, as seen in STA-MS results. This results in lower d-spacings of the I-S interstratification by collapsing of the smectite layers, which can be seen as an increasing intensity of the (00l) reflections (i.e. d = 10 Å and d = 5 Å), now including the interstratification and white mica (Figure 4.23, Appendix xxxii - Appendix xxxiii). Additionally, all peaks belonging to quartz are shifted to higher d-values because α-quartz changes its lattice parameters and is transformed into β-quartz at 573 °C. By heating to 400 °C, siderite and pyrite intensities start to decrease (Figure 4.23, Appendix xxx). With further heating to 500 °C, the intensity of the 7 Å-peak and other peaks belonging to kaolinite (i.e. 3.58 Å) decrease slightly, indicating the beginning of kaolinite dehydroxylation (Figure 4.23, Appendix xxxi - Appendix xxxiii). The intensities of the 2:1 layer silicates reflections remain constant. If heated to 600/650 °C, dehydroxylation of kaolinite is almost complete, hence, only remnants of former kaolinite peaks are visible and the basal reflections of the 2:1 layer silicates now decrease in intensity, in agreement with He *et al.* (1995) and Emmerich (2011) who investigated that for illite and kaolinite (Figure 4.23, Appendix xxxi - Appendix xxxiii). Additionally, the α-to-β-quartz phase transition is completed and most intensities of chlorite reflections decrease according to Zhan & Guggenheim (1995). Siderite and pyrite are completely decomposed and transformed into hematite (Figure 4.23, Appendix xxx).

Heating the sample to 950/1000 °C leads to further decrease of the 2:1 layer silicate basal reflections and now, a strong reduction of the non-basal reflections too (i.e. d = 4.45 Å or d = 2.57 Å), indicating structural decomposition of these silicates (in agreement with STA-MS results and with, e.g., He *et al.*, 1995). The members of the feldspar groups, with changing d-values and intensity ratios show phase transformations, with decomposition in this temperature range resulting in a strong decrease in reflection intensities (Figure 4.23). Similarly, a new phase is created with a maximum reflection at d = 3.25 Å (corresponding to recrystallisation temperature of 955 °C as seen in STA-MS measurements).

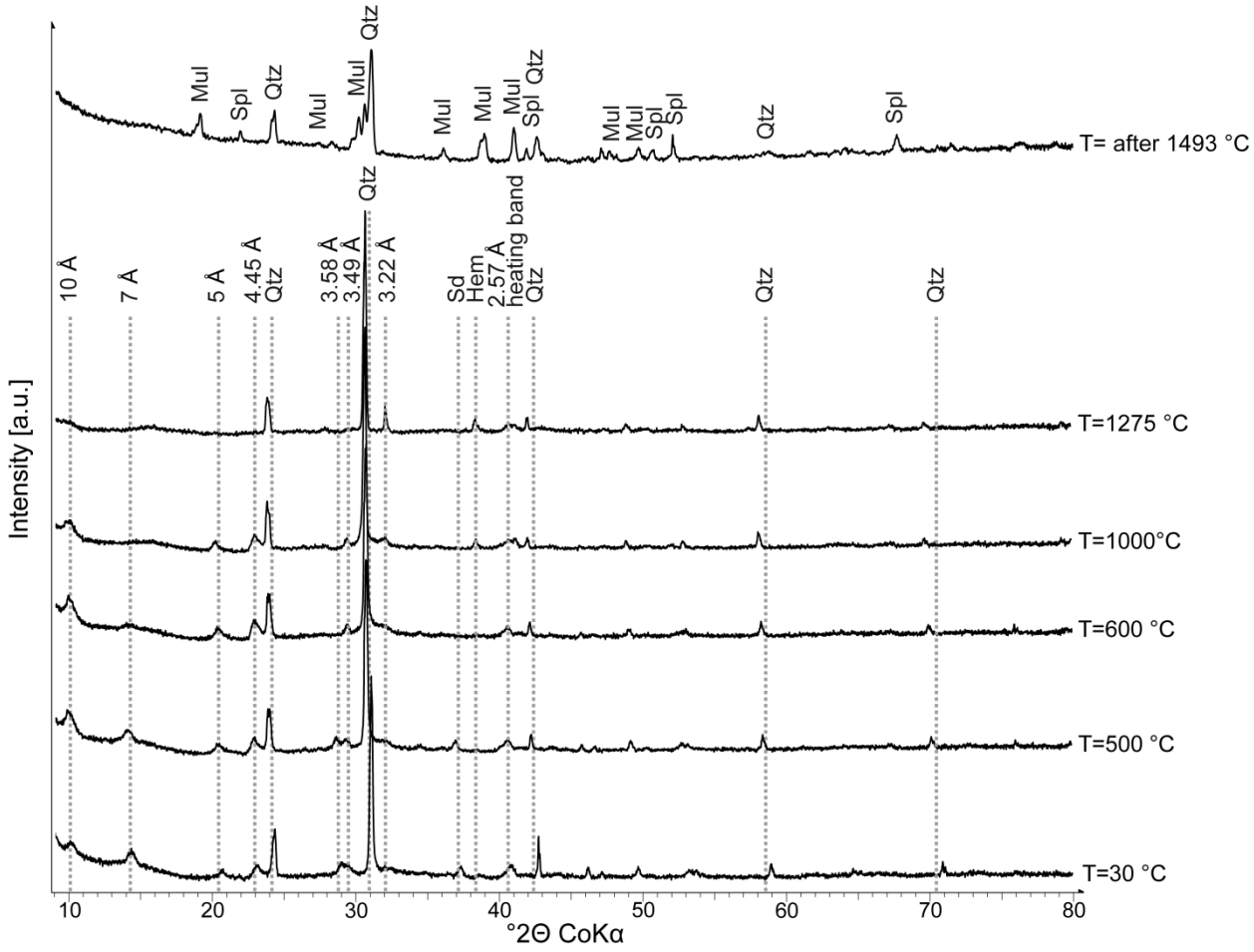

Figure 4.23. TXRD patterns of random powders of the Friedland clay bulk sample. The major phases are marked. In the case of overlapping of peaks (mostly for clay mineral phases), d-values were given. Qtz: quartz, Sd: siderite, Hem: hematite, Mul: mullite, Spl: spinel

Furthermore, former chlorite reflections disappear and some mineral phases partially melt, revealed by an amorphous hump and a decrease of most reflection intensities due to absorption of the X-rays (Figure 4.23). At a temperature of 1275 °C, the basal and non-basal reflections of the 2:1 layer silicates almost disappear and quartz reflection intensities decrease, indicating a complete structural decomposition of the 2:1 layer silicates and a transformation into an X-ray amorphous phase and recrystallisation to mullite, indicated by increasing reflection intensities (Figure 4.23). The new phase with a maximum reflection at d = 3.25 Å increase above 1000 °C. During rapid cooling of the sample this phase disappears, indicating a high-temperature phase that transforms while cooling. By rapid cooling, this phase transformation can be hindered and an intermediate structure between the high- and the low- temperature phase is preserved, resulting in an X-ray amorphous phase present at room temperature. Nevertheless, this phase could not be more precisely identified. At 1500 °C (Figure 4.23, the TXRD pattern was recorded after cooling), the newly formed phases mullite and at least two unspecified spinels are visible in addition to quartz according to Michael & McWhinnie (1989), representing the recrystallisation products of 2:1 layer silicates. Because recording this TXRD pattern after cooling, the α-phase of quartz is visible for the β-to-α transition is a displacive phase transition that cannot be prevented during cooling.

Results of both methods, STA-MS and TXRD, were consistent and complemented each other. However, some temperature differences between both methods are mainly caused by the following reasons: 1) TXRD patterns were recorded stepwise while STA-MS curves are recorded continuously. Although a certain reaction is finished by, e.g. 200 °C, the next TXRD pattern may be recorded at slightly higher temperatures, e.g. 250 °C. 2) STA-MS detects reactions, especially loss of gases such as water, while the sample is flushed by a dry gas promoting removal whereas TXRD samples are not surrounded by a flowing gas, but air that may result in heat and gas build-up delaying reactions. 3) The temperature measurement in the STA device shows a much higher precision and accuracy than TXRD temperature measurement. 4) In STA-MS a smaller amount of sample (100 mg) is used in a closed system while TXRD measures about one gram of sample in an open system resulting in a lower precision.

NMR

The coordination state of ^{27}Al in the activated clay was investigated as an important indicator for the reactivity (see section 1.2). Therefore, some Friedland clay bulk material was heated to 600°C, 650 °C, and 700-925 °C in steps of 25 °C for 2 hours and the cooled material powder was measured by NMR spectroscopy. In the untreated clay only 4- and 6-fold coordinated Al exists (Figure 4.9). The 4-fold coordinated Al ($Al^{[4]}$) is present in the tetrahedral sheet of the clay minerals, replacing Si, and in framework silicates like quartz and feldspars. In contrast, the 6-fold coordinated Al ($Al^{[6]}$) is exclusively located in the octahedral sheet of the clay minerals, often together with some Fe or Mg.

By heating the Friedland clay bulk sample, the $Al^{[6]}$ content decreases because dehydroxylation of the clay minerals results in a coordination change of the Al from $Al^{[6]}$ through $Al^{[5]}$ to $Al^{[4]}$ (see section 1.4). Hence, while the $Al^{[6]}$ content decreases, the content of $Al^{[5]}$ increases, reaching a maximum at about 650 °C (Figure 4.24-Figure 4.25; all NMR spectra and a list of fitted peaks are shown in the Appendix xxxiv - Appendix xxxviii). This is according to STA and TXRD results indicating that the dehydroxylation of clay minerals begins below 600°C that is mainly finished by 650 °C (highest degree of disorder) with subsequent reorganisation.

At the temperature where the major part of the clay is being dehydroxylated and thus is structurally most disordered, the NMR peak of $Al^{[4]}$ is broadest due to the overlap of many small peaks each reflecting slightly different O-Al-O distances. With increasing temperature, the dehydroxylation stage becomes complete and more stable and better ordered phases are formed that result in narrower peaks because most of the O-Al-O distances are very similar (Figure 4.25). As opposed to this, the $Al^{[6]}$ peak becomes broader because only a few 6-fold coordinated Al atoms are left with very different O-Al-O distances.

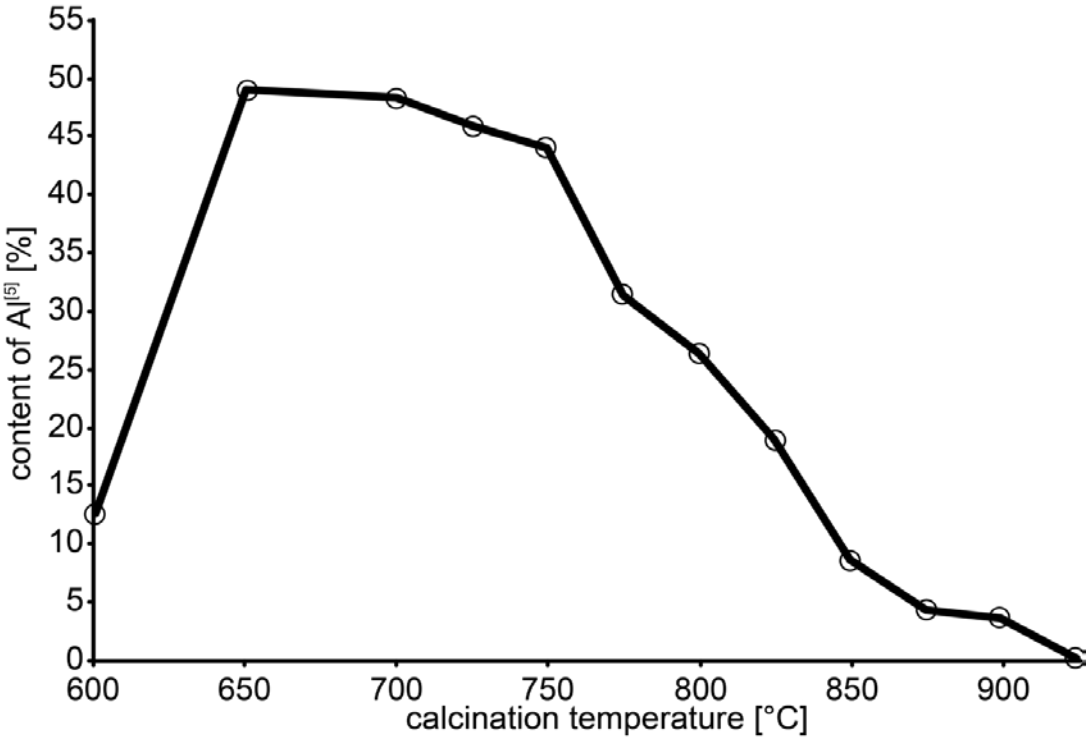

Figure 4.24. Plot of the $Al^{[5]}$ content of ^{27}Al, determined by NMR spectroscopy. The $Al^{[5]}$ content increases with increasing temperature, passing a maximum at about 650 °C with almost 50% $Al^{[5]}$, and then decreases until at 925 °C no $Al^{[5]}$ is left.

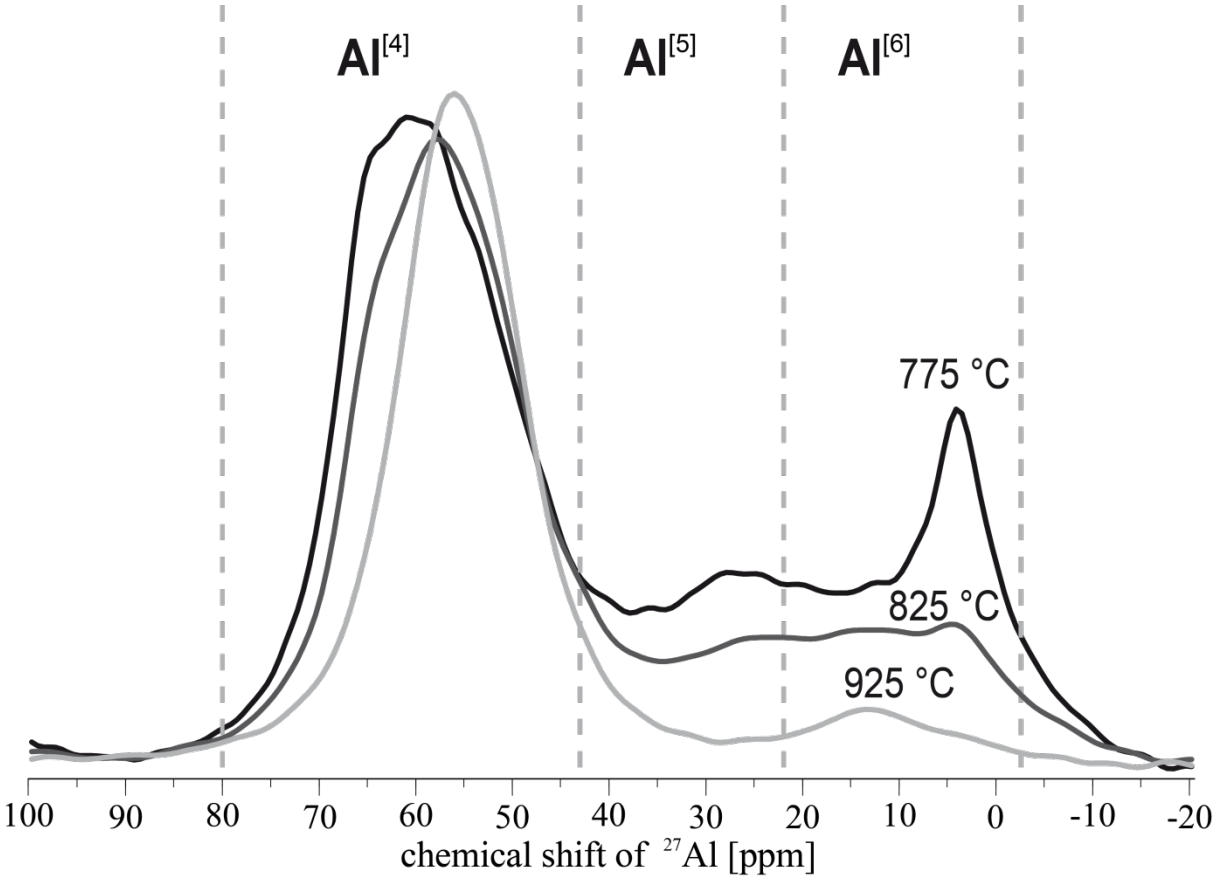

Figure 4.25. NMR spectra of ^{27}Al for the Friedland bulk sample heated to 775 °C, 825 °C, and 925 °C, respectively. The $Al^{[5]}$ content decreases above 775 °C with increasing temperature. The line widths of $Al^{[4]}$ get narrower because the structure gets ordered.

These results are in agreement with Buchwald *et al.* (2009), except they did not measure any $Al^{[5]}$ because of the device parameters applied. They, however, differ from that of Carroll *et al.* (2005) who investigated the amount of 4-, 5-, and 6-fold coordinated ^{27}Al in an illite-rich clay from Northern Hungary. Although they described it as illite, the high amount of Ca present indicates about 10-20% expandable/smectitic layers and thus, an illite-rich I-S instead of pure illite. Carroll *et al.* (2005) stated that the $Al^{[5]}$ content increases with increasing temperature, reaching a maximum at 900 °C and then strongly decreases, with no $Al^{[5]}$ at all at 1000 °C. But these data are not directly comparable because Carroll *et al.* (2005) studied almost pure I-S while the Friedland clay bulk sample comprises a complex mixture of many different non-clay and clay minerals most of them containing Al. Most of the clay minerals dehydroxylate at temperatures below 600 °C (Figure 4.7) resulting in a high $Al^{[5]}$ content at 650 °C, and dehydroxylation is close to completion. Because the $Al^{[5]}$ content is highest at/directly after dehydroxylation, it seems plausible that the maximum $Al^{[5]}$ content is reached at a temperature of 650 °C and decreases with further heating due to reorganization mechanisms. Carroll *et al.* (2005) used different device- and sample parameters such as heating rate and temperature (2 °C/min, maximum temperature for 2 hours), which make it hard to directly compare the data (according to Bertmer, 2013, pers. comm.). Additionally, because cations can have a strong effect on the formation of $Al^{[5]}$ and $Al^{[6]}$, the complex mixture of Friedland clay may behave differently from pure illite ("cation effect", Chan *et al.*, 1999). Different reactions of phases in the Friedland clay taking place simultaneously during heating may promote or inhibit the formation of $Al^{[5]}$ and $Al^{[6]}$, as known from other systems. In aluminoborate glasses for example, Na^+ ions inhibit the formation of $Al^{[5]}$ and $Al^{[6]}$, and almost exclusively $Al^{[4]}$ appears, whereas Ca^{2+} and Mg^{2+} ions promote the formation of $Al^{[5]}$ and $Al^{[6]}$ (Chan *et al.*, 1999).

"Static" heating

Figure 4.26 shows Friedland clay bulk material after heating in a muffle oven to different temperatures between 50 °C and 1100 °C. The native bluish-grey colour evolves over yellow-orange (450/550 °C), yellow-brown (650 °C), and orange (750-950 °C) to red-brown (1000/1100 °C). This illustrates the oxidation process of iron, present as siderite and pyrite in the sample (Fe^{2+}) that is oxidised to hematite (Fe^{3+}) at higher temperatures.

To evaluate the optimal heating temperature of Friedland clay, different heating temperatures were used. Because the content of 5-fold coordinated Al is highest at 650/700 °C, but dehydroxylation continues until about 900 °C, a temperature window between 775 °C and 925 °C was examined in detail. Samples within this window using 25 °C steps were produced and investigated by using dissolution experiments and compressive strength tests of the resultant GP binders.

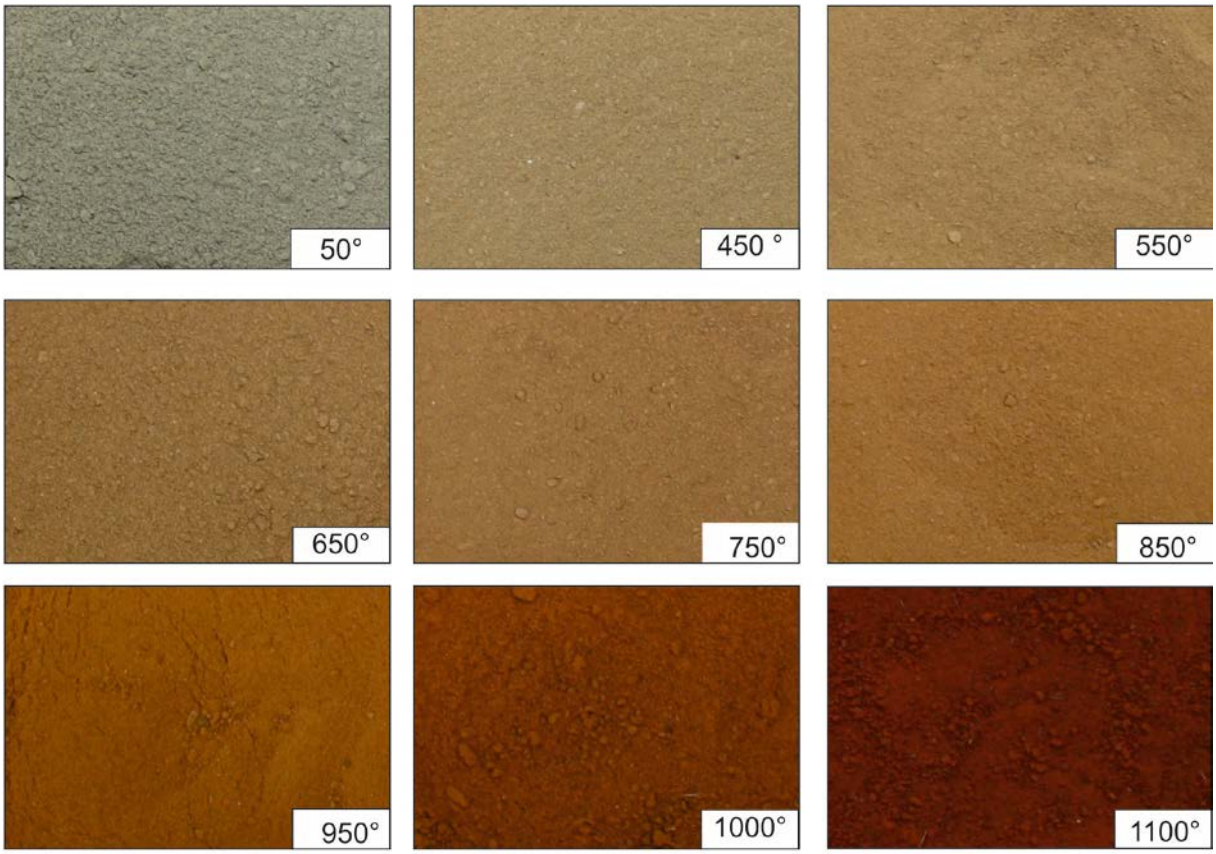

Figure 4.26. Photographs of Friedland clay bulk material heated to temperatures between 50 °C and 1100 °C illustrating the oxidation process of Fe by changing the colour of the material. (courtesy of J. Osterloh)

Dissolution experiments of Si and Al investigated by flame-AAS revealed that Si and Al content both decreased with increasing calcination temperature (Figure 4.27). The Si:Al ratio remained in a narrow range between 2.2 and 2.8, reaching an almost optimal value (1.6-2.2 according to Duxson *et al.*, 2007c; Bell *et al.*, 2009; Rickard, 2013, pers. comm.) between 825 °C and 875 °C, as shown by the grey shaded area in Figure 4.27. Decreasing Si concentrations and the Si:Al ratio data agree with Buchwald *et al.* (2009) who investigated the Si and Al solubility for Friedland clay heated to 550-950 °C (100 °C steps) in 10% Na(OH) solution at 60 °C with a solid:liquid ratio of 0.001. He *et al.* (1995) also investigated the solubility of pure illite heated to 650 °C, 790 °C, and 930 °C in 0.5 mol/L Na(OH) solution and found a Si:Al ratio between 1.8 and 2.4 without a distinct trend. However, increasing Al concentrations with increasing calcination temperature was reported by Buchwald *et al.* (2009). The decreasing Si and Al concentrations found in the present study indicate stoichiometric dissolution of clay minerals and are most likely caused by sintering effects of clay minerals taking place with increasing calcination temperature that result in larger sinter particles with a lower surface area to volume ratio. Hence, the inner volume of these particles is not or sparsely reached by the alkaline solution resulting in a lower Si and Al concentration. In order to test this hypothesis, A_S and pore size distribution measurements of the calcined Friedland clay samples were made.

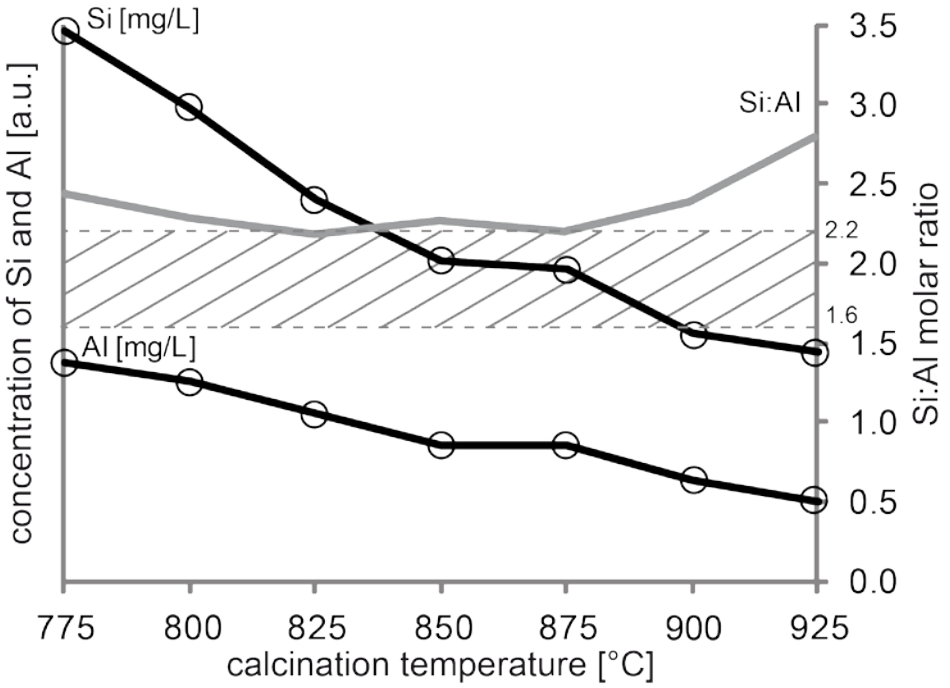

Figure 4.27. Si and Al concentration in a 5 mol/L K(OH) solution measured by flame-AAS. Si (black, upper curve) and Al (black, lower curve) concentrations decrease with increasing calcination temperature, while the Si:Al molar ratio (grey) slightly varies reaching almost the optimum (shaded area) between 825 °C and 875 °C.

These data show decreasing A_S values with increasing calcination temperature, demonstrating that larger sintered particles/agglomerates are formed during progressive heating (Figure 4.28; Table 4.17). The A_S value of untreated Friedland clay is 45.5 m²/g. These data confirm the study of He *et al.* (1995) who found similar changes in A_S values for a Silver Hill illite sample heated to 650 °C, 790 °C, and 930 °C.

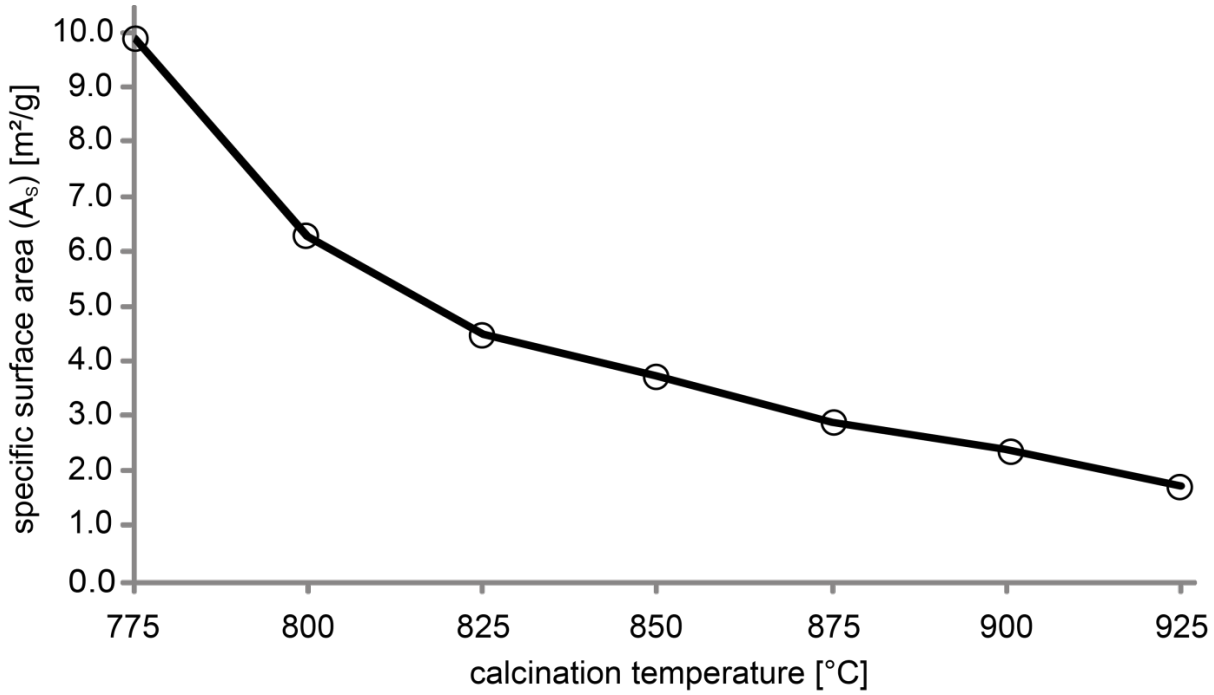

Figure 4.28. Specific surface area (A_S) measurements showing a decreasing A_S value with increasing calcination temperature indicating sintering processes. The A_S value of untreated Friedland clay is 45.5 m²/g.

The pore size distribution measurements also confirm this interpretation because the porosity of the sample strongly decreases from 6 volume-% (% V/V) to 1% V/V and small pores (micropores and mesopores) almost disappear to be replaced by macropores. During progressive heating, clay particles lose their adsorbed, intercalated, and structurally bound water, which contributes to sintering and formation of larger agglomerates. Hence, small pores (micro- and mesopores) present between flaky, rod-like, or curly shaped particles disappear, and larger pores (macropores) between freshly annealed grains now dominate. The porosity of the sintered clay thus generally decreases with increasing calcination temperature.

Table 4.17. A_S, pore size distribution and porosity of untreated and heated to 875 °C Friedland clay bulk sample.

Calcination temperature	A_S [m²/g]	Micropores (<20 Å) [% V/V]	Mesopores (20-500 Å) [% V/V]	Macropores (>500 Å) [% V/V]	Porosity [% V/V]
untreated	45.5	13.3	20.1	66.6	6.0
875 °C	2.9	0.3	3.8	95.9	1.0

"Dynamic" heating

"Static" heating in a muffle kiln is appropriate for laboratory applications, but is both time and energy consuming when used on an industrial scale. As only limited amounts of material can be heated simultaneously, large amounts of energy are rapidly wasted with heating and cooling between batch treatments. Using a higher sample amount would lead to better material-to-time and material-to-energy ratios, but also results in a high degree of heterogeneity where the outer material is heated longer and more intensive than inside the bulk sample. Homogenisation after the heating process is possible, but it is still a mix of different heat-treated clay which reduces the reactivity and worsens the properties of the final GP product. Hence, a stationary heating process is considered to be less suitable than a moving one, such as with a rotary oven where the sample can be continuously added, heated, and collected after passing predefined heating stages.

Preliminary tests using a small, laboratory, rotary oven with a 25 mm inner diameter steel tube, were hampered by problems with material sticking to the inner walls that resulted in over heating of this material and clogging of the steel tube. As a result, too many inert phases such as mullite formed. By using small amounts of sample due to the low inner diameter of the steel tube, the amount of overheated material was very high (about 12% w/w). Additionally, the material baked on the inner walls acted as an insulating material, which resulted in a much lower heating temperature of the material passing through (Figure 4.29). The material heat treated to 1100 °C for about 3 minutes still contained kaolinite in relatively high amounts. Usually, kaolinite dehydroxylates rapidly at temperatures between 500 °C and 650 °C. Using pre-dried material and increasing the angle of the steel tube reduced the clogging effect, but this procedure reduced the heating time required for good "metaclay" production.

As these issues could not be resolved at the laboratory scale, such a small rotary oven could not be effectively used to study the preparation of heated clay.

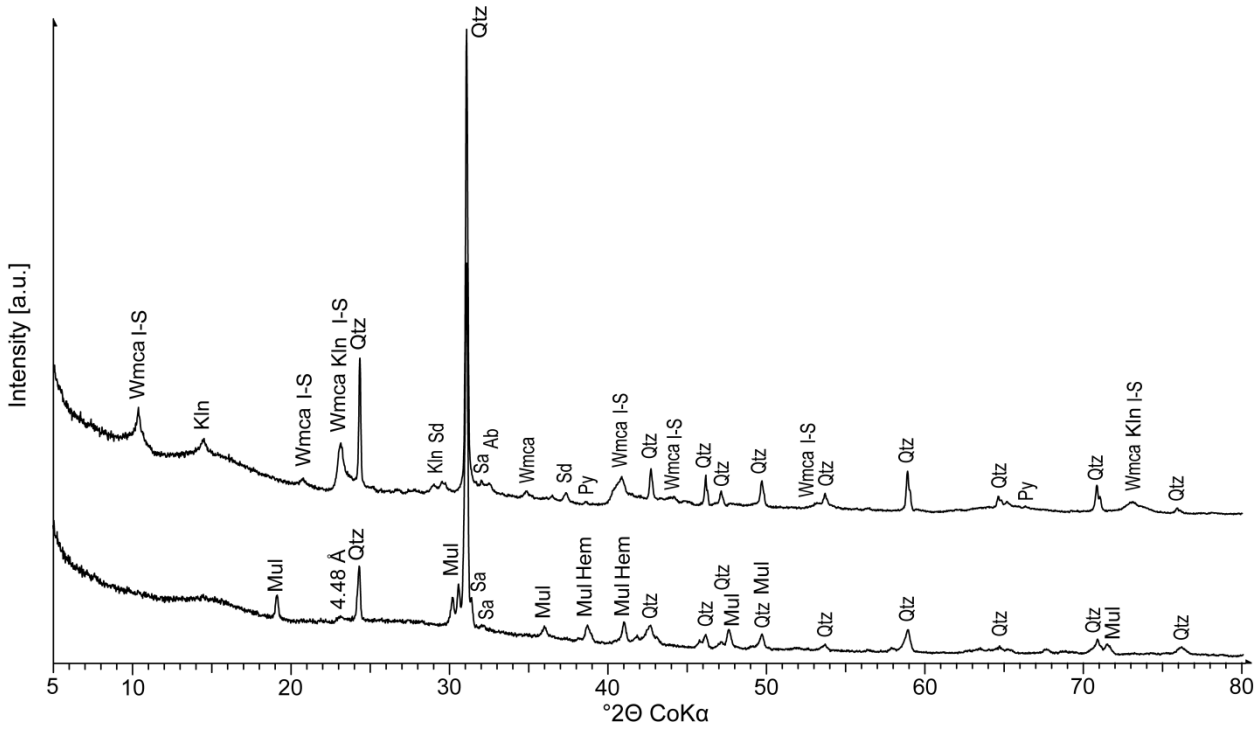

Figure 4.29. XRD patterns of random powders of the Friedland bulk sample, heated with a laboratory rotary oven. Some material stuck on the wall due to clogging effects and was thus heated to 1100 °C for a much longer period of time than conceived resulting in mullite formation (lower pattern). The material that flow through was treated with significantly lower temperatures due to isolating effects resulting in an insufficient heating process (upper pattern). The major phases are marked. Mul: mullite, Wmca: white mica, I-S: illite-smectite interstratification, Qtz: quartz, Sa: sanidine, Hem: hematite, Kln: kaolinite, Sd: siderite, Ab: albite, Py: pyrite

However, tests made using an industrial rotary oven (Figure 4.30) proved more successful. This study was contracted by the Mineralische Rohstoffmanagement GmbH – Blautonwerk Friedland (MRG).

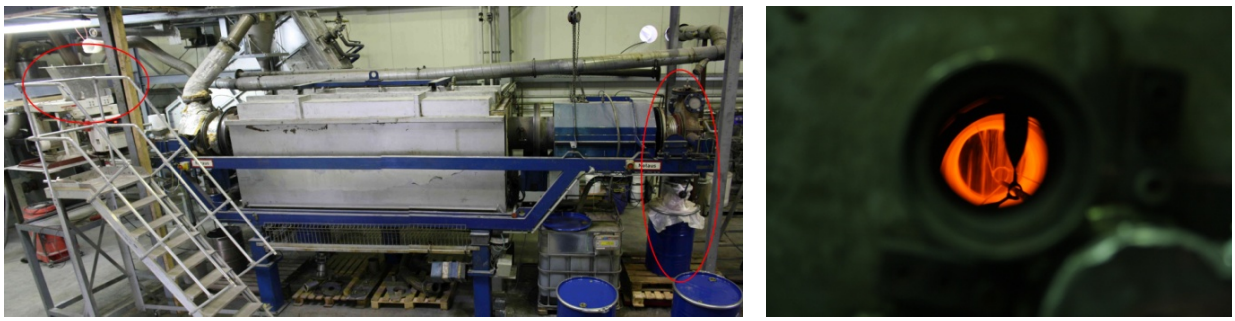

Figure 4.30. Left: Industrial rotary oven (side view). Left red mark: filler, right red mark: exit; Right: Look inside the oven with clay falling down.

An indirectly electrically heated rotary oven from IBU-tec AG, Germany, with 6 m in length with an inner diameter of 0.39 m was chosen. The oven had a heated length of 2.7 m with three indirectly selectable heating zones operating between 150 °C and 1200 °C. The temperature was measured by a thermocouple located directly in the heated clay material. The rotational speed can be chosen between 0 min^{-1} and 12 min^{-1}. About 30 kg/h Friedland clay bulk material was filled with the help of a batcher into

the oven, which had an inclination of 0.55 ° rotating around the own axis resulting in a constant movement of the clay through the oven. To increase the dwell time of the clay, shovels were installed in the oven. The experiment was operated in air atmosphere. The chosen process parameters influencing the heating time and temperature are given in Table 4.18.

Table 4.18. Process parameters of the industrial rotary oven varied for different precursor production.

Sample	Rotational speed [min^{-1}]	Calculated dwell time in heating zone [min]	Filling degree [% V/V]	Temperature [°C]
VP 1	3.5	40	5.7	825
VP 2	3.5	40	5.7	850
VP 3	3.5	40	5.7	875
VP 4	6	20	3.1	875
VP 5	9	13	2.1	875
VP 6	12	10	1.6	875

Only 1.8% w/w of the heated clay material was lost by dusting, showing the suitability of this kind of heating process and chosen parameters for clayey material. However, this value is still too high to use a directly heated rotary oven (flame directly blown into oven). Only indirectly heated ovens should be used. The samples VP 1-6 were analysed by XRD. XRD patterns of random powders and preferred oriented specimens show the destruction of kaolinite, siderite and pyrite for all samples indicating elevated temperatures of >500 °C (VP 1-6, Figure 4.31, Appendix xl - Appendix xlv). Ethylene glycol saturation of preferred oriented specimens showed no swelling behaviour of smectitic layers after heating indicating collapse of these layers (Appendix xl - Appendix xlv).

These results are consistent with STA and TXRD results, described before. VP 1 shows slightly lower integral intensities of all (00l) peaks of white mica and I-S, but the XRD pattern is still similar to that of untreated Friedland clay regarding white mica and I-S, except for I-S being dehydrated to produce a 10 Å reflection. Heating to higher temperatures (VP 2, 850 °C and VP 3, 875 °C) led to further destruction of clay mineral phases resulting in decreasing (00l) values. Diffraction patterns of VP 4 and VP 5 are quite similar to that of VP 3 showing the minimal peak intensity of all samples. VP 6 which shows an increasing intensity as well as decreasing FWHM-values, which is interpreted to reflect insufficient clay mineral destruction.

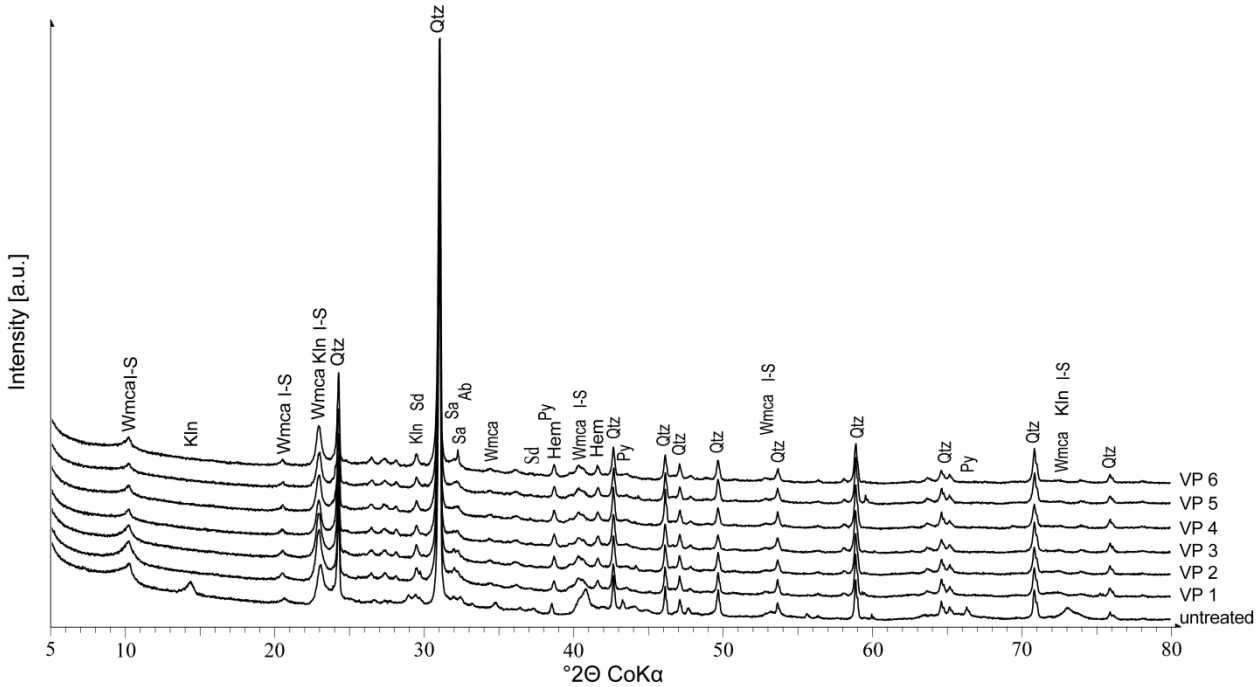

Figure 4.31. XRD patterns of random powders of the Friedland bulk sample, heated with an industrial rotary oven. The untreated material (lower pattern) was heated to 825 °C (VP 1), 850 °C (VP 2), and 875 °C (VP 3) for about 40 minutes. VP 4-6 material was heated to 875 °C for 12 minutes, 13 minutes, and 10 minutes, respectively. The major phases are marked. Wmca: white mica, I-S: illite-smectite interstratification, Kln: kaolinite, Qtz: quartz, Sd: siderite, Sa: sanidine, Ab: albite, Py: pyrite, Hem: hematite

Figure 4.32 shows the integral intensity of the 10 Å reflections (white mica + I-S) as well as the LOI values, determined for these samples. Because XRD data reveals the complete decomposition of kaolinite, siderite, and pyrite for all samples VP 1-6, differences in LOI values may reflect either rehydration or incomplete dehydroxylation of 2:1 layer silicates. All samples show a small LOI value different from zero indicating rehydroxylation or incomplete dehydroxylation. With increasing calcination temperature (VP 1-3), the LOI value decreases drastically from 1.00% w/w to 0.39% w/w indicating more complete dehydroxylation at 875 °C than at 825 °C. VP 4 (0.27% w/w) and VP 5 (0.26% w/w) show very similar values as VP 3 indicating a similar degree of dehydroxylation. The LOI value of VP 6 (0.35% w/w) is still low, but slightly increases again, indicating an incomplete state of dehydroxylation. The integral intensities of the 10 Å reflections of white mica and I-S show exactly same trend indicating most complete dehydroxylation at 875 °C for dwell times above 12 minutes (VP 3-5). Lower dwell times (VP 6) lead to incomplete dehydroxylation because evaporation of condensed water molecules requires some time. The water molecules need to find their way out of the structure which is even more complicated in the case of partially dehydroxylated structures, because dehydroxylation leads to partial destruction of the layer structure and water molecules need to diffuse through this 3D network.

These results are confirmed by STA-MS measurements of Friedland clay bulk sample heated with 10 K/min and 50 K/min showing that peak dehydroxylation of 2:1 layer silicates usually at 520 °C (10 K/min, Figure 4.7 A, B) is delayed by more than 50 °C to 574 °C when heated faster (50 K/min,

Appendix xlvi). Similar results were shown by rectorite STA-MS measurements (10 K/min and 50 K/min) indicating a delay of about 56 °C when using identical measurement parameters (Appendix xlvii). This effect is present because the rate of water loss does not keep up with the increase in temperature due to time consuming diffusion of water molecules through the disordered structure. Hence, this time delay requires higher temperature to achieve the same state of dehydroxylation.

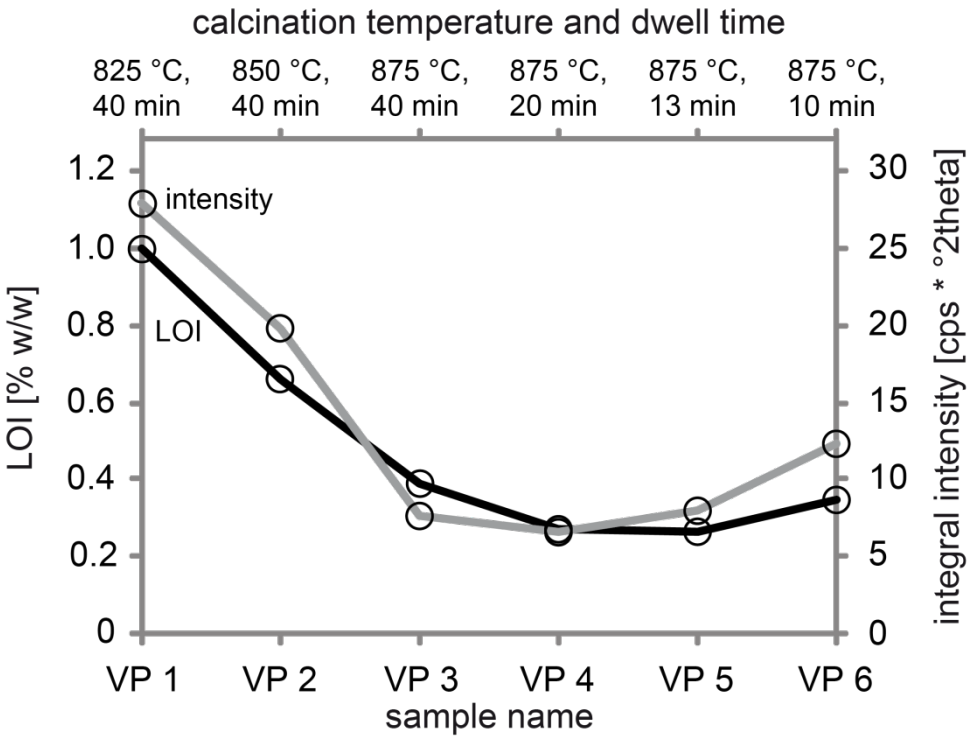

Figure 4.32. LOI values (black line) and integral intensities of the 10 Å reflection belonging to white mica and I-S interstratification (grey line) as a proxy for the degree of structural decomposition.

Both values are found to be suitable as a proxy for the dehydroxylation of 2:1 layer silicates, when plotted against each other have a correlation coefficient *r* of 0.972. Both values are easy to measure and these results fit well with TXRD and STA results.

Sample VP 4 was chosen to measure the A_S and the amount of $Al^{[5]}$ to compare it with clay heated at the same temperature in the laboratory muffle oven. Table 4.19 shows A_S, pore size distribution, porosity values, and amount of $Al^{[5]}$ of the VP 4 sample compared to untreated Friedland clay and clay heated to 875 °C in a laboratory muffle oven. A_S and pore size distribution values of the VP 4 sample fit very well with clay heated to 875 °C in the muffle oven. The A_S is almost identical while pore size distribution revealed a slightly lower amount of mesopores than clay heated in the muffle oven. The porosity of VP 4 is slightly higher, maybe due to a slightly lower degree of sintering due to dynamic mixing effects in the rotary oven. The amount of $Al^{[5]}$ is significantly higher in the VP 4 sample, presumable due to a faster heating and cooling rate that prevents the structure from reorganising into the more stable $Al^{[4]}$ state. However, flame-AAS measurements made for the VP 4 sample revealed about 10% w/w less Si and Al dissolved than in the 875 °C heated muffle oven sample.

Table 4.19. A_S, pore size distribution and porosity of the VP 4 sample compared to that of untreated Friedland clay and clay heated to 875 °C in a laboratory muffle oven.

Sample	A_S [m²/g]	Micropores (<20 Å) [% V/V]	Mesopores (20-500 Å) [% V/V]	Macropores (>500 Å) [% V/V]	Porosity [% V/V]	$Al^{[5]} : Al^{[4,5,6]}$ [%]
untreated	45.5	13.3	20.1	66.6	6.0	0
875 °C	2.9	0.3	3.8	95.9	1.0	4
VP 4 (875 °C)	3.0	0.3	0.6	99.1	1.5	25

These results indicate that clay heated to 875 °C for at least 13 minutes should be suitable for GP production (VP 3-5). Clay heated to lower temperatures (e.g. 850 °C) may also be suitable, but requires heating for a longer period of time than just 40 minutes (VP 2). Clay heated at even lower temperatures (825 °C, VP 1) or heated to 875 °C for a too short period of time (VP 6) are considered not suitable for GP production due to insufficient dehydroxylation. Overall these results show that the industrial rotary oven is highly suitable for the dehydroxylation of clayey materials and is relatively fast and cheap if applied on a large scale. The clogging effects, already described for the laboratory rotary oven are negligible because the adhering layer is limited to several millimetres or centimetres. This layer strongly influences the material flowing through a small steel tube of 2.5 cm (laboratory oven), but is negligible for a diameter of 39 cm (industrial oven).

The heating parameters determined for the industrial rotary oven should be verified using other rotary ovens to evaluate the influence of each device on the optimal heating temperature and dwell time. A temperature higher than 875 °C and a lower dwell time as used for industrial flash heating of vermiculites or perlites (e.g. 900-1000 °C for a few seconds or minutes; Hindman, 2006; Hillier *et al.*, 2013) could be investigated as an alternative way of heating.

pH value of heated clay

During the calcination of clay, some of the non-layer silicate mineral phases such as carbonates, sulphates, or sulphides are oxidised forming metal oxides. Dehydroxylation of clay minerals also leads to increasing amounts of metal oxides in their former octahedral sheet by forming Al-O, Fe-O, or Mg-O bonds. If placed into water, these metal oxides form hydroxides by hydrolysis and interlayer cations are exchanged by H^+ (Kaufhold *et al.*, 2008), both increasing the pH value of the solution/suspension. Hence, increasing the calcination temperature of Friedland clay should lead to increasing pH values which could be used as a proxy for monitoring the optimum degree of calcination. Kaufhold *et al.* (2008) investigated the pH of 2% w/w aqueous bentonite suspensions and found that traces of carbonates as well as hydrolysis of clay minerals and their interlayer cations such as Na^+ both increase the pH of the suspension. Higher solid:liquid weight ratios were found to result in a pH value depending more on

interlayer cations than on carbonates which are more important at low solid:liquid weight ratios (≤2% w/w). In the present study, a solid:liquid weight ratio of 100% w/w was used.

Siderite and pyrite in Friedland clay (and others) are fully oxidised up to 700 °C (Smykatz-Kloss, 1974; Emmerich, 2011) and therefore increasing the pH value of all samples compared to the untreated clay, but do not contribute to relative changes between samples calcined at 775-925 °C. This extends to the hydrolysis of interlayer cations.

Although dehydroxylation of clay mineral phases is almost finished at 600 °C, minor amounts of water are still released, indicating an ongoing reaction (Figure 4.7 B, F). Hence, metal oxide bonds formed by dehydroxylation of clay minerals additionally influence the pH value of the calcined samples until dehydroxylation is entirely completed (850-900 °C, according to STA results).

Gypsum that is present in the bulk sample with 1.2% w/w transforms into anhydrite and later into CaO in an oxidative atmosphere (equation 4.15 - 4.16). Because decomposition of these minerals occurs in a temperature range between 850 °C and 1000/1100 °C (Figure 4.7 D, H, equation 4.16 - 4.17) and therefore are active reactions in the temperature range used for calcination of clays, they may influence the pH value of samples heated between 775-925 °C relative to each other.

$$Ca(SO_4) * 2H_2O \rightarrow Ca(SO_4) + 2\,H_2O \uparrow$$
$$gypsum \rightarrow anhydrite + water \uparrow \quad (4.15)$$

$$Ca(SO_4) \rightarrow CaO + SO_3 \uparrow$$
$$anhydrite \rightarrow calcium\ oxide + sulfur\ trioxide \uparrow \quad (4.16)$$

$$2SO_3 \rightarrow 2SO_2 + O_2$$
$$sulfur\ trioxide \rightarrow sulfur\ dioxide + oxygen \quad (4.17)$$

The newly formed CaO reacts with water forming $Ca(OH)_2$ while increasing the pH value (equation 4.18).

$$CaO + H_2O \rightarrow Ca(OH)_2$$
$$calcium\ oxide + water \rightarrow calcium\ hydroxide \quad (4.18)$$

The untreated Friedland clay bulk sample as well as the clay previously heated between 775 °C and 925 °C in steps of 25 °C and investigated by NMR spectroscopy, flame AAS measurements, and determination of the A_S were monitored for pH after adding water (100% w/w suspension; Figure 4.33; Figure 4.34). The first pH value was measured after 20 min when pH stabilised (amongst others caused by the pH electrode). The pH value increased with increasing calcination temperature (step 1), whereas pH values of clay heated to 850-900 °C showed identical values (7.51-7.55) considering analytical errors

(step 2, Figure 4.33). These results confirm preliminary considerations indicating the presence of metal oxides increasing the pH value. With increasing temperature, clay minerals are dehydroxylated resulting in increasing pH values (step 1). According to STA measurements (Figure 4.7 A-D), dehydroxylation is completed in the temperature range between 850-900 °C and no oxidation reactions occur resulting in a constant pH value (step 2). Further increasing the temperature leads to oxidation of anhydrite as indicated by STA-MS (Figure 4.7 D) leading to further increasing pH values (925 °C, step 3). Hence, the pH value can be used as a proxy to investigate the degree of dehydroxylation if no other oxidation reactions occur in this temperature range superimposing this effect.

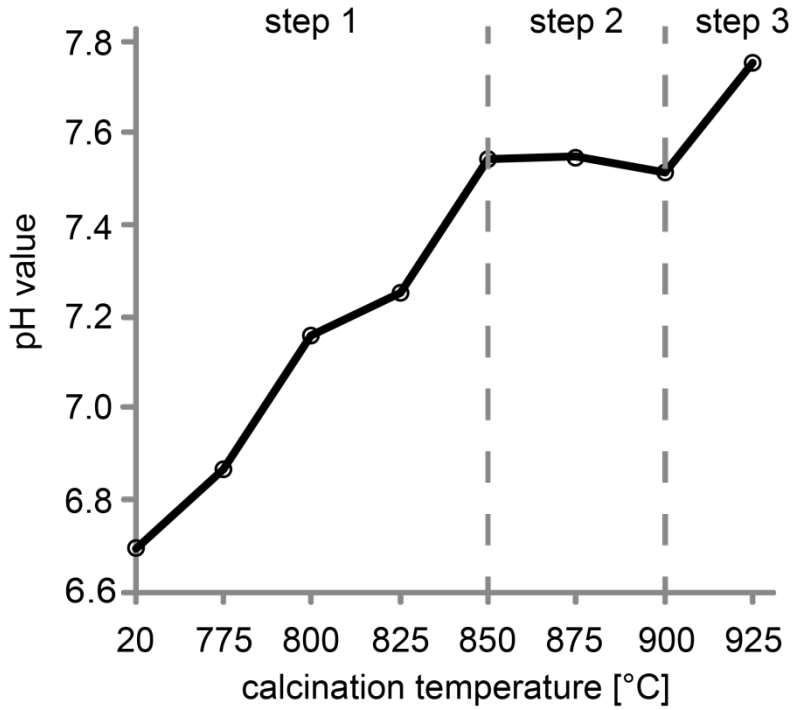

Figure 4.33. pH values of untreated Friedland clay (20 °C), and clays heated to 775-925 °C in steps of 25 °C mixed with water with a weight ratio of 1. Measurements were made after 20 min when pH value stabilised.

In Figure 4.34 the pH values are shown as a function of time, measured after 20 min, 80 min, and 140 min. The pH values of all heated samples were higher at any time (6.9-7.8) than that of untreated Friedland clay (6.7-6.8), indicating the presence of metal oxides as explained before. Considering analytical errors, the pH value of untreated clay is constant with time indicating no presence of reactive metal oxides, whereas the pH of clay heated varies with time. The pH of clay heated to 775-825 °C increases significantly with time, whereas the pH of clay heated to 875-925 °C decreases with time, and the pH of 850 °C heated clay is first constant and then decreases after 80 minutes. The increasing pH of clay heated to 775-825 °C with time can be attributed to the slow formation of $Ca(OH)_2$ because the sulphate phases are only partially decomposed and minor hydrolysis of the clay mineral and interlayer cations. Hence, more time is needed for complete decomposition. With increasing calcination temperature (850-925 °C), pH decreases with time because decomposition of sulphates was more complete and more CaO reacted within the first 20 minutes increasing the pH. The decreasing of the pH value with time is assumed to be caused by rehydroxylation as dehydroxylated clay minerals have the

ability to reincorporate hydroxyl groups into their structure. The amount of re-absorbed water depends on the cis/trans-vacancy ratio, type of interlayer cations and other features. Emmerich (2000) investigated rehydroxylation for a Ca-dominated cis-vacant smectite. For a Na-dominated, cis- and trans-vacancy mixed smectite, dehydroxylated at 700 °C for one hour, about 20% w/w rehydroxylation occurs (Emmerich, unpublished data). Assuming similar rehydroxylation behaviour for the smectite-rich interstratification present in Friedland clay, small variations of pH can be explained. Rehydroxylation means regaining of $(OH)^-$-groups from water. Hence, hydronium ions remain lowering the pH value of the suspension. This effect is supposed to influence pH more strongly than hydrolysis so that the effect of hydrolysis is superimposed.

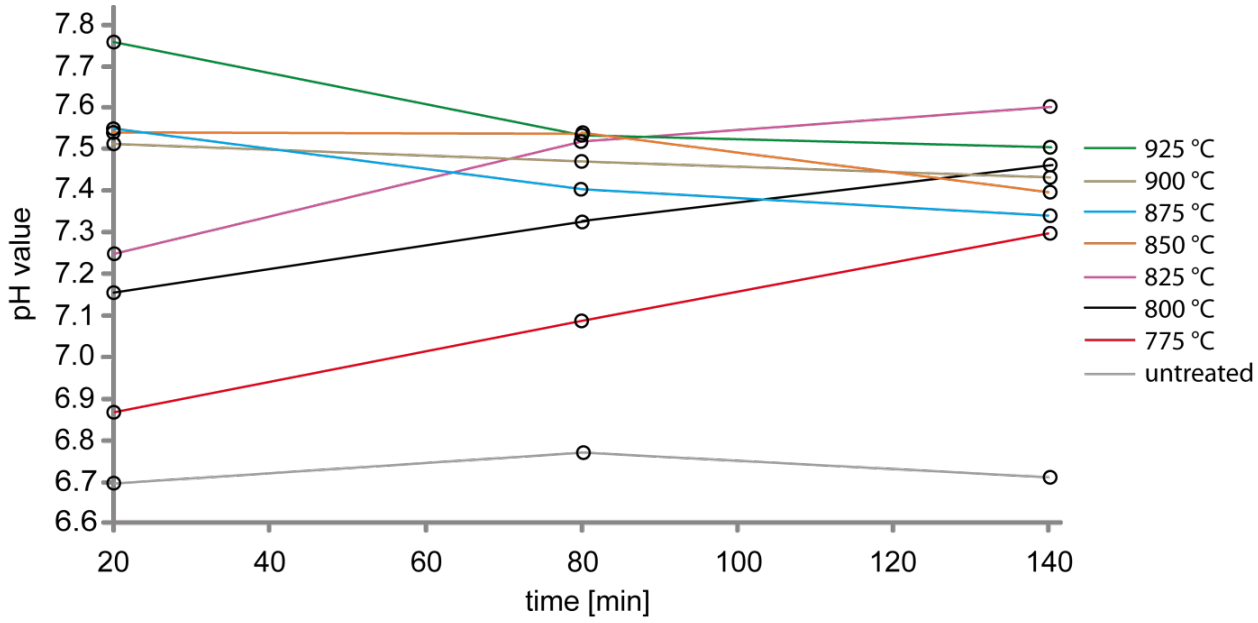

Figure 4.34. pH values of untreated Friedland clay, and clays heated to 775-925 °C in steps of 25 °C mixed with water with a weight ratio of 1. Measurements were made after 20 min, 80 min, and 140 min.

A long term experiment of the 875 °C heated sample revealed that after 24 hours the pH slowly decreased from 7.5 to 6.9 (Appendix xlviii - Appendix xlix). This time scale is similar to Emmerich (2000) who described rehydroxylation occurring within hours or days, whereby the fastest reaction was within the first 12 hours.

The pH value of the VP 4 sample was investigated and found to be significantly lower (6.6 after 20 min) than that of untreated clay, then increasing up to 6.8 (after 80 min) and then decreasing again to 6.5 (after 140 min). The low starting pH could be possibly explained by fast heating and cooling of the sample where pyrite and others are not completely oxidised to Fe_2O_3 and the $Fe[SO_4]$ that forms sulphuric acid when placed into water lowers the pH value. Then the pH increases possibly by slow CaO (and other metal oxides) formation as well as hydrolysis of clay minerals including interlayer cations due to incomplete oxidation. After this reaction, it is possibly superimposed by rehydroxylation which is assumed to be faster and more intense due to incomplete decomposition indicated by the high amount of $Al^{[5]}$ present.

However, pH variations up to 1 pH unit are considered not to influence the pH value of the alkaline activated system, because pH scale is logarithmic and slight changes in pH at pH ≈7 are negligible in a 5 mol/L K(OH) solution with a pH value of ≈14.7. Hence, metal oxides and undersaturated bonds influencing pH are unlikely to play an important role in GP cement mechanisms. In summary, pH was found to be an indicator for the degree of dehydroxylation.

4.2.2 Mechanical-activation

The goal to partially destroy the clay minerals structure to create a highly reactive precursor material as a substitute for heated clay can be studied by using different mills with increasing grinding energy (according to MacKenzie, 2009). MacKenzie *et al.* (2008) showed that intense ball milling of 2:1 layer silicates led to occurrence of 4-, 5-, and 6-fold coordinated Al. Yang *et al.* (2005) investigated the effect of grinding on illite and concluded that the BET value (A_S), as well as porosity decreased with increasing milling time. To evaluate the effect of grinding on Friedland clay, XRD patterns were recorded and decreasing intensities were assumed to reflect the degree of structural breakdown. Milling was first undertaken using a Retsch PM 4 planetary mill with an agate grinding set and a low grinding ball:clay ratio of 1.34. The milling results were tested by powder XRD. Increasing destruction/disordering of the structure should lead to increasing FWHM values of all reflections until only a broad hump or even no diffraction can be recognised.

Because grinding for 10 hours using an agate grinding garniture led to insufficient destruction of the clay minerals structures (Table 4.20, Figure 4.35), another planetary ball mill using steel balls and a tungsten carbide jar (Fritsch Pulverisette 7) was used (Table 4.20). This mill introduces more energy to the system due to heavier grinding balls and thus, higher impact energies. After 2 hours, the XRD patterns were almost identical with that of untreated clay or clay milled for 10 hours with the Fritsch Pulverisette (Figure 4.35). Using a grinding time of 11 hours and 16 hours with steel balls and a tungsten carbide jar, respectively, led to almost identical grinding results (Appendix l). To introduce even more energy to the system, a disc mill was used (Table 4.20). Grinding 20 g clay for 5 minutes yielded better results because a strong decrease of clay mineral reflection intensities was observed by XRD, but it was still not considered enough for GP production. Increasing the grinding time to 30 minutes and 1 hour, the grinding results significantly enhanced the result with a distinct decrease of all clay mineral reflections (Figure 4.35). Only quartz, pyrite, and some minor feldspar phases were not completely destroyed, but increased FWHM values presumably reflect increasing micro strain. Because 20 g of milled clay acquired for one run is far too little for laboratory and especially for industrial purposes, the amount of clay milled simultaneously increased. Using 40 g of clay and a grinding time of 1 hour led to similar results as when using 20 g and 5 minutes (Figure 4.35). Increasing the milling time to 2 hours led to better results. The maximum load of 50 g clay was tested and milled for 3 hours, which produced excellent milling results with almost no remaining clay mineral reflections (Figure 4.35).

Table 4.20. Types of mills, amount of sample, and milling times used for mechanical activation. —— insufficient: no/almost no differences to untreated sample; — poor: barely recognizable lowered clay mineral reflections; + sufficient: intensities of some clay mineral reflections decrease noticeably; ++ good: intensities of most clay mineral reflections decrease; +++ very well: almost no clay mineral reflections left, broad hump noticeably

Type of mill	Manufacturer, model	Amount of sample	Duration of milling	Result
Planetary ball mill	Retsch PM 4	70 g	10 h	——
Planetary ball mill	Fritsch Pulverisette 7	30 g	2 h	——
		30 g	11 h	——
		30 g	16 h	——
Disc mill	VEB Bergbau- und Hüttenkombinat Freiberg, Type MSL 2	20 g	5 min	—
		20 g	30 min	+
		20 g	1 h	++
		40 g	1 h	+
		40 g	2 h	++
		50 g	3 h	+++

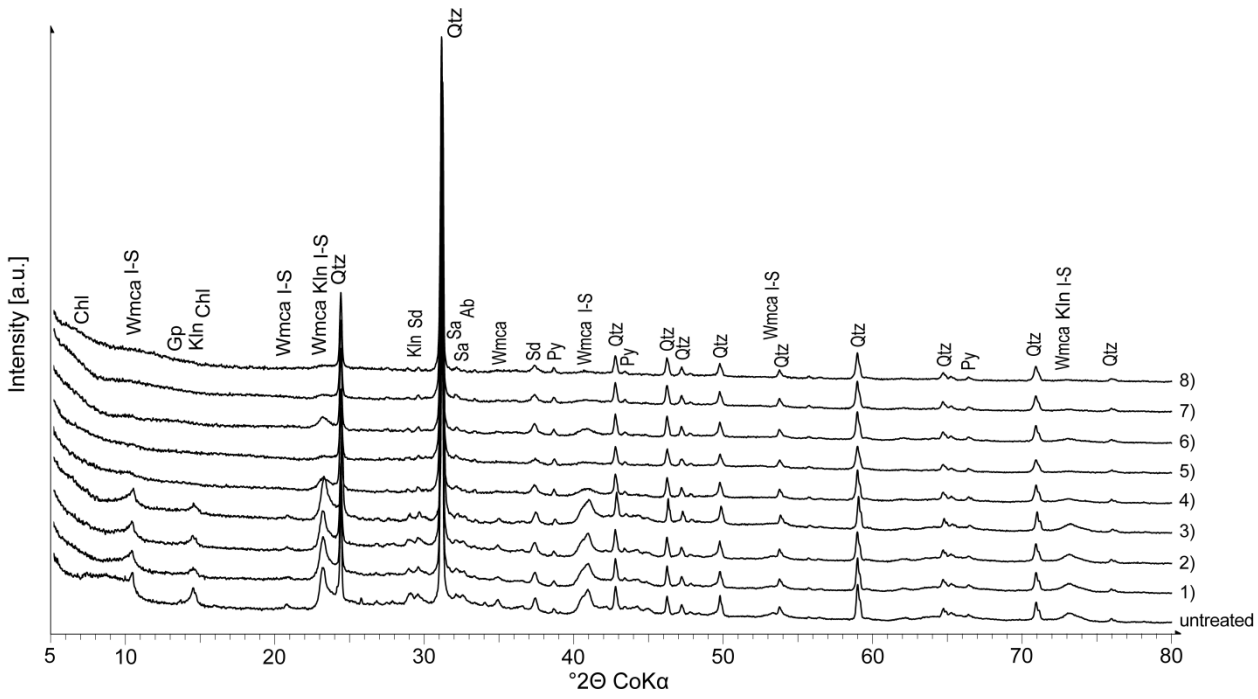

Figure 4.35. XRD patterns of powdered Friedland clay bulk material. From lower to upper pattern: untreated clay, 1) 30 g milled with Fritsch Pulverisette 7 for 2 h; 2) 70 g milled with Retsch PM 4 for 10 h; 3) 20 g milled with a disc mill for 5 min; 4) 20 g milled with a disc mill for 30 min; 5) 20 g milled with a disc mill for 1 h; 6) 40 g milled with a disc mill for 1 h; 7) 40 g milled with a disc mill for 2 h; 8) 50 g milled with a disc mill for 3 h. Chl: chlorite, I-S: illite-smectite interstratification, Wmca: white mica, Gp: gypsum, Kln: kaolinite, Qtz: quartz, Sd: siderite, Sa: sanidine, Ab: albite, Py: pyrite

Additionally to powder XRD, TEM selected area electron diffraction (SAED) was used to measure single particles instead of bulk samples as in XRD. Electron diffraction revealed that no or only diffuse diffraction occurs, in accordance to XRD data (Figure 4.36, Appendix li). Hence, 20 g milling for 1 hour,

40 g milling for 2 hours, or 50 g milling for 3 hours led to good results (almost/no visible reflections). The absence of reflections in XRD and SAED for the 3 hours milled sample indicates (partial) destruction of the clay mineral structure. Whether the extremely low particle size (too low coherent scattering domains for positive interferences) and/or an extremely high degree of microstrain (high broadening of the reflections) led to the absence of sharp reflections and the occurrence of broad humps remains unclear, but a combination of both these mechanisms is likely. These results are similar to that of Dellisanti & Valdré (2005) who investigated structural properties of bentonite after ball milling.

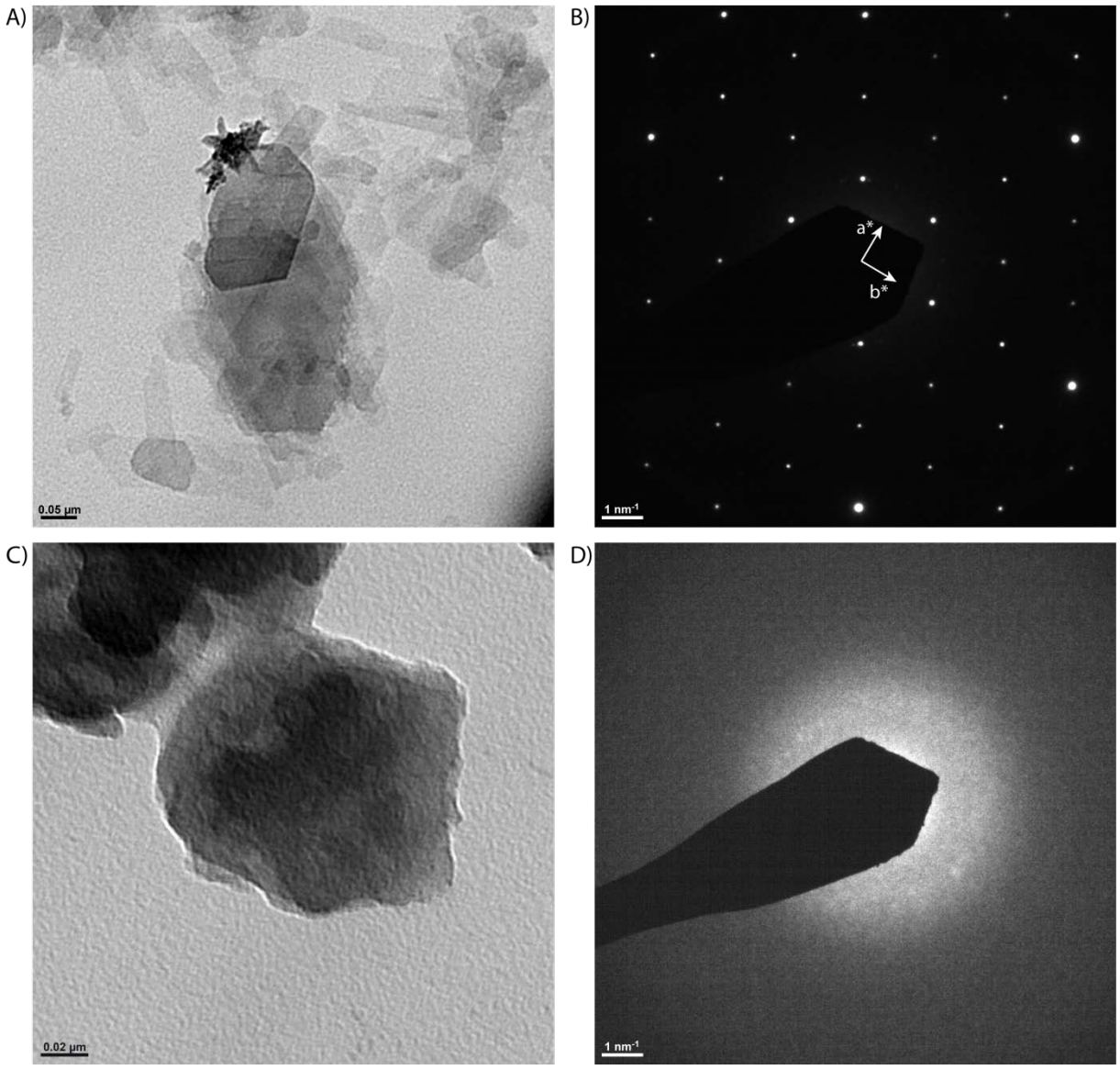

Figure 4.36. Electron micrographs and selected area electron diffraction patterns (SAED) of powdered Friedland clay bulk material. A) electron micrograph of untreated clay particle with B) typical pseudohexagonal SAED pattern and C) electron micrograph of a milled clay particle with D) no diffraction pattern due to highly disordered structure.

Further GP tests using this milled material revealed that although Al and Si concentrations in the alkaline solution increased, about 30% w/w more alkaline solution must be added to achieve the same workability as when using heated clay (L.N. Warr, 2014, pers. comm.). This is according to Yariv &

Lapides (2000) who found that adsorption of water from the atmosphere is increased by increasing milling times. The precursor material did not form satisfactory cements indicating that although amorphous, the material is insufficiently dehydroxylated to produce a GP cement (Warr, 2014, pers. comm.). These results are according to MacKenzie *et al.* (2008), indicating highly disturbed clay mineral structures resulting in the presence of 4-, 5-, and 6-fold coordinated Al. However, the results of Yang *et al.* (2005) indicating decreasing A_S as well as decreasing porosity with increasing milling time do not fit to the observations made, but may indicate particle agglomeration by extensive milling as described by Yariv & Lapides (2000). The increased requirement of more alkaline solution to produce a viscous liquid indicates higher porosities and an increased liquid adsorption capacity due to a higher A_S caused by milling. These higher porosities would lead to a lower compressive strength and in general a lower physical and chemical resistance of the GP binder. Materials with a higher A_S generally provide higher reactive surface area, and in this sense are activated. If these porosities are additionally connected and filled with excess solution, after drying salts may crystallize that lead to corrosion and failure in binder materials. Furthermore, Yariv & Lapides (2000) stated that trioctahedral clay minerals are much less effective to grind than dioctahedral. Hence, using this type of activation may only be suitable for clays dominated by dioctahedral clay minerals. Additionally, the batch milling procedure required (disc mill, 50 g milled for at least 3 hours) is unfavourable for an industry procedure, for similar reasons as those mentioned for heating clays in a muffle oven. Hence, milling clay as a substitute for heating is not considered suitable for industrial GP material production because it increases the reactive surface area, but dehydroxylation does not occur.

However, milling was found to be helpful for breaking large that aggregates originate by heating of the clay as a preparation stage between heating (dehydroxylation) and alkaline activation. The low surface area of sintered particles originated by sintering processes probably presents alkaline solution from entering the internal parts of the grain and isolated micropore space. By fracturing these sinter particles, the surface area is increased and internal pore space become more accessible to alkaline solution.

4.3 Compressive strength

To evaluate the optimal calcination parameters of the clay, the compressive strength of a GP based on Friedland clay bulk material heated to 775 °C to 925 °C in steps of 25 °C were tested. A 5 mol/L K(OH) solution was added to the precursors (solid:liquid weight ratio of 2.0), intensively mixed and allowed to harden at 50°C and >90% r.h. for 180 days.

Calcination temperatures between 775 °C and 825 °C resulted in compressive strengths of 2-4 N/mm² (Figure 4.37; compressive strength values see Appendix lii). With increasing calcination temperature, compressive strengths increased and reached a maximum value of 20 N/mm² at 875 °C and then decreasing again to 15 N/mm² (925 °C). Hence, calcination temperatures <850 °C and >925 °C for Friedland clay is not suitable for GP production because of its low compressive strength. This bulk material should be heated to ca. 875 °C to obtain the maximal compressive strength. Buchwald *et al.* (2009) investigated the suitability of Friedland clay heated between 550 °C and 950 °C in steps of 100 °C as a GP raw material and concluded that Friedland clay heated to 850 °C and 950 °C resulted in GPs with the highest compressive strength (≈13 N/mm²). Although the 950 °C heated sample showed a similar compressive strength, the error was much higher possibly reflecting a decreasing compressive strength for clay calcined at higher temperatures. However, the recipe given by Buchwald *et al.* (2009) using clay heated for one hour at maximum temperature and 6 mol/L Na(OH) solution (solid:liquid ratio of 2.5) was slightly different than that used here and although using a higher molarity, the compressive strengths measured were significantly lower, presumably due to lower curing times. He *et al.* (1995) investigated the compressive strength of OPC mixed with illite, sand, and water (0.7:0.3:3.0:0.6) without alkaline activation and found increasing compressive strength of the binder mix with increasing calcination temperatures of illite (20 °C, 650 °C, 790 °C, 930 °C) after 28 days. However, all compressive strengths were significantly lower than pure OPC (52-79% of OPC compressive strength).

Sperberga *et al.* (2011) also investigated an illitic clay using samples that were not activated with an alkaline solution and samples that were activated with 2-8 mol/L K(OH). Afterwards they calcined the clays at 20-900 °C. They concluded that untreated clay and clay heated to 100 °C, both activated with 6 mol/L K(OH) produced GPs with the highest compressive strengths. Low as well as high molarities resulted in decreasing compressive strengths. These results are opposing to that presented in this work, as well as He *et al.* (1995) and Buchwald *et al.* (2009) due the very different conditions used to make the GP. Apparently, Sperberga *et al.* (2011) first activated the clay with alkaline solution and then heated the mixture to 100 °C, and 700-900 °C.

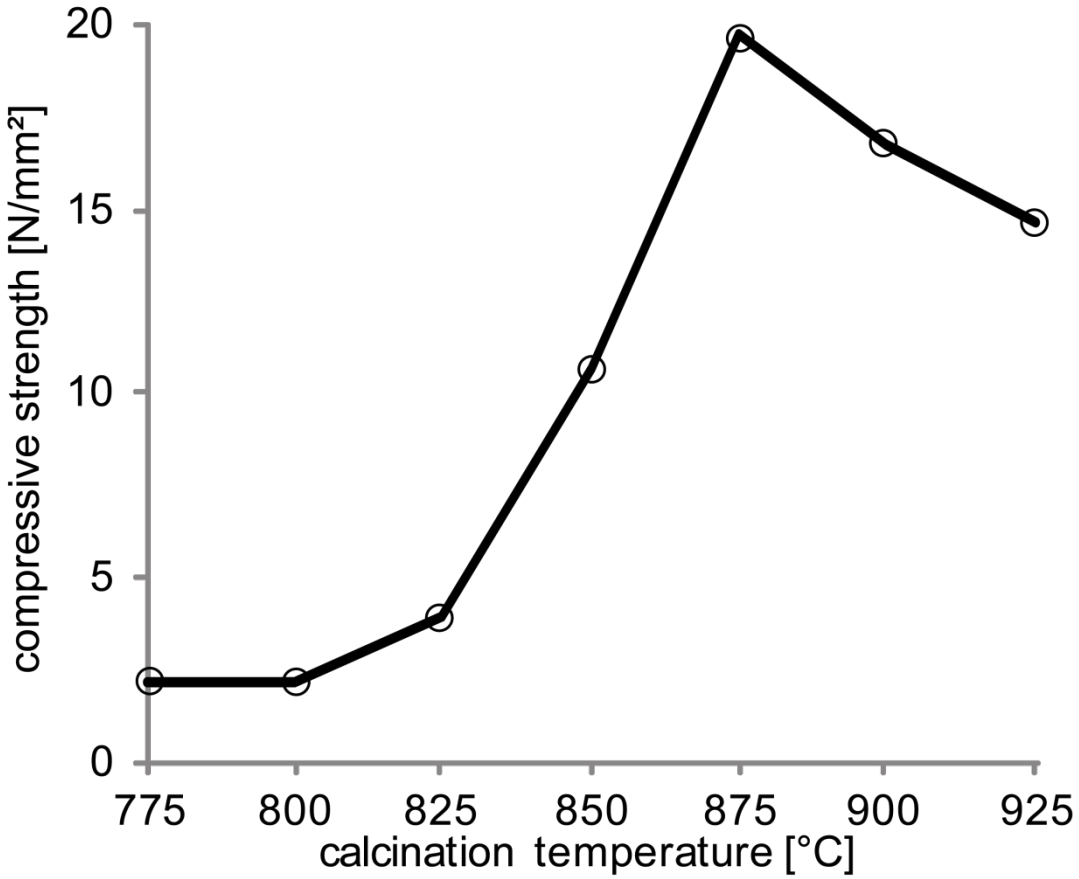

Figure 4.37. Average compressive strength of Friedland clay bulk samples heated between 775 °C and 925 °C in steps of 25 °C.

5 Discussion of the suitability of illitic clays for GP synthesis

Friedland clay heated to 875 °C was found to be most suitable to produce a GP with high compressive strength (20 N/mm²; Figure 4.37). Lower calcination temperatures led to significantly lower compressive strengths, while higher calcination temperatures led to slightly lower compressive strengths. These results are similar to that of Buchwald *et al.* (2009) who found 850-950 °C heated clay to be most suitable (using calcination steps of 100 °C), but these authors could not identify the underlying reasons. MacKenzie *et al.* (2008) investigated the suitability of pyrophyllite for GP productions and found that no stable GP cement could be produced from that material, although a significant change of the Al coordination occurred, $Al^{[5]}$ was proved, and recrystallisation occurs earliest at 1100 °C (e.g. Heller, 1962; Schomburg, 1985) indicating that the amount of $Al^{[5]}$ may not play the key role for producing GP binder materials as indicated by the literature.

Table 5.1 summarises measured values and parameters determined in this study using Friedland clay. The compressive strength of the rotary oven-based GP cements were provided by Warr (2012, pers. comm.). Most parameters, except for the $Al^{[5]}$ content were not determined for clay heated to <775 °C because no stable GP could be produced from these precursors. The rotary oven samples were chosen to investigate possible XRD related proxies for dehydroxylation that are especially valuable for industrial purposes. Sample VP4 was chosen to be further investigated as this sample was the most suitable precursor formed by rotary oven heating.

Table 5.1. Overview of measured parameter value of untreated Friedland clay and clay heated with a laboratory muffle oven as well as an industrial rotary oven. n.d. not determined, n.s. not stable (no compressive strength measurement possible), [1)] values from Warr, 2012, pers. comm.

Type of oven	Sample name	Calcination temperature [°C]	Dwell time [min]	Amount of Al[5] [%]	Amount of Si in solution [mg/L]	Amount of Al in solution [mg/L]	Amount of Si+Al in solution [mg/L]	Si:Al molar ratio in solution
--	Untreated clay	--	--	0	n.d.	n.d.	n.d.	n.d.
Muffle oven	FT_600	600	120	13	n.d.	n.d.	n.d.	n.d.
	FT_650	650	120	49	n.d.	n.d.	n.d.	n.d.
	FT_700	700	120	48	n.d.	n.d.	n.d.	n.d.
	FT_725	725	120	46	n.d.	n.d.	n.d.	n.d.
	FT_750	750	120	44	n.d.	n.d.	n.d.	n.d.
	FT_775	775	120	31	1288	509	1797	2.4
	FT_800	800	120	26	1104	464	1568	2.3
	FT_825	825	120	19	892	390	1282	2.2
	FT_850	850	120	9	746	314	1060	2.3
	FT_875	875	120	4	730	317	1047	2.2
	FT_900	900	120	4	577	233	810	2.4
	FT_925	925	120	0	535	186	720	2.8
Rotary oven	VP1	825	40	n.d.	n.d.	n.d.	n.d.	n.d.
	VP2	850	40	n.d.	n.d.	n.d.	n.d.	n.d.
	VP3	875	40	n.d.	n.d.	n.d.	n.d.	n.d.
	VP4	875	20	25	688	264	951	2.5
	VP5	875	13	n.d.	n.d.	n.d.	n.d.	n.d.
	VP6	875	10	n.d.	n.d.	n.d.	n.d.	n.d.

Table 5.1 continued. Overview of measured parameter value of untreated Friedland clay and clay heated with a laboratory muffle oven as well as an industrial rotary oven. n.d. not determined, n.s. not stable (no compressive strength measurement possible), [1] values from Warr, 2012, pers. comm.

Type of oven	Sample name	Calcination temperature [°C]	Dwell time [min]	A_S [m²/g]	Integral intensity of 10 Å reflection [cps*°2θ]	LOI [% w/w]	pH value after 20 min	Compressive strength of resultant GP [N/mm²]
--	Untreated clay	--	--	44.9	n.d.	6.61	6.70	n.s.
Muffle oven	FT_600	600	120	n.d.	n.d.	n.d.	n.d.	n.s.
	FT_650	650	120	n.d.	n.d.	n.d.	n.d.	n.s.
	FT_700	700	120	n.d.	n.d.	n.d.	n.d.	n.s.
	FT_725	725	120	n.d.	n.d.	n.d.	n.d.	n.s.
	FT_750	750	120	n.d.	n.d.	n.d.	n.d.	n.s.
	FT_775	775	120	9.9	n.d.	n.d.	6.87	0.5
	FT_800	800	120	6.3	n.d.	n.d.	7.16	0.5
	FT_825	825	120	4.5	n.d.	n.d.	7.25	4.0
	FT_850	850	120	3.7	n.d.	n.d.	7.54	10.8
	FT_875	875	120	2.9	n.d.	n.d.	7.55	20.0
	FT_900	900	120	2.4	n.d.	n.d.	7.51	16.9
	FT_925	925	120	1.7	n.d.	n.d.	7.76	14.8
Rotary oven	VP1	825	40	n.d.	27.9	1.00	n.d.	5.7 [1]
	VP2	850	40	n.d.	19.7	0.66	n.d.	12.4 [1]
	VP3	875	40	n.d.	7.7	0.39	n.d.	16.2 [1]
	VP4	875	20	3.0	6.6	0.27	6.59	21.1 [1]
	VP5	875	13	n.d.	8.0	0.26	n.d.	18.3 [1]
	VP6	875	10	n.d.	12.4	0.35	n.d.	n.d.

To explain the suitability of the precursor material and to identify the key parameters, the optimal precursor properties known from the literature to create a homogeneous GP with low porosity and high compressive strength must be considered (see Table 1.2). Suitable precursors should:

1) Have a high Si and Al content (Brew & MacKenzie, 2006; Heller-Kallai & Lapides, 2007; Duxson *et al.*, 2007c; Duxson & Provis, 2008)
2) Have an appropriate Si:Al ratio (1.6-2.2) (Heller-Kallai & Lapides, 2007; Duxson *et al.*, 2007c)
3) Have a suitable content of alkali and alkaline earth elements (Xu & van Deventer, 2003; Duxson & Provis, 2008)
4) Have a higher content of alkali than alkaline earth elements (Duxson & Provis, 2008)
5) Be amorphous or poorly crystalline (Duxson & Provis, 2008)
6) Have round particles (Duxson & Provis, 2008)
7) Have an intact surface (Duxson & Provis, 2008)
8) Have a high content of 5-fold coordinated Al (MacKenzie *et al.*, 2008; Wang *et al.*, 2010)

Some of these properties such as a high Si and Al content and a suitable content of alkali and alkaline earth elements are intrinsic to most clays. As summarised in Table 5.2, the clays investigated here have high amounts of SiO_2 and Al_2O_3 (Friedland clay bulk 84% w/w SiO_2 + Al_2O_3, Rectorite <0.1 µm fraction 93% w/w SiO_2 + Al_2O_3, "sárospatakite" bulk 87% w/w SiO_2 + Al_2O_3, each normalised to the dry state). The Si:Al molar ratio directly influences the type of species created and thus strongly affects hardening time and compressive strength of the resultant GP (e.g. Heller-Kallai & Lapides, 2007; Duxson *et al.*, 2007c), whereas the optimal Si:Al molar ratio is assumed 1.6-2.2 (Heller-Kallai & Lapides, 2007; Duxson *et al.*, 2007c; Bell *et al.*, 2009). XRF data revealed the Si:Al ratio of Friedland clay bulk material is higher than the optimal ratio resulting in slower hardening of the cement, but higher final compressive strength (according to Sagoe-Crentsil & Weng, 2007), while rectorite <0.1 µm indicates a too low Si:Al ratio, and the ratio of "sárospatakite" fits the lower limit of the optimal ratio (Table 5.3). Hence, rectorite based GP can be predicted to show fast hardening but lower final compressive strength compared to clays with optimal Si:Al ratios, such as "sárospatakite" if no additional Si is added.

Flame-AAS measurements after Friedland clay leaching tests were made to determine the Si:Al ratio dissolved in the alkaline solution. Based on leaching experiments using solid:liquid weight ratios of 0.004-0.01 literature data indicate clay minerals such as I-S or kaolinite are dissolved congruently at pH > 13 (Bauer *et al.*, 1998; Bauer & Velde, 1999). Flame-AAS measurements of Friedland clay using a solid:liquid weight ratio of 0.1 indicate similar Si:Al ratios compared to the solid material (Table 5.3). Between 1.7-2.3 mol-% of Si and 1.7-2.9 mol-% of Al present in heated Friedland clay was dissolved within 24 hours. Si and Al contents decrease with increasing calcination temperature (Figure 5.1) while the Si:Al molar ratio varies in a narrow range between 2.2-2.8. Ratios <2.8, which is the value of the solid material, either indicate less quartz dissolution or sample heterogeneities. Based on these results, the

Si:Al molar ratios for rectorite and "sárospatakite" calculated from XRF measurements are also considered representative for the ratio dissolved in the 5 M K(OH) solution.

All silicates present in Friedland clay are assumed to contribute to the GP reaction although being dissolved in varying amounts in the alkaline solution. The most important phases are the 2:1 layer silicates including I-S and mica (muscovite/illite) because they make up ≈50% w/w of Friedland clay. Phases with small particle sizes or poorly crystallised ones such as I-S or illite are assumed to be more reactive than well crystallised phases such as muscovite. Kaolinite that makes up about 12% w/w is also likely to strongly contribute to the GP reaction, as demonstrated by Duxson *et al.* (2007a). XRD data indicated two types of kaolinite are present in Friedland clay from which the well crystallised kaolinite is assumed to be dissolved less strongly than the highly disordered kaolinite with lower particle size because of its higher surface area and lower lattice enthalpy. The dissolution of chlorite is not assumed to influence GP reaction because of its minor abundance. Quartz (23% w/w in the bulk sample), however, can be expected to provide additional Si for the GP reaction, as significant dissolution at these pH values (<10) is expected (according to Brady & Walther, 1990). Although feldspars are suitable raw materials for GP (Xu & van Deventer, 2003), they are not assumed here to influence the GP reactions due to their minor abundance (6% w/w). Overall, because <5 mol-% of the total Si and Al present in the clay is dissolved, high amounts of unreacted particles remain to form filler and clast material bound together by the GP phase. These particles are of high importance as filler and clasts that are bound by the GP phase.

Table 5.2: Extract of the chemical analyses of Friedland clay, rectorite, and "sárospatakite", normalised to the dry state.

Sample	$SiO_2+Al_2O_3$ [% w/w]	$Na_2O+K_2O+CaO+MgO$ [% w/w]	$(Na_2O+K_2O+CaO+MgO)$ / $(SiO_2+Al_2O_3)$ molar ratio	(Na+K) / (Ca+Mg) molar ratio
Friedland clay bulk	84.35	6.90	0.09	1.42
Rectorite <0.1 µm	93.03	5.63	0.07	6.51
"Sárospatakite" bulk	87.31	12.42	0.15	1.36

To adjust the Si:Al ratio to an optimal value, additional components such as silica fume or amorphous silica can be added to increase the ratio (e.g. for rectorite <0.1 µm fraction) or alternatively, gibbsite to decrease it. For "sárospatakite" no additives are assumed necessary. To decrease the Si:Al ratio of Friedland clay, 10% w/w gibbsite was added befor GP mixing. Gibbsite transforms into $Al(OH)_4^-$ species when dissolved in highly alkaline solution (Hemingway *et al.*, 1978) which is favourable for GP reaction. Assuming similar proportions of Al dissolved from gibbsite as measured for clay, the Si:Al molar ratio of the mixture can be adjusted to the optimal ratio of 1.8-2.1. As gibbsite is transformed to a chemically stable and less soluble Al_2O_3 phase above 400 °C with a much higher lattice enthalpy, it is important to mix this mineral additive with the dehydroxylated clay prior to alkali treatment and not prior to thermal treatment of the illitic clay.

Table 5.3. The optimum Si:Al molar ratio for a GP and the Si:Al molar ratio of selected dioctahedral 2:1 layer silicates (according to [1)] Duxson *et al.*, 2007c, Bell *et al.*, 2009, Rickard, 2013, pers. comm.; [2)] Rieder *et al.*, 1998; [3)] Emmerich *et al.*, 2009), as well as the Si:Al molar ratio of Friedland clay, rectorite, and "sárospatakite" measured by XRF, and dissolved from Friedland clay, measured by flame-AAS. n.d. not determined

Description	Sample	Si:Al molar ratio
Ideal solid	Geopolymer	1.6 – 2.2 [1)]
	Muscovite / paragonite	1.0 – 1.8 [2)]
	Illite / brammallite	1.1 – 2.3 [2)]
	Dioctahedral smectites	1.3 – 4.1 [3)]
Measured solid	Friedland clay bulk sample	2.8
	Friedland clay <0.1 µm fraction sample	2.2
	Rectorite bulk sample	n.d.
	Rectorite <0.1 µm fraction sample	1.2
	"Sárospatakite" bulk sample	1.6
	"Sárospatakite" <0.1 µm fraction sample	1.6
Measured solution	Friedland clay bulk sample	2.2 – 2.8

The actual Si:Al ratio of the real GP mixtures used is, however, not precisely known due to the high solid:liquid weight ratios used (e.g. 2.0 in this study), which is distinctly different from that used in the leaching tests. A ratio of 2.0 results in a muddy paste from which no solution can be extracted for measuring Si and Al by flame-AAS. Additionally, precipitation of any Al-Si-compounds during the dissolution process cannot be excluded. Therefore in this study an identical or very similar Si:Al ratio in the "GP mixture" as measured in the leaching test is assumed.

The molar ratio of $(Na_2O+K_2O+CaO+MgO) / (SiO_2+Al_2O_3)$ is considered to have an optimal of ≈0.2 (Bell *et al.*, 2004, Kriven, 2013, pers. comm.). The molar ratio in this study varied between 0.07 for rectorite and 0.15 for "sárospatakite" (Table 5.2). Considering the amount of K(OH) solution added which, in the case of Friedland clay and "sárospatakite" doubles or in the case of rectorite triples the amount of alkali + alkaline earth elements in the GP mixture, the ratio is increased to 0.22 (Friedland clay bulk), 0.18 (rectorite <0.1 µm), and 0.28 ("sárospatakite"), respectively, which is quite close to the optimum value. Adding minor amounts of an Al or Si source up to 15% w/w does not influence this value significantly.

All three clays investigated in this study had a molar ratio of alkali to alkaline earth elements >1.0 as reported for many GP precursor materials by Duxson & Provis (2008). When adding the alkaline solution, additional K^+ is introduced so that all of these mixtures are dominated by alkaline elements rather than alkaline earth elements (Table 5.2). However, according to Emmerich (2011) the amount and proportion of alkali and alkaline earth elements is not assumed to influence dehydroxylation

significantly, but as a flux may decrease the melting temperature and thus lower the upper temperature boundary for preparing heated clay suitable for GP synthesis.

Some features such as the amorphous character of the raw material must be adjusted by processing the clay. An amorphous or poorly crystalline character of the precursor was achieved by two separate ways, heating and milling of the untreated clay. First, the suitable calcination temperature range of the three interstratification-rich clays based on the degree of dehydroxylation was investigated by STA-MS and, for Friedland clay, by TXRD. The amorphous content of heated samples was not quantified due to of the lack of structural models of dehydroxylated clay mineral phases. However, dehydroxylated clay minerals are considered to take part in GP reactions in large proportions. The minor amount of amorphous material present in heated clay is considered to also take part, but is not representative for the suitability of the clay to produce high compressive strength GPs due to its low abundance. Buchwald *et al.* (2009) quantified heated Friedland clay using the Rietveld method. Hoever, no structural models are available to accurately quantify dehydroxylated phases. Hence, these results should be treated with causion. The future developing of structural models for dehydroxylated clay minerals would enable better quantification of these calcined materials.

During heating, dehydration and desorption of water molecules was complete by 200 °C for all clays investigated, based on STA-MS and TXRD results. The mass loss up to ≈300 °C was 4.88% w/w, 6.76% w/w, and 3.00% w/w for bulk Friedland clay, rectorite <0.1 μm and "sárospatakite" <0.1 μm, respectively, determined by STA-MS. Any additional water in the raw clay may cause the clay to stick to the sides of the rotary oven, which is detrimental to the preparation of the heated clay. Sticking also causes the clay to stay in the ove longer that may lead to cloggin and decreasing temperatures inside the oven as in the case of the laboratory rotary oven. Hence, pre-drying of the clay at 100-250 °C may be required prior to dehydroxylation of moist clay.

Dehydroxylation and simultaneous/subsequent decomposition of 2:1 layer silicates of Friedland clay and "sárospatakite" was complete by ≈800 °C according to STA-MS, TXRD, and NMR. This is the most important requirement for preparing an effective precursor because of the highly disturbed structure and broken structural bonds formed by thermal activation. However, domination of tv layers as in the case of rectorite leads to dehydroxylation finished by 700 °C. Using, however, in the case of the Arkansas rectorite that contains cookeite, the maximum temperature required for completed dehydroxylation may be increased somewhat due to the trioctahedral layers present in that mineral. Based on the thermal behaviour of all three illitc clays studied, a suitable temperature range for each sample can be defined whereby the lowest temperature is set at the point dehydroxylation finished and the highest temperature at the point where recrystallisation begins (Table 5.4). The latter represent conditions at which chemically stable phases such as spinels or mullite form, which require only small energy changes (Mukhopadhyay *et al.*, 2010). These reactions significantly decrease the amount of dissolved Si and Al due to the high lattice energies involved. Based on these results, the suitable temperature range was

found to be 800-955 °C for Friedland clay, 700-1000 °C for rectorite, and 800-1000 °C for "sárospatakite" as summarised in Table 5.4. The temperature window described for illite by Jiang *et al.* (2008) between 1093 °C and 1100 °C seems not to fit to the present samples because recrystallisation occurrs at temperatures >1000 °C. Recrystallisation at lower temperatures may also be promoted by elevated amounts of fluxing agents such as Na in the case of Friedland clay and rectorite and Ca in the case of "sárospatakite".

Organic compounds as well as siderite and pyrite present in the Friedland clay and rectorite sample that may disturb the GP reaction by reacting with K(OH) solution were destroyed between 300 °C and 600 °C (STA-MS and TXRD) and outgased or converted into more stable phases such as hematite. The solubility of hematite in 5 mol/L K(OH) solution at ambient conditions is very low (<0.01 g/L, Ishikawa *et al.*, 1997) and thus negligible for the GP reaction.

Table 5.4. Temperature range between dehydroxylation and recrystallisation of all interstratification-rich clays investigated here. [1)] Ignoring dehydroxylation of minor trioctahedral chlorite layers at 762 °C

Description	Sample	Suitable temperature range [°C]
Investigated clays	Friedland clay (tv dominated)	800 – 955
	Rectorite <0.1 µm fraction (tv dominated)	700[1)] – 1000
	"Sárospatakite" <0.1 µm fraction (tv/cv)	800 – 1000
Supposed overall suitable temperature range		800 – 955

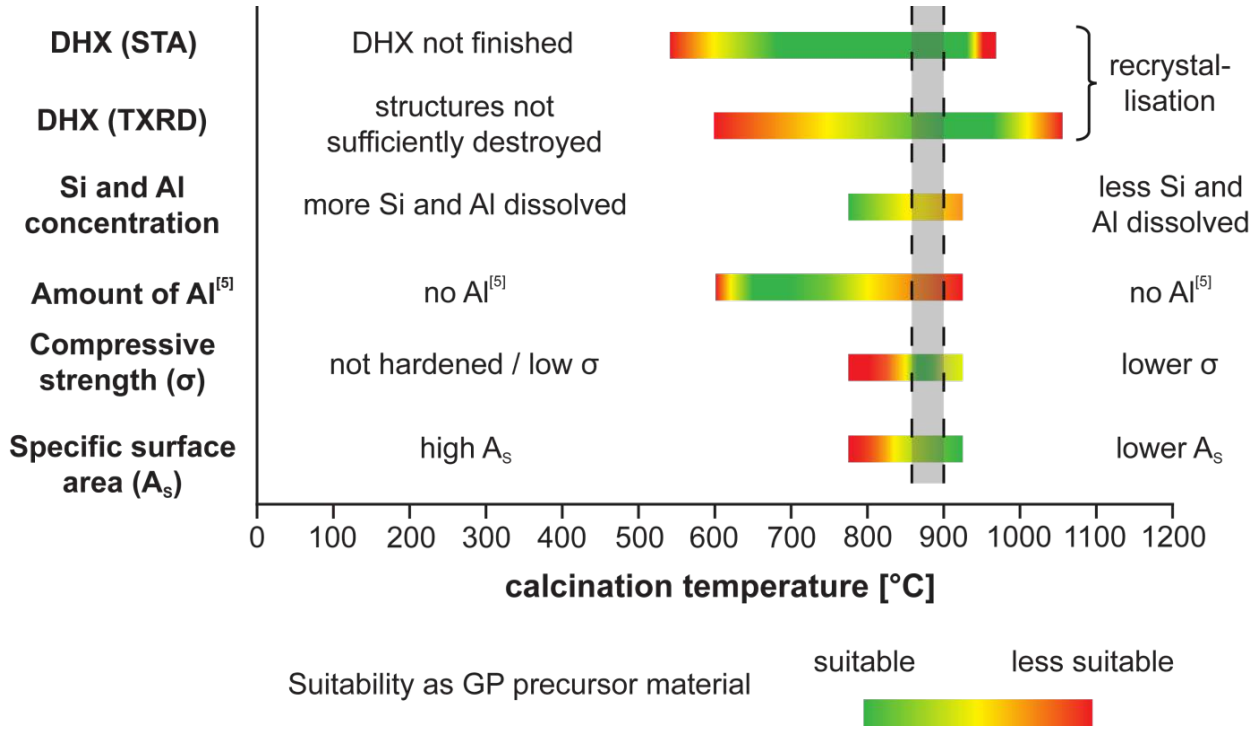

Figure 5.1. Overview of the important features of dehydroxylated Friedland clay influencing the suitability as a precursor material for GP production. The grey area marks the temperature range at which suitable GP cements can be produced. DHX: Dehydroxylation

Milling the clay was not found to be an alternative for heating. Although milled clay is highly reactive, resulting in high Si and Al concentrations in solution, about 30% w/w more alkaline solution was needed compared to heated clay (Duxson *et al.,* 2007c). Furthermore it was not possible to create a GP with even moderate compressive strengths and low porosity (Warr, 2014, pers. comm.). However, moderate milling was found helpful as a preparation step after heating to break up sintered aggregates and create pathways for alkali solution. As a result, the reactive surface area is increased and more Si and Al was dissolved from the sintered material. The GP phase is formed between these particles by a solution-precipitation process binding them strongly and closing the pathways. This results in low porosity and low permeability GPs with higher compressive strengths. Hence, round particles and intact surfaces of the particles as stated to be necessary by Duxson *et al.* (2007c) was not found suitable. Milling to increase the surface by breaking up aggregates was found to increase the compressive strength significantly. The milling process will produce more angular shaped grains with higher surface area by breaking and fracturing instead of rounded grains as produced by sintering.

Data published by several authors indicate the amount of $Al^{[5]}$ plays a key role in producing GPs with high compressive strength from heated clays because increasing $Al^{[5]}$ enhances the solubility of the octahedral sheets and thus the amount of Al (and Si) dissolved (e.g. Wang *et al.*, 2010). This feature was confirmed by NMR measurements and leaching tests of heated Friedland clay. The highest amount of $Al^{[5]}$ was found to be present directly after dehydroxylation at 650/700 °C (≈50% $Al^{[5]}$) and decreased with increasing calcination temperature, as did the total Al concentration in solution, between 775 °C and 925 °C (Table 5.1, Figure 5.1). Because higher amounts of dissolved Si and Al directly lead to higher amounts of GP phase resulting in favourable properties such as high compressive strength (e.g. Wang *et al.*, 2010), these results imply that clay heated to 650-700 °C should produce GPs with the highest compressive strength which is contradictory to measured data (Table 5.1, Figure 5.1). Hence, it can be concluded that the amount of $Al^{[5]}$ is not the only factor that influences the resultant compressive strength of GPs produced from variably heated illitic clays.

Using other illitic clays than investigated here, the suitable calcination temperature range may vary because of being strongly depended on the type of octahedral cations and the tv/cv ratio. Domination of tv layers and high octahedral Fe contents decrease dehydroxylation and decomposition temperatures of clay minerals significantly to <500 °C because of the lower thermal strength of Fe-OH compared to Al-OH and Mg-OH bonds (Köster, 1993; Wolters & Emmerich, 2007; Emmerich, 2011). The amount of Fe incorporated in the structure of clay minerals is generally not considered in the GP literature. The effect of Fe on the long-term stability and corrosion of GP binder materials, and whether Fe is incorporated in the GP structure or whether it is precipitated as a separate phase such as hematite that could be transformed if pH, Eh or activities of certain elements change should be considered and investigated.

Based on the results presented in this study, the Reichweite of an interstratification is not considered to influence the suitability of an illitic GP raw material. The difference of binding energies caused by

variations in Reichweite is negligible and neither influences dehydroxylation or dissolution that occurs at the edge of particles and is no layer-by-layer process. However, the amount of expandable layers may influence the required predrying process, because of the higher amount of water present in the interlayer. Additionally, alkaline solution may be intercalated and removed from reactive edge site where dissolution takes place and where it acts as a transport medium of dissolved species. A different dissolution behaviour of illitic and smectitic layers is not considered likely and results published by Bauer & Velde (1999) indicate that smectite layers may be converted to illite in K(OH) solutions at temperatures as low as 35 °C.

Impurities present in illitic clays such as other clay minerals, framework silicates, sulphides/sulphates or organic matter and amorphous silica may also influence the quality and suitability of clays as a GP raw material in terms of the environmently impact and the properties of the resultant GP such as compressive strength or permeability. Kaolinite is generally considered to take part in GP reactions whereby disordered kaolinites are assumed to increase the amount of GP phase created more strongly than well crystallised ones. However, due to low concentrations (<15% w/w) kaolinite is not considered to significantly influence the properties of the illitic-based GP cements. Due to the lower dehydroxylation temperatures (peak dehydroxylation 500-600 °C) and similar recrystallisation temperatures (>925 °C; Brindley & Nakahira, 1959a,b; Guggenheim & Koster van Groos, 2001; Emmerich, 2011), the ideal calcination window of kaolinite-bearing illitic clay is also not expected to change with varying abundance of kaolinite. Although kaolinite introduces Si and Al, additional Si may be necessary because of the lower Si:Al ratio. Many authors (e.g., Duxson *et al.*, 2007a) have demonstrated the suitability of kaolinite as a GP raw material using similar treatments as described here.

Significant amounts of trioctahedral layer silicates, e.g. clinochlore, may influence the need of additives and the required calcination temperature because of a lower Si:Al ratio, an increased amount of Mg instead of alkali elements, and higher dehydroxylation and lower recrystallisation temperatures that narrows the optimal temperature window (Emmerich, 2011). Whether or not trioctahedral layer silicates are generally suitable as a raw material for GP production and which calcination temperatures are necessary has not been well studied. The occurrence of significant amounts of vermiculite may be detrimental because recrystallisation of these minerals occurs generally at lower temperatures between 841-878 °C (Smykatz-Kloss, 1974; Steudel, 2008; Emmerich, 2011).

Chlorite including dioctahedral sheets such as cookeite (e.g. present in the Arkansas rectorite bulk sample) or donbassite may reduce the Si:Al ratio and the amount of alkali/alkaline earth elements in the clay. But the dehydroxylation temperature is similar to that of dioctahedral 2:1 layer silicates (Smykatz-Kloss, 1974) and chlorite can be assumed to dissolve by the same mechanisms as 2:1 layer silicates in high molar solutions. The dehydroxylation temperature of trioctahedral chlorite is higher (often >700 °C) while the recrystallisation temperature is lower (Smykatz-Kloss, 1974; Emmerich, 2011) that may result

in less dissolved Si+Al. Hence, chlorites containing dioctahedral sheets are assumed likely to influence the suitable calcination temperature of the clay less than chlorites only containing trioctahedral sheets. However, chlorite is considered not to influence the suitability strongly if present as a minor comonent. The influence of admixtures of chlorite in large quantities cannot be predicted here with confidence.

Quartz and amorphous or poorly crystalline silica are likely to strongly increase the Si:Al ratio as these phases are assumed to be dissolved significantly at high pH values (Brady & Walther, 1990). Hence, having high amounts of SiO_2-phases, e.g. quartz in the case of Friedland clay and the Arkansas rectorite bulk material, may require addition of gibbsite to decrease the Si:Al ratio.

The occurrence of feldspar is not considered to influence the suitability of illitic heated clay in a significant way because dissolution of these minerals will increase the Si+Al conent without changing the Si:Al ratio significantly. Xu & van Deventer (2003), for example, did demonstrate that feldspar-rich rocks can be used as suitable precursors for GP synthesis using treatments similar to those described in this study.

The presence of other accessory minerals, such as carbonates, sulphates and sulphides may also lower the quality of the precursor by releasing more environmently unfriendly gases during calcination such as CO_2 and SO_2. Organic matter also lowers the quality due to the emission of H_2O, SO_2, NO_2, and CO_2 the letter two known as green house gases, by denaturation and decomposition during heating (<400 °C) or at least during alkaline activation. CO_2 is considered to strongly influence global warming (Lashof & Ahuja, 1990) while SO_2 forms sulphuric acid and thus promotes acidic rain and soil acidification (Helyar & Porter, 1989). Hence, large amounts of carbonates and organic matter in the raw material will reduce the advantage of “green cement” with a low CO_2 footprint. Whereas these minerals are not considered to influence the resultant GP properties directly, low-sulphur and -carbon clay is much more favourable than those with high sulphur and carbon contents. However, there is still significantly less CO_2 evolved from illitic clays compared to OPC using ≈85% w/w carbonates as raw material (compare to section 1.1). Assuming a maximum carbonate + organic matter content of 10% w/w in illitic clays (according to Rimmer & Greenland, 1976), only <15% w/w CO_2 is emitted during calcination. However, other aspects should be considered such as energy consumption during calcination and CO_2 emissions due to transportation of raw materials (compare to McLellan et al., 2011). Ti-oxides are not considered to influence the suitability of the clay due to their chemical stability in high pH solutions (Bhola *et al.*, 2009) as well as beeing present in trace amounts. However, although several impurities may increase the optimal calcination temperature of the clay, GP manufacturing is still less energy consuming compared to OPC because the highest suitable temperature for 2:1 layer silicates (1000 °C) is significantly lower than that used for OPC (1450 °C; compare to section 1.1).

Although geopolymerisation is a complex reaction system known to be influenced by the degree of dehydroxylation, the Si:Al ratio and the amount of $Al^{[5]}$, these parameters alone do not explain why Friedland clay heated to 875 °C was found to produce a GP with the highest compressive strength.

The specific surface area determined for the heated Friedland clay showed decreasing A_S values as calcination temperature increases (Table 5.1). These results reflect sintering processes occurring during calcinations which is supported by pore size distribution data showing a strong decrease of micropores and mesopores (98% and 81% lowered, respectively), and a 83% lower porosity. Although the concentration of Al in solution and the amount of $Al^{[5]}$ showed a strong correlation in the measured temperature range (775-925 °C, correlation coefficient r = 0.97), the Al concentration seems to depend more on A_S (correlation coefficient between 775-925 °C r = 0.93). Decreasing A_S values with a simultaneous reduction of porosity leads to a lower surface area, resulting in decreasing amounts of Si and Al in solution (lower accessibility of Al ad Si). At high pH values Al and Si are dissolved from clay minerals with less influence of their coordination state. The higher the pH value the more Si and Al will be dissolved from these dehydroxylated structures.

These results lead to the conclusion that A_S plays a significant role for evaluating the suitability of clays as precursor materials for GP production. However, the amount of Si and Al dissolved remains essential because it is assumed to be a direct proxy for the amount of GP phase created. High concentrations of Si+Al in solution are necessary to create enough GP phase to cement remaining particles. But to produce a binder material with high compressive strength, all grains must be cemented strongly. The BET surface area of the clay decreases with temperature due to sintering effects indicating larger but fewer grains. Both reactions are counteracting and an optimum must be reached to produce the GP with highest compressive strength. Thus, the amount of GP created (expressed by the sum of dissolved Si and Al) divided by the surface area of grains that must be covered with the GP phase (expressed by the specific surface area A_S of the dehydroxylated clay) can be used as a useful proxy for predicting the optimal calcination temperature to yield the highest compressive strength of GP cements produced from heated clay precursors. This (Si+Al) / A_S parameter explains the strong decrease of the compressive strength vs. temperature function below 875 °C, as well as the shallow decrease above (Figure 4.37). The specific surface area decreases more strongly until 875 °C because of delayed evolving water and ongoing sintering, but less strongly above 875 °C (Figure 4.28). By plotting the compressive strength against (Si+Al) / A_S (Figure 5.2), the correlation becomes visible (correlation coefficient r = 0.82). The (Si+Al) / A_S value at 925 °C is assumed to be overestimated, due to an overestimation of Si+Al concentration and/or an underestimation of the A_S value, both possibly caused by clay heterogeneity. While the decrease of Si+Al solubility from 900 °C to 925 °C is much lower than the decrease for all other temperature steps, A_S decreases more strongly resulting in a higher (Si+Al) / A_S value. Hence, the amount of Si and Al dissolved and the specific surface area of the heated clay were found to be the key parameters for evaluating the suitability of a dioctahedral 2:1 layer silicate rich clay as a raw material for GP production. However, a suitable mixing process is essential and may strongly improve GP properties such as compressive strength. Additionally, the (Si+Al) / A_S parameter should be confirmed using different clays.

A distinct increase of molarity of the alkaline solution to, e.g. 15 mol/L or 20 mol/L would be expected to lower the influence of the specific surface area because a higher proportion of solid phases are dissolved and less residual grains would remain that require cemented. In this special case, the (Si+Al) / A_S parameter would tend to infinity. Such a strong increase of the pH value is, however, undesirable in terms of health and safety problems during mixing the binder material and subsequent environmental problems if such high alkaline solutions leaked into soils or drinking water.

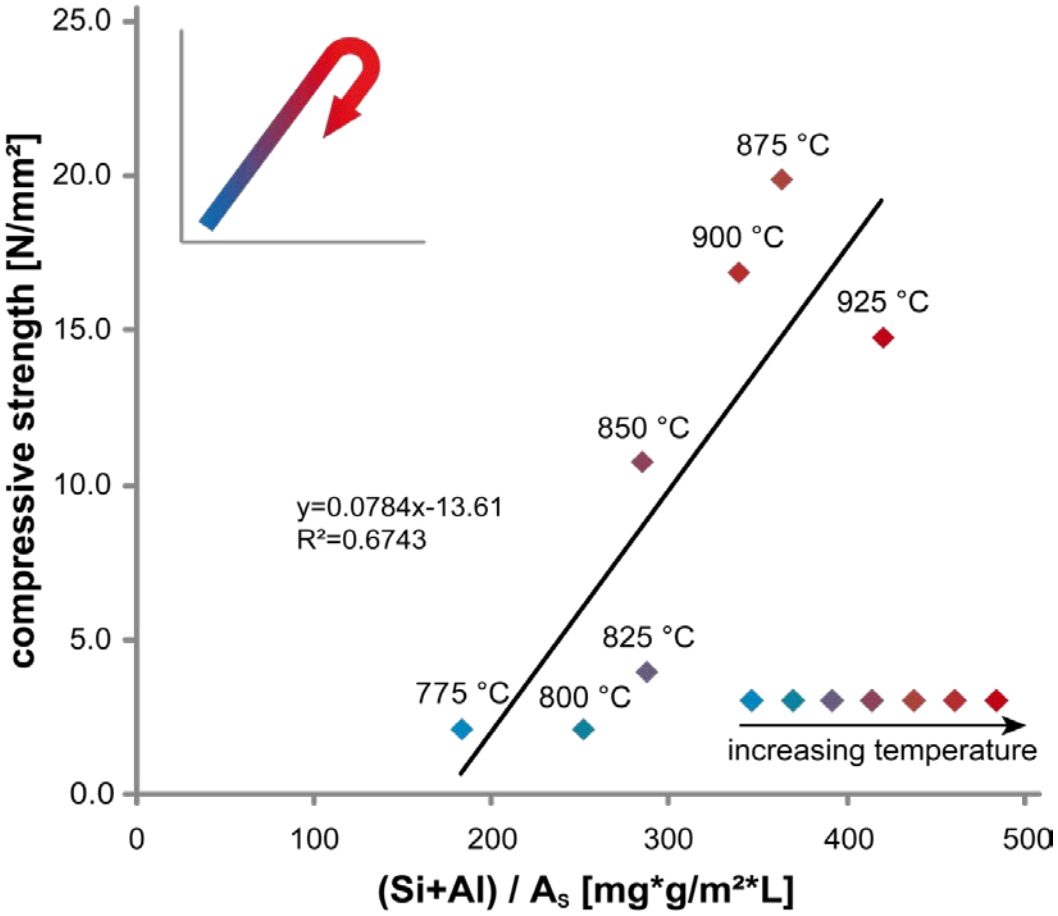

Figure 5.2. Plot of the compressive strength of the created GP binder material versus the sum of Si and Al dissolved divided by the specific surface area of the heated clay (Si+Al)/A_S. Each sample point represents Friedland clay heated to a temperature between 775 °C and 925 °C.

Because sintering is assumed one of the most important reactions for the present investigation, further investigation, characterisation and quantification of sintering processes by observation with SEM/TEM and determination of the amount of closed porosity by, e.g., Focused Ion Beam technology (FIB-SEM) would help to understand this process and could help to identify its critical parameters.

Proxies to assess the suitability of illitic heated clays

Based on the results presented here, all illitic clays with different types of I-S interstratifications and dioctahedral micas are assumed suitable as GP raw materials but especially the specific surface area of the heated clay, the temperature window, and the Si:Al molar ratio should be investigated for each illitic clay of potential use for GP production. If the exact Si:Al ratio dissolved is unknown, using a lower ratio

may be the better choice than using a ratio with excess Si. Al promotes and accelerates geopolymerisation, and in systems with a high Si:Al molar ratio (>3) geopolymerisation can be drastically slowed down (Sagoe-Crentsil & Weng, 2007). Using Al in excess, some polysialate species form at a Si:Al molar ratio of 1.0 without influencing the polymerisation process as much as significantly elevated Si:Al ratios (Sun *et al.*, 2004). This is according to Duxson *et al.* (2007c) and Kumar & Kumar (2011) who measured Si:Al molar ratios down to 1.0 and 1.3 for GP phases, respectively. By variation of the Si:Al ratio (variation of amount of gibbsite added), the compressive strength can be adjusted directly by influencing the polymerisation (see Table 1.1).

Two other useful proxies were found to determine the optimal calcination temperature range for illitic heated clay. Firstly, the integral intensity of the 10 Å reflection of the clay minerals was found to be highly correlated to the LOI (r = 0.972), which is a parameter used to determine the degree of dehydroxylation of the clay minerals (Figure 4.32, Table 5.1). This proxy is suitable for minerals of the mica and smectite group, as well as I-S interstratifications with different Reichweite values or regularly interstratified minerals such as rectorite. This parameter is fast and easy to determine and a measurement to identify the lowest calcination temperature and dwell time necessary to obtain a highly reactive precursor material by oven heating. Although it was determined using material heated in an industrial rotary oven, it is not assumed to be suitable only for industrial purposes, but also for clay heated in a muffle oven. However, more parameters than just the degree of dehydroxylation must be considered, hence, this proxy is only valid to determine the optimal calcination temperature with respect to the required conditions of dehydroxylation.

A second proxy for the state of dehydroxylation is the pH value of the heat treated clay in water (Table 5.1). Metal oxides present in partially dehydroxylated clay minerals (Fe-O, Mg-O, Al-O in the octahedral sheet) and impurities in the clay, such as carbonates or sulphides both formed during calcination, gather hydrogen from water (hydrolysis, Kaufhold *et al.*, 2008) and hence, increase the pH value. Between 775-850 °C (Figure 5.3) the pH increases with temperature due to the dehydroxylation of clay minerals. According to STA-MS results, dehydroxylation is complete between 850-900 °C resulting in a constant pH value. Further increasing the temperature to 925 °C, pH increases again due to sulphate oxidation of anhydrite as indicated by STA-MS. Small temperature variations between endothermal/exothermal reactions detected by STA-MS and temperature-dependend pH changes can be explained by the usage of different methods: STA-MS as an in-situ continuous heating method and clay heated in the muffle oven as a “static heating” with subsequent (after cooling), ex-situ pH investigation.

Although the effect of rehydroxylation and reaction of metal oxides with water on the pH value of an alkaline activated suspension is negligible, the pH value can be used as a proxy to investigate the degree of dehydroxylation if no other oxidation reactions occur in this temperature range superimposing this effect. Hence, this proxy is suitable for locating the lower limit for the suitable temperature window, but

cannot be used to find the upper limit. However, the lower limit is considered to be much more important because of energy saving aspects.

Comparison of the pH value of heated clay with the compressive strength of the resultant GP indicates a correlation between these values (r = 0.849; Figure 5.3). This relationship reflects the fact that the degree of dehydroxylation does strongly influence the compressive strength of the resultant GP.

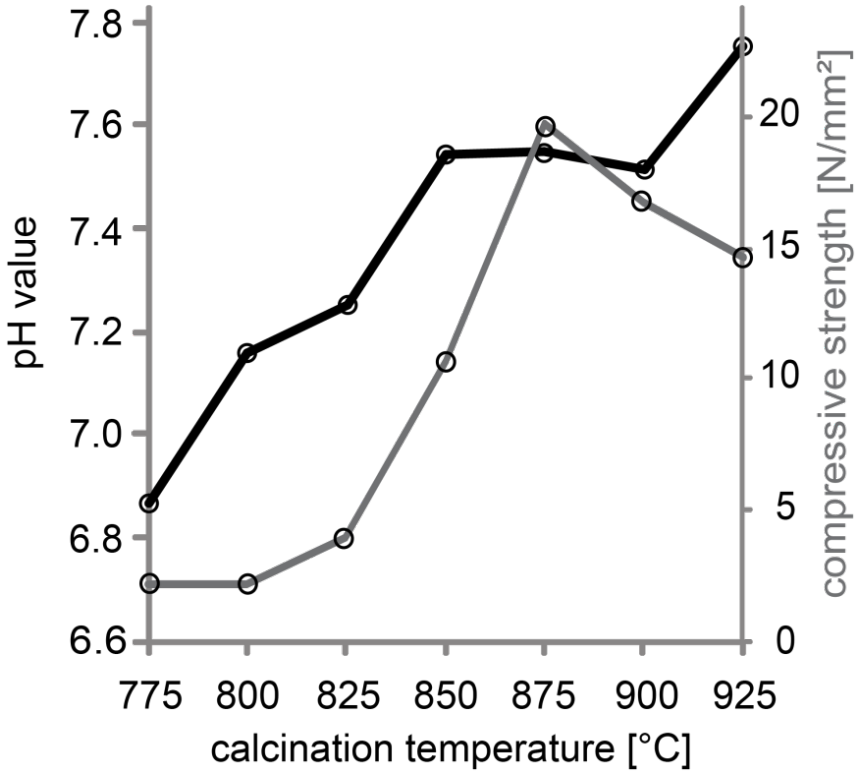

Figure 5.3. Comparison of the measured pH value of heated clay (solid:liquid weight ratio 1.0; black) and the compressive strength of the resultant GP (grey).

Reaction model

Based on the results presented, the following conceptual model is presented to explain the reaction mechanisms of illitic heated clays (Figure 5.4):

At low calcination temperatures (e.g. <300 °C; left pictures in Figure 5.4), the amount of Si and Al dissolved is highest, because the clays porosity, which includes micro-, meso-, and macropores allows high accessibility of the alkaline solution. But because no sintering occurred due to the low calcination temperatures, the amount of particles is very high resulting in a very high specific surface area. The amount of GP phase formed (illustrated as green matrix in Figure 5.4) although being high, is still too low to cement all particle surfaces, which results in a GP with low compressive strength and high porosity. Increasing calcination temperatures to e.g. 750 °C (middle left pictures in Figure 5.4) leads to decreasing amounts of GP but there is still a large amount of clay particles that need to be bound together (still high A_S due to incomplete dehydroxylation). Although the amount of dissolved Si and Al is still high, there is still not enough GP created to cement all particles resulting in a low compressive

strength or no stable GP at all. With increasing calcination temperatures to e.g. 875 °C (middle right pictures in Figure 5.4) intense sintering takes place and the amount of particles decrease by forming larger sintering aggregates. Although there is less Si and Al dissolved, there is still enough GP binder formed to cement the sintering aggregates together. If calcination temperature increases further (e.g. 1000 °C; left pictures in Figure 5.4), sintering aggregates continue to form together with the recrystallisation of mullite or spinels, which reduces the amount of GP phases by consumption of Si and Al. In this case insufficient cement is formed to bind all remaining and newly formed particles and compressive strengths of the material decreases. In addition weakening mechanisms may be attributed to the increased size of sintered aggregates, which contain longer intraparticle grain boundaries that may act as sites of fracture and failure (Figure 5.4).

In this conceptual model, the unsuitability of milled but unheated Friedland clay for GP production, which releases high concentrations of Al and Si into solution but produces no stable GP cement, is equivalent to the first stage of development shown in Figure 5.4 (T <300 °C). Here, a high amount of GP phase is formed, but remains insufficient to bind the large amount of milled particles of very low particle size. These results show clearly that although grinding the illitic heated clay is advantageous in terms of enhancing the materials reactivity, it will only lead to harder cements if more GP is produced than the increase in specific surface area generated by the grinding process.

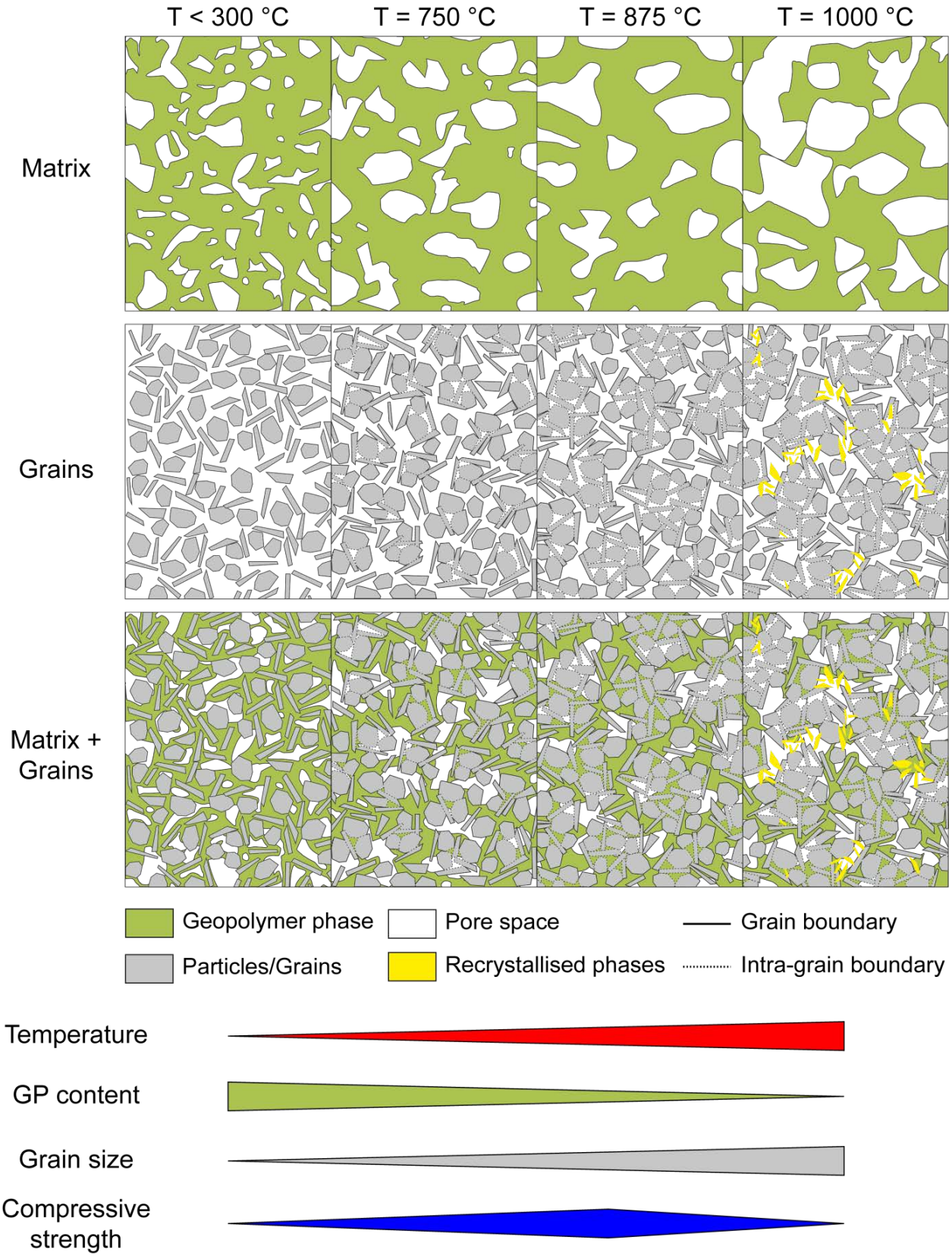

Figure 5.4. Schematic model to illustrate the influence of GP content, pore space, grain size, and recrystallisation effects on the compressive strength of the GP binder material.

6 Summary and Conclusions

In this study, three mica-smectite interstratification-rich clays were characterised by a multiple of analytical methods to evaluate the suitability of illitic clays as raw materials for GP cements and to establish the necessary preparation steps. Friedland clay containing a R0 interstratifications, rectorite from Arkansas as a regular interstratification, and "sárospatakite" containing an R3 interstratification were investigated, whereby the dehydroxylation behaviour is of particular importance. Preparing a suitable precursor was found to be a complex issue whereby the driving factors stated in the literature mainly based on kaolin as raw material appear not to be the only important factors that need to be considered for ilitic clays. Several parameters are determined to be important such as calcination temperature, Si:Al molar ratio, and A_S that must be considered for each individual illitic clay. The Reichweite of an interstratification or the polytypism of 2:1 layer silicates was found not to influence the suitable heating temperature or solubility of Si and Al, but cv/tv ratios, tetrahedral and octahedral Fe-content, or particle size may affect the optimal calcination temperature.

Two different approaches of clay activation were made including heating and milling. Both were found to be important preparation steps, but milling was not useful without preceding thermal activation because of the much higher porosity, alkaline solution consumption and lower compressive strength of the resultant GPs. Heating the clay to 850-925 °C (optimum 875 °C for Friedland clay) in a muffle oven for about two hours and subsequent milling using an agate ball mill was found to produce a highly suitable precursor. This temperature range is assumed accurate for illitic clays in general, but the optimal temperature should be investigated for each clay individually. The amount of $Al^{[5]}$ was found not to be the key parameter as documented for metakaolin precursors. With increasing calcination temperature, a counteracting reaction occurs between the decreasing Si and Al solubility (less GP phase created) and the decreasing surface area of the heated clay (less GP needed to cement all particles), which was found to play the key role in cement hardening. The (Si+Al) / A_S parameter of heated clay is presented as a representative quantity for predicting the optimal calcination temperature to yield the highest compressive strength of illitic clay-based GPs and explains the suitability of Friedland clay heated at higher temperatures than indicated by the amount of $Al^{[5]}$.

The heating parameters for Friedland clay on an industrial scale were investigated using a rotary oven and found optimal heating at 875 °C for at least 13 minutes. Heating the clay this way produced similar results regarding the Si and Al content and the Si:Al ratio in solution and the A_S parameter as clay heated at 875 °C for two hours in a laboratory muffle oven. Only the amount of $Al^{[5]}$ (higher) and the pH value (lower) was different compared to muffle oven heated clay indicating highly disordered dehydroxylated clay minerals and less metal oxides resulting in a lower pH value. Both parameters indicate an incomplete oxidation process compared to muffle oven heated clay due to rapid cooling. Using a laboratory rotary oven was not successful because of clay sticking on the inner walls which becomes

dominant when the rotary tube is of restricted diameter and the released water cannot effectively escape.

Friedland clay was found to be highly suitable as a GP raw material although minor impurities of carbonates, sulphates/sulphides, and organic matter lower its quality by worsen the environmental impact. Adding 10% w/w gibbsite to decrease the Si:Al molar ratio to an optimum is useful. Rectorite may be suitable as a raw material if some Si (e.g. silica fume) is added to increase the Si:Al ratio. But because rectorite is a rare material it is unlikely to be useful as a GP raw material. In contrast, "sárospatakite" was found to be highly suitable for GP cements with an optimal Si:Al molar ratio and contains minimal quantities of impurities that may release unwanted gases.

Additionally, based on Friedland clay two additional useful proxies were found to identify the minimum degree of calcination required to obtain a highly reactive precursor. The integral intensity of 10 Å reflections as determined by XRD as well as the pH value of heated clay/water suspensions were found to be indicators for the LOI value. The fast and easy to determine 10 Å reflection proxy can be applied to minerals of the mica and smectite group as well as I-S. Based on these results, a conceptual model was developed to explain both the suitability of clay heated to 875 °C and the unsuitability of milled clay without dehydroxylation to produce GPs with high compressive strengths.

Overall, GP cements based on illitic clay were produced successfully with compressive strengths up to 20 N/mm², which equals an OPC compressive strength class C16/20 following the Germany Industry Standard (DIN) and European Standard (EN) 206-1 (Table 6.1). The suitability of 2:1 layer silicates, particularly I-S interstratifications as possible raw material for GP cements was proven, in contrast to MacKenzie *et al.* (2008) or Sperberga *et al.* (2011), but in accordance to Buchwald *et al.*, (2009). Hence, the tetrahedral-octahedral-tetrahedral (2:1) layer does not prevent dissolution/GP formation as proposed for pyrophyllite (MacKenzie *et al.*, 2008). GP binder materials with elevated compressive strengths were produced from Friedland clay heated between 850 °C and 925 °C whereby the maximal compressive strength was reached with clay heated to 875 °C. By further enhancements of GP recipes by adjusting e.g. type and molarity of the alkaline solution or curing time and temperature, higher compressive strengths are considered possible.

Table 6.1. Compressive strength classes of standard and heavy concrete without high-strength concrete (after DIN EN 206-1).

Compressive strength class	Characteristic minimum compressive strength of cylinders [N/mm²]	Characteristic minimum compressive strength of cubes [N/mm²]
C8/10	8	10
C12/15	12	15
C16/20	16	20
C25/30	25	30
C30/37	30	70
C35/45	35	45
C40/50	40	50
C45/55	45	55
C50/60	50	60

List of literature

A

Ahn, J.H., Peacor, D.R., Essene, E.J. (1985): Coexisting paragonite-phengite in blueshist eclogite: a TEM study. American Mineralogist **70**, 1193-1204.

Ahn, J.H., Buseck, P.R. (1990): Layer-stacking sequences and structural disorder in mixed-layer illite/smectite: Image simulation and HRTEM imaging. American Mineralogist **75(3-4)**, 267-275.

Altaner, S.P., Ylagan, R.E. (1997): Comparison of structural models of mixed-layer illite-smectite and reaction mechanisms of smectite illitization. Clays & Clay Minerals **45**, 517-533.

Anthony J.W., Bideaux R.A., Bladh K.W., Nichols M.C. (eds.): Rectorite. Handbook of Mineralogy, Mineralogical Society of America, Chantilly, VA 20151-1110, USA.
http://www.handbookofmineralogy.org/

Aróstegui, J., Sangüesa, F.J., Nieto, F., Uriarte, J.A. (2006): Thermal models and clay diagenesis in the Tertiary-Cretaceous sediments of the Alava block (Basque-Cantabrian basin, Spain). Clay Minerals **41**, 791-809.

B

Bai, T.B., Guggenheim, S., Wang, S.J., Rancourt, D.G., Koster van Groos, A.F. (1993): Metastable phase relations in the chlorite-H_2O system. American Mineralogist **78**, 1208–1216.

Bailey, S.W. (1982): Nomenclature for regular interstratifications. American Mineralogist **67**, 394-398.

Bajnóczi, B., Molnár, F., Maeda, K., Izawa, E. (2000): Shallow level low-sulphidation type epithermal systems in the regéc caldera, Central Tokaj Mts., NE-Hungary. Geologica Carpathica **51(4)**, 217-227.

Barrett, E. P., Joyner, L. G., Halenda, P. P. (1951): The determination of pore volume and area distributions in porous substances. I. Computations from nitrogen isotherms. Journal of the American Chemical Society **73(1)**, 373-380.

Barron, P.F., Slade, P., Frost, R.L. (1985a): Solid-state silicon-29 spin-lattice relaxation in several 2:1 phyllosilicate minerals. Journal of Physical Chemistry **89**, 3305-3310.

Barron P.F., Slade P., Frost R.L. (1985b) Ordering of aluminum in tetrahedral sites in mixed-layer 2:1 phyllosilicates by solid-state high-resolution NMR. Journal of Physical Chemistry **89**, 3880-3885.

Bauer, A., Velde, B., Berger, G. (1998): Kaolinite transformation in high molar KOH solutions. Applied Geochemistry **13(5)**, 619-629.

Bauer, A., Velde, B. (1999): Smectite transformation in high molar KOH solutions. Clay Minerals **34**, 259-273.

Beckhoff, B., Kanngießer, B., Langhoff, N., Wedell, R., Wolff, H. (Eds.) (2006): Handbook of practical X-ray Fluorescence Analysis. Springer, Berlin, Heidelberg, New York, 863 pp.

Bell, J.L., Driemeyer, P.E., Kriven, W.M. (2009): Formation of ceramics from metakaolin-based geopolymers. Part II: K-based geopolymer. Journal of the American Ceramic Society **92(3)**, 607-615.

Bergmann, J., Friedel, P., Kleeberg, R. (1998): BGMN – a new fundamental parameter based Rietveld program for laboratory X-Ray sources, its use in quantitative analysis and structure investigations. CPD Newsletter, Commission of Powder Diffraction, International Union of Crystallography **20**, 5-8.

Bethke, C.M., Altaner, S.P. (1986): Layer-by-layer mechanism of smectite illitization and application to a new rate law. Clays & Clay Minerals **34**, 136–145.

Bethke, C.M., Vergo, N., Altaner, S.P. (1986): Pathways of smectite illitization. Clays & Clay Minerals **34**, 125–135.

Beutelspacher, H., van der Marel, H. W. (1968): Atlas of electron microscopy of clay minerals and their admixtures. A picture atlas. Elsevier, Amsterdam, 333 pp.

BGMN handbook (2004): BGMN home. Handbook of the BGMN program, last changed on December 4th 2004.

Bhola, R., Bhola, S.M., Mishra, B., Olson, D.L. (2009): Electrochemical behavior of Titanium and its alloys as dental implants in normal saline. Research Letters in Physical Chemistry **2009**, Article ID **574359**, 4 pp.

Bishop, M.E., Dong, H., Kukkadapu, R.K., Liu, C., Edelmann, R.E. (2011). Bioreduction of Fe-bearing clay minerals and their reactivity toward pertechnetate (Tc-99). Geochimica et Cosmochimica Acta **75**, 5229-5246.

Börner, A. (2013): Entstehung und Verbreitung von Steine- und Erden-Rohstoffen in Mecklenburg-Vorpommern. Schriftenreihe des Landesamtes für umwelt, naturschutz und Geologie Mecklenburg-Vorpommern. Güstrow, Germany, 7-17.

Boss, C.B., Fredeen, K.J. (1997): Concepts, Instrumentation, and Techniques in Inductively Coupled Plasma Optical Emission Spectrometry. Perkin Elmer, USA, 90 pp.

Brady, P.V., Walther, J.V. (1990): Kinetics of quartz dissolution at low temperatures. Chemical Geology **82**, 253-264.

Bragg, W. H., Bragg, W. L. (1913): The reflection of X-rays by crystals. Proceedings of the Royal Society A: Mathematical, Physical and Engineering Sciences **88**, 428-438.

Brackett, R.N., Williams, J.F. (1891): Newtonite and rectorite – two new minerals of the kaolinite group. American Journal of Science **42**, 11-21.

Bradley, W.F. (1950): Alternating layer sequence of rectorite. American Mineralogist **35**, 590-595.

Bray, H.J., Redfern, S.A.T. (1999): Kinetics of dehydration of Ca-montmorillonite. Physics and Chemistry of Minerals **26**, 591-600.

Brew, D.R.M., MacKenzie, K.J.D. (2007): Geopolymer synthesis using silica fume and sodium aluminate. Journal of Materials Science **42**, 3990-3993.

Brigatti, M.F., Guggenheim, S. (2002): Mica crystal chemistry and the influence of pressure, temperature, and solid solution on atomistic models. Reviews in Mineralogy and Geochemistry **46(1)**, 1-97.

Brigatti, M.F., Galán, E., Theng, B.K.G. (2013): Structure and mineralogy of clay minerals. In: Bergaya, F., Lagaly, G. (Eds.): Handbook of clay science. Elsevier, Amsterdam, 21-81.

Brindley, G.W., Ali, S.Z. (1950): X-ray study of thermal transformation in some magnesian chlorite minerals. Acta Crystallographica **3**, 25-30.

Brindley, G.W. (1956): Allevardite, a swelling double-layer mica mineral. American Mineralogist **41**, 91-103.

Brindley, G.W., Nakahira, M. (1959a): The kaolinite-mullite reaction series: II, Metakaolin. Journal of the America Ceramic Society **42(7)**, 314-318.

Brindley, G.W., Nakahira, M. (1959b): The kaolinite-mullite reaction series: III, The high-temperature phases. Journal of the America Ceramic Society **42(7)**, 319-324.

Brindley, G. W., Chang, T.-S.(1974): Development of long basal spacings in chlorites by thermal treatment. American Mineralogist **59(1-2)**, 152-158.

Brindley, G. W., Brown, G. (1984): Crystal structures of clay minerals and their X-ray identification. Mineralogical Society Monograph **f**, London, 349-356.

Brown, G., Weir, A.H. (1963): The identity of rectorite and allevardite. in “Proceedings of the International Clay Conference Stockholm 1”, I.T. Rosenqvist & P. Graff-Petersen, eds., Pergamon, Oxford, U.K., 27-35.

Bruker AXS (2005): Bruker AXS User Manual. Temperature Chambers for D8 Advance/D8 Discover. Order-Nr. DOC-M88-EXX047 V4.

Brunauer, S., Emmett, P. H., Teller, E. (1938): Adsorption of gases in multimolecular layers. Journal of the American Chemical Society **60**, 309-319.

Buatier, M.D., Peacor, D.R., O´Neil, J.R. (1992): Smectite-illite transition in Barbados accretionary wedge sediments: TEM and AEM evidence for dissolution/crystallization at low temperature. Clays & Clay Minerals **40(1)**, 65-80.

Buchwald , A., Hohmann , M., Posern, K., Brendler, E. (2009): The suitability of thermally activated illite/smectite clay as raw material for geopolymer binders. Applied Clay Science **46**, 300–304.

Buseck, P.R. (1992): Principles of Transmission Electron Microscopy. In: Buseck, P.R. (Ed.): Minerals and Reactions at the Atomic Scale: Transmission Electron Microscopy, Reviews in Mineralogy **27**, Mineralogical Society of America, Washington, DC, USA, 1-36.

C

Callière, S., Hénin, S., (1950): Sur un nouveau silicate phylliteux: la allevardite. C. R. Acad. Sci. **230**, 668-669.

Carlson, L. (2004): Bentonite Mineralogy. Part 1: Methods of investigation – a Literature review. Part 2: Mineralogical research of selected bentonites. Posiva Oy, Olkiluoto. Working Report **2004-02**. 78 pp.

Carrillo-Rosua, J., Morales-Ruano, S., Esteban-Arispe, I., Fenoll Hach-Alí, P. (2009): Significance of phyllosilicate mineralogy and mineral chemistry in an epithermal environment. Insights from the Palai-Islica Au-Cu deposit (Almería, SE Spain). Clays & Clay Minerals **57**, 1–24.

Carroll, D.L., Kemp, T.F., Bastow, T.J., Smith, M.E. (2005): Solid-state NMR characterisation of the thermal transformation of a Hungarian white illite. Solid State Nuclear Magnetic Resonance **28**, 31-43.

Carter, D.L., Mortland, M.M., Kemper, W.D. (1986): Specific surface. In: Methods of Soil Analyses, Part 1. Physical and Mineralogical Methods, Agronomy Monograph 9 (2nd Edition), Soil Science Society of America, Madison, USA, 413-423.

Chan, J.C.C., Bertmer, M., Eckert, H. (1999): Site connectivities in amorphous materials studied by double-resonance NMR of quadrupolar nuclei: High-resolution $^{11}B \leftrightarrow ^{27}Al$ spectroscopy of aluminoborate glasses. Journal of the American Chemical Society **121**, 5238-5248.

Christidis, G.E. (1995): Mechanism of illitization of bentonites in the geothermal field of Milos Island, Greece. Evidence based on mineralogy, chemistry, particle thickness and morphology. Clays & Clay Minerals **43**, 569-585.

Čícel, B., Kranz, G. (1981): Mechanism of montmorillonite structure degradation by percussive grinding. Clay Minerals **16**, 151-162.

Cioffi, R., Maffucci, L., Santoro, L. (2003): Optimization of geopolymer synthesis by calcinations and polycondensation of a kaolinitic residue. Resources, Conservation and Recycling **40**, 27-38.

Clauer, N., Środoń, J., Francu, J., Šucha, V. (1997): K-Ar dating of illite fundamental particles separated from illite-smectite. Clay Minerals **32**, 181-196.

Clauer, N. (2006): Towards an isotopic modelling of the illitization process based on data of illite-type fundamental particles from mixed-layer illite-smectite. Clay Minerals **32**, 181-196.

Cohen, K.M., Finney, S.M., Gibbard, P.L., and Fan, J.-X. (2013): The ICS International Chronostratigraphic Chart., Episodes **36(3)**, 199-204.

Cole, W.F. (1955): Interpretation of differential thermal curves of mixed-layer minerals of illite and montmorillonite. Nature **175**, 248-274.

Comodi, P., Zanazzi, P.F. (1997): Pressure dependence of structural parameters of paragonite. Physics and Chemistry of Minerals **24**, 274-280.

Comodi, P., Zanazzi, P.F. (2000): Structural thermal behavior of paragonite and its dehydroxylate: a high-temperature single-crystal study. Physics and Chemistry of Minerals **27**, 377-385.

Csongrádi, J., Tungli, G., Zelenka, T. (1996): Relation between the postvolcanic activities and mineralisation in the Koromhegy-Koromtető (Füzérradvány) area. – Földt. Közl. (Bulletin of the Hungarean Geological Society) **126(1)**, 67-75.

Cuadros, J., 2010. Crystal-chemistry of mixed-layer clays. In: Fiore, S., Cuadros, J., Huertas, F.J. (Eds.), Interstratified Clay Minerals. Origin, Characterization and Geochemical Significance. AIPEA Educational Series, vol. 1. Digilabs, Bari, Italy, 11–33.

D

Davidovits, J. (1988): Geopolymer chemistry and properties. In: Geopolymer 1988, 25-48.

Davidovits, J. (1991): Geopolymers. Journal of Thermal Analysis and Calorimetry **37(8)**, 1633-1656.

Davidovits, J. (1999): Chemistry of geopolymeric systems, terminology. In: Davidovits, J., Davidovits, R., James, C. (Eds.): Second international conference géopolymère. Saint-Quentin, 9-40.

Dellisanti, F., Valdré, G. (2005): Study of structural properties of ion treated and mechanically deformed commercial bentonite. Applied Clay Science **28**, 233-244.

Dietel, J., Steudel, A., Warr, L.N., Emmerich, K. (2015): Crystal chemistry of Na-rich rectorite from North Little Rock, Arkansas. Clay Mineral, in press.

DIN EN12390-3 (2009): Compressive strength of test specimens. Deutsches Institut für Normung e.V. (German National Standard)

DIN EN 206-1 (2001): Specification, performance, production and conformity. Deutsches Institut für Normung e.V. (German National Standard)

Dódony, I. (1985): Transmission electron microscopic investigations of crystal chemical relations and lattice geometry of layer silicates. C. Sc. Thesis, Hungarian Academy of Sciences, Budapest, 115 pp.

Drits, V.A., Besson, G., Muller, F. (1995): An improved model for structural transformation of heat-treated aluminous dioctahedral 2:1 layer silicates. Clay & Clay Minerals **43**, 718-731.

Drits, V.A., Lindgreen, H., Salyn, A.L. (1997): Determination by XRD of content and distribution of fixed ammonium in illite-smectite. Application to North Sea illite-smectite. American Mineralogist **82**, 80-88.

Drits, V.A., Lindgreen, H., Salyn, A.L., Ylagan, R., McCarty, D.K. (1998): Semiquantitative determination of trans-vacant and cis-vacant 2:1 layer silicates in illites and illite-smectites by thermal analysis and X-ray diffraction. American Mineralogist **83**, 1188-1198.

Drits, V.A., Tchoubar, C. (1990): X-Ray Diffraction by disordered lamellar structures. Springer, Berlin, 371 pp.

Drits, V.A., Zviagina, B.B. (2009): Trans-vacant and cis-vacant 2:1 layer silicates: Structural features, identification, and occurrence. Clays & Clay Minerals **57(4)**, 405-415.

Dudek, T., Środoń, J. (2003): Thickness distribution of illite crystals in shales II: origin of the distribution and the mechanism for the illitization of shales. Clays & Clay Minerals **51**, 529-542.

Duxson, P. (2009): Geopolymer precursor design. In: Provis, J.L., van Deventer, J.S.J. (Eds.): Geopolymers – structure, processing, properties and industrial applications. Woodhead Publishing Limited and CRC Press LLC, 37-49.

Duxson, P., Lukey, G.C., van Deventer, J.S.J. (2007a): Physical evolution of Na-geopolymer derived from metakaolin up to 1000°C. Journal of Material Sciences **42**, 3044-3054.

Duxson, P., Mellicoat, S.W., Lukey, G.C., Kriven, W.M., van Deventer, J.S.J. (2007b): The effect of alkali and Si/Al ratio on the development of mechanical properties of metakaolin-based geopolymers. Colloids and Surfaces A: Physicochemical and Engineering Aspects **292(1)**, 8-20.

Duxson, P., Fernández-Jiménez, A., Provis, J.L., Lukey, G.C., Palomo, A., van Deventer, J.S.J. (2007c): Geopolymer technology: the current state of the art. Journal of Materials Science **42**, 2917-2933.

Duxson, P., Provis, J.L., Lukey, A., van Deventer, J.S.J. (2007d): The role of inorganic polymer technology in the development of "green concrete". Cement and Concrete Research **37(12)**, 1590-1597.

Duxson, P., Provis, J.L. (2008): Designing precursors for geopolymer cements. Journal of the American Ceramic Society **91(12)**, 3864-3869.

E

Eberl, D.D., Blum, A.E., Serravezza, M. (2011): Anatomy of a metabentonite: Nucleation and growth of illite crystals and their coalescence into mixed-layer illite/smectite. American Mineralogist **96**, 586–593.

Eberl, D.D., Środoń, J. (1988): Ostwald ripening and interparticle diffraction effects for illite crystals. American Mineralogist **73**, 1335-1345.

Emmerich, K. (2000): Spontaneous rehydroxylation of a dehydroxylated cis-vacant montmorillonite. Clays & Clay Minerals **48(3)**, 405-408.

Emmerich, K., Wolters, F., Kahr, G., Lagaly, G. (2009): Clay profiling: The classification of montmorillonites. Clays & Clay Minerals **57(1)**, 104-114.

Emmerich, K. (2011): Thermal analysis in the characterization and processing of industrial minerals. EMU Notes in Mineralogy **9**, **Chapter 5**, 129-170.

Emmerich K., Koeniger F., Kaden H., Thissen P. (2015): Microscopic structure and properties of discrete water layer in Na-exchanged montmorillonite. Journal of Colloid and Interface Science **448**, 24-31.

Essene, E.J., Peacor, D.R. (1995): Clay Mineral Thermometry – A critical Perspective. Clays & Clay Minerals **43**, 540-553.

F

Ferrage, E., Lanson, B., Sakharov, B.A., Geoffroy, N., Jaquot, E., Drits, V.A. (2007): Investigation of dioctahedral smectite hydration properties by modeling of X-ray diffraction profiles: Influence of layer charge and charge location. American Mineralogist **92**, 1731-1743.

Ferrari, S., Gualtieri, A.F. (2006): The use of illitic clays in the production of stoneware tile ceramics. Applied Clay Science **32**, 73-81.

Fiquet, G., Richet, P., Montagnac, G. (1999): High-temperature thermal expansion of lime, periclase, corundum and spinel. Physics and Chemistry of Minerals 27, 103-111.

Fitzgerald, J.J., DePaul, S.M. (1999): Solid-State NMR Spectroscopy of Inorganic Materials: An Overview. In: Fitzgerald, J.J. (Ed.): Solid-State NMR Spectroscopy of inorganic Materials, ACS Symposium Series **717**, American Chemical Society, Washington, DC, 2-133.

Freude, D., Haase, J. (2014): Quadropole Effects in Solid-State NMR, Basic Principles and Experimental Techniques for nuclei with Half-integer Spins., www.quad-nmr.de (March 2015)

Furlan, S., Clauer, N., Chaudhuri, S., Sommer, F. (1996): K transfer during burial diagenesis in the Mahakam delta basin (Kalimantan, Indonesia). Clays & Clay Minerals **44**, 157-169.

G

Galán, E., Ferrell, R.E. (2013): Genesis of clay minerals. In: Bergaya, F., Lagaly, G. (Eds.): Handbook of clay science. Elsevier, Amsterdam, 83-126.

García, R., Báez, A.P. (2012): Atomic Absorption Spectrometry (AAS). In: Farrukh, M.A. (Ed.): Atomic Absorption Spectroscopy, InTech, 1-12.

Gluchovskij, V.D. (1959): Gruntosilikaty. Grosstrojizdat Kiev, Patent USSR 245627 (1967), Patent USSR 449894.

Gradusov, B.P., Chizhikova, N.P., Travnikova, L.S. (1968): The nature of interlayer spaces in rectorite from Dagestan. Doklady Akademii Nauk SSSR Earth Science Section **180**, 130-132.

Greene-Kelly, R. (1952): A test for montmorillonite. Nature **170**, 1130-1131.

Grim, R.E., Bradley, W.F. (1948): The illite clay minerals (abstract). International Geological Congress, 18th Session, London, Great Britain. Volume of Titles and Abstracts, 127-128.

Grim, R.E., Bradley, W.F. (1952): The illite clay minerals (abstract). International Geological Congress, 18th Session, London, Great Britain. Part XIII, Section M, 302.

Grim, R.E., Rowland, R.A. (1942): Differential thermal analysis of clay minerals and other hydrous materials. Part 2. American Mineralogist **27(12)**, 801-818.

Gualtieri, A.F., Ferrari, S. (2008): Kinetics of illite dehydroxylation. Physics and Chemistry of Minerals **33**, 490-501.

Gualtieri, A.F., Ferrari, S., Leoni, M., Grathoff, G., Hugo, R., Shatnawi, M., Paglia, G., Billinge, S. (2008): Structural characterization of the clay mineral illite-1M. Journal of Applied Crystallography **41**, 402-415.

Guggenheim, S., Adams, J.M., Bain, D.C., Bergaya, F., Brigatti, M.F., Drits, V.A., Formoso, M.L.L., Galán, E., Kogure, T., Stanjek, H. (2006): Summary of recommendations of nomenclature committees relevant to clay mineralogy: report of the Association international pour l´Etude des Argiles (AIPEA) nomenclature committee for 2006. Clay Minerals **41**, 863-877.

Guggenheim, S., Kaoster van Groos, A.F. (2001): Baseline studies of the clay minerals society source clays: thermal analysis. Clays & Clay Minerals **49**, 433-443.

Gyarmati, P. (1977): Intermediate volcanism in the Tokaj Mts. - Annales Instituti Geologici Publici Hungarici (Annals of the Hung. Geol. Inst.) **58**, 196 pp.

H

Halamickova, P., Detwiler, R.J., Bentz, D.P., Garboczi, E.J. (1995): Water permeability and chlorite ion diffusion in Portland cement mortars: Relationship to sand content and critical pore diameter. Cement and Concrete Research **25(4)**, 790-802.

Hamzaoui, R., Muslim, F., Guessasma, S., Bennabi, A., Guillin, J. (2015): Structural and thermal behaviour of proclay kaolinite using high energy ball milling process. Powder Technology **271**, 228-237.

Harvey, C.C., Lagaly, G. (2013): Industrial Applicationd. In: Bergaya, F., Lagaly, G. (Eds.): Handbook of clay science. Elsevier, Amsterdam, 451-490.

Hawkes, P.W., Spence, J.C.H. (Eds.) (2007): Science of Microscopy. Springer, New York, 1227 pp.

Hay, R.L. (1986): Geologic occurrence of zeolites and some associated minerals. Pure and Applied Chemistry **58(10)**, 1339-1342.

He, C., Makovicky, E., Osbæck, B. (1995): Thermal stability and pozzolanic activity of calcined illite. Applied Clay Science **9**, 337-354.

Heller, L. (1962): The thermal transformation of pyrophyllite to mullite. American Mineralogist **47(1-2)**, 156-157.

Heller-Kallai, L., Lapides, I. (2007): Reactions of kaolinites and metakaolinites with NaOH – comparison of different samples (Part 1). Applied Clay Science **35**, 99-107.

Helyar, K.R., Porter, W.M. (1989): Soil acidification, its measurement and the processes involved. In: Robson, A.D. (Ed.), Soil acidity and plant growth. Academic Press Australia, Marrickville, NSW, 61-101.

Hemingway, B.S., Robie, R.A., Kittrick, J.A. (1978): Revised values for the Gibbs free energy of formation of [$Al(OH)^-_{4\ aq}$], diaspore, boehmite and bayerite at 298.15 K and 1 bar, the thermodynamic properties of kaolinite to 800 K and 1 bar, and the heats of solution of several gibbsite samples. Geochimica et Cosmochimica Acta **42**, 1533-1543.

Hemminger, W.F., Cammenga, H.K. (1989): Methoden der Thermischen Analyse. Springer Verlag, Heidelberg, 299 pp.

Henning, K.-H. (1968): Mineralogische Untersuchungen eozäner Tone aus der Lagerstätte Friedland und aus Bohrungen in Mecklenburg. Doctoral thesis, University Greifswald.

Henning, K.-H., Störr, H. (1986): Electron micrographs (TEM, SEM) of clays and clay minerals. Schriftenreihe für Geologische Wissenschaften 25, Akademie-Verlag, Berlin, 350.

Henning, K.-H. & Kasbohm, J. (1998): Mineralbestand und Genese feinkörniger quartärer und präquartärer Sedimente in Nordostdeutschland unter besonderer Berücksichtigung des „Friedländer Tones“. Jahrestagung der deutschen Ton- und Tonmineralgruppe (DTTG) in Greifswald 1998, Band **6**, 147-162.

Hindman, J.R. (2006): Vermiculite. In: Kogel, J.E., Trivedi, N.C., Barker, M.J., Krukowski, S. (Eds.): Industrial Minerals and Rocks, Commodities, Markets and Uses. 7th ed. Society of Mining, Metallurgy and Exploration, 1015-1026.

Hillier, S., Marwa, E.M.M., Rice, C.M. (2013): On the mechanism of exfoliation of ´Vermiculite´. Clay Minerals **48**, 563-582.

Hofmann, U., Jacob, A., Loofman, H. (1941): Untersuchung der Tonfraktion der Böden mit dem Elektronen-Mikroskop. Bodenkunde und Pflanzenernährung **25**, 5-6, 257-271.

Hofmann, U., Klemen, E. (1950): Verlust der Austauschfähigkeit von Lithiumionen an Bentonit durch Erhitzung. Zeitschrift für Anorganische und Allgemeine Chemie **262**, 95-99.

Hounsi, A.D., Lecomte-Nana, G.L., Djétéli, G., Blanchart, P. (2013): Kaolin-based geopolymers: Effect of mechanical activation and curing process. Construction and Building Materials **42**, 105-113.

Hu, N. (2015): Geopolymerizsation of illite/smectite (Friedland Clay) – An investigation of reaction processes, microstructure and strength development. Dissertation. Submitted.

I

Ilkeyné Perlaki, E., Pentelényi, L. (1968): Hollóháza – Füzérkajata. – Explanatory notes on the geological map of the Tokaj Mts., Series 1:25.000. 1-77. Hungarian Institute of Geology, Budapest.

Inoue, A., Kohyama, N., Kitagawa, R., Watanabe, T. (1987): Chemical and morphological evidence for the conversion of smectite to illite. Clays & Clay Minerals **35**, 111-120.

Inoue, A., Velde, B., Meunier, A., Touchard, G. (1988): Mechanism of illite formation during smectite to illite conversion in a hydrothermal system. American Mineralogist **73**, 1325-1334.

Ishikawa, K., Yoshioka, T., Sato, T., Okuwaki, A. (1997): Solubility of hematite in LiOH, NaOH and KOH solutions. Hydrometallurgy **45**, 129-135.

J

Jagodzinski, H. (1949): Eindimensionale Fehlordnung in Kristallen und ihr Einfluss auf die Röntgeninterferenzen. I. Berechnung des Fehlordnungsgrades aus den Röntgenintensitäten. Acta Crystallographica **2**, 201-207.

Jakobsen, H.J., Nielsen, N.C., Lindgreen, H. (1995): Sequences of charged sheet in rectorite. American Mineralogist **80**, 247-252.

Jeans, C.V., Fisher, M.J., Merriman, R.J. (2005): Origin of the clay mineral assemblages in the Germanic facies of the English Trias: application of the spore colour index method. Clay Minerals **40**, 115-129.

Jiang, T., Li, G., Qiu, G., Fan, X., Huang, Z. (2008): Thermal activation and alkali dissolution of silicon from illite. Applied Clay Science **40**, 81-89.

K

Karnland, O., Olsson, S., Nilsson, U. (2006): Mineralogy and sealing properties of various bentonites and smectite-rich clay materials. Technical Report **TR-06-30**. Svensk Kärnbränslehantering AB (SKB), Stockholm, 70 pp.

Katzung, G. (2004): Geologie von Mecklenburg-Vorpommern. Schweizerbart´sche Verlagsbuchhandlung, Science Publishers, Stuttgart, Germany, 580 pp.

Kaufhold, S., Dohrmann, R., Koch, D., Houben, G. (2008): The pH of aqueous bentonite suspensions. Clays & Clay Minerals **56(3)**, 338-343.

Kaufhold, S., Dohrmann, R., Stucki, J.W., Anastácio, A.S. (2011): Layer charge density of smectite – closing the gap between the structural formula method and the alkylammonium method. Clays & Clay Minerals **59(2)**, 200-211.

Kaufhold, S., Hein, M., Dohrmann, R., Ufer, K. (2012): Quantification of the mineralogical composition of clays using FTIR spectroscopy. Vibrational Spectroscopy **59**, 29-39.

Kemp, S.J., Merriman, R.J., Bouch, J.E. (2005): Clay mineral reaction progress - the maturity and burial history of the Lias Group of England and Wales. Clay Minerals **40**, 43-61.

Kestin, J., Sokolov, M., Wakeham, W.A. (1978): Viscosity of Liquid Water in the Range -8°C to 150°C. Journal of Physical and Chemical Reference Data **7(3)**, 941-948.

Kim, Jin-Keun, Yi, Seong-Tae (2002): Application of size effect to compressive strength of concrete members. Sadhana **27(4)**, 467-484.

Kiss, L., Takáts, T. (1963): Mineralogical investigations on the material of the Füzérradvány illite mines with respect of the fine ceramic industry. - Építésanyagipari Központi Kutató Intézet, Tudományos Közlemények **10**, 1-62, 1-35. melléklet. ÉM. Építésügyi Dokumentációs Iroda, Budapest.

Kitagawa, R. (1997): Surface microtopography of rectorite (allevardite) from Allevard, France. Clay Minerals **32**, 89-95.

Kleeberg, R. (1996): Quantitative Röntgenphasenanalyse an schichtsilikathaltigen Gesteinen mit der RIETVELD-Methode – Probleme, Erfolge und Grenzen. Beiträge zur Jahrestagung der DTTG Freiberg 1996, 127-137.

Kleeberg, R., Bergmann, J. (2002): Quantitative phase analysis using the Rietveld method and a fundamental parameter approach. Proceedings of the II International School on Powder Diffraction, 63-76.

Kleeberg, R. (2005): Results of the second Reynolds Cup contest in quantitative mineral analysis. International Union of Crystallography (IUCr) Commission for Powder Diffraction (CPD) Newsletter **30**, 22-26.

Kleeberg, R. (2009): State-of-the-art and trends in quantitative phase analysis of geological and raw materials. Zeitschrift für Kristallographie Supplements **30**, 47-52.

Klimentidis, R.E., Mackinnon, I.D.R. (1986): High resolution imaging of ordered mixed-layer clays. Clays & Clay Minerals **34**, 155-164.

Kloprogge, J.T., Ruan, H.D., Frost, R.L. (2002): Thermal decomposition of bauxite minerals: infrared emission spectroscopy of gibbsite, boehmite and diaspore. Journal of Materials Science **37(5)**, 1121-1129.

Kodama, H. (1966): The nature of the component layers of rectorite. American Mineralogist **51**, 1035-1055.

Koskinen, V. (2012): Uniaxial backfill block compaction. Fortum Power and Heat Oy. Working Report **2012-21**. 46 pp.

Köster, H.M. (1993): Dreischichtminerale oder 2:1 Schichtsilikate. In: Jasmund, K., Lagaly, G. (Eds.), Tonminerale und Tone. Steinkopff Verlag, Darmstadt, Germany, 42-58.

Kühn, H. (2014): Straßenbau A-Z. Sammlung Technischer Regelwerke und Amtlicher Bestimmungen für das Straßenwesen. Forschungsgesellschaft für Straßen- und Verkehrswesen (ed.), Erich Schmidt Verlag, Berlin, 16976 pp.

Kumar, S., Kumar, R. (2011): Mechanical activation of fly ash: Effect on reaction, structure and properties of resulting geopolymer. Ceramics International **37**, 533-541.

Kumpulainen, S., Kiviranta, l. (2010): Mineralogical and chemical characterization of various bentonite and smectite-rich clay materials. POSIVA Oy. Working Report 2010-52. Eurajoki, Finland, 55 pp.

L

Lagaly, G., Weiss, A. (1971): Neue Methoden zur Charakterisierung und Identifizierung quellungsfähiger Dreischichttonminerale. Zeitschrift für Pflanzenernährung und Bodenkunde **130(1)**, 9-24.

Lagaly, G. (1981): Characterization of clays by organic compounds. Clay Minerals **16**, 1-21.

Langmuir, I. (1918): The adsorption of gases on plane surfaces of glass, mica and platinum. Journal of the American Chemical Society **40**, 1361-1402.

Lantenois, S., Muller, F., Beny, J.-M., Mahiaoui, J., Champallier, R. (2008): Hydrothermal synthesis of beidellites: characterization and study of the cis- and trans-vacant character. Clays & Clay Minerals **55**, 39-48.

Lashof, D.A., Ahuja, D.R. (1990): Relative contribution of greenhouse gas emissions to global warming. Letters to Nature **344**, 529-531.

Lee, W.K.W., van Deventer, J.S.J. (2002): The effects of inorganic salt contamination on the strength and durability of geopolymers. Colloids and Surfaces A: Physicochemical and Engineering Aspects **211(2-3)**, 115-126.

Lemmon, E. W., Penoncello, S. G. (1994): The Surface Tension of Air and Air Component Mixtures. Advances in Cryogenic Engineering **39**, 1927-1934.

Liebau, F. (1985): Structural Chemistry of Silicates: Structure, bonding and classification. Springer-Verlag, Berlin, Heidelberg, 354 pp.

Liu, H.-B., Sun, Y., Chen, Y.-G. (2010): CCDC 683103: Experimental Crystal Structure Determination. Cambridge Crystallographic Data Centre, http://dx.doi.org/10.5517/ccqxtl0.

M

MacEwan, D.M.D. (1958): Fourier transform methods for studying X-ray scattering from lamellar systems. II. The calculation of X-ray diffraction effects from various type of interstratification. Kolloidzeitschrift **156**, 61-67.

Mackenzie, R. C. (1951): A micromethod for determination of cation-exchange capacity of clay. Journal of Colloid Science **6**, 219-222.

Mackenzie, R.C. (1964): The thermal investigation of soil clays. In: Rich, C.I., Kunze, G.W. (Eds.): Soil Clay Mineralogy, The University of North Caroline Press, Chapel Hill, North Caroline, USA, 200-244.

MacKenzie, K.J.D., Komphanchai, S., Vagana, R. (2008): Formation of inorganic polymers (geopolymers) from 2:1 layer lattice aluminosilicates. Journal of the European Ceramic Society **28(1)**, 177-181.

MacKenzie, K.J.D. (2009): Utilisation of non-thermally activated clays in the production of geopolymers. In: Provis, J., van Deventer, J.S.J. (Eds.): Geopolymers. Structure, processing, properties and industrial applications, Woodhead Publishing Limited, Cambridge, UK, 294-314.

Maegdefrau, E., Hofmann, U. (1937): Glimmerartige Mineralien als Tonsubstanzen. Zeitschrift für Kristallographie **98(1)**, 31-59.

Massiot, D., Fayon, F., Capron, M., King, I., Le Calé, S., Alonso, B., Durand, J.-O., Bujoli, B., Gan, Z., Hoatson, G. (2002): Modelling one- and two-dimensional solid-state NMR spectra. Magnetic resonance in chemistry **40**, 70-76.

Mátyás, E. (1974): A recently explored high-quality clay deposit rich in illite at Füzérradvány. - Bány. Koh. L., Bányászat **107(3)**, 187-196.

Matsuda, T., Kodama, H., Yang, A.F. (1997): Ca-rectorite from Sano Mine, Nagano Prefecture, Japan. Clays & Clay Minerals **45(6)**, 773-780.

McCarty, D.K. (2002): Quantitative mineral analysis of clay bearing mixtures: The Reynolds Cup contest. International Union of Crystallography (IUCr) Commission for Powder Diffraction (CPD) Newsletter **27**, 12-16

McFarland, J.D. (2004): Stratigraphic summary of Arkansas. Information Circular 36, Arkansas Geological Commission, Little Rock, Arkansas, 38 pp.

McHardy, W.J., Wilson, M.J., Tait, J.M. (1982): Electron microscope and X-ray diffraction studies of filamentous illitic clay from sandstones of the Magnus Field. Clay Minerals **17**, 23-39.

McLellan, B.C., Williams, R.P., Lay, J., van Riessen, A., Corder, G.D. (2011): Costs and carbon emissions for geopolymer pastes in comparison to ordinary portland cement. Journal of Cleaner Production **19(9-10)**, 1080-1090.

Meier, L. P., Kahr, G. (1999): Determination of the cation exchange capacity (CEC) of clay minerals using the complexes of copper(II) ion with triethylenetetramine and tetraethylenepentamine. Clays & Clay Minerals **47(3)**, 386-388.

Méring, P.J. (1949): L´Interférence des rayons X dans les systèms à stratification désordonée. Acta Crystallographica **2**, 371-377.

Merriman, R.J. (2005): Clay minerals and sedimentary basin history. European Journal of Mineralogy **17**, 7-20.

Meunier, A. (2005): Clays. Springer, Berlin, 472 pp.

Meunier, A., 2010. Formation mechanisms of mixed-layer clay minerals. In: Fiore, S., Cuadros, J., Huertas, F.J. (Eds.), Interstratified Clay Minerals. Origin, Characterization and Geochemical Significance. AIPEA Educational Series, Vol. 1. Digilabs, Bari, Italy, 53-71.

Michael, P.J., McWhinnie, W.R. (1989): Mössbauer and ESR studies of the thermochemistry of illite and montmorillonite. Polyhedron **8(22)**, 2709-2718.

Miser, H.D., Milton, C. (1964): Quartz, rectorite, and cookeite from the Jeffrey Quarry, near North Little Rock, Pulaski County, Arkansas. Arkansas Geological Commission Bulletin **21**, 29 pp.

Molnár, F., Zelena, T., Mátyás, E., Pécskay, Z., Bajnóczi, B., Kiss, J., Horváth, I. (1999): Epithermal mineralization of the Tokaj Mountains, Northeast Hungary: Shallow levels of low-sulfidation type systems. In: Molnár, F., Lexa, J., Hedenquist, J.W. (Eds.): Epithermal mineralization of the Western Carpathians. Society of Economic Geologists, Guidebook Series **31**, 109-153.

Moore, D.M., Reynolds Jr., R.C. (1997): X-ray Diffraction and the Identification and Analysis of Clay Minerals. Oxford University Press, Oxford, New York, 378 pp.

Morse, J.W., Casey, W.H. (1988): Ostwald processes and mineral paragenesis in sediments. American Journal of Science **288**, 537–560.

Mukhopadhyay, T.K., Ghatak, S., Maiti, H.S. (2010): Pyrophyllite as raw material for ceramic applications in the perspective of its pyro-chemical properties. Ceramics INternational **36**, 909–916.

N

Nadeau, P.H., Wilson, M.J., McHardy, W.J., Tait, J.M. (1984a): Interparticle diffraction: A new concept for interstratified clays. Clay Minerals **19**, 757-769.

Nadeau, P.H., Wilson, M.J., McHardy, W.J., Tait, J.M. (1984b): Interstratified clays as fundamental particles. Science **225**, 923-925.

Nadeau, P.H., Wilson, M.J., McHardy, W.J., Tait, J.M. (1985): The conversion of smectite to illite during diagenesis: evidence from some illitic clays form bentonites and sandstones. Mineralogical Magazine **49**, 393-400.

Nemecz, E., Varju, G. (1970): Chemical and structural investigation of Sárospatakites (Illite/montmorillonite). - Földt. Közl. (Bulletin of the Hungarian Geological Society) **100(1)**, 11-22.

Nieto, F., Ortega-Huertas, M., Peacor, D., Arostegui, J. (1996): Evolution of illite-smectite from early diagenesis through incipient metamorphism in sediments of the Basque-Can-tabrian basin. Clays & Clay Minerals **44**, 304–323.

Nieto, F., Arroyo, X. (2013): Identification and characterization with microscopic methods. In: Fiore, S., Cuadros, J., Huertas, F.J. (Ed.): Interstratified Clay Minerals. Origin, Characterization & Geochemical Significance, AIPEA Educational Series **1**, Digilabs, Bari, Italy, 73-88.

O

Omotoso, O., McCarty, D.K., Hillier, S., Kleeberg, R. (2006): Some successful approaches to quantitative mineral analysis as revealed by the 3rd Reynolds Cup contest. Clays & Clay Minerals **54(6)**, 748-760.

P

Pareira, J.A.M., Schwaab, M., Dell´Oro, E., Pinto, J.C., Monteiro, J.L.F., Henriques, C.A. (2009): The kinetics of gibbsite dissolution in NaOH. Hydrometallurgy **96**, 6-13.

Patzkó, Á., Szántó, F. (1983): Peptisation and organophylisation of Füzérradvány illite (abstract). Symposium on Illite of the Hungarian Geological Society, Zamárdi, 1983, Program, 23.

Peacor, D.R. (1992):. Diagenesis and low-grade metamorphism of shales and slates. In: Buseck, P.R. (Ed.), Minerals and Reactions at the Atomic Scale: Transmission Electron Microscopy. Reviews in Mineralogy **27**, Mineralogical Society of America, Washington, DC, 335–380.

Pécskay, Z., Balogh, K., Széky-Fux, V., Gyarmati, P. (1986): Geochronological investigations on the Neogene volcanism of the Tokaj Mountains. Geologica Carpathica **37**, 635-655.

Pécskay,Z., Balogh, K., Széky-Fux, V., Gyarmati, P. (2006): Geochronology of Neogene magmatism in the Carpathian arc and intra-Carpathian area. Geologica Carpathica **57**, 511-530.

Pennycook, S.J., Nellist, P.D. (Eds.) (2011): Scanning Transmission Electron Microscopy. Springer Science+Business Meadia, New York, Dordrecht, Heidelberg, London, 774 pp.

Perrin-Sarazin, F., Sepehr, M., Bouaricha, S., Denault, J. (2009): Potential of ball milling to improve clay dispersion in nanocomposites. Polymer Engineering and Science **49**, 651-665.

Pevear, D.R. (1999): Illite and hydrocarbon exploration. Proceedings of the National Academy of Sciences of the United States of America **96**, 3440-3446.

Podlech, C. (2013): Untersuchung thermischen Verhaltens (bis 1000 °C) verschiedener Korngrößenfraktionen von Friedlandton. Bachelor of Science (B.Sc.) thesis, University Greifswald, Germany, unpublished.

Pusch, R. (1998): Backfilling with mixtures of bentonite/ballast material or natural smectitic clay. Technical report, TR-98-16. Svensk Kärnbränslehantering AB (SKB), Stockholm, 52 pp.

Pusch, R. (2001): The buffer and backfill handbook. Part 2: Materials and techniques. Technical Rangan, B.V. (2010): Fly ash-based geopolymer concrete. Proceedings of the international workshop on geopolymer cement and concrete, Allied Publishers Private Limited, Mumbai, India, Dec 2010, 68-106.

R

Reynolds, R.C. (1980): Interstratified clay minerals. In: Brindley, G.W., Brown, G. (Eds.), Crystal Structures of Clay Minerals and their X-ray identification. Mineralogical Society, London, 249-303.

Reynolds, R.C. (1985): NEWMOD, a computer program for the calculation of the basal diffraction intensities of mixed-layered clay minerals. R.E. Reynolds, 8 Brook Rd. Hanover NH.

Reynolds, R. C. jr. (1992): X-ray diffraction studies of illite/smectite from rocks, <1 μm randomly oriented powders, and <1 μm oriented powder aggregates: the absence of laboratory-induced artifacts. Clays & Clay Minerals **40(4)**, 387-396.

Richards, I.J., Connelly, J.B., Gregory, R.T., Gray, D.R. (2002): The importance of diffusion, advection, and host-rock lithology on vein formation: A stable isotope study from the Paleozoic Ouachite orogenic belt, Arkansas and Oklahoma. Geological Society of America Bulletin **114(11)**, 1343-1355.

Richter, F. (2000): Glazialtektonische Untersuchungen in der Eozänlagerstätte Friedland (Tagebau „Siedlungsscholle“). Neubrandenburger Geologische Beiträge **1**, 91-101.

Rieder, M., Cavazzini, G., D´Yakonov, Y.S., Frank-Kamenetskii, V.A., Gottardi, G., Guggenheim, S., Koval, P.V., Müller, G., Neiva, A.M.R., Radoslovich, E.W., Robert, J.-L., Sassi, F.P., Takeda, H., Weiss, Z., Wones, D. (1998): Nomenclature of micas. Canadian Mineralogist **36**, 41-48.

Rietveld, H. M. (1967): Line profiles of neutron powder-diffraction peaks for structure refinement. Acta Crystallographica **22**, 151-152.

Rietveld, H. M. (1969): A profile refinement method for nuclear and magnetic structures. Journal of Applied Crystallography **2**, 65-71.

Rimmer, D.L., Greenland, D.J. (1976): Effects of calcium carbonate on the swelling behaviour of a soil clay. Journal of Soil Science **27**, 129-139.

Rocha, J., Klinowski, J. (1990): 29Si and 27Al Magic-angle-spinning NMR studies of the thermal transformation of kaolinite. Physics and Chemistry of Minerals **17**, 179-186.

S

Sagoe-Crentsil, K., Weng, L. (2007): Dissolution processes, hydrolysis and condensation reactions during geopolymer synthesis: Part II. High Si/Al ratio systems. Journal of Materials Science **42**, 3007-3014.

Schollenberger, C. J., Dreibelbis, F. R. (1930): Analytical methods in base exchange investigations on soils. Soil Science **30(3)**, 161-174.

Schomburg, J. (1985): Thermal investigations of pyrophyllites. Thermochimica Acta **93**, 521-524.

Seisenbaeva, G. A., Daniel, G., Nedelec, J.-M., Kessler, V.G. (2013): CCDC 915222: Experimental Crystal Structure Determination., Cambridge Crystallographic Data Centre, http://dx.doi.org/10.5517/cczqc9b.

Smykatz-Kloss, W. (1967): Über die Möglichkeit der halbquantitativen Mineralbestimmung mit der DTA ohne Flächenintegration. Contributions to Mineralogy and Petrology **16**, 481-502.

Smykatz-Kloss, W. (1974): Differential thermal analysis. Application and results in mineralogy. Springer-Verlag, Berlin, Heidelberg, New York, 185 pp.

Sperberga, I., Sedmale, G., Stinkulis, G., Zeila, K., Ulme, D. (2011): Comparative study of illite clay and illite-based geopolymer products. IOP Conference Series: Materials Science and Engineering **18(222027)**, 1-4.

Środoń, J. (1984): X-ray powder diffraction identification of illitic materials. Clays & Clay Minerals **32(5)**, 337-349.

Środoń, J., Eberl, D.D. (1984): Illite. In: Bailey, S.W. (Ed.), Micas. Reviews in Mineralogy, **13**. Mineralogical Society of America, 495-544.

Środoń, J., Andreoli, C., Elsass, E., Robert, M. (1990): Direct high resolution transmission electron microscopic measurements of expandability of mixed-layer illite-smectite in bentonite rock. Clays & Clay Minerals **38**, 373-379.

Środoń, J., Elsass, F., McHardy, W.J., Morgan, D. J. (1992): Chemistry of illite-smectite inferred from TEM measurements of fundamental particles. Clay Minerals **27(2)**, 137-158.

Środoń, J. (2010): Evolution of mixed-layer clay minerals in prograde alteration systems. In: Fiore, S., Cuadros, J., Huertas, F.J. (Eds.), Interstratified Clay Minerals. Origin, Characterization and Geochemical Significance. AIPEA Educational Series, vol. 1. Digilabs, Bari, Italy, 114–175.

Środoń, J. (2013): Identification and Quantitative Analysis of Clay Minerals. In: Bergaya, F., Lagaly, G. (Eds.): Handbook of Clay Science, Elsevier, Amsterdam, 25-49.

Steudel, A. (2008): Selection strategy and modification of layer silicates for technical applications. Fakultät für Bauingenieur-, Geo- und Umweltwissenschaften, Karlsruhe. Universität Fridericiana zu Karlsruhe (TH), Germany, 168 pp.

Steudel, A., Weidler, P.G., Schuhmann, R., Emmerich, K. (2009): Cation exchange reactions of vermiculite with Cu-triethylenetetramine as affected by mechanical and chemical treatment. Clays & Clay Minerals **54 (4)**, 486-493.

Steudel, A., Emmerich, K. (2013): Strategies for the successful preparation of homoionic smectites. Applied Clay Science **75-76**, 13-21.

Stevens, R.E. (1946): A system for calculating analyses of micas and related minerals to end members. United States Geological Survey Bulletin **950**, 101-119.

Stone, D.M., Lumsden, D.N. (1984): Secondary porosity in the upper Jackfork Sandstone (Pennsylvanian), Little Rock-Arkadelphia, Arkansas. Journal of Sedimentary Petrology **54(3)**, 899-907.

Sun, W., Zhang, Y., Liu, Z. (2004): In situ monitoring of the hydration process of K-PS geopolymer cement with ESEM. Cement and Concrete Research **34**, 935-940.

Szegedi, Á. (1988): Mixed layer character of "illites" from Füzérradvány, Hungary. In: Konta, J. (ed.): Tenth Conference on Clay Mineralogy and Petrology, Ostrava, 1986, 249-254. Univerzita Karlova, Praha.

T

Temuujin, J., Minjigmaa, A., Rickard, W., Lee, M., Williams, I., van Riessen, A. (2009): Preparation of metakaolin based geopolymer coatings on metal substrates as thermal barriers. Applied Clay Science **46(3)**, 265-270.

Treacy, M.M.J., Newsam, J.M., Deem, M.W. (1991): A general recursion method for calculating diffracted intensities from crystals containing planar faults. Proceedings of the Royal Society of London. Series A: Mathematical and Physical Sciences **433(1889)**, 499-520.

Tributh, H., Lagaly, G. (1986): Aufbereitung und Identifizierung von Boden- und Lagerstättentonen. II. Korngrößenanalyse und Gewinnung von Tonsubfraktionen. GIT Fachzeitung **30**, 771-776.

Tsipursky, S.I., Drits, V.A. (1984): the distribution of octahedral cations in the 2:1 layers of dioctahedral smectites studied by oblique texture electron diffraction. Clay Minerals **19**, 177-192.

U

Ufer, K., Stanjek, H., Roth, G., Dohrmann, R., Kleeberg, R., Kaufhold, S., (2008): Quantitative phase analysis of bentonites by the Rietveld method. Clays & Clay Minerals **60(5)**, 507-534.

Ufer, K., Kleeberg, R., Bergmann, J., Dohrmann, R. (2012a): Rietveld refinement of disordered illite-smectite mixed-layer structures by a recursive algorithm. I: One-dimensional patterns. Clays & Clay Minerals **60(5)**, 507-534.

Ufer, K., Kleeberg, R., Bergmann, J., Dohrmann, R. (2012b): Rietveld refinement of disordered illite-smectite mixed-layer structures by a recursive algorithm. II: Powder-pattern refinement and quantitative phase analysis. Clays & Clay Minerals **60(5)**, 535-552.

V

Veblen, D.R., Guthrie jr., G.D., Livi, K.J.T., Reynolds jr., R.C. (1990): High-resolution transmission electron microscopy and electron diffraction of mixed-layer illite/smectite: experimental results. Clays & Clay Minerals **38(1)**, 1-13.

Viczián, I. (1997): Hungarian investigations on the “Zempleni” illite. Clays & Clay Minerals 45(1), 114-115.

Viczián, I., Zelenka, T., Molnár, F. (2004): Clay deposits and the “illite” at Korom Hill, Füzérradvány, Tokay Mts. In: Raucsik, B., Viczián, I. (Eds.): 2nd Mid-European Clay Conference, Miskolc, 2004. Field guide, 24-33.

Villieras, F., Yvon, J., Cases, J.M., De Donate, P., Lhote, F., Baeza, R. (1994): Development of microporosity in clinochlore upon heating. Clays & Clay Minerals **42(6)**, 649-688.

W

Wang, X., Du, Y., Luo, J., Lin, B., Kennedy, J.F. (2006): Chitosan/organic rectorite nanocomposite films: Structure, characteristic and drug delivery behavior. Carbohydrate Polymers **69**, 41-49.

Wang, M.R., Jia, D.C., He, P.G., Zhou, Y. (2010): Influence of calcination temperature of kaolin on the structure and properties of final geopolymer. Materials Letters **64(22)**, 2551-2554.

Warr, L.N., Grathoff, G.H. (2012): Geoscientific applications of particle detection and imaging techniques with special focus on the monitoring clay mineral reactions. In: Grupen, C., Buvat, I. (Ed.): Handbook of Particle Detection and Imaging, Springer, Berlin, Heidelberg, 1226 pp.

Weaver, C.E. (1979): Geothermal alteration of clay and shales: Diagenesis. ONWI-21, Technical Report. Georgia Institute of Technology, Atlanta, GA, 176 pp.

Wolters, F., Emmerich, K. (2007): Thermal reactions of smectites – Relation of dehydroxylation temperature to octahedral structure. Thermochimica Acta **462**, 80-88.

Wolters, F., Lagaly, G., Kahr, G., Nueesch, R., Emmerich, K. (2009): A comprehensive characterization of dioctahedral smectites. Clays & Clay Minerals **57(1)**, 115-133.

X

Xu, H., van Deventer, J.S.J. (2003): The effect of alkali metals on the formation of geopolymeric gels from alkali-feldspars. Colloids and Surfaces A: Physicochemical and Engineering Aspects **216(1-3)**, 27-44.

Y

Yang, H., Yang, W., Hu, Y., Du, C., Tang, A. (2005): Effect of Mechanochemical Processing on Illite Particles. Particle & Particle Systems Characterization **22**, 207-211.

Yariv, S., Lapides, I. (2000): The effect of mechanochemical treatments on clay minerals and the mechanochemical adsorption of organic materials onto clay minerals. Journal of Materials Synthesis and Processing **8**, 223-233.

Yusihami, E., Gilkes, R. (2012): Rehydration of heated gibbsite, kaolinite and goethite: An assessment of properties and environmental significance. Applied Clay Science **64**, 61-74.

Z

Zhan, W., Guggenheim, S. (1995): The dehydroxylation of chlorite and the formation of topotactic product phases. Clays & Clay Minerals **43(5)**, 622-629.

Zhang, Z.S., Sun, W., Li, J.Z. (2005): Hydration process of interfacial transition in potassium polysialate (K-PSDS) geopolymer concrete. Magazine of Concrete Research **57**, 33-38.

Zumsteg, R., Puzrin, A.M. (2012): Stickness and adhesion of conditioned clay pastes. Tunnelling and underground Space Technology **31**, 86-96.

Zumsteg, R., Plötze, M., Puzrin, A.M. (2013a): Reduction of the clogging potential of clays: new chemical applications and novel quantification approaches. Géotechnique **63(4)**, 276-286.

Zumsteg, R., Plötze, M., Puzrin, A.M. (2013b): Effects of dispersing foam and polymers on the mechanical behaviour of clays pastes. Géotechnique **63(11)**, 920-933.

Index of figures

Index of tables

Acknowledgements

I am using this opportunity to express my gratitude to all persons who supported me throughout the course of this thesis. First of all, I would like to thank my supervisors, Prof. Laurence N. Warr, Ph.D., and Georg H. Grathoff, Ph.D. for valuable discussions and a critical revision of the manuscript. Thank you for your patience and many helpful ideas and constructive suggestions throughout the geopolymer project and my thesis. Thank you for giving your time so generously. Next I would like to express my special appreciation and thanks to PD Dr. Katja Emmerich and Dr. Annett Steudel (Karlsruhe Institute of Technology) for their introduction into STA-MS and CEC measurements, constructive criticism including hours of helpful discussions and invaluably friendly advices. Thank you for your constant support. I want to thank Dr. Marko Bertmer (Leipzig University) who introduced me to solid state NMR spectroscopy and who gave me the opportunity to visit his laboratory for making NMR measurements. Advice and an advanced introduction into BGMN program and structural models of interstratifications given by Dr. Reinhard Kleeberg (TU Freiberg) and Dr. Kristian Ufer (BGR Hannover) have been a tremendous help. Your constant support by answering countless of questions is acknowledged. Furthermore I want to thank Dr. Kristian Ufer and Dr. Stephan Kaufhold (BGR Hannover) for helpful and interesting discussions and valuable comments to the manuscript. A special thanks to Dr. Alexander Kämpfe (TU Freiberg / Federal Environment Agency) for many helpful discussions and brilliant comments and suggestions concerning organic and inorganic chemistry. Thank you for your support as a chemist and as a friend.

Prof. Dr. Maria-Theresia Schafmeister, Dr. Tammo Meyer, Gabriele Wiederholt, Dr. Jürgen Eidam and Robert Mrotzek provided opportunity and support for flame-AAS and XRF measurements and Dr. Heike Kahlert for pH measurements. Thank you. My special thanks go to Manfred Zander who provided assistance concerning TEM measurements and technical issues. I would like to extend my thanks to our secretary Renate Martens for support with administration issues. Christian Städtke (Bauten und Umweltinstitut Friedland) is acknowledged for discussions about compressive strength. Additionally, I am very grateful to all colleagues including students who supported me with their laboratory work.

I would like to offer my special thanks to Dr. Ulrich König, Klaus Jugl, and Bodo Warnke (all Mineralische Rohstoffmanagement GmbH) for providing the Friedland clay samples used in this study. I also want to acknowledge the funding source of the geopolymer project making up a large part of this thesis, the "Förderung von Forschung, Entwicklung und Innovation" funded by the „Ministerium für Wirtschaft, Bau und Tourismus Mecklenburg-Vorpommern". Thank you, German Clay and Clay Mineral Group (DTTG) for financial support that gave me the opportunity to visit the 51st Annual CMS Conference 2014 in Texas.

Finally, I sincerely wish to thank my whole family and friends for their continuous support and encouragement they gave me over all the years and Jasmaria for her help with graphics and text of this thesis and her appreciative patience and unconfined backing. Thank you!

Appendix

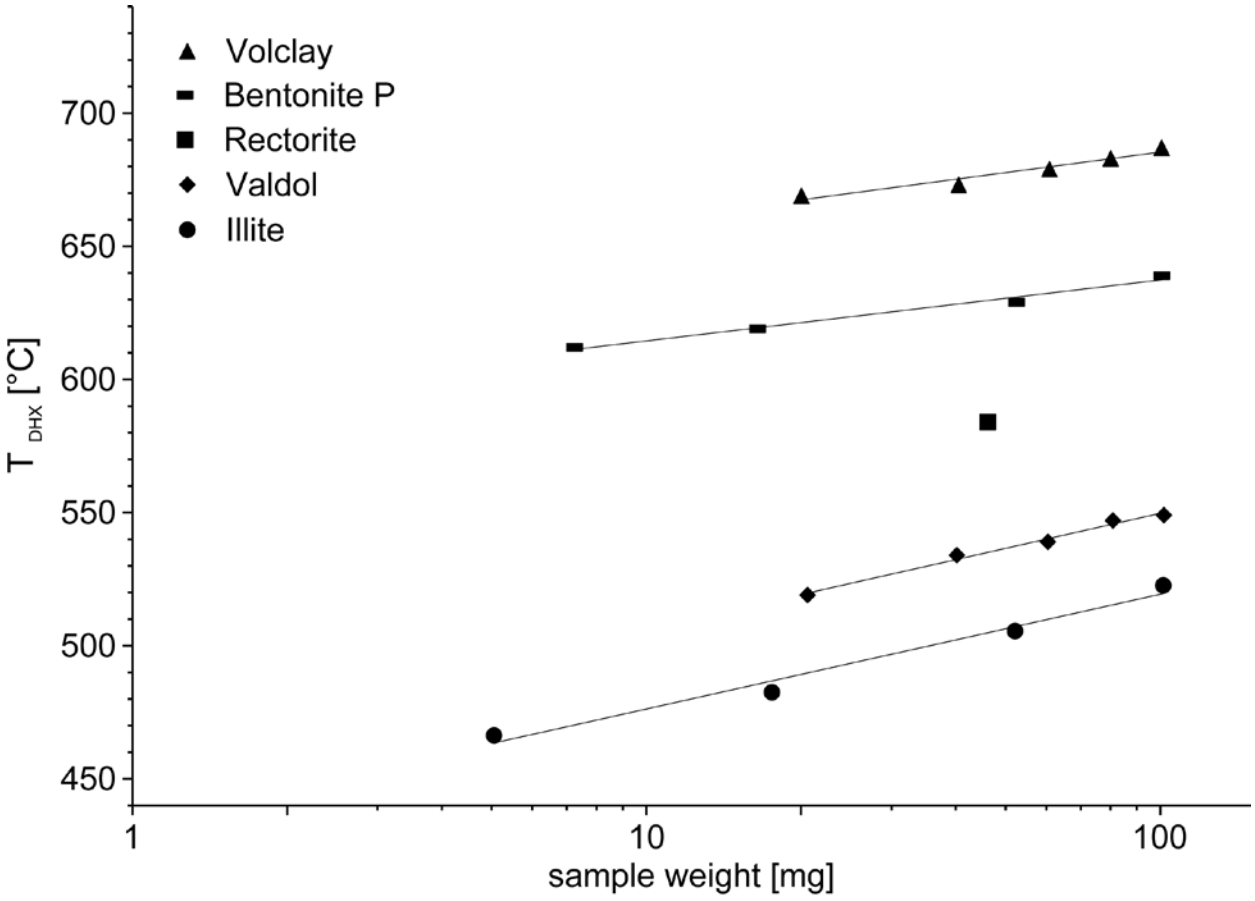

Appendix i. PA curves of smectite and illite reference materials to estimate the PA of rectorite.

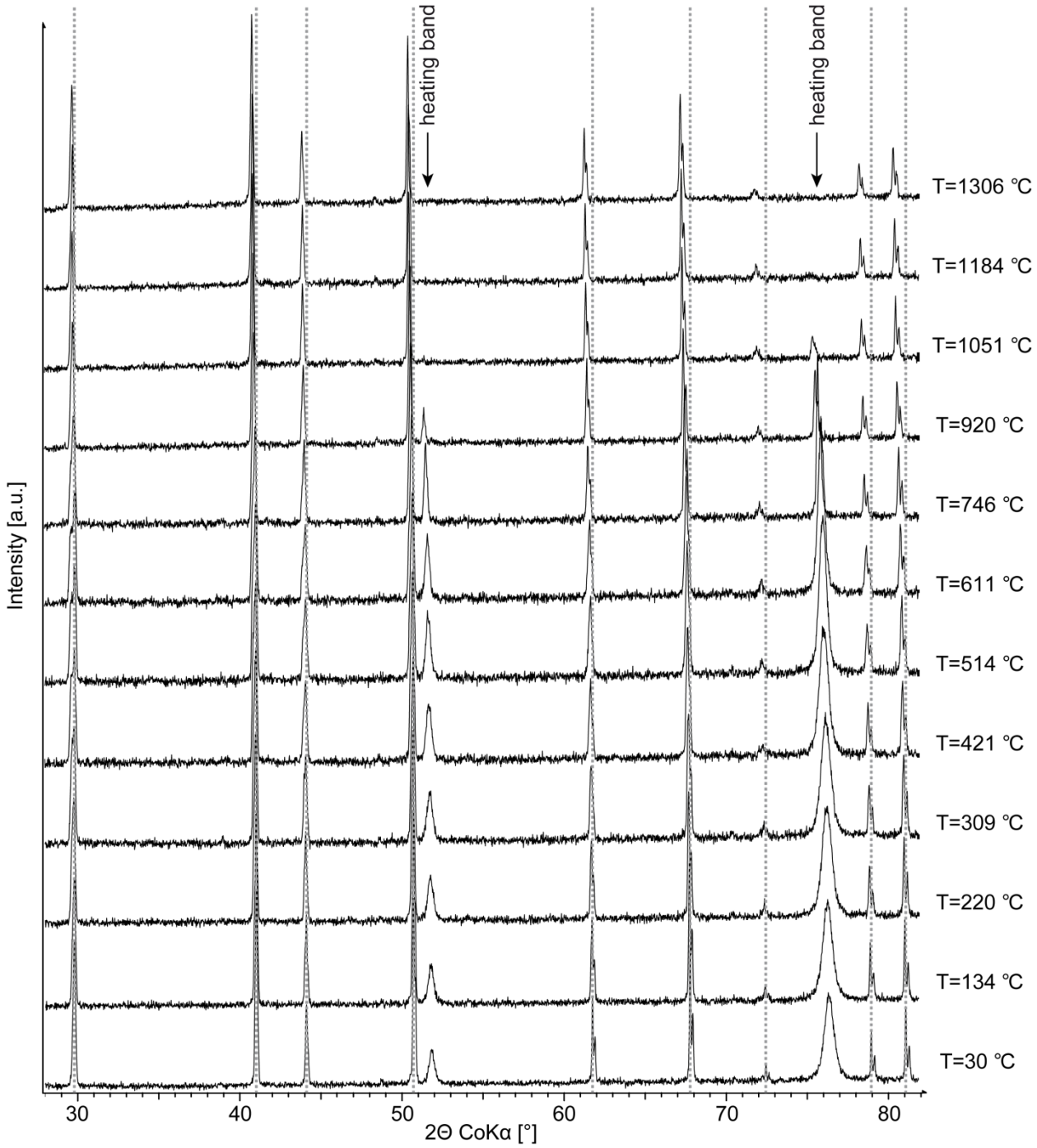

Appendix ii. TXRD patterns of corundum to determine lattice parameters as a calibration test (2012).

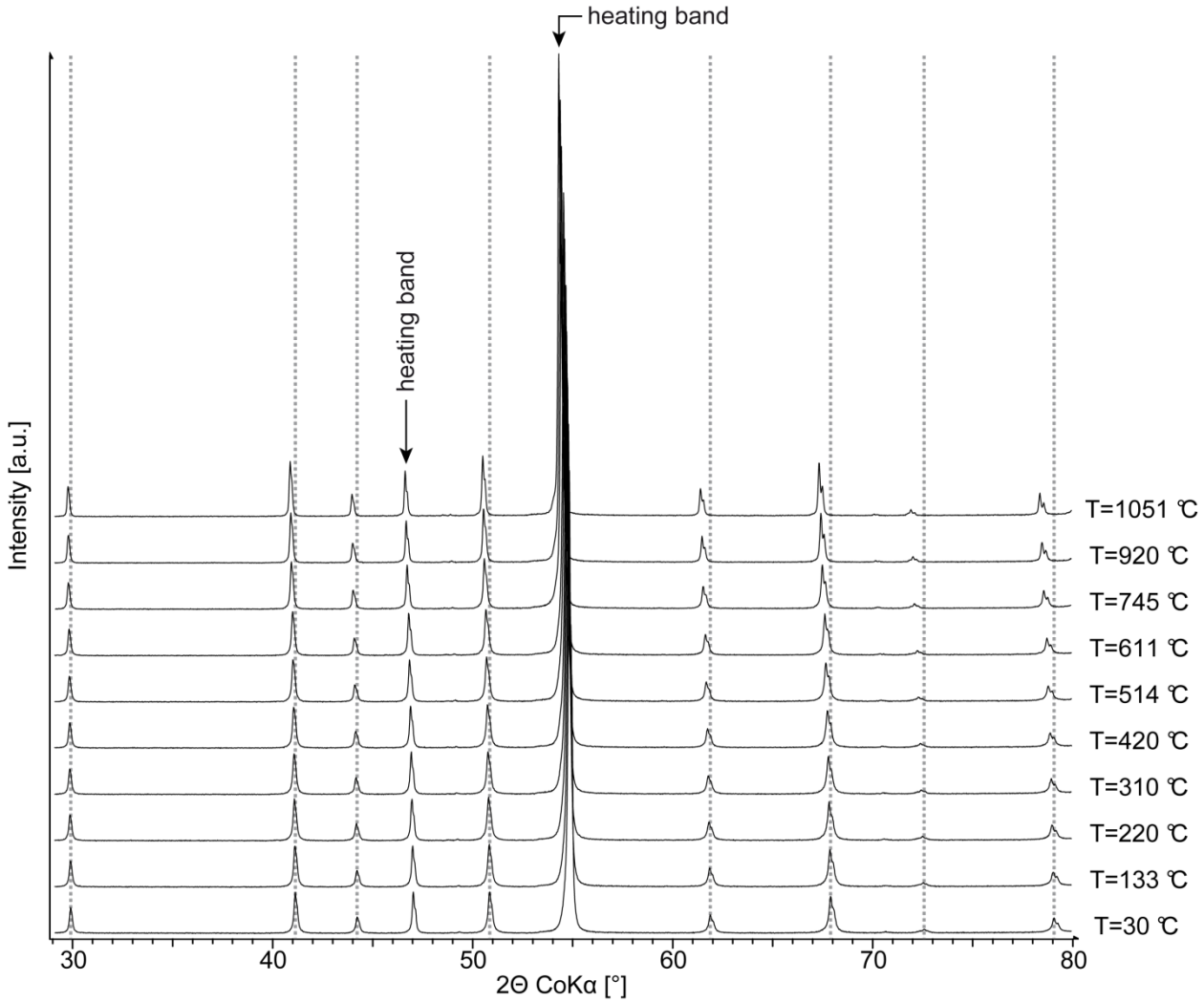

Appendix iii. TXRD patterns of corundum to determine lattice parameters as a calibration test (2013).

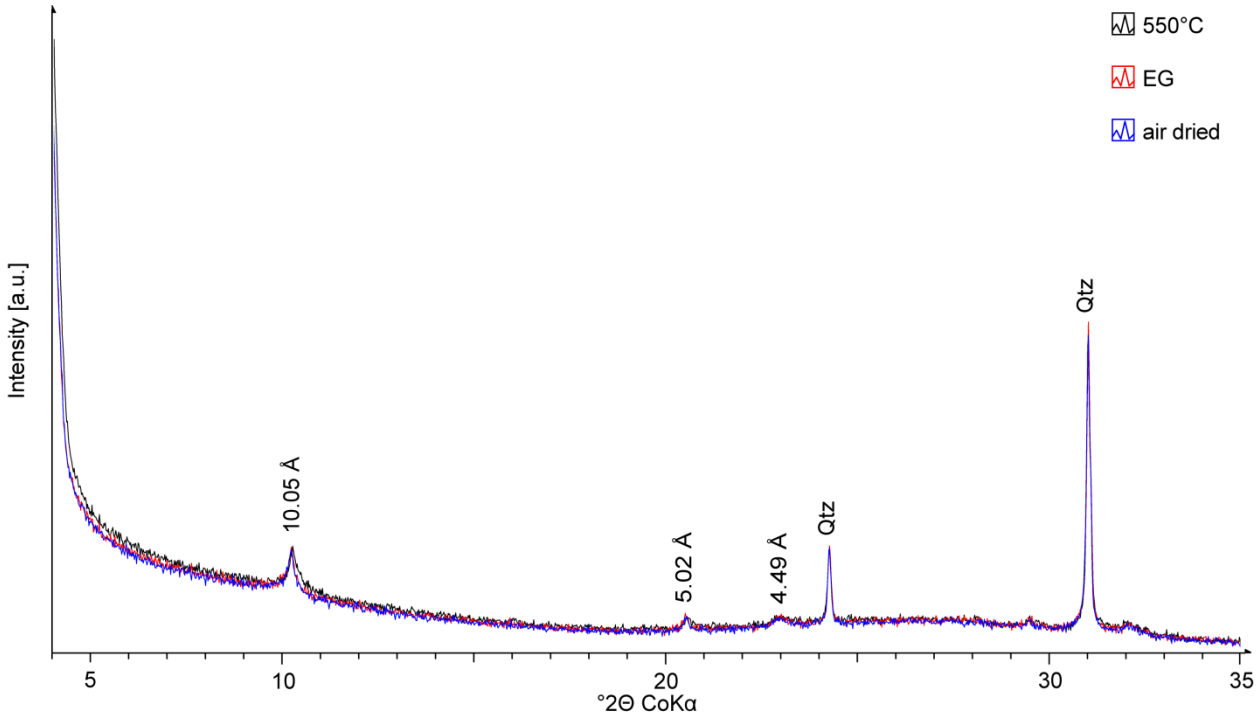

Appendix iv. XRD patterns of preferred oriented specimens of Na-saturated and heated (875 °C) Friedland clay bulk material. The major phases are marked. The d-values given belong to dehydroxylated I-S interstratification and to dehydroxylated white mica. Qtz: quartz

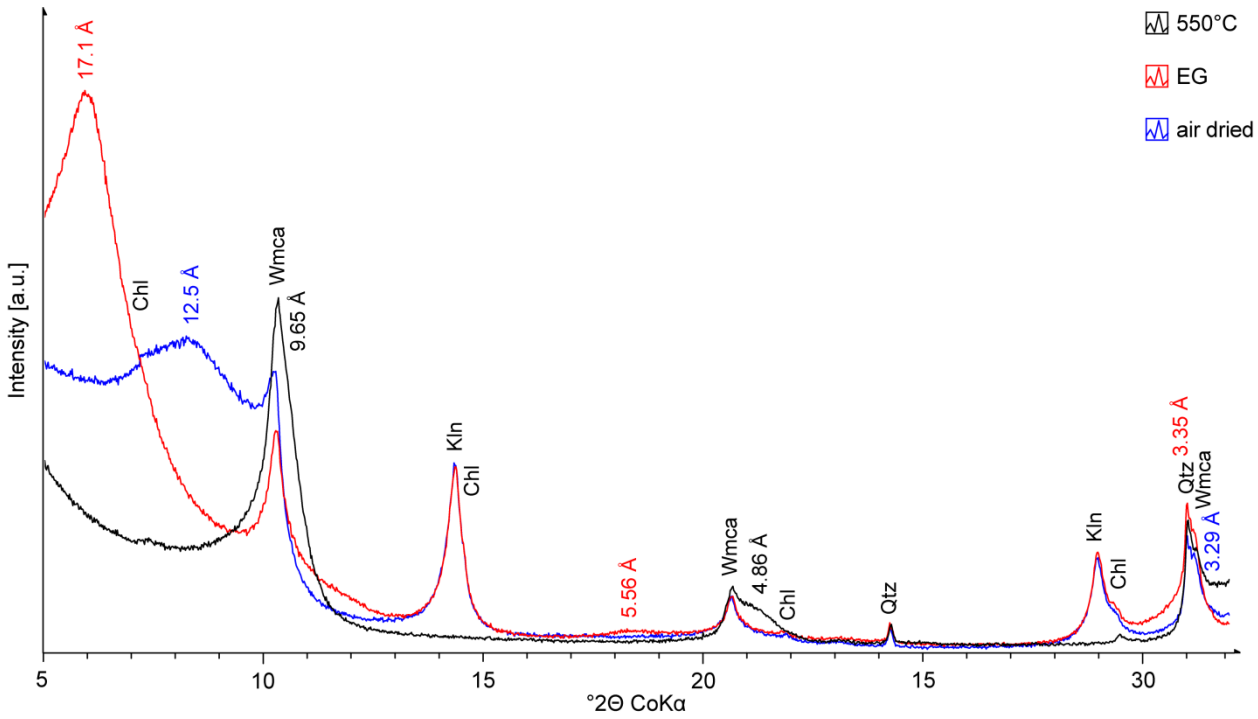

Appendix v. XRD patterns of preferred oriented specimens of the Friedland clay <0.2 µm fraction. The major phases are marked. d-values belong to the I-S interstratification, Chl: chlorite, Wmca: white mica, Kln: kaolinite, Qtz: quartz

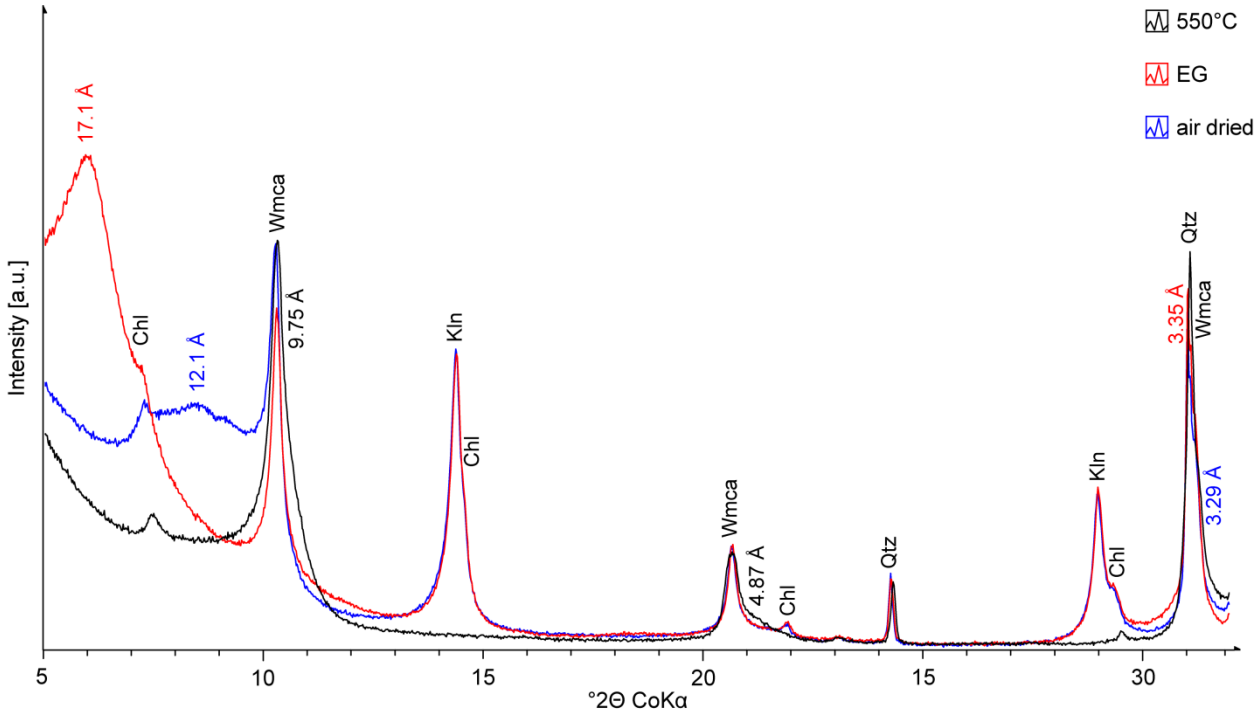

Appendix vi. XRD patterns of preferred oriented specimens of the Friedland clay 0.2-2 µm fraction. The major phases are marked. d-values belong to the I-S interstratification, Chl: chlorite, Wmca: white mica, Kln: kaolinite, Qtz: quartz

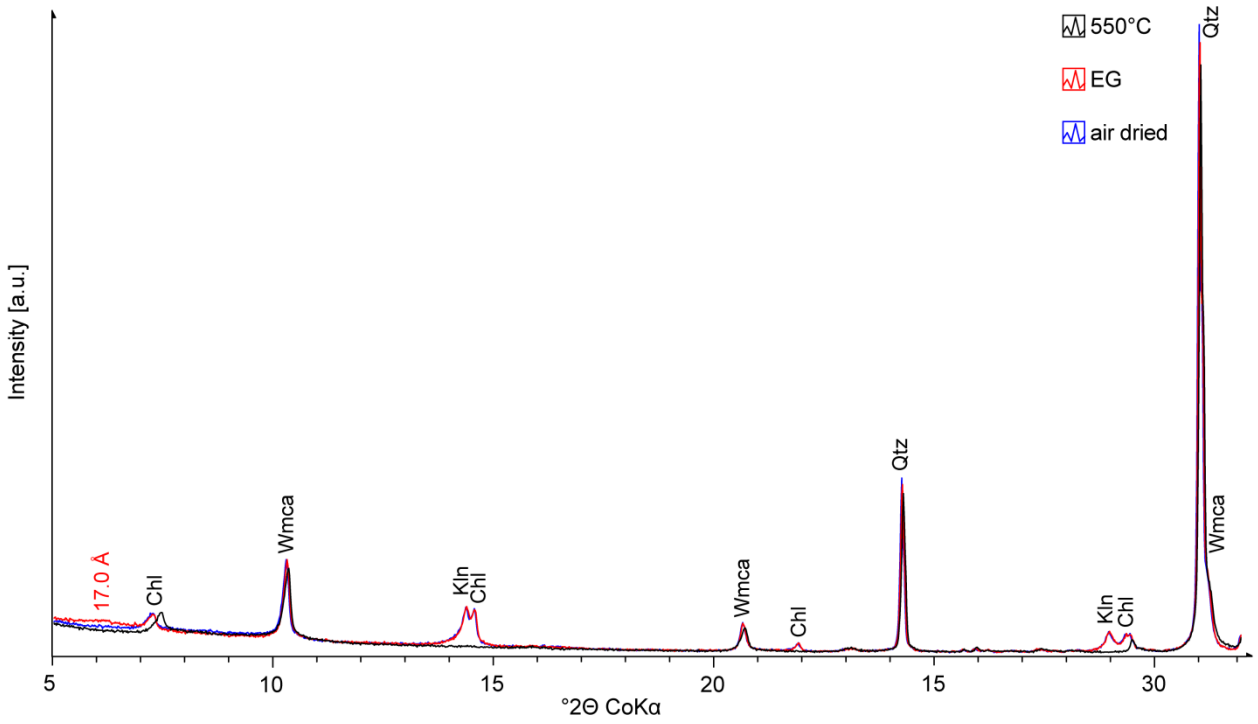

Appendix vii. XRD patterns of preferred oriented specimens of the Friedland clay 2-10 µm fraction. The major phases are marked. d-values belong to the I-S interstratification, Chl: chlorite, Wmca: white mica, Kln: kaolinite, Qtz: quartz

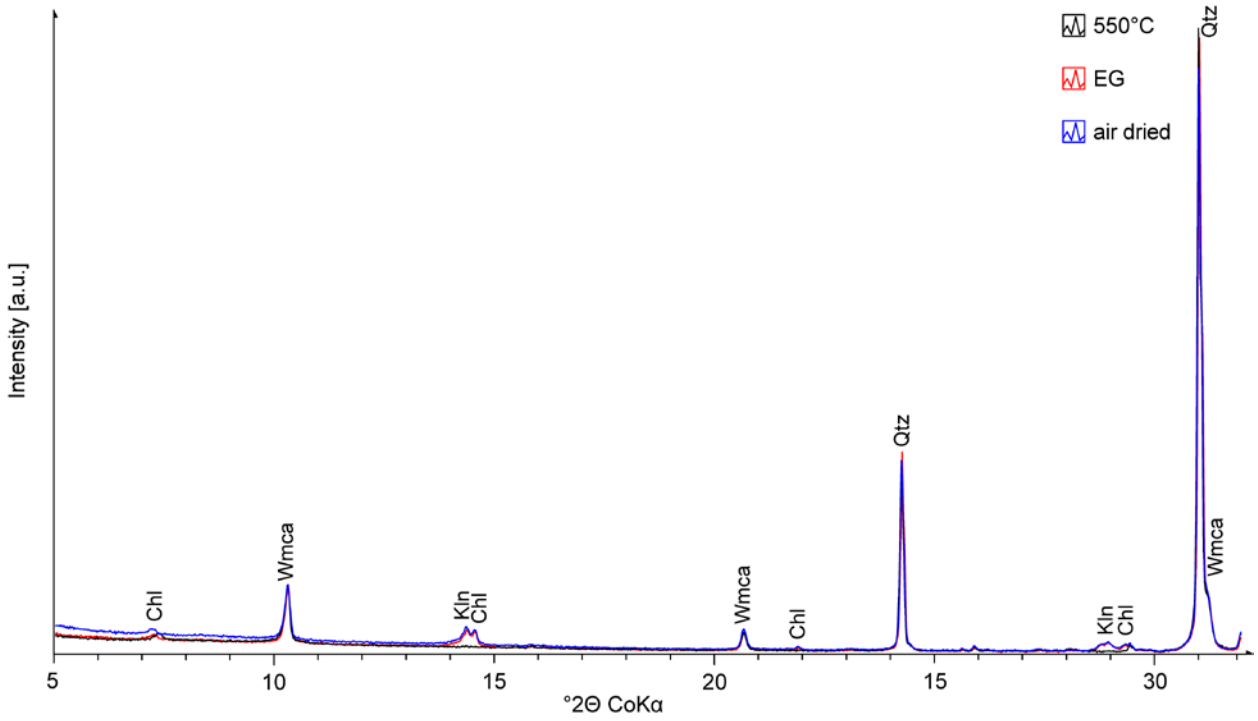

Appendix viii. XRD patterns of preferred oriented specimens of the Friedland clay >10 µm fraction. The major phases are marked. Chl: chlorite, Wmca: white mica, Kln: kaolinite, Qtz: quartz

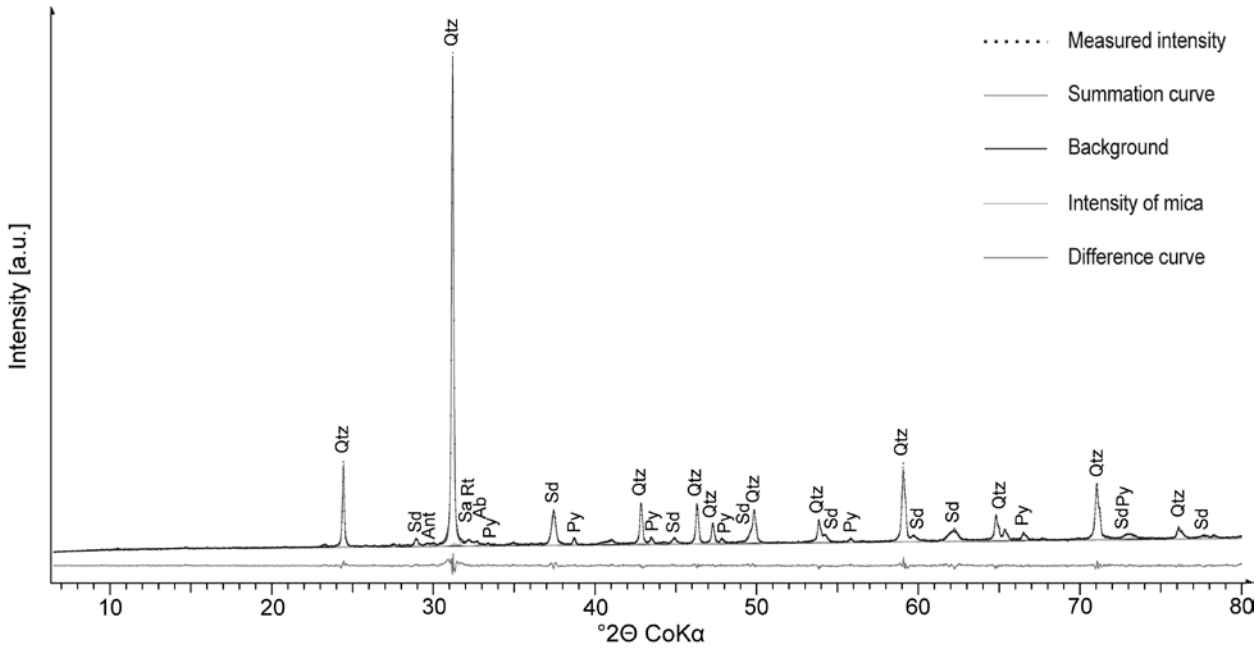

Appendix ix. BGMN fit of the Friedland clay >10 µm fraction. The major phases are marked. Qtz: quartz, Sd: siderite, Ant: anatase, Sa: sanidine/microcline, Rt: rutile, Ab: albite, Py: pyrite (Rwp = 2.92%, Rexp = 1.87%)

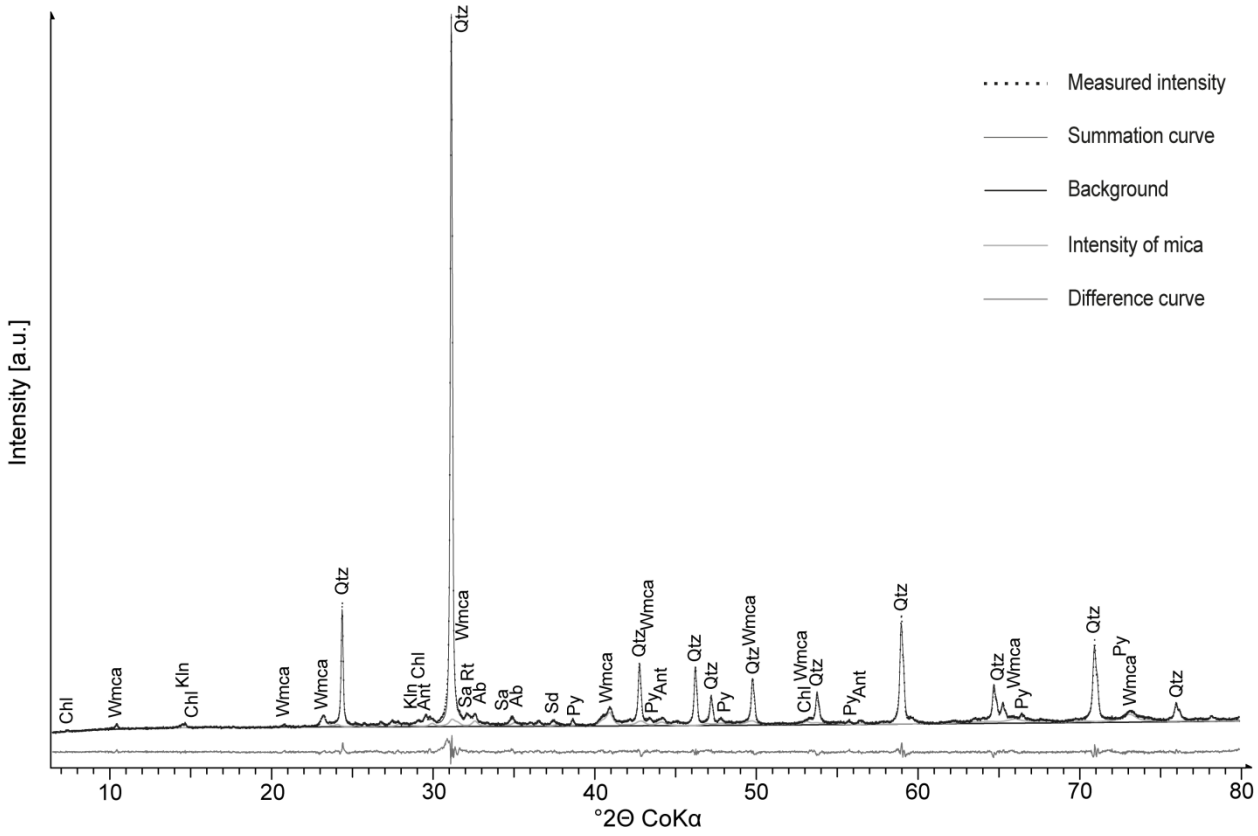

Appendix x. BGMN fit of the Friedland clay 2-10 µm fraction. The major phases are marked. Chl: chlorite, Wmca: white mica, Kln: kaolinite, Qtz: quartz, Ant: anatase, Sa: sanidine/microcline, Rt: rutile, Ab: albite, Sd: siderite, Py: pyrite (Rwp = 3.53%, Rexp = 2.12%)

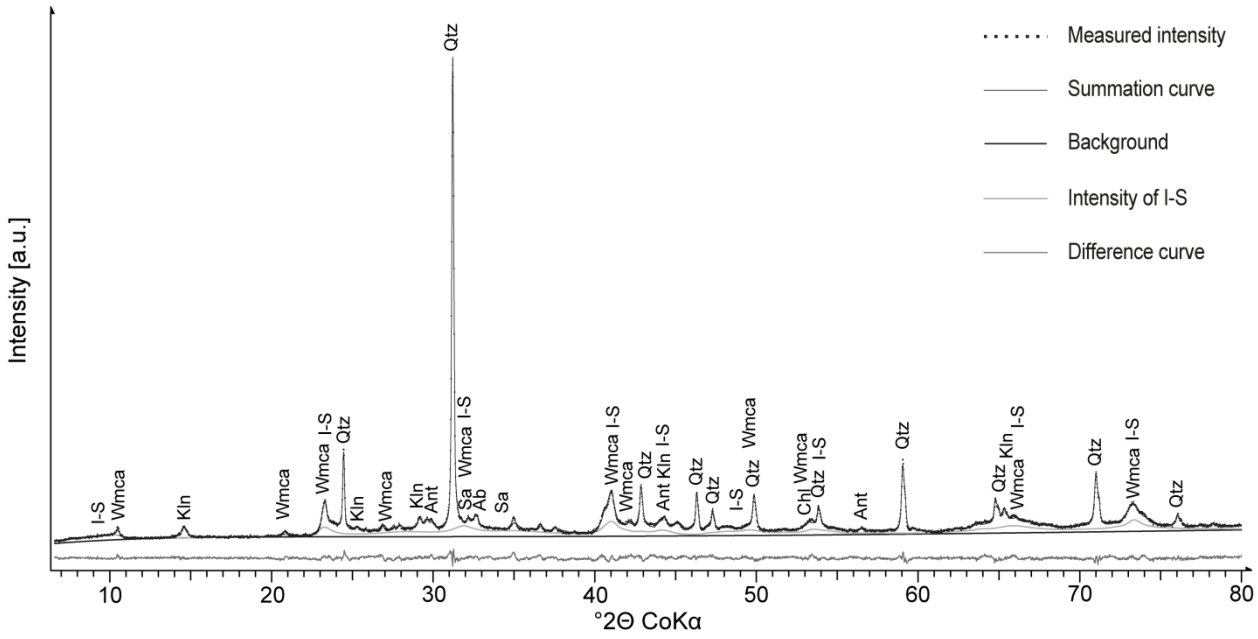

Appendix xi. BGMN fit of the Friedland clay 0.2-2 µm fraction. The major phases are marked. I-S: illite-smectite interstratification, Wmca: white mica, Kln: kaolinite, Qtz: quartz, Ant: anatase, Sa: sanidine/microcline, Ab: albite (Rwp = 3.80%, Rexp = 2.07%)

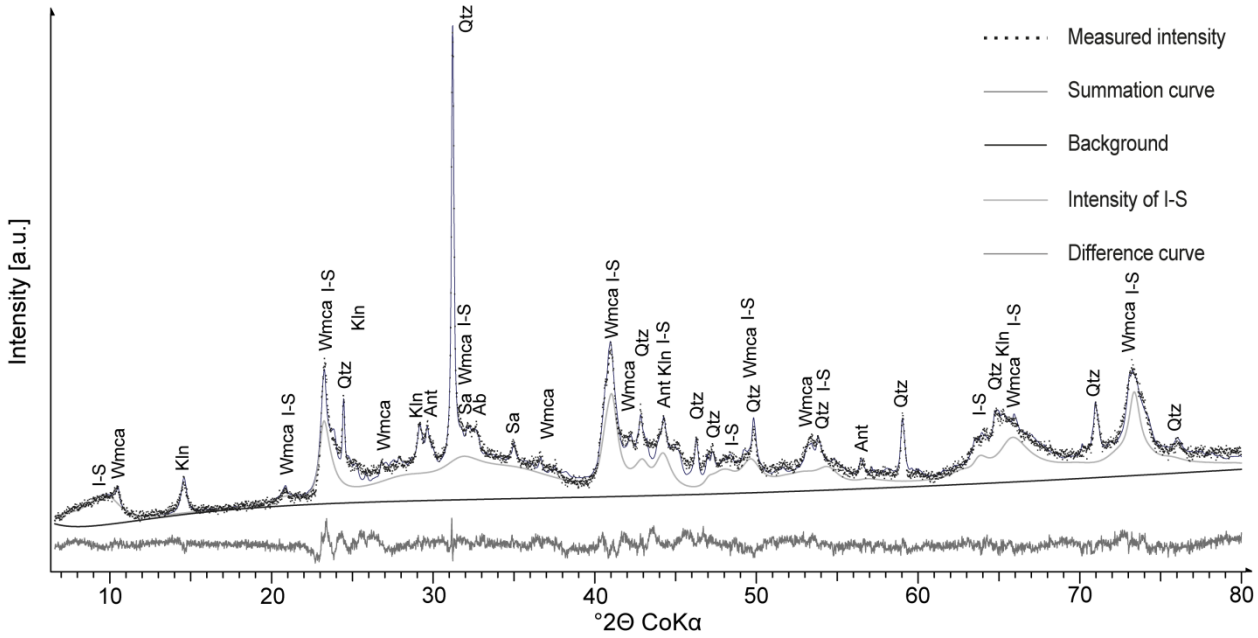

Appendix xii. BGMN fit of the Friedland clay <0.2 µm fraction. The major phases are marked. I-S: illite-smectite interstratification, Wmca: white mica, Kln: kaolinite, Qtz: quartz, Ant: anatase, Sa: sanidine/microcline, Ab: albite (Rwp = 3.46%, Rexp = 1.98%)

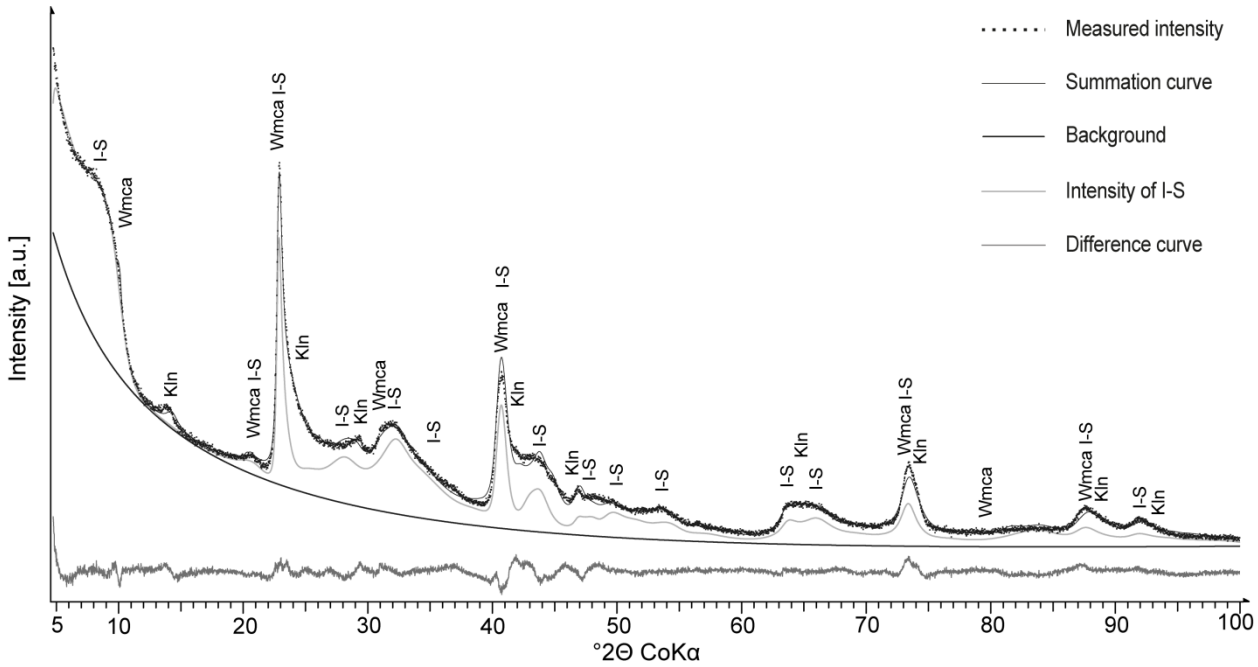

Appendix xiii. BGMN fit of the Friedland clay <0.1 µm fraction. The major phases are marked. I-S: illite-smectite interstratification, Wmca: white mica, Kln: kaolinite (Rwp = 2.38%, Rexp = 1.01%)

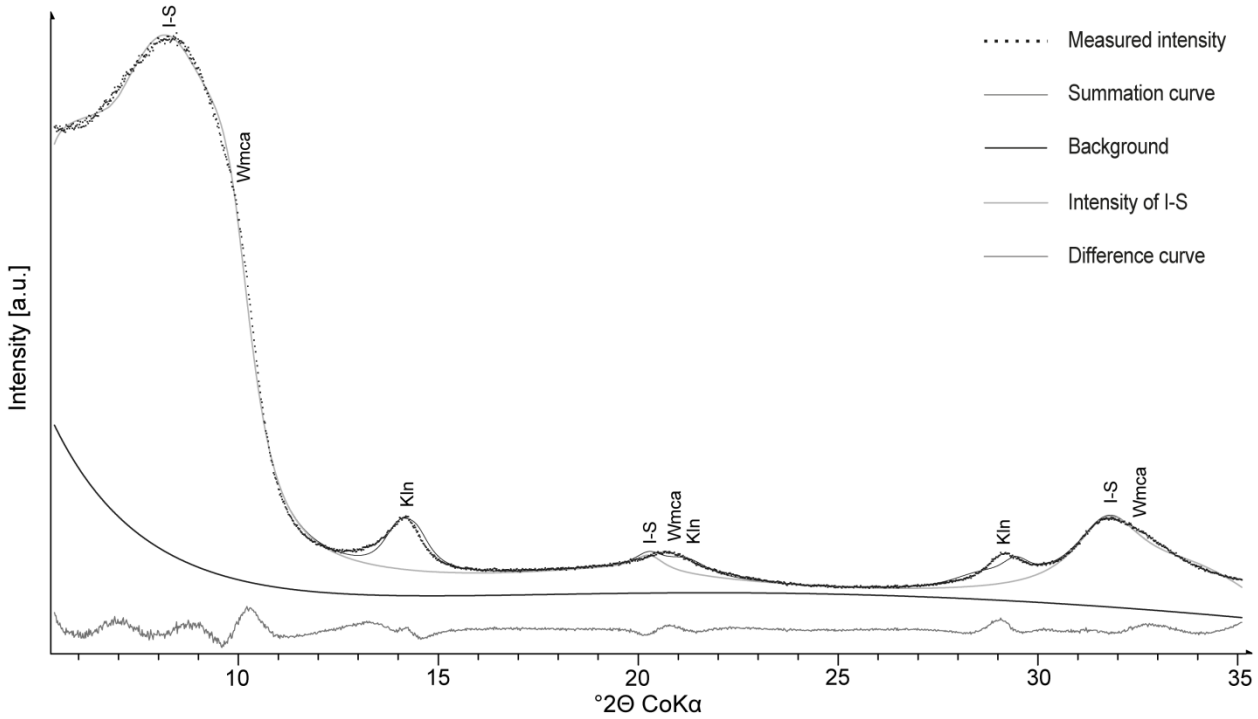

Appendix xiv. BGMN fit an air-dried preferred oriented specimen of the Friedland clay <0.1 µm fraction. The major phases are marked. I-S: illite-smectite interstratification, Wmca: white mica, Kln: kaolinite (Rwp = 3.58%, Rexp = 0.97%)

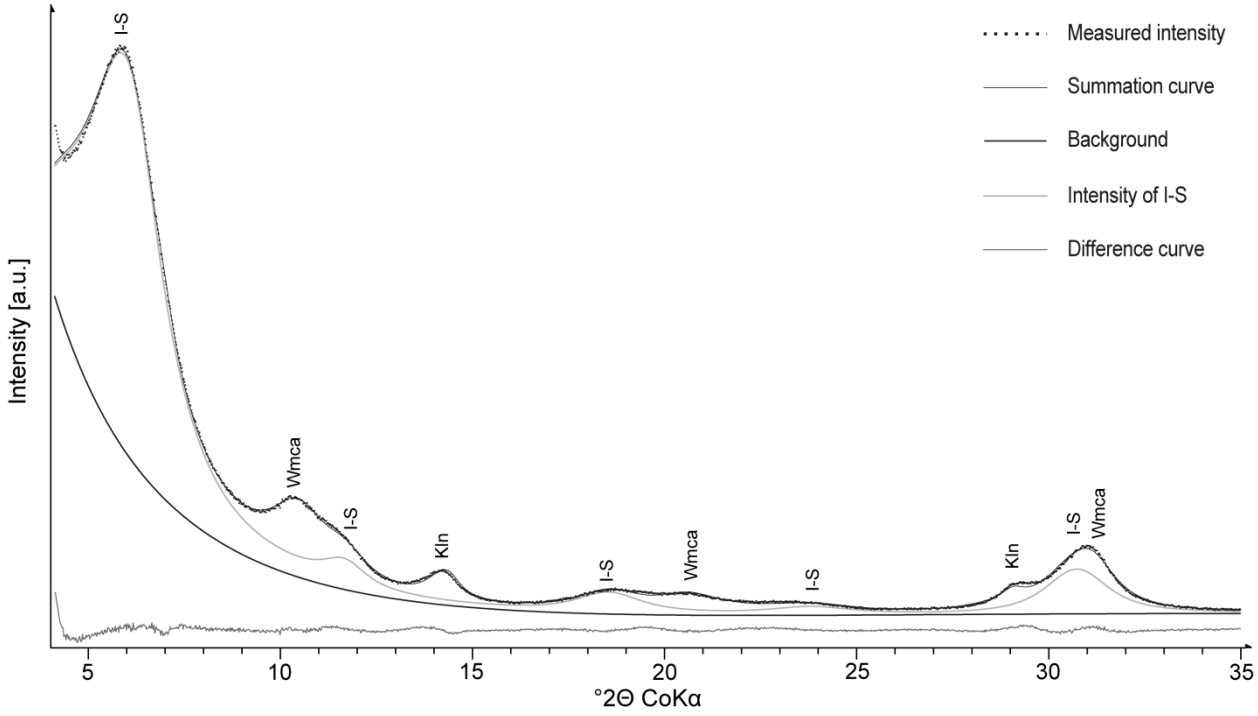

Appendix xv. BGMN fit an ethylene glycol saturated preferred oriented specimen of the Friedland clay <0.1 µm fraction. The major phases are marked. I-S: illite-smectite interstratification, Wmca: white mica, Kln: kaolinite (Rwp = 2.32%, Rexp = 0.97%)

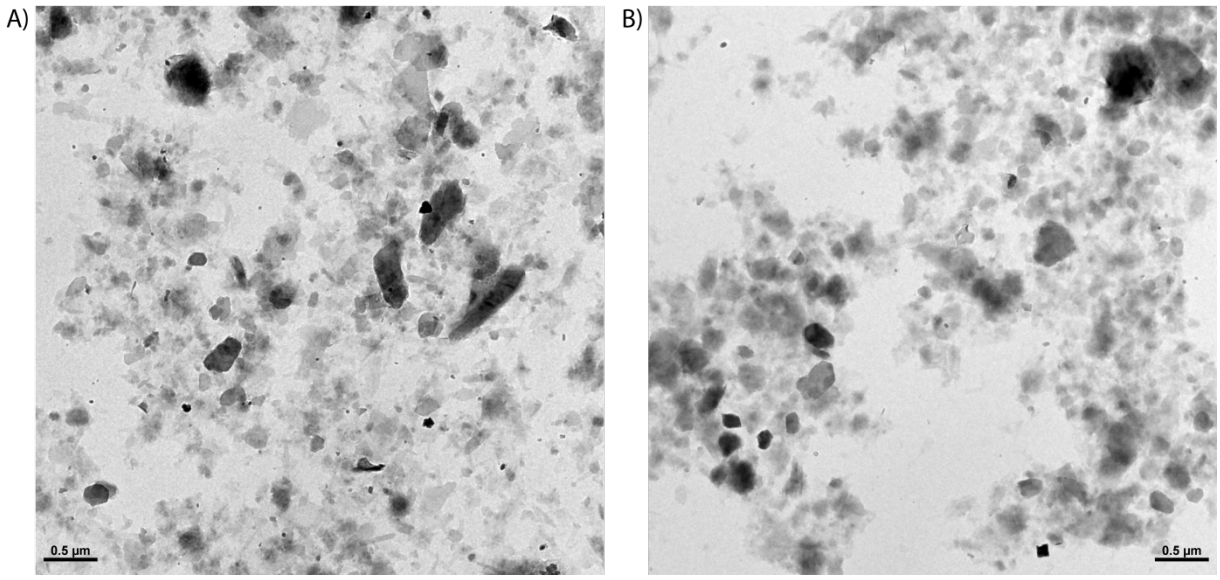

Appendix xvi. TEM images of untreated Friedland clay bulk material.

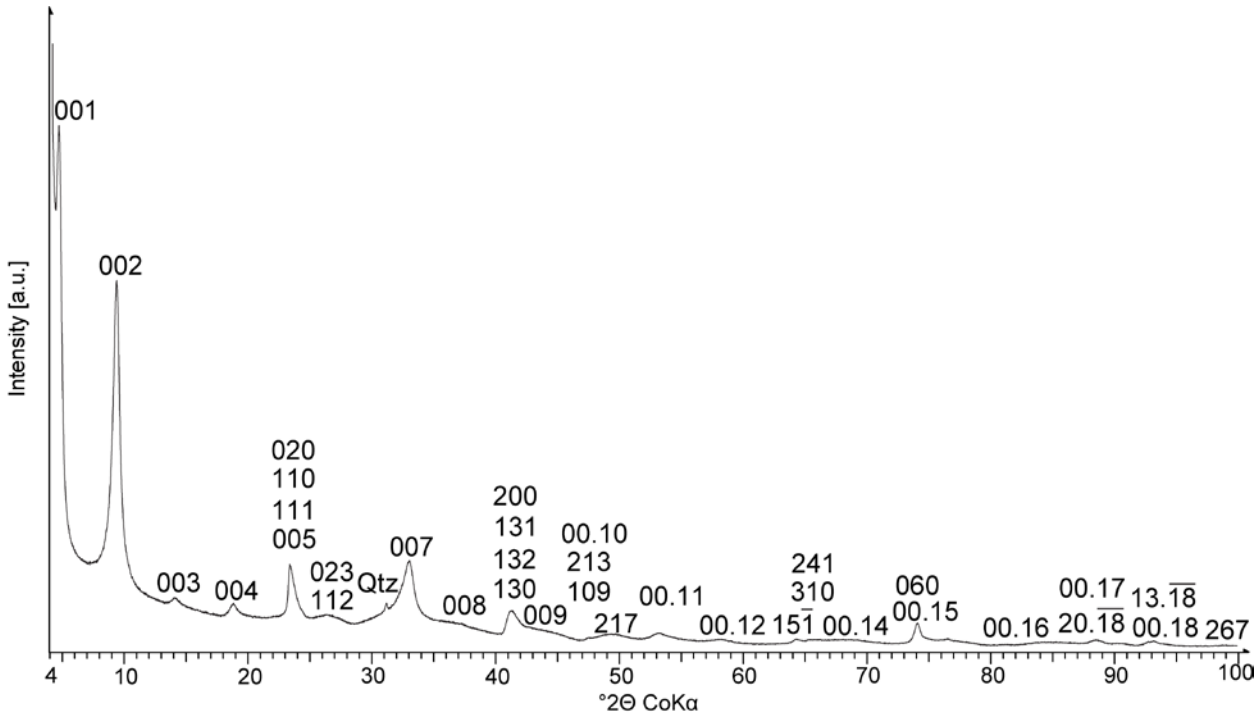

Appendix xvii. Powder XRD patterns of the rectorite <0.1 µm fraction. Miller indices given for rectorite (non-basal reflection indices were taken according to Kodama, 1966). Qtz: quartz

Appendix xviii. Coefficient of variation (CV) and Full width at half maximum (FWHM) calculation of Arkansas rectorite. All values determined from an XRD pattern of an ethylene glycol saturated, preferred oriented sample of the rectorite <0.1 fraction. FWHM values after kα2 stripping and angular broadening correction.

Rectorite <0.1 µm fraction

order l of (00l)	d-value	l*d(00l)	FWHM [°2θ]
1	26.78	26.78	0.41
2	13.32	26.63	0.46
3	8.90	26.69	0.43
4	6.66	26.63	0.36
5	5.32	26.58	0.35
6	4.44	26.64	0.38
7	3.80	26.62	0.33
8	3.32	26.59	0.44
9	2.96	26.60	0.41
10	2.66	26.59	0.32
12	2.22	26.66	0.41
13	2.05	26.61	0.28
14	1.90	26.60	0.39
15	1.77	26.61	0.45
17	1.57	26.61	0.45
arithmetic mean		**26.63**	**0.39**
standard deviation		**0.05**	**0.05**
coefficient of variation (CV)		**0.19**	

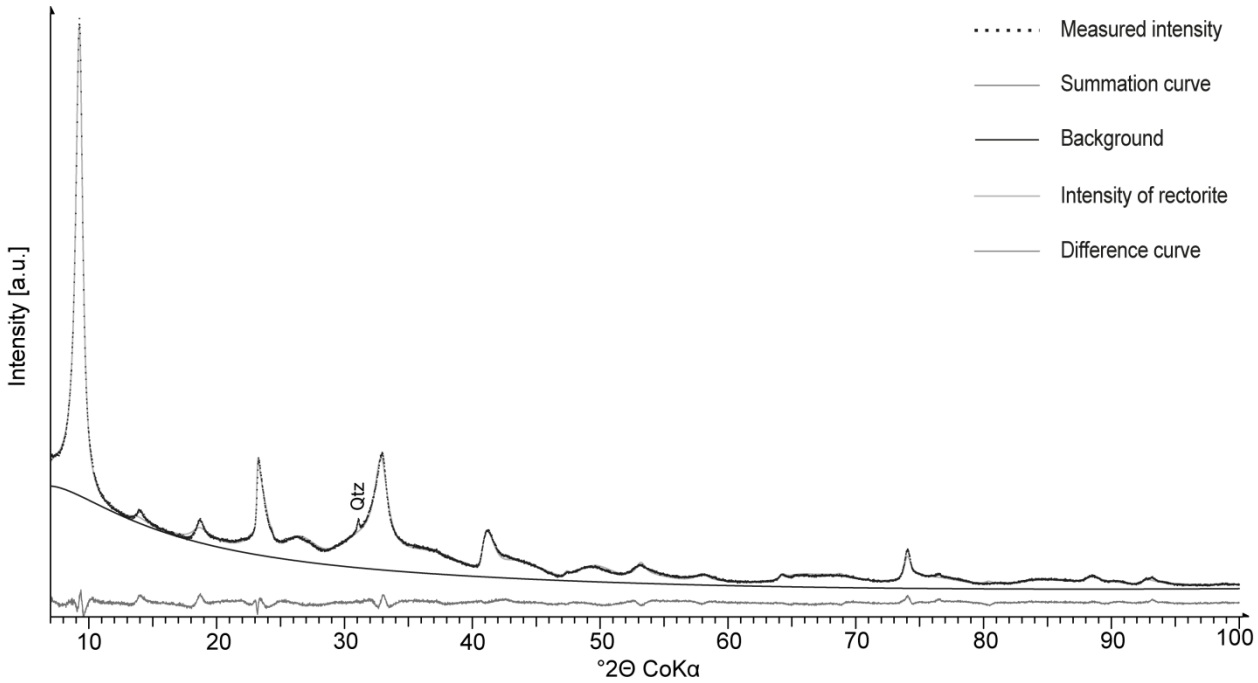

Appendix xix. BGMN fit of the rectorite <0.1 µm fraction. All reflections belong to rectorite except for ≈31 °2θ. Qtz: quartz (Rwp = 3.41%, Rexp = 1.28%)

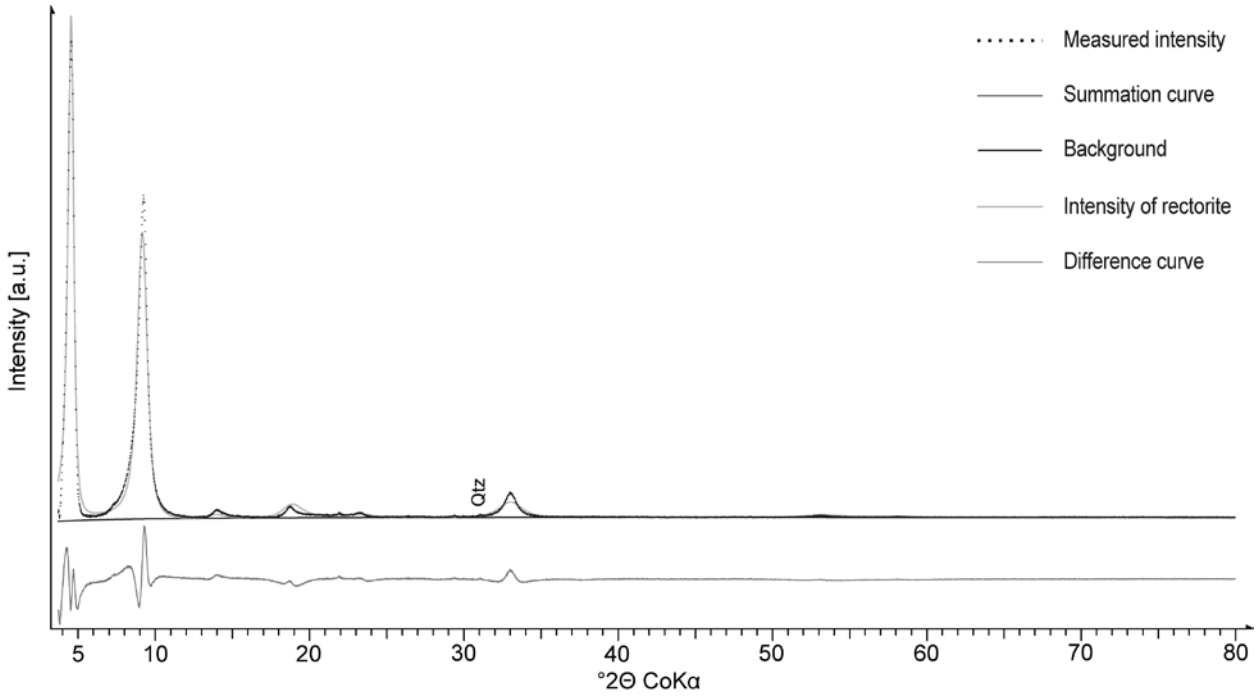

Appendix xx. BGMN fit an air dried preferred oriented specimen of the rectorite <0.1 µm fraction. All reflections belong to rectorite except for ≈31 °2θ. Qtz: quartz (Rwp = 12.28%, Rexp = 2.21%)

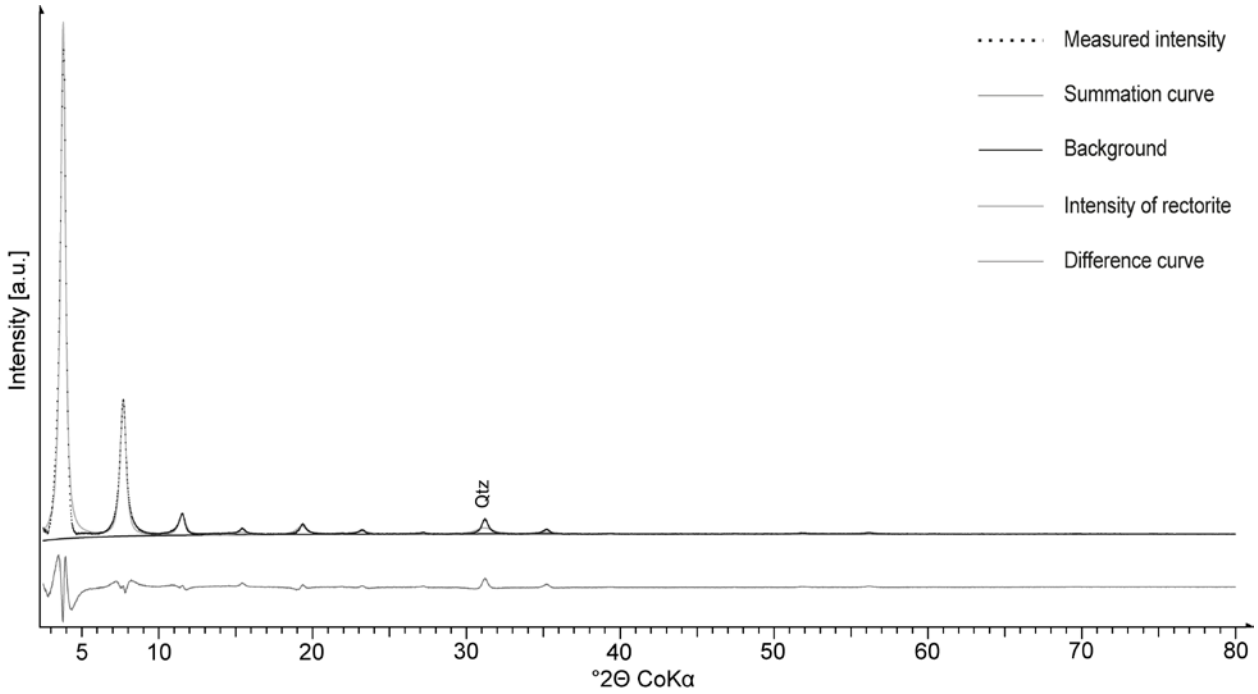

Appendix xxi. BGMN fit an ethylene glycol saturated preferred oriented specimen of the rectorite <0.1 µm fraction. All reflections belong to rectorite except for ≈31 °2θ. Qtz: quartz (Rwp = 12.35%, Rexp = 2.22%)

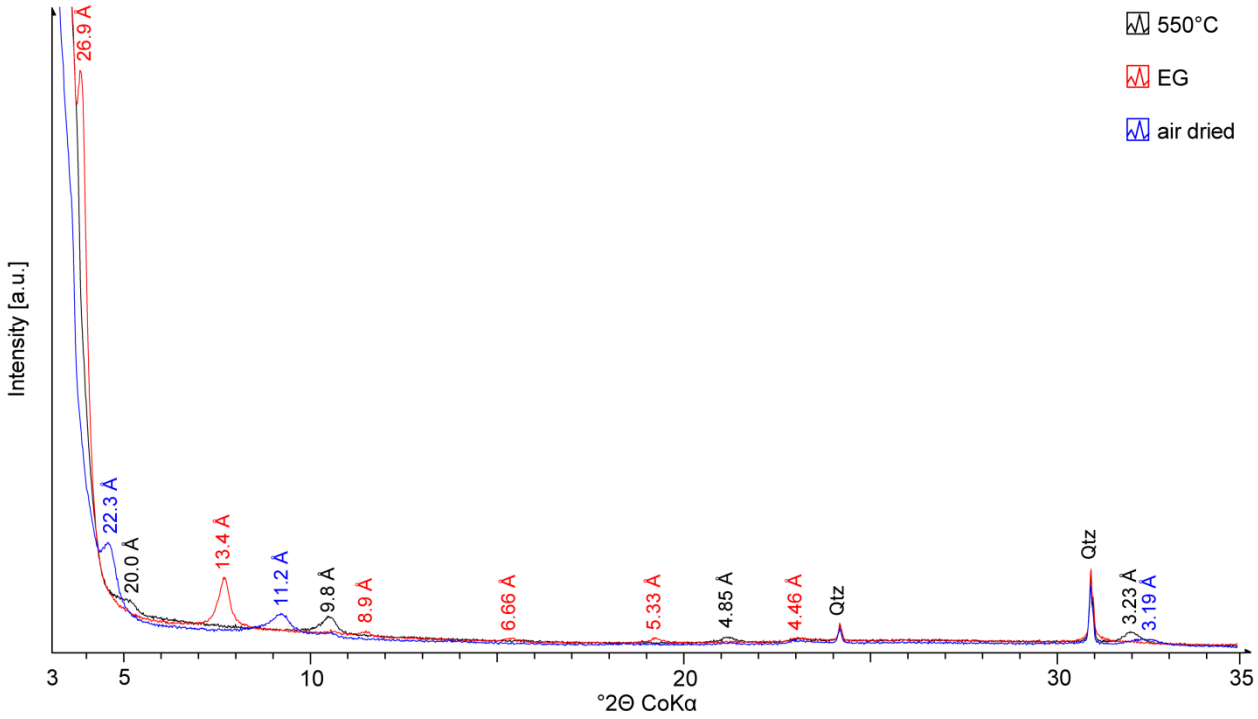

Appendix xxii. XRD patterns of preferred oriented specimens of Na-saturated and heated (875 °C) rectorite bulk material. The d-values given belong to dehydroxylated rectorite. Qtz: quartz

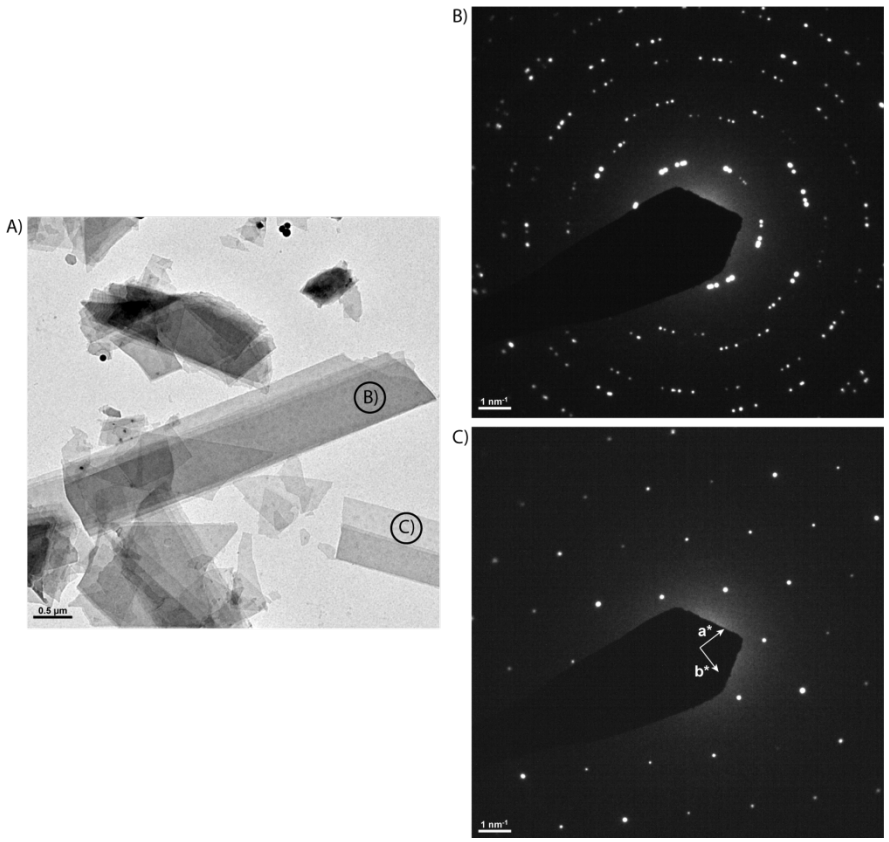

Appendix xxiii. Electron micrograph and selected area electron diffraction patterns (SAED) of powdered rectorite bulk material. A) Electron micrograph of rectorite particles with B) and C) typical pseudohexagonal SAED patterns.

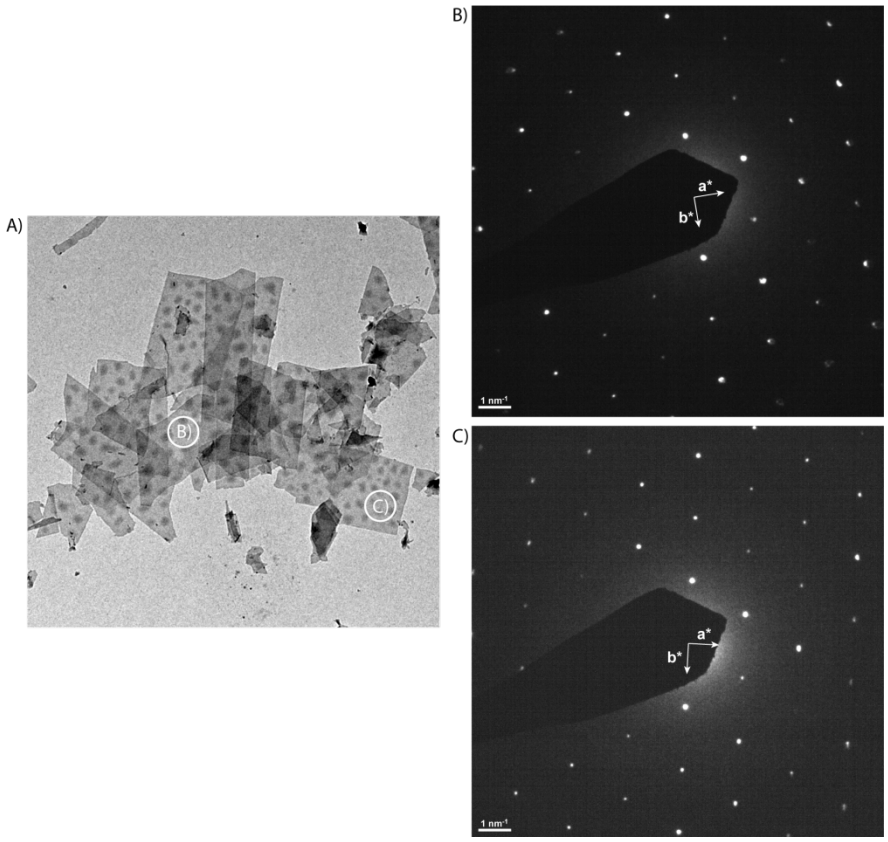

Appendix xxiv. Electron micrograph and selected area electron diffraction patterns (SAED) of the rectorite <0.1 µm fraction. A) Electron micrograph of rectorite particles with B) and C) typical pseudohexagonal SAED patterns.

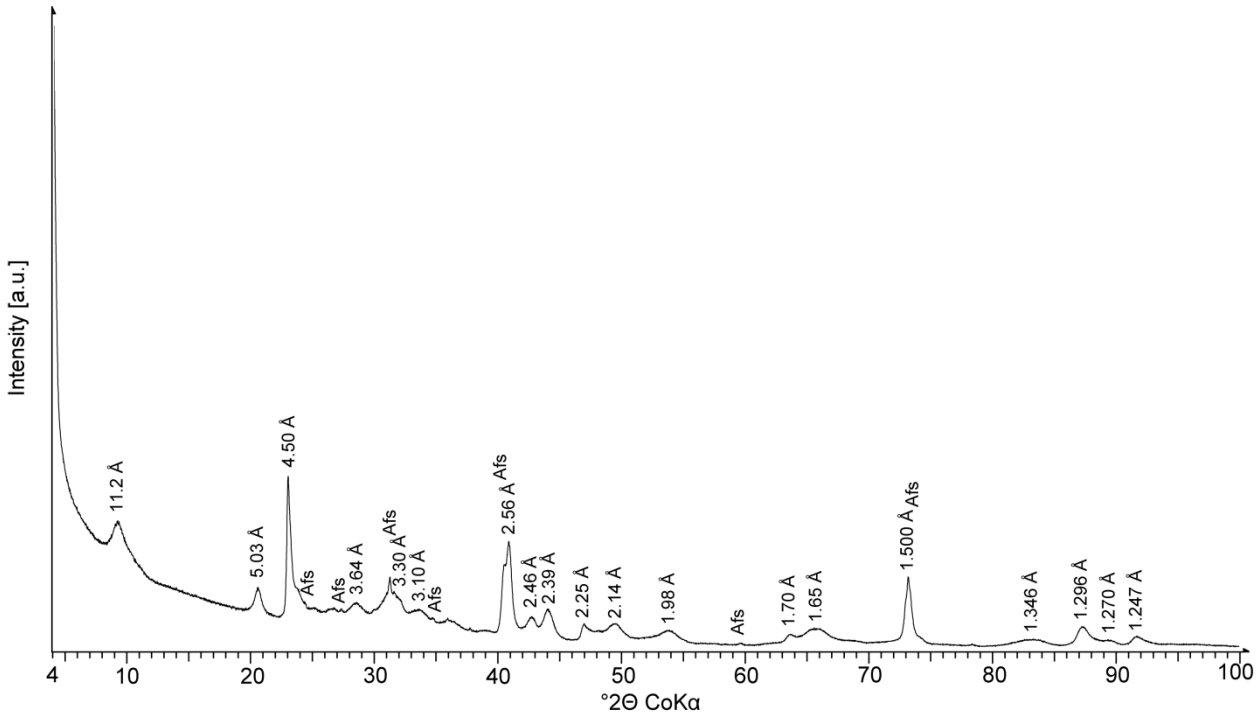

Appendix xxv. Powder XRD pattern of the "sárospatakite" bulk sample. d-values given for the I-S interstratification. Afs: alkalifeldspar

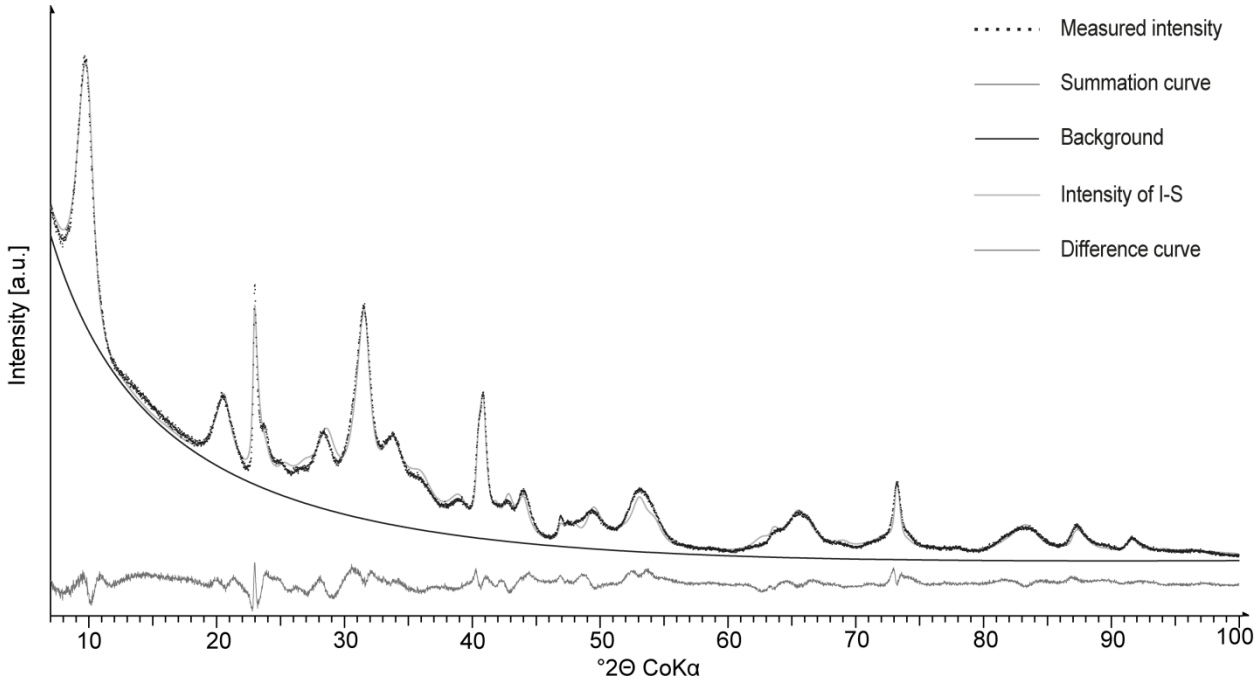

Appendix xxvi. BGMN fit of the "sárospatakite" <0.1 µm fraction. All reflections belong to I-S. (Rwp = 5.19%, Rexp = 1.41%)

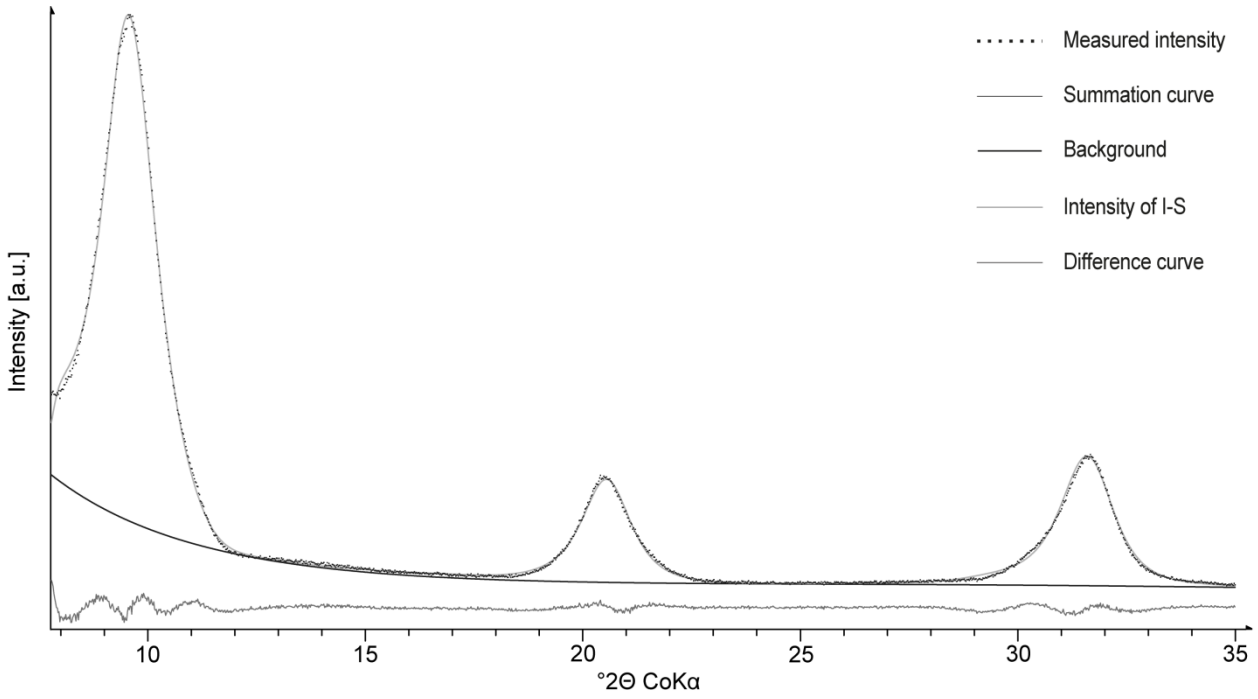

Appendix xxvii. BGMN fit an air dried preferred oriented specimen of the "sárospatakite" <0.1 µm fraction. All reflections belong to I-S (Rwp = 3.41%, Rexp = 1.48%)

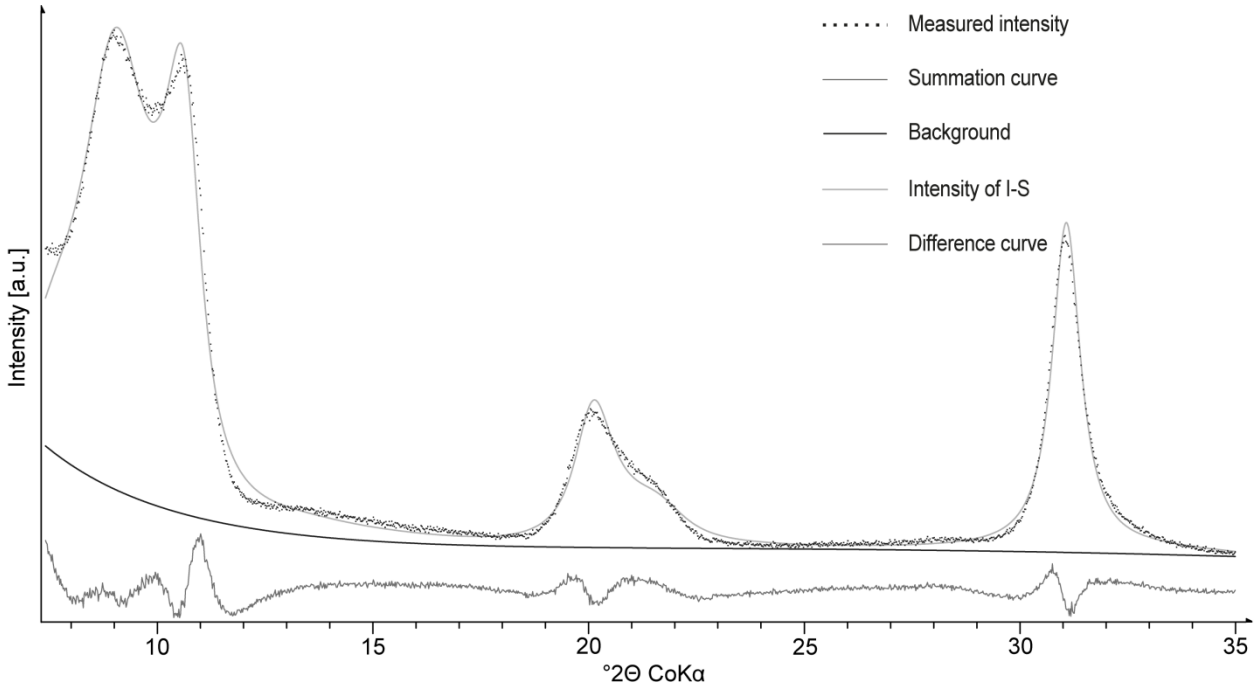

Appendix xxviii. BGMN fit an ethylene glycol saturated preferred oriented specimen of the "sárospatakite" <0.1 µm fraction. All reflections belong to I-S. (Rwp = 6.21%, Rexp = 1.54%)

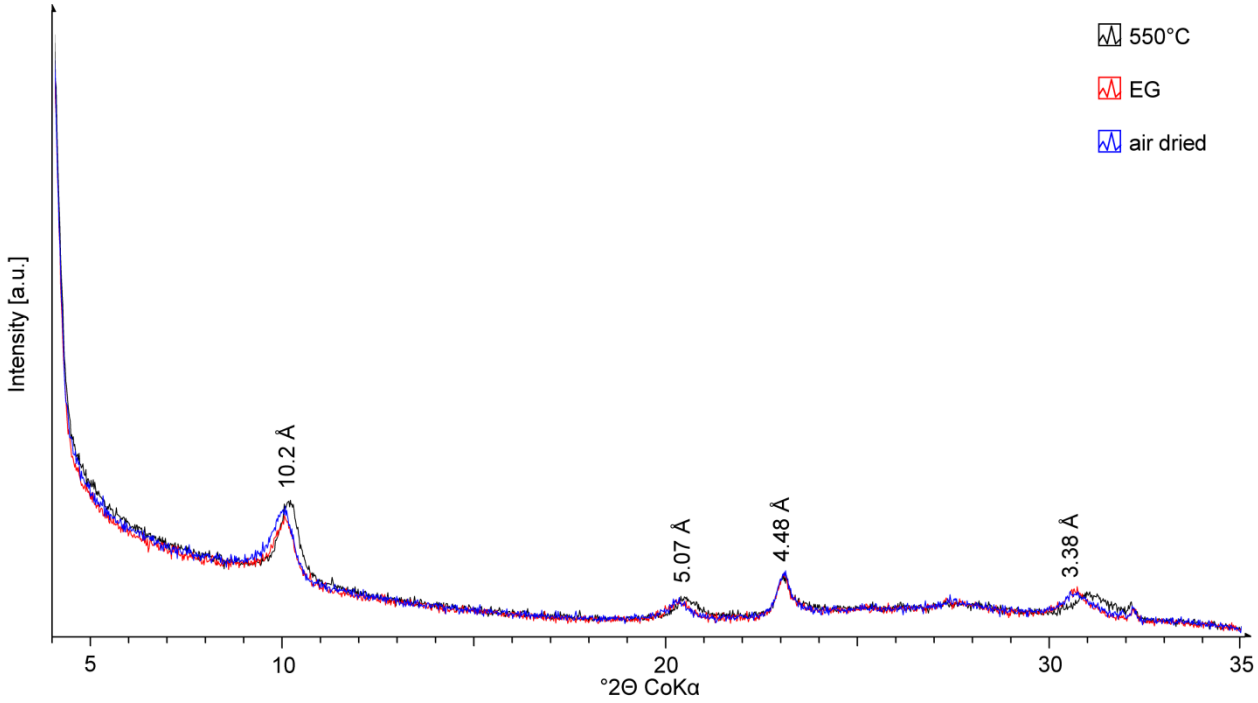

Appendix xxix. XRD patterns of preferred oriented specimens of Na-saturated and heated (875 °C) "sárospatakite" <0.1 µm fraction. The d-values given belong to dehydroxylated I-S.

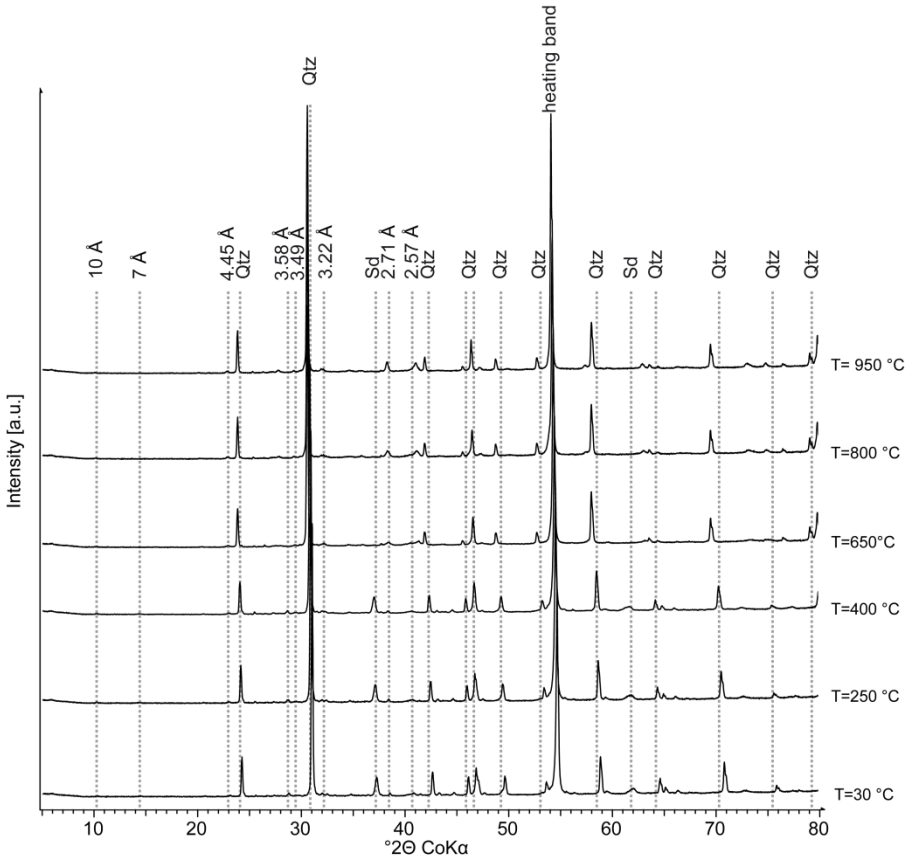

Appendix xxx. TXRD patterns of the Friedland clay >10 µm fraction heated to 30 °C, 250 °C, 400 °C, 650 °C, 800 °C, and 950 °C. d-values given belong do clay minerals such as I-S, mica, or kaolinite. Qtz: quartz, Sd: siderite

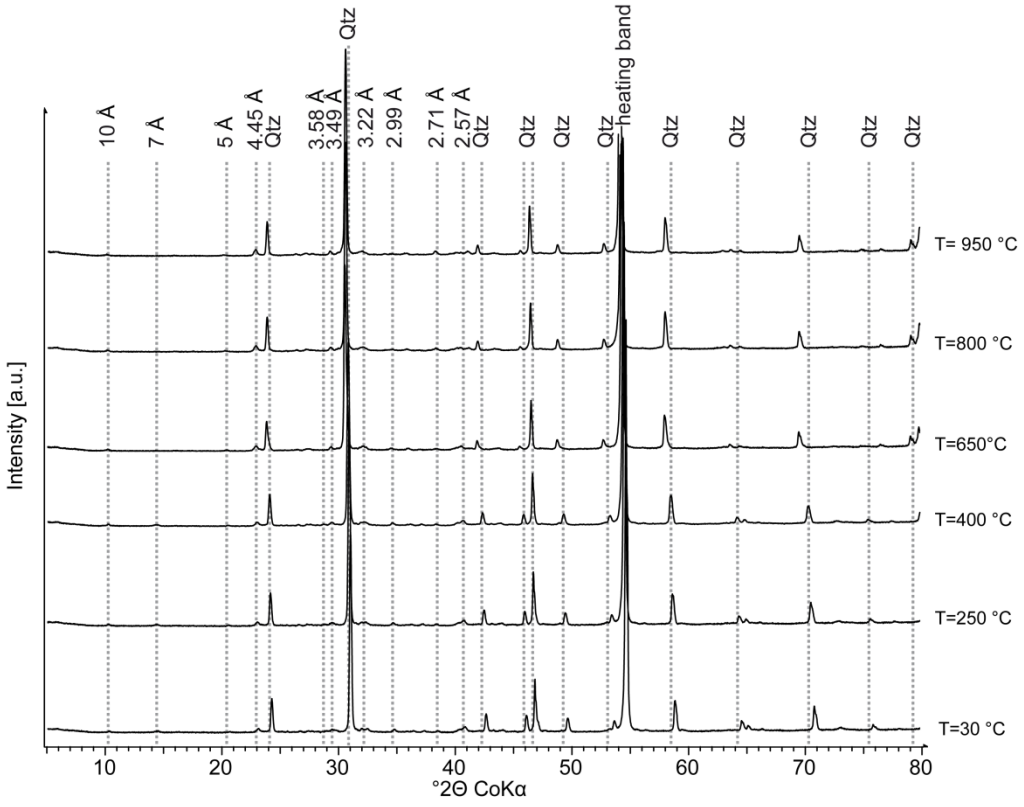

Appendix xxxi. TXRD patterns of the Friedland clay 2-10 µm fraction heated to 30 °C, 250 °C, 400 °C, 650 °C, 800 °C, and 950 °C. d-values given belong do clay minerals such as I-S, mica, or kaolinite. Qtz: quartz

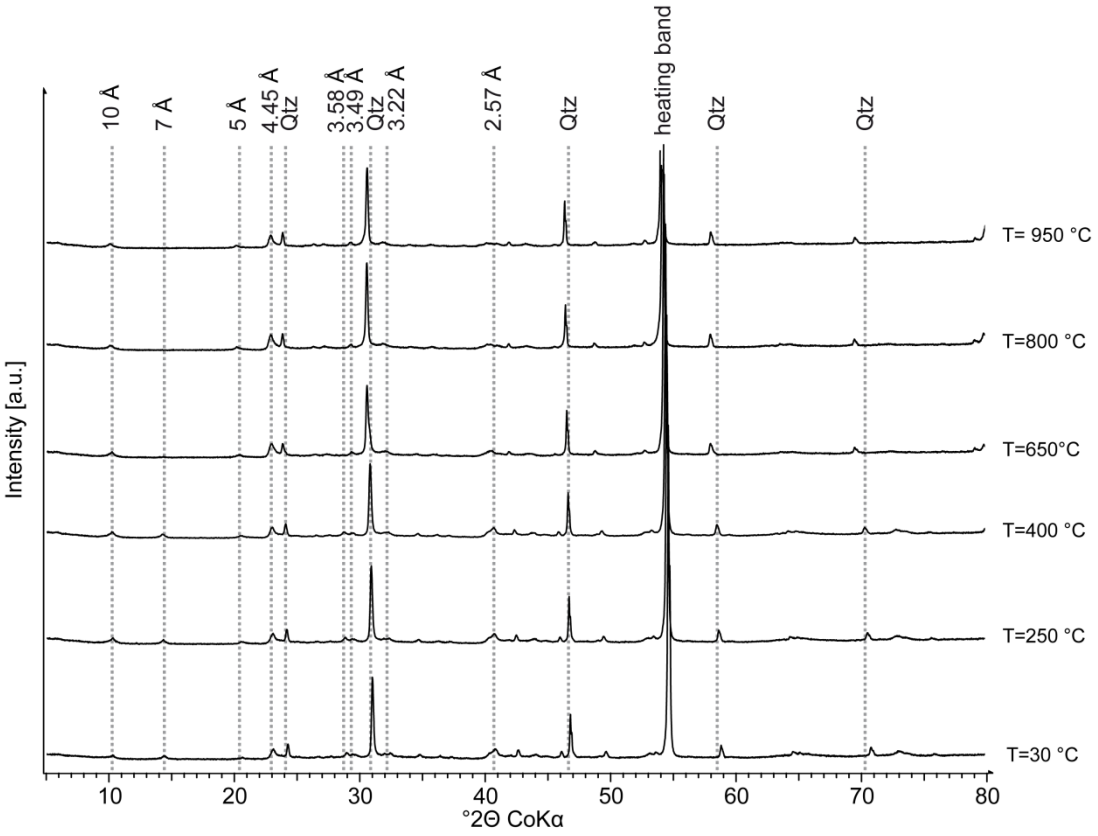

Appendix xxxii. TXRD patterns of the Friedland clay 0.2-2 µm fraction heated to 30 °C, 250 °C, 400 °C, 650 °C, 800 °C, and 950 °C. d-values given belong do clay minerals such as I-S, mica, or kaolinite. Qtz: quartz

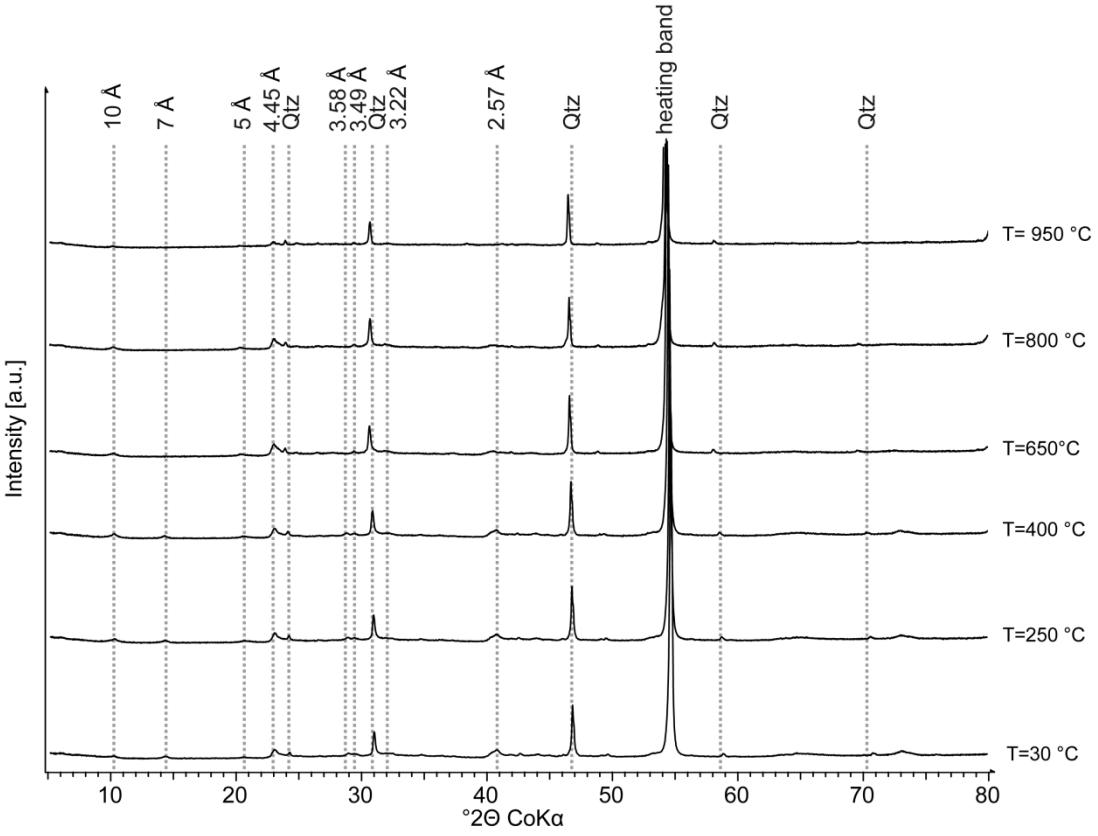

Appendix xxxiii. TXRD patterns of the Friedland clay <0.2 µm fraction heated to 30 °C, 250 °C, 400 °C, 650 °C, 800 °C, and 950 °C. d-values given belong do clay minerals such as I-S, mica, or kaolinite. Qtz: quartz

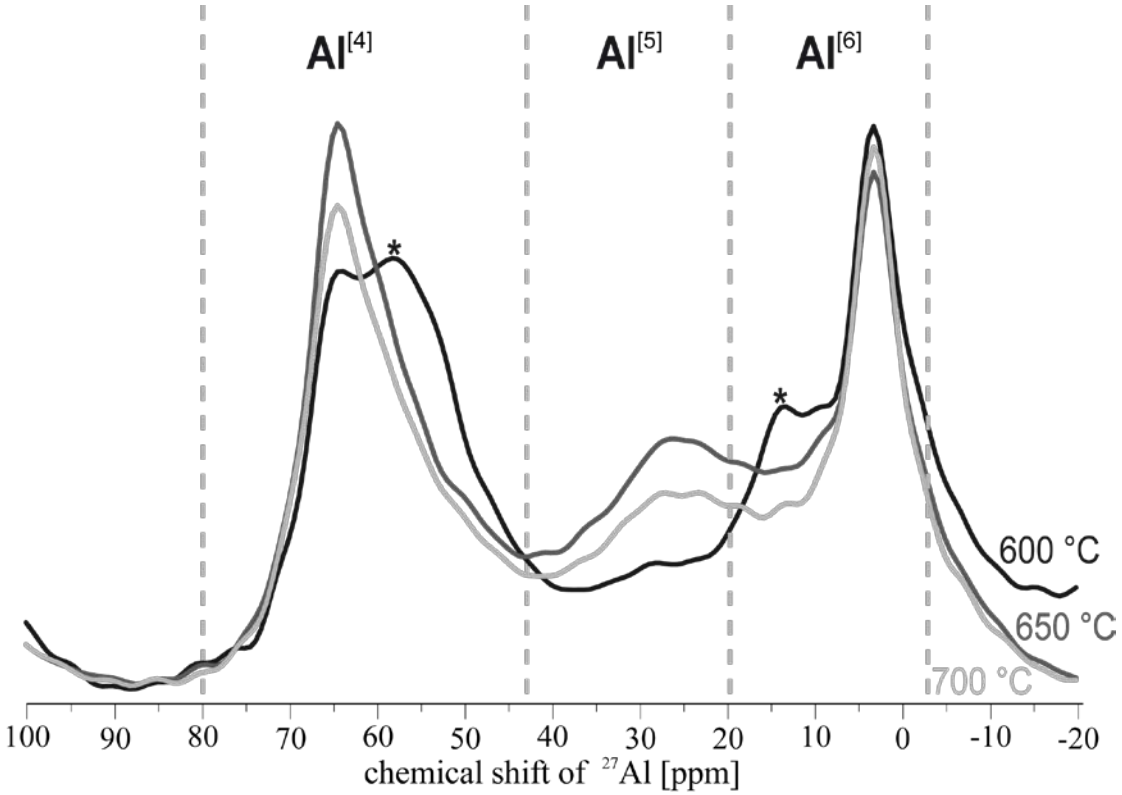

Appendix xxxiv. NMR spectra of ^{27}Al for the Friedland bulk sample heated to 600 °C, 650 °C, and 700 °C, respectively. The Al$^{[5]}$ content increases with increasing temperature. The line widths of Al$^{[4]}$ gets broader because of increasing structural disorder. * spinning sidebands for 600 °C measurement

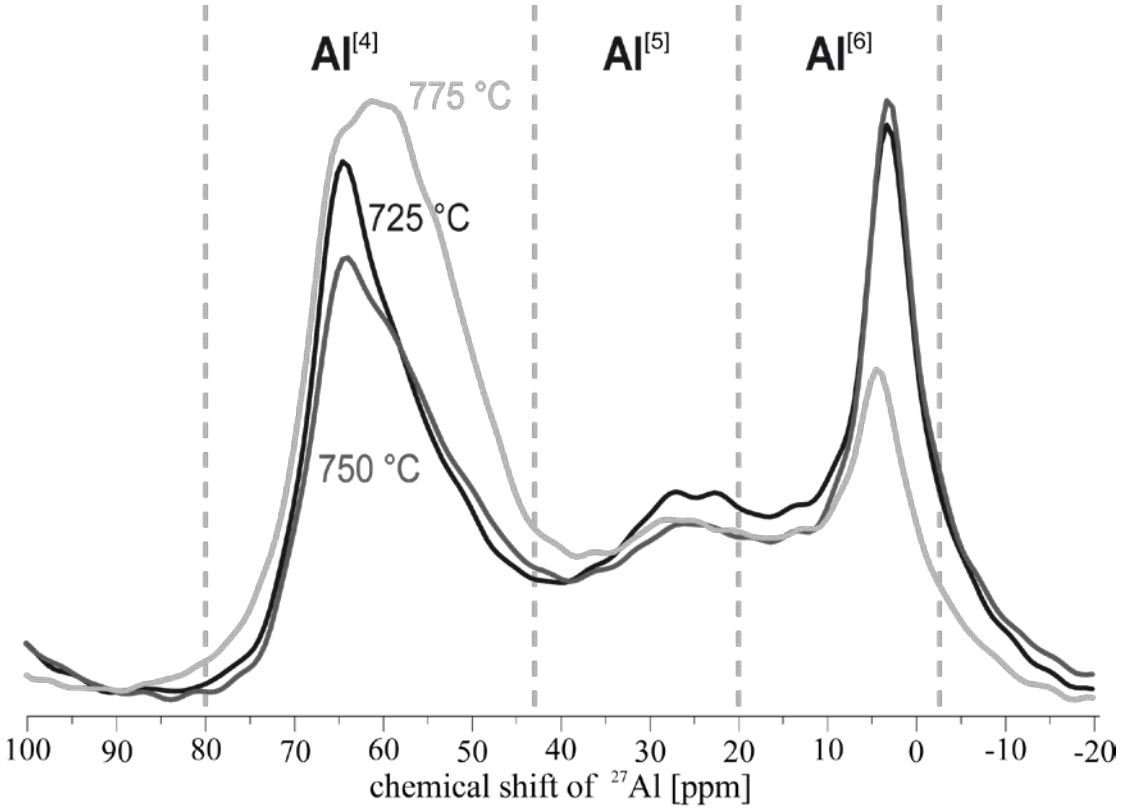

Appendix xxxv. NMR spectra of ^{27}Al for the Friedland bulk sample heated to 725 °C, 750 °C, and 775 °C, respectively. The Al$^{[5]}$ content increases with increasing temperature until 775 °C. The line widths of Al$^{[4]}$ gets broader because of increasing structural disorder.

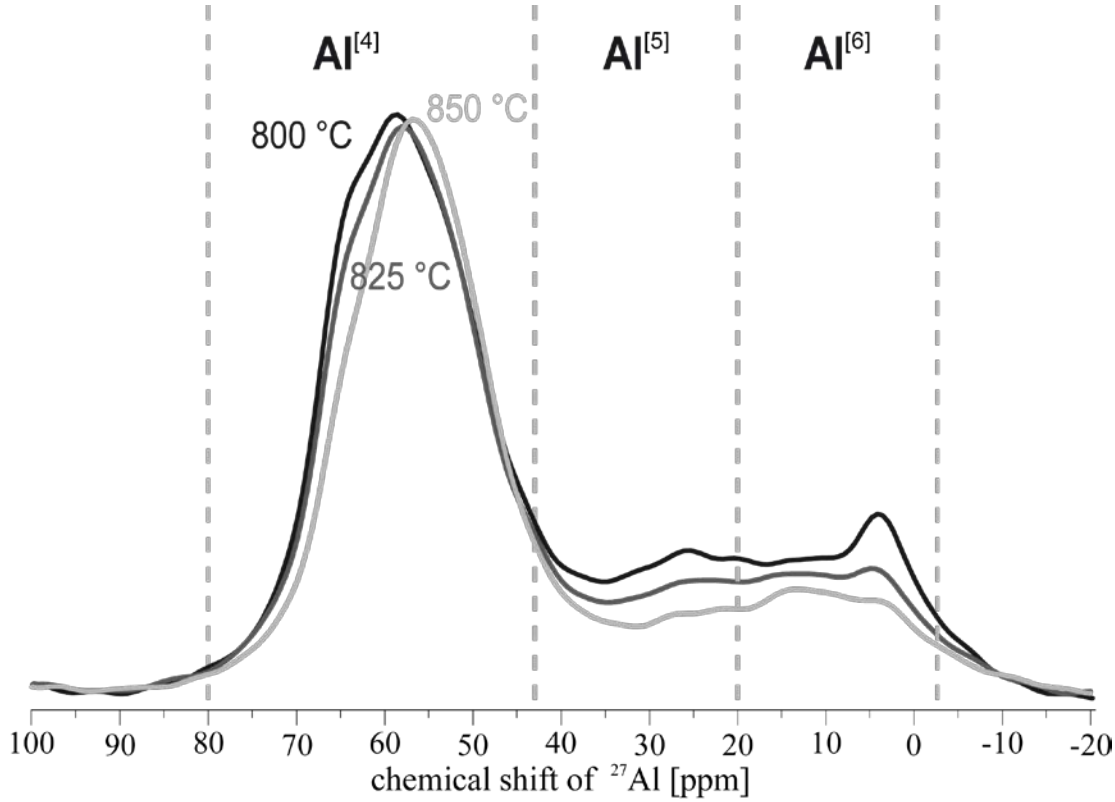

Appendix xxxvi. NMR spectra of ^{27}Al for the Friedland bulk sample heated to 800 °C, 825 °C, and 850 °C, respectively. The Al$^{[5]}$ content decreases with increasing temperature. The line widths of Al$^{[4]}$ gets narrower because of increasing structural order.

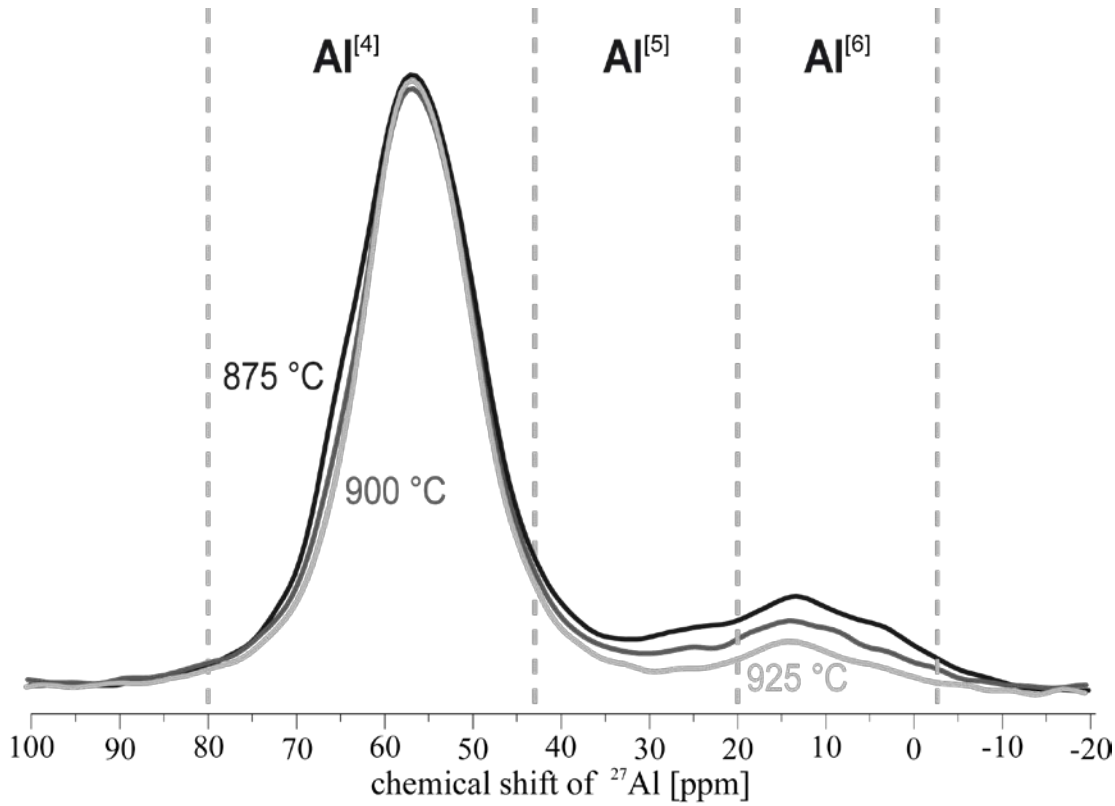

Appendix xxxvii. NMR spectra of ^{27}Al for the Friedland bulk sample heated to 875 °C, 900 °C, and 925 °C, respectively. The Al$^{[5]}$ content decreases with increasing temperature. The line widths of Al$^{[4]}$ gets narrower because of increasing structural order.

Appendix xxxviii. Gausian peaks used to fit NMR spectra of ^{27}Al for the untreated Friedland bulk sample as well as heated between 600-925 °C.

Temperature	Peak 1			Peak 2			Peak 3			Peak 4			Peak 5		
	position [ppm]	width [ppm]	area [%]	position [ppm]	width [ppm]	area [%]	position [ppm]	width [ppm]	area [%]	position [ppm]	width [ppm]	area [%]	position [ppm]	width [ppm]	area [%]
untreated	3.88	6.94	16.48	18.32	12.69	8.68	55.76	9.28	17.59	69.64	11.13	10.71	3.51	15	33.59
600	3.13	4.5	7.76	13.52	7.74	7.85	58.29	4.82	4.75	63.81	9.02	23.85	1.37	13.51	23.06
		VI		spinning sideband				IV			IV			VI	
650	63.09	11.24	15.67	64.93	4.2	3.26	55.74	25.11	25.08	2.95	4.74	5.88	3.39	20.43	25.96
700	63.59	11.39	14.84	65.03	4.37	2.85	56.17	23.89	25.73	3	5.01	8.35	3.03	20.02	25.52
725	63.34	12.14	16.41	64.99	4.84	3.92	55.57	22.35	23.73	2.96	5.09	8.56	2.93	19.82	25.03
750	63.02	12.94	18.93	65.17	4.86	2.61	53.66	20.75	23.36	2.9	5.11	10.09	2.02	19.08	24.21
775	59.96	17.84	51.74	65.64	4.71	2.37	47.78	11.04	3.72	4.08	4.87	3.28	3.56	15.81	11.19
800	58.55	18.26	60.28	65.13	4.69	2.12	45.19	12.99	3.72	3.91	5.80	2.56	0.26	13.42	5.50
825	57.71	18.39	67.36	65.13	4.05	1.42	41.61	11.62	2.84	3.83	7.16	2.45	-1.26	13.80	4.32
850	56.49	17.82	74.11	65.27	2.35	0.30	38.87	10.02	2.79	2.89	3.93	0.32	9.66	23.47	16.25
875	56.51	17.33	79.33	66.02	1.53	0.07	39.32	7.03	1.54	3.22	16.13	3.41	15.38	23.17	12.30
900	56.41	17.14	82.27	66.03	0.27	0.01	39.43	7.35	1.58	5.91	18.00	6.85	20.32	17.65	6.34
925	56.39	12.97	60.94	69.35	14.81	5.31	51.11	19.88	24.18	6.17	16.07	3.15	19.56	24.86	4.77
coordination		**IV**			**IV**			**IV - V**			**VI**			**VI**	

Appendix xxxviii continued. Gausian peaks used to fit NMR spectra of ^{27}Al for the untreated Friedland bulk sample as well as heated between 600-925 °C.

Temperature	Peak 6			Peak 7			Peak 8			Peak 9			$Al^{[4]}$ [%]	$Al^{[5]}$ [%]	$Al^{[6]}$ [%]
	position [ppm]	width [ppm]	area [%]	position [ppm]	width [ppm]	area [%]	position [ppm]	width [ppm]	area [%]	position [ppm]	width [ppm]	area [%]			
untreated	54.25	19.3	13.5										17.62	0.00	82.38
600	54.42	6.95	11.27	8.98	2.51	0.48	24.43	25.33	10.26	49.09	11.56	10.73	48.62	12.68	38.69
	spinning sideband			VI				V			IV				
650	25.78	20.76	24.13	14.19	1.34	0.01							18.93	49.21	31.85
700	25.97	21.52	22.68	13.58	1.19	0.03							17.69	48.41	33.90
725	25.78	21.58	22.32	13.93	1.72	0.04							20.33	46.05	33.63
750	25.78	22.53	20.71	16	4.05	0.11							21.54	44.06	34.40
775	26.27	32.39	27.66	13.40	1.86	0.05							54.10	31.38	14.52
800	25.12	27.79	22.59	10.58	10.40	3.24							62.39	26.31	11.30
825	25.02	22.96	16.22	11.13	11.91	5.38							68.79	19.06	12.15
850	27.77	15.01	5.88	14.06	4.90	0.36							74.40	8.67	16.93
875	31.03	12.75	2.71	13.52	5.77	0.64							79.40	4.25	16.35
900	32.17	11.46	2.08	13.58	7.04	0.88							82.27	3.66	14.07
925	32.40	2.51	0.06	13.89	8.28	1.58							90.44	0.06	9.50
coordination		**V**			**VI**										

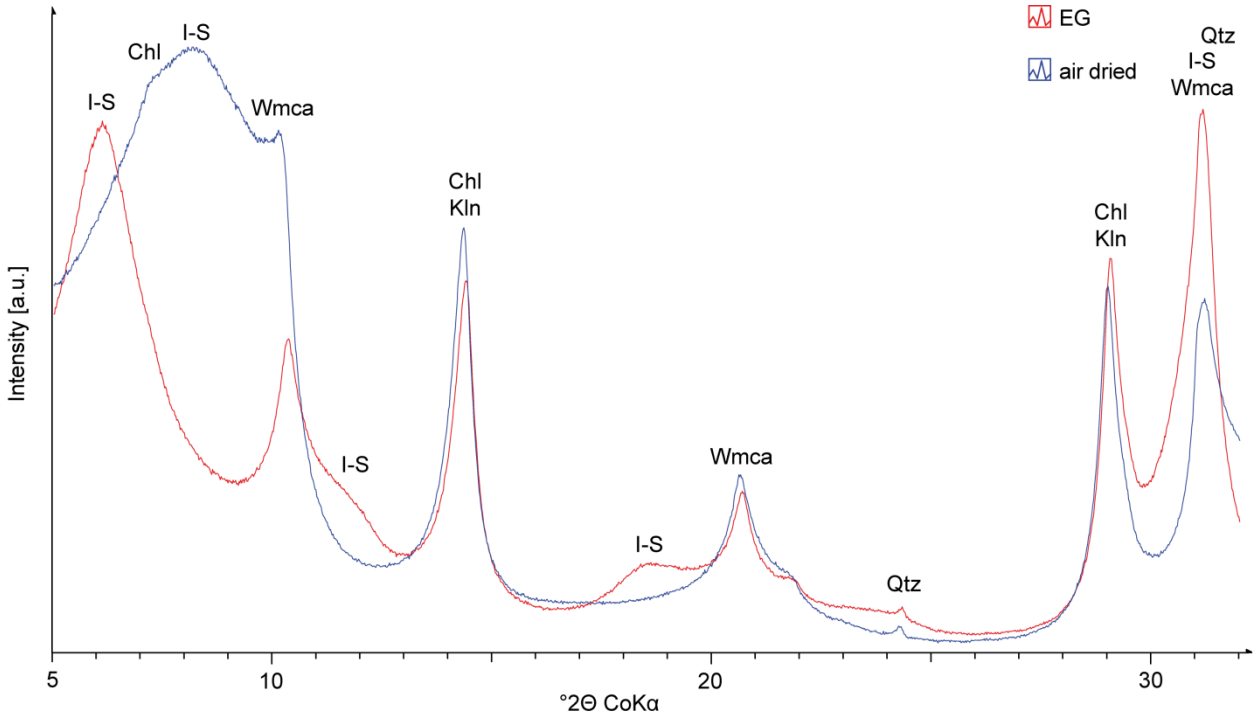

Appendix xxxix. XRD patterns of preferred oriented specimens of untreated Friedland clay bulk material. The major phases are marked. I-S: illite-smectite interstratification, Chl: chlorite, Wmca: white mica, Kln: kaolinite, Qtz: quartz

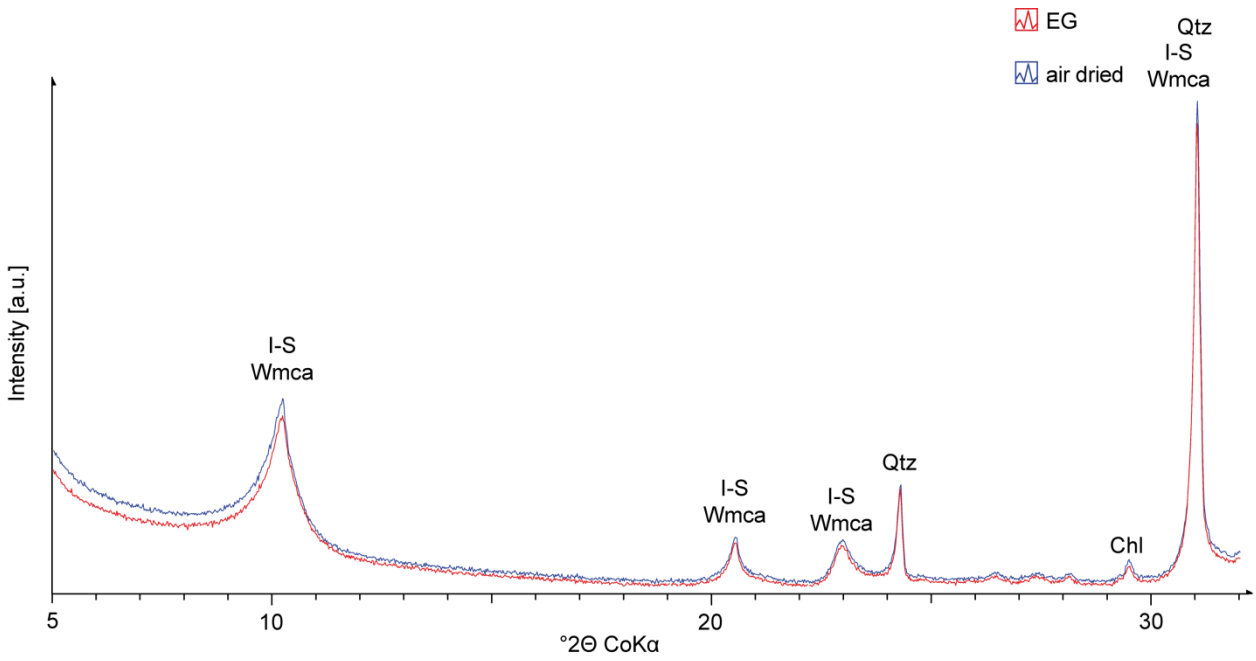

Appendix xl. XRD patterns of preferred oriented specimens of rotary oven heated material (VP1). The major phases are marked. I-S: illite-smectite interstratification, Wmca: white mica, Qtz: quartz, Chl: chlorite

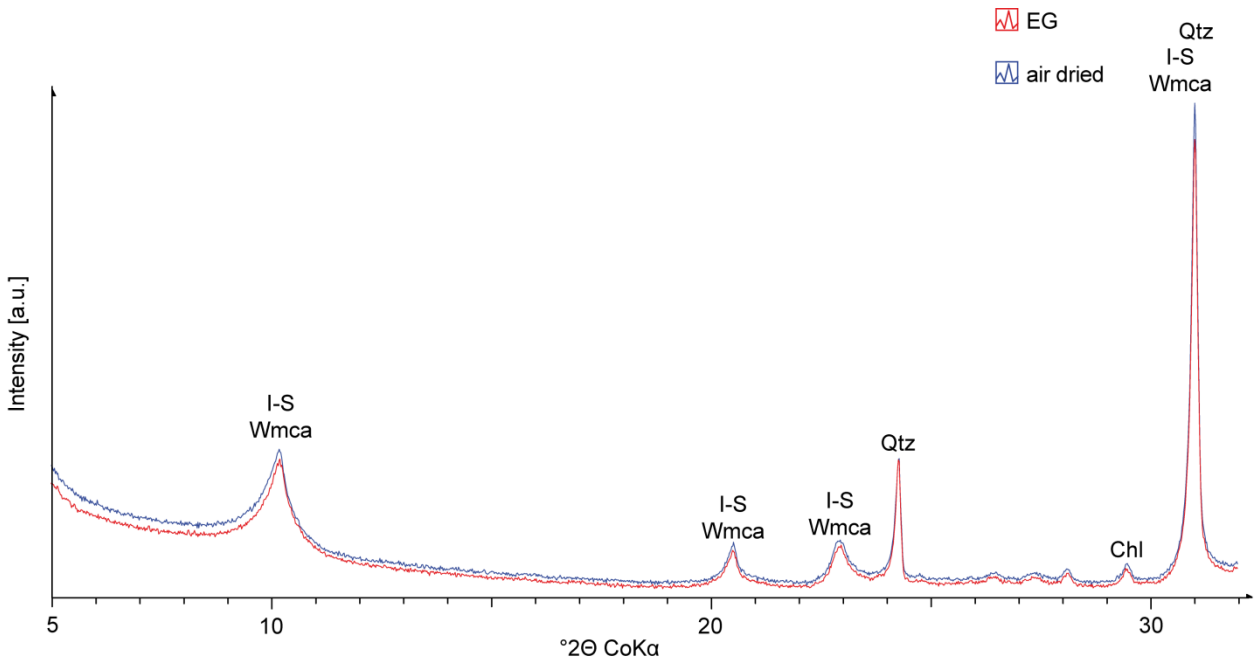

Appendix xli. XRD patterns of preferred oriented specimens of rotary oven heated material (VP2). The major phases are marked. I-S: illite-smectite interstratification, Wmca: white mica, Qtz: quartz, Chl: chlorite

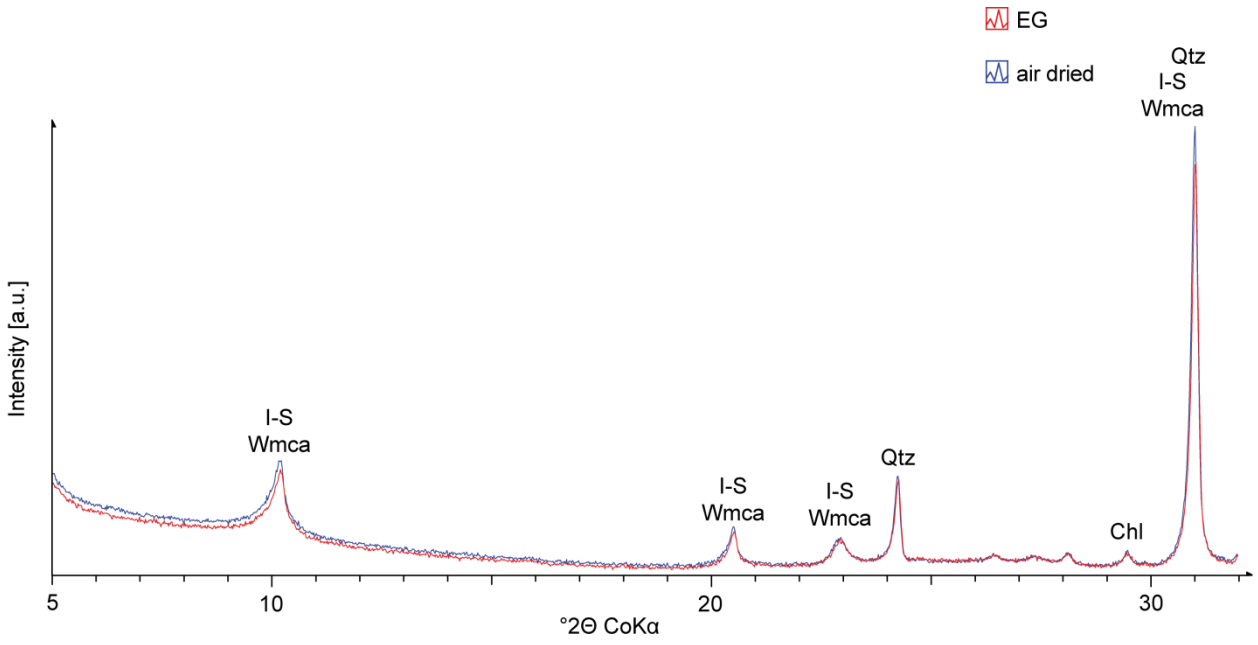

Appendix xlii. XRD patterns of preferred oriented specimens of rotary oven heated material (VP3). The major phases are marked. I-S: illite-smectite interstratification, Wmca: white mica, Qtz: quartz, Chl: chlorite

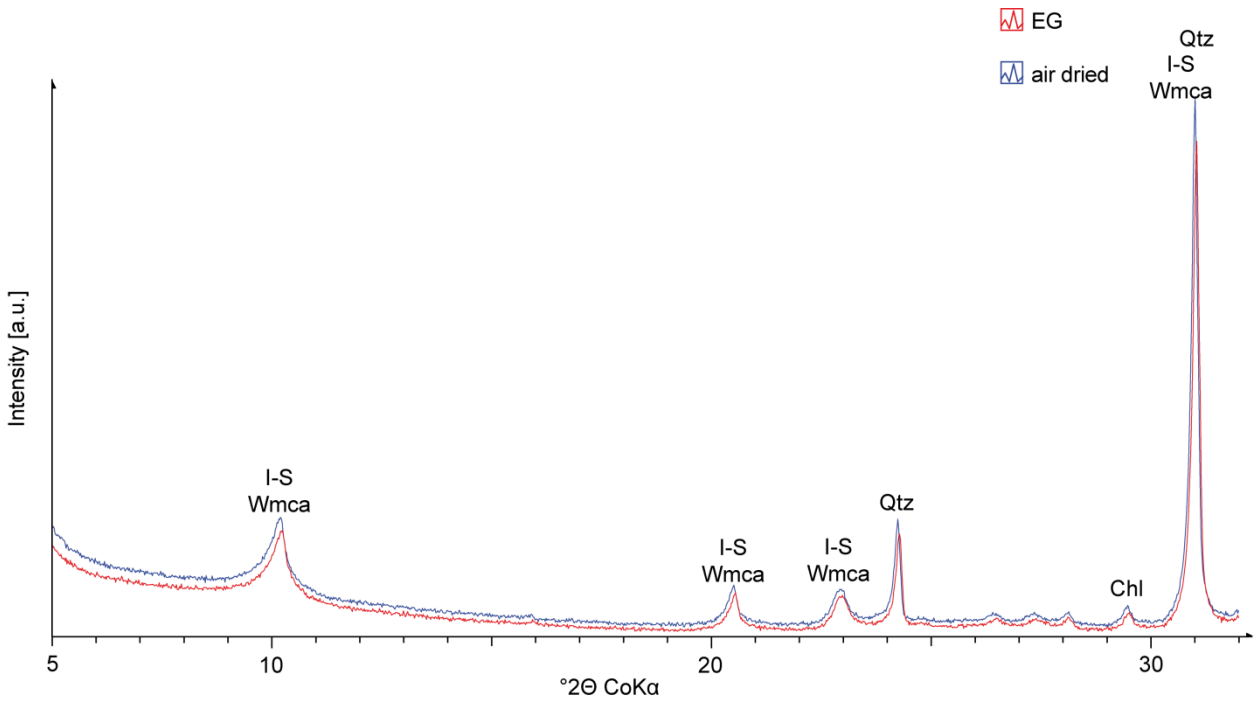

Appendix xliii. XRD patterns of preferred oriented specimens of rotary oven heated material (VP4). The major phases are marked. I-S: illite-smectite interstratification, Wmca: white mica, Qtz: quartz, Chl: chlorite

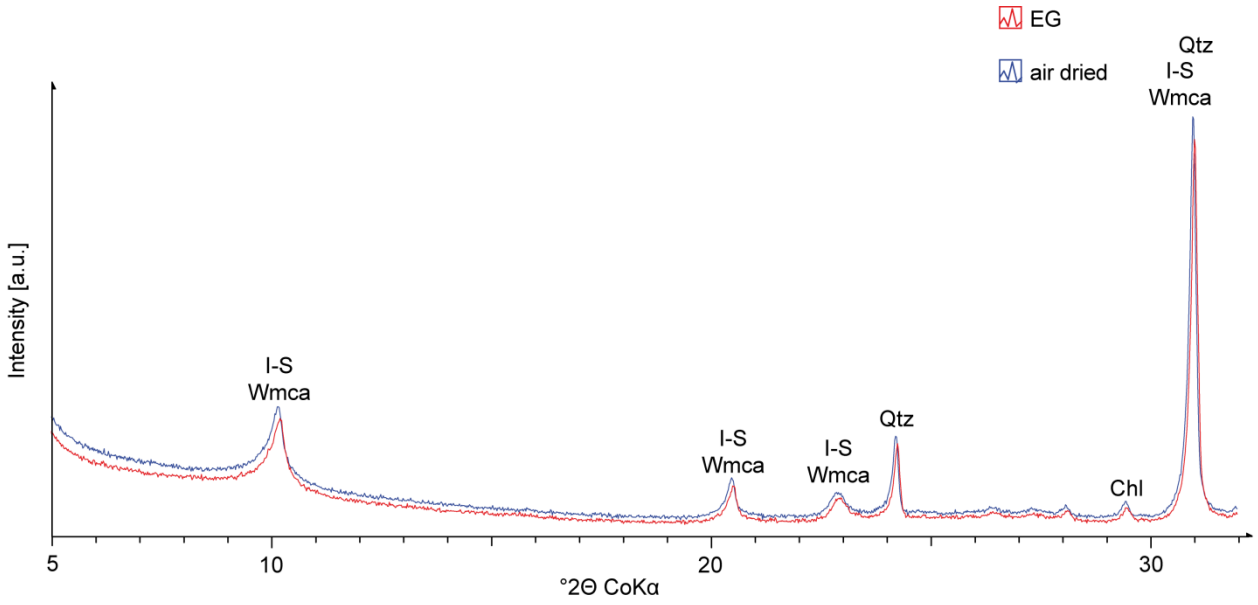

Appendix xliv. XRD patterns of preferred oriented specimens of rotary oven heated material (VP5). The major phases are marked. I-S: illite-smectite interstratification, Wmca: white mica, Qtz: quartz, Chl: chlorite

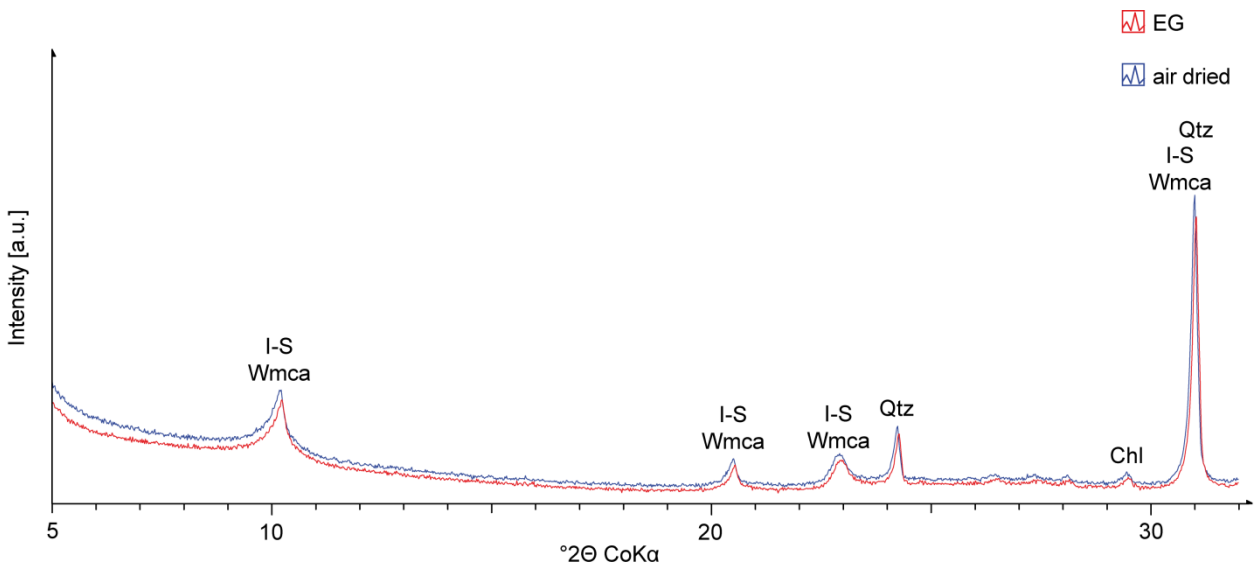

Appendix xlv. XRD patterns of preferred oriented specimens of rotary oven heated material (VP6). The major phases are marked. I-S: illite-smectite interstratification, Wmca: white mica, Qtz: quartz, Chl: chlorite

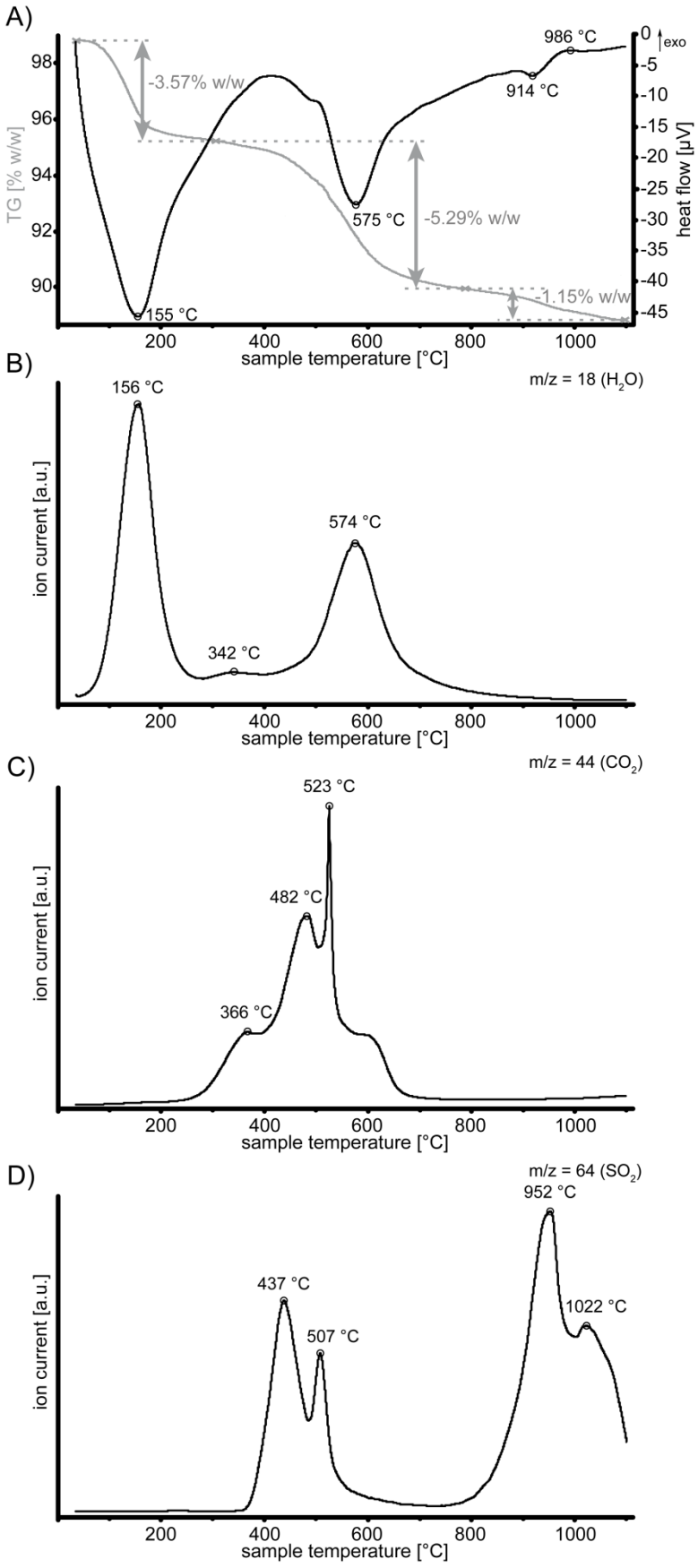

Appendix xlvi. STA-MS curves of the Friedland clay bulk sample using a heating rate of 50 K/min (A-D). A) TG (grey) and DSC (heat flow, black) curve; B) Water ion current; C) CO_2 ion current; D) SO_2 ion current. TG starting value 98.76% w/w, sample amount 101 mg

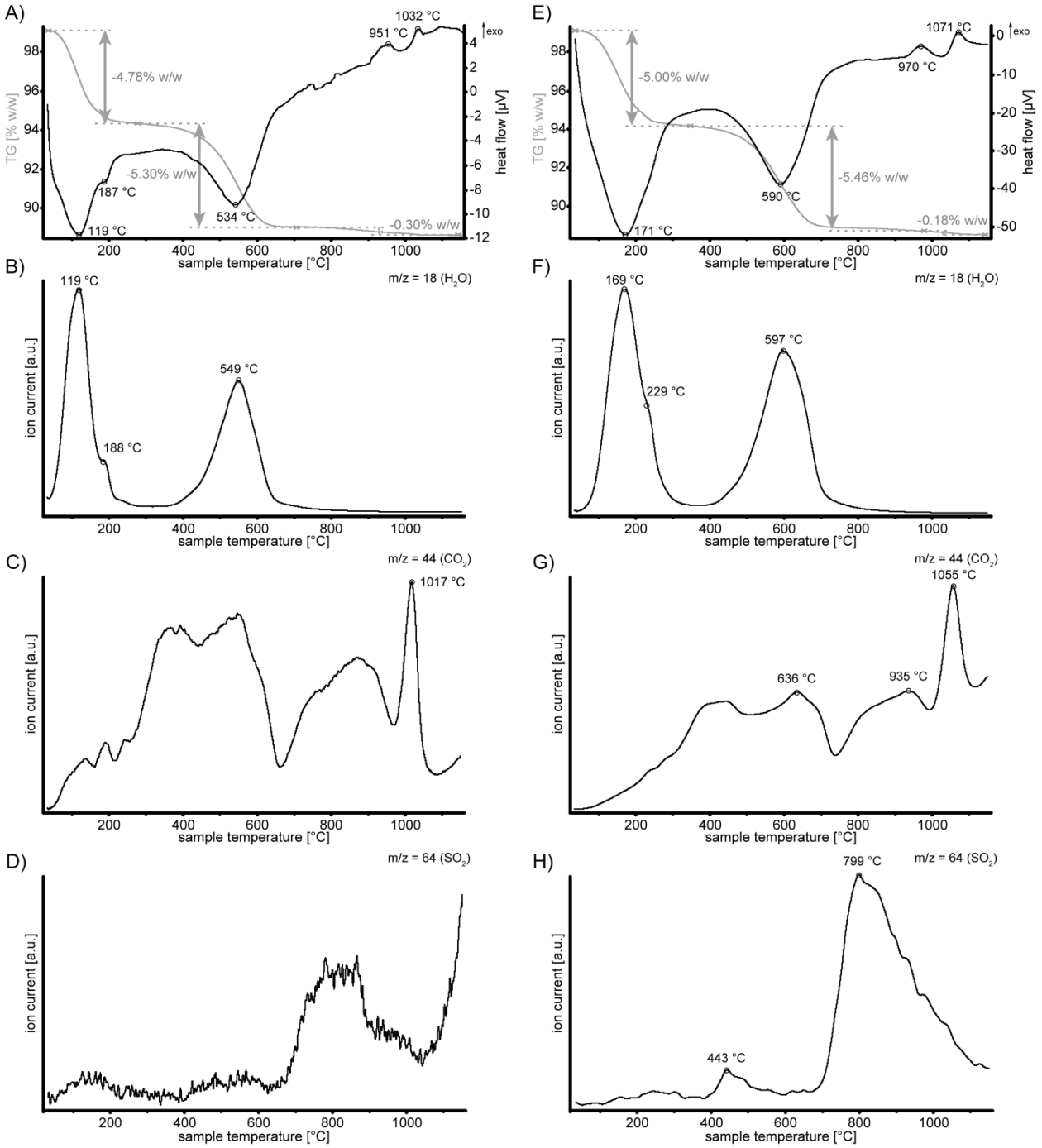

Appendix xlvii. STA-MS curves of the rectorite <0.1 µm fraction using heating rate of 10 K/min (A-D) and 50 K/min (E-H). A) TG (grey) and DSC (heat flow, black) curve; B) Water ion current; C) CO_2 ion current; D) SO_2 ion current; E) TG (grey) and DSC (heat flow, black) curve; F) Water ion current; G) CO_2 ion current; H) SO_2 ion current. TG starting value 10 K/min 99.10% w/w, sample amount 106 mg; TG starting value 50 K/min 99.16% w/w, sample amount 104 mg

Appendix xlviii. Measured voltage and calculated pH values of 875 °C heated Friedland clay bulk material - water suspension. Voltage was measured every minute for 500 minutes (8 h 20 min).

time [min]	voltage [mV]	pH	time [min]	voltage [mV]	pH
0	49.3	7.54	43	52.4	7.49
1	45.7	7.60	44	52.5	7.48
2	44.9	7.62	45	52.7	7.48
3	44.8	7.62	46	52.8	7.48
4	44.8	7.62	47	53.0	7.48
5	45.0	7.62	48	53.1	7.47
6	45.1	7.61	49	53.3	7.47
7	45.3	7.61	50	53.4	7.47
8	45.6	7.61	51	53.6	7.47
9	45.8	7.60	52	53.7	7.46
10	46.1	7.60	53	53.8	7.46
11	46.3	7.59	54	53.9	7.46
12	46.5	7.59	55	54.0	7.46
13	46.8	7.58	56	54.2	7.45
14	46.9	7.58	57	54.3	7.45
15	47.1	7.58	58	54.5	7.45
16	47.4	7.57	59	54.6	7.45
17	47.6	7.57	60	54.7	7.45
18	47.9	7.56	61	54.9	7.44
19	48.1	7.56	62	54.9	7.44
20	48.3	7.56	63	55.1	7.44
21	48.5	7.55	64	55.2	7.44
22	48.7	7.55	65	55.3	7.43
23	48.9	7.55	66	55.4	7.43
24	49.1	7.54	67	55.5	7.43
25	49.3	7.54	68	55.7	7.43
26	49.5	7.54	69	55.8	7.43
27	49.7	7.53	70	56.0	7.42
28	49.9	7.53	71	56.1	7.42
29	50.1	7.53	72	56.1	7.42
30	50.3	7.52	73	56.2	7.42
31	50.5	7.52	74	56.3	7.42
32	50.6	7.52	75	56.4	7.42
33	50.8	7.51	76	56.5	7.41
34	50.9	7.51	77	56.6	7.41
35	51.1	7.51	78	56.7	7.41
36	51.3	7.51	79	56.8	7.41
37	51.4	7.50	80	56.9	7.41
38	51.6	7.50	81	57.0	7.41
39	51.7	7.50	82	57.1	7.40
40	51.9	7.49	83	57.2	7.40
42	52.2	7.49	84	57.3	7.40

Appendix xlviii continued. Measured voltage and calculated pH values of 875 °C heated Friedland clay bulk material - water suspension. Voltage was measured every minute for 500 minutes (8 h 20 min).

time [min]	voltage [mV]	pH	time [min]	voltage [mV]	pH
85	57.4	7.40	127	59.9	7.35
86	57.5	7.40	128	59.9	7.35
87	57.6	7.39	129	60.0	7.35
88	57.7	7.39	130	60.0	7.35
89	57.8	7.39	131	60.1	7.35
90	57.9	7.39	132	60.2	7.35
91	58.0	7.39	133	60.2	7.35
92	58.1	7.39	134	60.2	7.35
93	58.3	7.38	135	60.3	7.35
94	58.3	7.38	136	60.3	7.35
95	58.4	7.38	137	60.4	7.35
96	58.5	7.38	138	60.5	7.34
97	58.5	7.38	139	60.5	7.34
98	58.6	7.38	140	60.6	7.34
99	58.7	7.38	141	60.6	7.34
100	58.8	7.37	142	60.7	7.34
101	58.9	7.37	143	60.8	7.34
102	59.0	7.37	144	60.8	7.34
103	59.0	7.37	145	60.8	7.34
104	59.1	7.37	146	60.9	7.34
105	59.2	7.37	147	60.9	7.34
106	59.3	7.37	148	61.0	7.33
107	59.4	7.36	149	61.0	7.33
108	59.4	7.36	150	61.1	7.33
109	59.5	7.36	151	61.1	7.33
110	59.6	7.36	152	61.2	7.33
111	59.7	7.36	153	61.2	7.33
112	59.8	7.36	154	61.3	7.33
113	59.8	7.36	155	61.3	7.33
114	59.9	7.35	156	61.4	7.33
115	60.0	7.35	157	61.4	7.33
116	60.0	7.35	158	61.5	7.33
117	60.1	7.35	159	61.5	7.33
118	60.2	7.35	160	61.6	7.33
119	60.2	7.35	161	61.6	7.32
120	60.3	7.35	162	61.7	7.32
121	60.2	7.35	163	61.8	7.32
122	60.0	7.35	164	61.8	7.32
123	59.9	7.35	165	61.9	7.32
124	59.9	7.35	166	61.9	7.32
125	59.9	7.35	167	62.0	7.32
126	59.9	7.35	168	62.0	7.32

Appendix xlviii continued. Measured voltage and calculated pH values of 875 °C heated Friedland clay bulk material - water suspension. Voltage was measured every minute for 500 minutes (8 h 20 min).

time [min]	voltage [mV]	pH	time [min]	voltage [mV]	pH
169	62.1	7.32	211	64.4	7.28
170	62.2	7.31	212	64.5	7.27
171	62.3	7.31	213	64.6	7.27
172	62.3	7.31	214	64.6	7.27
173	62.4	7.31	215	64.6	7.27
174	62.5	7.31	216	64.7	7.27
175	62.6	7.31	217	64.8	7.27
176	62.6	7.31	218	64.8	7.27
177	62.7	7.31	219	64.9	7.27
178	62.7	7.30	220	65.0	7.27
179	62.8	7.30	221	65.0	7.26
180	63.0	7.30	222	65.0	7.26
181	63.1	7.30	223	65.1	7.26
182	63.2	7.30	224	65.2	7.26
183	63.2	7.30	225	65.2	7.26
184	63.3	7.30	226	65.2	7.26
185	63.3	7.30	227	65.3	7.26
186	63.3	7.29	228	65.3	7.26
187	63.4	7.29	229	65.4	7.26
188	63.4	7.29	230	65.4	7.26
189	63.4	7.29	231	65.5	7.26
190	63.4	7.29	232	65.5	7.26
191	63.4	7.29	233	65.6	7.26
192	63.5	7.29	234	65.6	7.25
193	63.6	7.29	235	65.6	7.25
194	63.6	7.29	236	65.7	7.25
195	63.7	7.29	237	65.8	7.25
196	63.8	7.29	238	65.8	7.25
197	63.8	7.29	239	65.9	7.25
198	63.9	7.28	240	65.9	7.25
199	63.9	7.28	241	65.9	7.25
200	63.9	7.28	242	66.0	7.25
201	64.0	7.28	243	66.0	7.25
202	64.1	7.28	244	66.1	7.25
203	64.2	7.28	245	66.1	7.25
204	64.2	7.28	246	66.2	7.24
205	64.3	7.28	247	66.2	7.24
206	64.3	7.28	248	66.3	7.24
207	64.4	7.28	249	66.3	7.24
208	64.4	7.28	250	66.4	7.24
209	64.4	7.28	251	66.4	7.24
210	64.4	7.28	252	66.5	7.24

Appendix xlviii continued. Measured voltage and calculated pH values of 875 °C heated Friedland clay bulk material - water suspension. Voltage was measured every minute for 500 minutes (8 h 20 min).

time [min]	voltage [mV]	pH	time [min]	voltage [mV]	pH
253	66.6	7.24	295	68.5	7.20
254	66.6	7.24	296	68.5	7.20
255	66.7	7.24	297	68.6	7.20
256	66.7	7.24	298	68.7	7.20
257	66.8	7.23	299	68.8	7.20
258	66.8	7.23	300	68.8	7.20
259	66.9	7.23	301	68.9	7.20
260	66.9	7.23	302	68.9	7.20
261	67.0	7.23	303	68.9	7.20
262	67.0	7.23	304	69.0	7.20
263	67.0	7.23	305	69.0	7.19
264	67.1	7.23	306	69.1	7.19
265	67.2	7.23	307	69.2	7.19
266	67.2	7.23	308	69.2	7.19
267	67.3	7.23	309	69.3	7.19
268	67.3	7.22	310	69.4	7.19
269	67.4	7.22	311	69.4	7.19
270	67.5	7.22	312	69.4	7.19
271	67.5	7.22	313	69.5	7.19
272	67.6	7.22	314	69.5	7.19
273	67.6	7.22	315	69.6	7.19
274	67.7	7.22	316	69.6	7.18
275	67.7	7.22	317	69.6	7.18
276	67.8	7.22	318	69.7	7.18
277	67.8	7.22	319	69.7	7.18
278	67.8	7.22	320	69.8	7.18
279	67.8	7.22	321	69.8	7.18
280	67.9	7.21	322	69.9	7.18
281	67.9	7.21	323	70.0	7.18
282	67.9	7.21	324	70.1	7.18
283	68.0	7.21	325	70.1	7.18
284	68.0	7.21	326	70.2	7.17
285	68.1	7.21	327	70.3	7.17
286	68.1	7.21	328	70.3	7.17
287	68.2	7.21	329	70.4	7.17
288	68.2	7.21	330	70.4	7.17
289	68.3	7.21	331	70.4	7.17
290	68.3	7.21	332	70.5	7.17
291	68.4	7.21	333	70.6	7.17
292	68.4	7.21	334	70.6	7.17
293	68.5	7.20	335	70.6	7.17
294	68.5	7.20	336	70.7	7.16

Appendix xlviii continued. Measured voltage and calculated pH values of 875 °C heated Friedland clay bulk material - water suspension. Voltage was measured every minute for 500 minutes (8 h 20 min).

time [min]	voltage [mV]	pH	time [min]	voltage [mV]	pH
337	70.8	7.16	379	72.6	7.13
338	70.9	7.16	380	72.6	7.13
339	70.9	7.16	381	72.7	7.13
340	70.9	7.16	382	72.7	7.13
341	71.0	7.16	383	72.7	7.13
342	71.0	7.16	384	72.8	7.13
343	71.0	7.16	385	72.8	7.13
344	71.1	7.16	386	72.9	7.13
345	71.2	7.16	387	72.9	7.13
346	71.2	7.16	388	73.0	7.13
347	71.3	7.16	389	73.0	7.13
348	71.3	7.16	390	73.0	7.13
349	71.3	7.15	391	73.0	7.12
350	71.4	7.15	392	73.1	7.12
351	71.4	7.15	393	73.2	7.12
352	71.4	7.15	394	73.2	7.12
353	71.5	7.15	395	73.2	7.12
354	71.6	7.15	396	73.2	7.12
355	71.7	7.15	397	73.3	7.12
356	71.7	7.15	398	73.3	7.12
357	71.7	7.15	399	73.4	7.12
358	71.8	7.15	400	73.4	7.12
359	71.9	7.15	401	73.5	7.12
360	71.9	7.14	402	73.5	7.12
361	71.9	7.14	403	73.5	7.12
362	72.0	7.14	404	73.6	7.12
363	72.0	7.14	405	73.6	7.11
364	72.0	7.14	406	73.6	7.11
365	72.0	7.14	407	73.7	7.11
366	72.1	7.14	408	73.7	7.11
367	72.1	7.14	409	73.7	7.11
368	72.1	7.14	410	73.8	7.11
369	72.1	7.14	411	73.8	7.11
370	72.2	7.14	412	73.9	7.11
371	72.2	7.14	413	73.9	7.11
372	72.3	7.14	414	73.9	7.11
373	72.3	7.14	415	74.0	7.11
374	72.4	7.14	416	74.0	7.11
375	72.4	7.14	417	74.1	7.11
376	72.4	7.13	418	74.1	7.11
377	72.5	7.13	419	74.2	7.11
378	72.6	7.13	420	74.2	7.10

Appendix xlviii continued. Measured voltage and calculated pH values of 875 °C heated Friedland clay bulk material - water suspension. Voltage was measured every minute for 500 minutes (8 h 20 min).

time [min]	voltage [mV]	pH	time [min]	voltage [mV]	pH
421	74.2	7.10	463	76.3	7.07
422	74.3	7.10	464	76.3	7.07
423	74.3	7.10	465	76.4	7.07
424	74.3	7.10	466	76.4	7.07
425	74.4	7.10	467	76.4	7.06
426	74.4	7.10	468	76.5	7.06
427	74.5	7.10	469	76.5	7.06
428	74.5	7.10	470	76.6	7.06
429	74.5	7.10	471	76.7	7.06
430	74.6	7.10	472	76.7	7.06
431	74.6	7.10	473	76.8	7.06
432	74.7	7.10	474	76.8	7.06
433	74.7	7.09	475	76.8	7.06
434	74.8	7.09	476	76.9	7.06
435	74.8	7.09	477	77.0	7.06
436	74.9	7.09	478	77.0	7.05
437	74.9	7.09	479	77.1	7.05
438	75.0	7.09	480	77.1	7.05
439	75.0	7.09	481	77.2	7.05
440	75.1	7.09	482	77.2	7.05
441	75.1	7.09	483	77.3	7.05
442	75.2	7.09	484	77.3	7.05
443	75.2	7.09	485	77.4	7.05
444	75.3	7.09	486	77.4	7.05
445	75.3	7.08	487	77.5	7.05
446	75.4	7.08	488	77.5	7.05
447	75.5	7.08	489	77.6	7.05
448	75.5	7.08	490	77.6	7.04
449	75.6	7.08	491	77.7	7.04
450	75.6	7.08	492	77.7	7.04
451	75.7	7.08	493	77.8	7.04
452	75.7	7.08	494	77.9	7.04
453	75.7	7.08	495	77.9	7.04
454	75.8	7.08	496	78.0	7.04
455	75.8	7.08	497	78.0	7.04
456	75.9	7.07	498	78.1	7.04
457	76.0	7.07	499	78.2	7.04
458	76.0	7.07	500	78.2	7.03
459	76.1	7.07			
460	76.1	7.07			
461	76.2	7.07			
462	76.2	7.07			

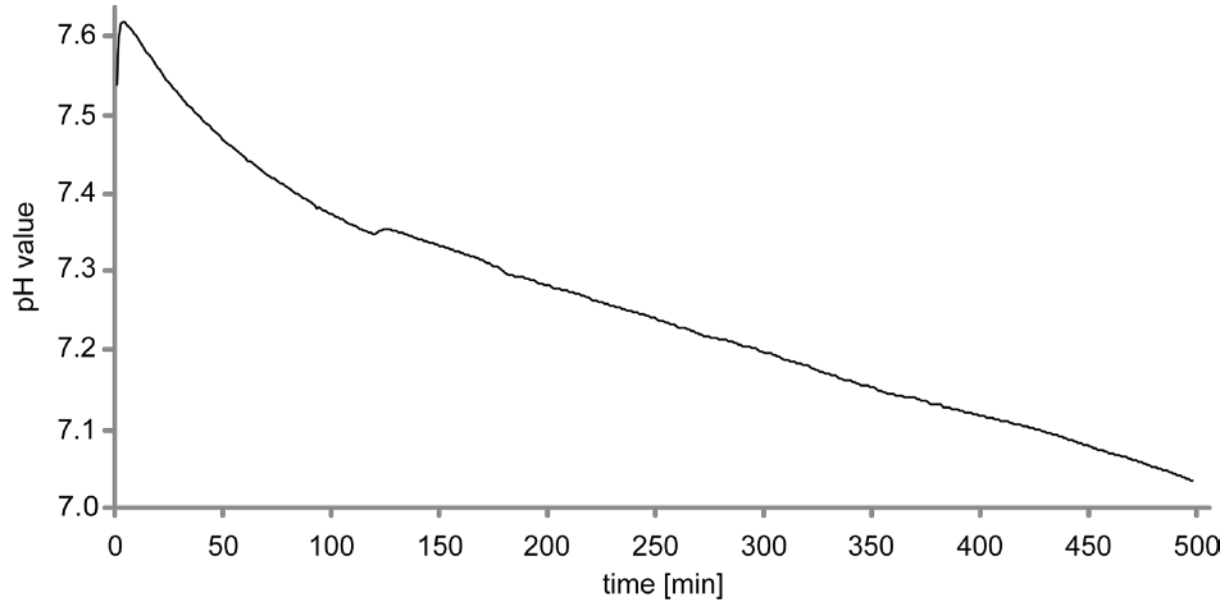

Appendix xlix. pH values of 875 °C heated Friedland clay bulk material - water suspension measured every minute for 500 minutes (8 h 20 min).

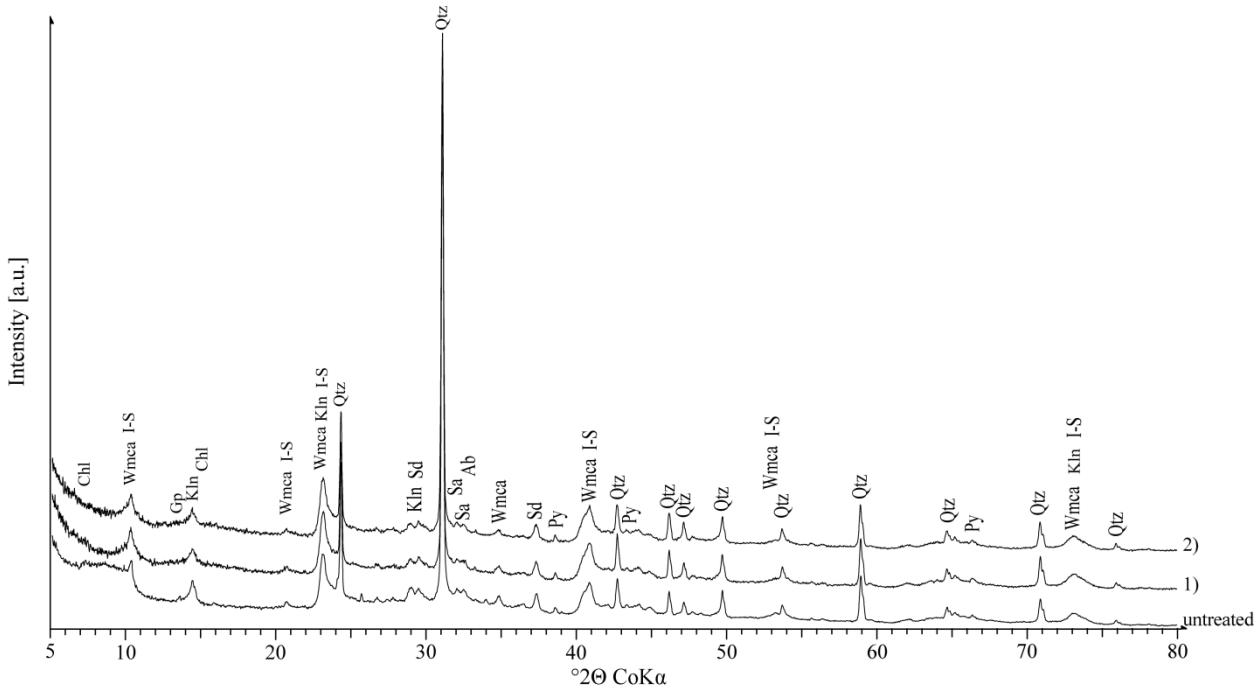

Appendix l. XRD patterns of powdered Friedland clay bulk material. From lower to upper pattern: untreated clay, 1) 30 g milled with Fritsch Pulverisette 7 for 11 h; 2) 30 g milled with Fritsch Pulverisette 7 for 16 h. Chl: chlorite, I-S: illite-smectite interstratification, Wmca: white mica, Gp: gypsum, Kln: kaolinite, Qtz: quartz, Sd: siderite, Sa: sanidine, Ab: albite, Py: pyrite

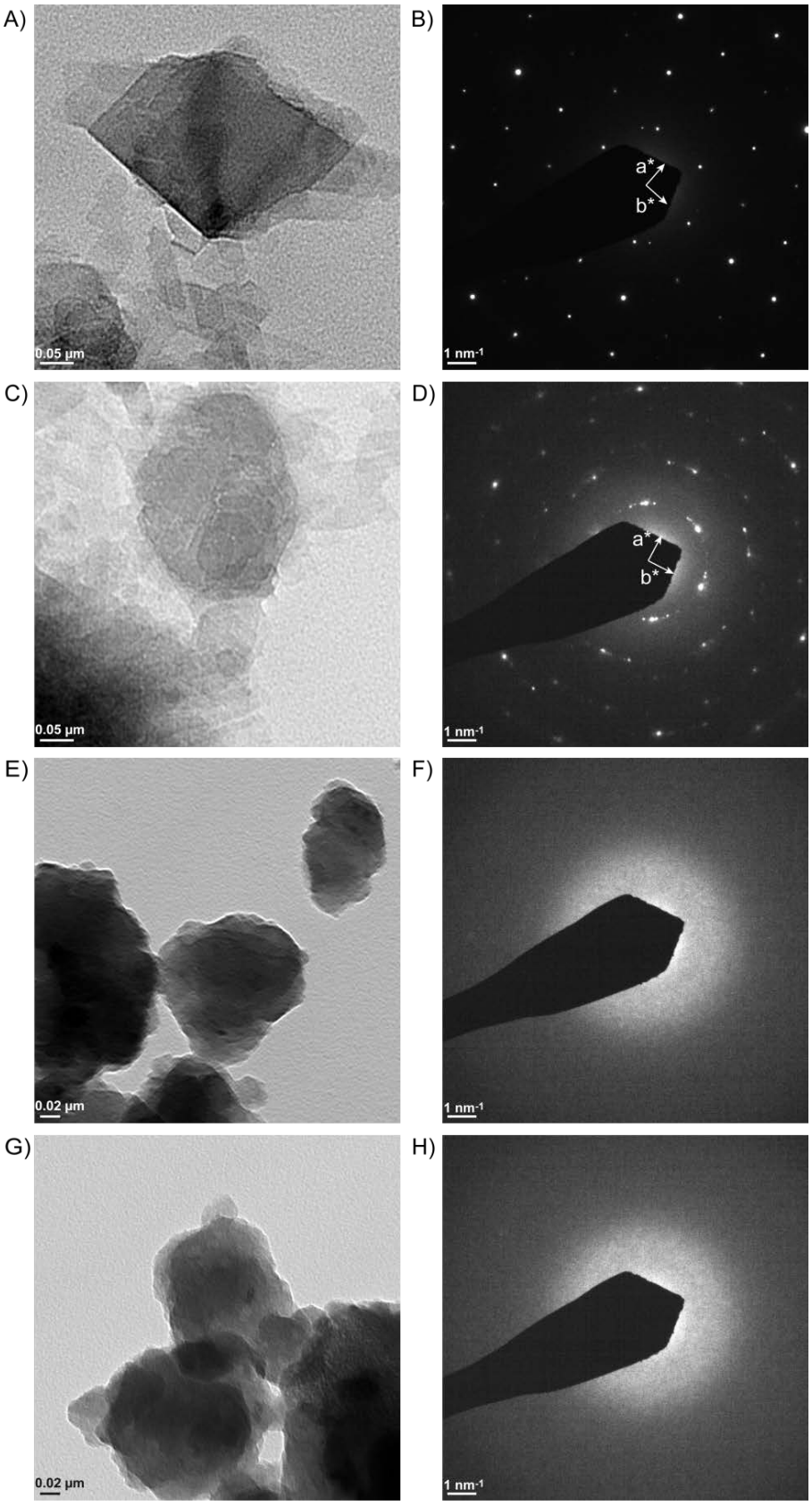

Appendix li. Electron micrographs and selected area electron diffraction patterns (SAED) of powdered Friedland clay bulk material. A) electron micrograph of untreated clay particle with B) typical pseudo-hexagonal SAED pattern, C) electron micrograph of overlaying clay particles with D) overlapping SAED patterns, and electron micrographs of milled clay particles (E and G) with no diffraction pattern due to highly disordered structures (F and H).

Appendix lii. Compressive strengths of geopolymer binders based on Friedland clay, heated to temperatures between 775 °C and 925 °C in steps of 25 °C.

Calcination temperature [°C]	Compressive strength [N/mm²]								Average compressive strength [N/mm²]
775	2.1	--	--	--	--	--	--	--	2
800	2.1	--	--	--	--	--	--	--	2
825	3.8	4.7	3.8	--	--	--	--	--	4
850	17.6	8.8	10.0	9.4	8.3	--	--	--	11
875	21.8	13.6	24.2	14.3	13.0	27.1	24.8	21.1	20
900	21.8	21.8	16.9	20.4	14.9	11.8	11.8	16.2	17
925	8.8	10.6	18.3	18.3	18.3	--	--	--	15